# TRANSPARENT MICROELECTRODES FOR ELECTROPHYSIOLOGICAL RECORDING AND ELECTROCHEMICAL SENSING

By

Weiyang Yang

## A DISSERTATION

Submitted to
Michigan State University
in partial fulfillment of the requirements
for the degree of

Electrical Engineering——Doctor of Philosophy

2021

#### **ABSTRACT**

# TRANSPARENT MICROELECTRODES FOR ELECTROPHYSIOLOGICAL RECORDING AND ELECTROCHEMICAL SENSING

By

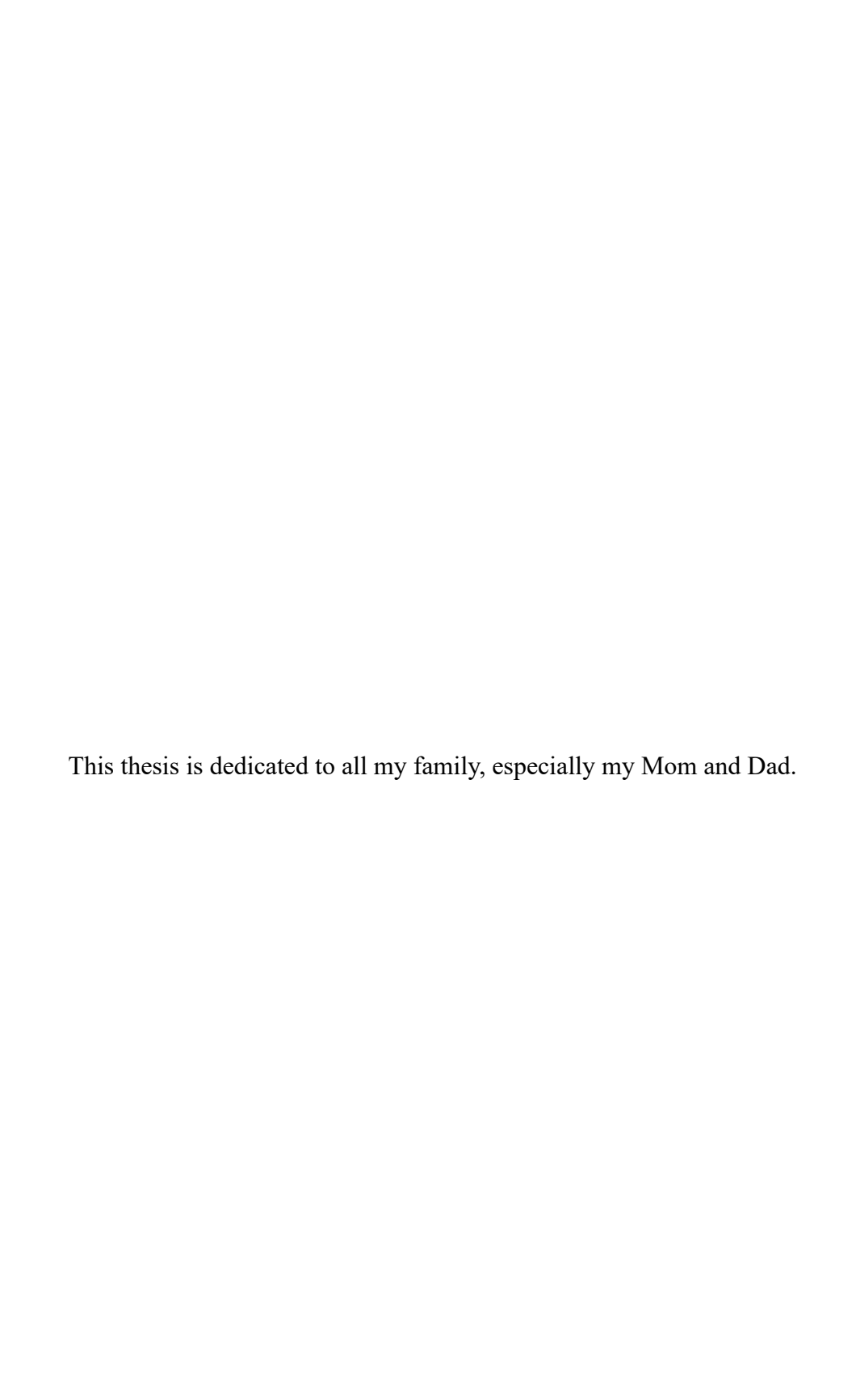
## Weiyang Yang

Indium Tin Oxide (ITO) is a well-known n-type semiconductor material that is often utilized in transparent microelectrodes. ITO has high conductivity, excellent transparency over the entire visible spectrum due to a large bandgap of around 4 eV, as well as confirmed biocompatibility. Because of numerous advantages of ITO, in this dissertation, ITO as a base material will be applied in both electrophysiological recording and electrochemical sensing. Optogenetics is a revolutionary neuromodulation technique that utilizes light to excite or inhibit the activity of genetically targeted neurons, expressing light-sensitive opsin proteins. To fully realize the potential of the optogenetics tools, neural interface devices with both recording and stimulating capabilities are vital for future engineering development, and improving their spatial precision is a topic of constant research. Conventional transparent recording microelectrodes made of a single material. such ITO. ultrathin metals. graphene, and poly-(3, 4-ethylene dioxythiophene)/poly(styrene sulfonate) (PEDOT:PSS), have limitations and hardly possess the desired combination of broadband transmittance, low electrical resistivity, mechanical flexibility, and biocompatibility.

One direction of this dissertation work is to develop multilayered electrophysiological microelectrodes with high transparency, outstanding conductivity, low electrochemical impedance, high charge storage capacity, excellent mechanical properties, and ultra-flexibility. Chapter 1

briefly introduced the background, current challenges, and motivations of this dissertation. Chapter 2 concluded a review of electrical materials for neurophysiology recording implants. Chapter 3 proposed a probe with a combined ITO-PEDOT:PSS electrode configuration by spinning thin PEDOT:PSS films on ITO microelectrodes, for applications in low-impedance neural recordings. The characteristics of the ITO-PEDOT:PSS microelectrodes were analyzed as a preliminary study for the following transparent electrophysiology recording array research. Chapter 4 reported an ultra-flexible, conductive, transparent thin film using a PEDOT:PSS-ITO-Ag-ITO multilayer structure on Parylene C deposited at room temperature. The material characterization demonstrated enhanced conductivity, remarkable and wavelength-tunable transmittance, significantly reduced electrochemical impedance, increased charge storage capacity, good stability, good adhesion, and confirmed mechanical properties of the combined film. Next, Chapter 5 demonstrated two 32-channel transparent µECoG arrays using this PEDOT:PSS-ITO-Ag-ITO multilayered thin film structure on Parylene C. These two µECoG arrays proved to work effectively in vivo for the electrophysiological detection in the living brain tissue. Last but not least, Chapter 6 first discussed the ongoing work to develop a 120-channel high spatial resolution transparent micro-ECoG array. The other subsection of this chapter is to fabricate an ITO-based transparent and miniaturized electrochemical sensor for continuous and quantitative monitoring of the concentrations of copper (Cu) and manganese (Mn) ions in bodies and soil environment by utilizing Differential Pulse Stripping Voltammetry (DPSV).

Copyright by WEIYANG YANG 2021



#### **ACKNOWLEDGEMENTS**

First and foremost, I would like to acknowledge and offer my special thanks to my respectful supervisor, Prof. Wen Li. Her invaluable advice, continuous support, far-sighted insight, and patience led me to correctly conduct and achieve my research for my PhD study. Her rational and critical thinking also taught me how to sharpen my thinking and become a qualified and excellent researcher.

Secondly, I would like to express my sincere gratitude to my committee members: Prof. Qi Hua Fan, Prof. Tim Hogan, and Prof. Peter Lillehoj for their helpful support and useful suggestions for my PhD study. I owe special thanks to Prof. Qi Hua Fan whose course named Thin Film Optics contributed to the significant part of my PhD research work. In addition, both Prof. Tim Hogan and Prof. Peter Lillehoj gave valuable comments and their assistance at every stage of my research project.

Next, I would like to extend my sincere thanks to our collaborators: Prof. Arthur Weber, Prof. Zhen Qiu, Prof. Aitor Aguire, Prof. Christina Chan and Prof. Yaoyao Jia for their cooperation opportunities and technical guidance. In addition, I would like to thank their graduate students and postdocs: Cheng-You Yao, Bo Li, Yan Lewis-Israeli, Brett Volmert, Dr. Maheshwar Shrestha, Dr. Xue Jiang and Dr. Ryan Thompson for collaborations on projects.

Meanwhile, I would like to express my appreciation to my colleagues at Microtechnology Lab: Dr. Bin Fan, Dr. Wasif Kha, Dr. Mohannad Hossein Mazaheri Kouhani, Yue Guo and Yan Gong. I also want to acknowledge other previously our lab's independent researchers Jiajia Wu, Rui Luo, Emma

Savage and Anthony Doan for their help and contributions to my projects. Besides, I would like to thank other colleagues at Michigan State University, especially Dr. Baokang Bi from Keck Cleanroom, Mr. Brian Wright from ECE shop, Ms. Roxanne Peacock from ECE order office and Mr. Karl Dersch from ERC Cleanroom for their help, support, and training.

As a female engineering PhD student, I also would like to thank my friends in and out of campus, especially some females also majored in engineering. Their support, accompany, and communication gave me great courage to pursue and finish up my PhD study.

Last but not least, I would like to thank my family for their selfless and endless support all the time to give me enough encouragement to finish my studies.

# TABLE OF CONTENTS

LIST OF TABLES	xi
LIST OF FIGURES	xii
KEY TO ABBREVIATIONS	xviii
CHAPTER 1: Introduction	1
CHAPTER 2: Electrode Materials for Neurophysiology Recording Implants	7
2.1 Introduction	7
2.2 Key Challenges of Neural Implants	10
2.2.1 Tissue Responses	10
2.2.2 Surgical Challenges	11
2.3 Key Characteristics of Electrode Materials	13
2.3.1 Electrical Properties	13
2.3.2 Biocompatibility	16
2.3.3 Stability	17
2.3.4 Biodegradability/bioresorbability	
2.3.5 Mechanical Properties	
2.3.6 Optical Transparency	
2.3.6.1 Opto-stimulators	
2.4 Electrode Materials	
2.4.1 Inorganic Materials	
2.4.1.1 Metals	
2.4.1.2 Semiconductors	
2.4.2 Organic Materials	
2.4.2.1 Conducting Polymers (CP)	
2.4.3 Carbon-based Materials	
2.4.3.1 Graphene	
2.4.3.2 Carbon Nanostructures	
2.4.3.3 Glassy Carbon	
2.4.3.4 Diamond	
2.5 Conclusion	38
CHAPTER 3: Characteristics of Transparent, PEDOT:PSS Coated ITO Microelectrodes	43
3.1 Introduction	44
3.2 Materials and Methods	45

3.2.1 Design and Fabrication of Microelectrode Probes	45
3.2.2 Testing Methods	
3.3 Results and Discussion	49
3.3.1 Electrochemical Impedance	49
3.3.2 Charge Storage Capacity	53
3.3.3 Optical Transmittance	56
3.3.4 Equivalent Circuit Model	57
3.4 Conclusion	60
CHAPTER 4: Highly Conductive, Transparent, and Anti-reflective PEDOT:PSS-ITC	)-Ag-ITO on
Parylene C with Tunable Peak Transmittance	
4.1 Introduction	62
4.2 Materials and Methods	65
4.2.1 Fabrication	
4.2.1.1 ITO Films Deposition	
4.2.1.2 Design Methodology for Multilayer Anti-reflection Coatings	
4.2.1.3 Fabrication of PEDOT:PSS-ITO-Ag-ITO Thin Films	
4.2.1.4 TEM Samples Preparation and Test	
4.2.2 Testing Methods	
4.2.2.1 Transmittance and Conductivity Measurements	70
4.2.2.2 Electrochemical Measurements	
4.2.2.3 Peel-off Tests	
4.2.2.4 Bending Tests and Young's Modulus Measurements	
4.3 Results and Discussion	
4.3.1 Temperature Study of ITO	
4.3.2 Conductivity and Transmittance	
4.3.3 Electrochemical Impedance and Charge Storage Capacity	
4.3.4 Stability	
4.3.5 Adhesion	
4.3.6 Bending Test	
4.3.7 Young's Modulus	
4.4 Conclusion	90
CHAPTER 5 A F 11 T	
CHAPTER 5: A Fully Transparent, Flexible PEDOT: PSS-ITO-Ag-ITO Based Mi	
Array for ECoG Recording	
5.1 Introduction	
5.2.1 Fabrication of µECoG Array	
5.2.2.1 Electrochemical Impedance	

5.2.2.2 Transmittance Measurements	97
5.2.2.3 Signal to Noise Ratios (SNRs) Measurements	97
5.2.2.4 <i>In vivo</i> Animal Experiment	
5.3 Results and Discussion	
5.3.1 Fabricated Microscale ECoG Microelectrode Arrays	99
5.3.2 Electrochemical Impedance	
5.3.3 Transmittance Measurements	103
5.3.4 Signal to Noise Ratios (SNRs) Measurements	105
5.3.5 <i>In vivo</i> Animal Experiment	
5.4 Conclusion	111
CHAPTER 6: Exploratory and Future Work	114
6.1 120-channel Transparent μECoG Array	115
6.1.1 Transparent µECoG Array Design	115
6.1.1.1 Mask Designs	115
6.1.1.2 Fabrication Procedures	115
6.1.2 Connection Part	118
6.1.2.1 PCB Design	118
6.1.2.2 Recording System Setup	119
6.2 A Transparent and Miniaturized ITO-based Electrochemical Ser	nsor for Continuous and
Quantitative Monitoring of the Concentrations of Copper (Cu) and Mang	anese (Mn) Ions in Bodies
and Soil Environment	120
6.2.1 Introduction	120
6.2.2 Materials and Methods	122
6.2.2.1 Fabrication of Transprent ITO sensors	122
6.2.2.2 Testing Methods	124
6.2.2.2.1 Test Setup	124
6.2.2.2.2 Cu and Mn Ions Solutions Preparation	
6.2.2.2.3 Testing and Cleaning Recipes	125
6.2.3 Results and Discussion	125
6.2.3.1 Cu/Mn Ions	125
6.2.3.2 Linearity and Repeatability	128
6.2.3.3 SEM and EDS	131
6.2.3.4 BDD Electrodes	131
6.2.4 Conclusion and Future Study	132
APPENDIX	134
BIBLIOGR APHY	138

# LIST OF TABLES

Table 1. Summary of various electrode materials with key properties	41
Table 2. Summary of the fitted values by utilizing the equivalent circuit models	59
Table 3. Peeling test results with 5 samples	85
Table 4. Benchmark table of transparent ECoG arrays	112
Table 5. Admittance loci simulation	135

## LIST OF FIGURES

Figure 1. Key material characteristics of neural recording implants. (A) Electrical properties. The example shows a neural recording probe (upper) with ITO (white) /ITO-PEDOT:PSS (blue) microelectrodes. The added PEDOT:PSS has been proved to improve electrochemical impedance (lower left) and charge storage capacity (lower right) due to the increased surface roughness (reprinted with permission from (Yang et al., 2017)). (B) Biocompatibility. The example shows the neuronal preservation and the severity of astrogliosis (left) around implanted SU-8 devices (right) (reprinted with permission from (Márton et al., 2020)). (C) Stability. The example shows an electrode array made of mechanically and chemically stable, boron-doped polycrystalline diamond (BDD) (upper). Morphological response of rat cortical neurons on the Parylene C and microcrystalline diamond (MCD) substrates (lower) appeared similarly to the control substrate (reprinted with permission from (Fan et al., 2020)). (D) Biodegradability and bioresorbability. The example indicates patterned molybdenum (Mo) electrodes on the resorbable substrate (PLLA/PCL (reprinted with permission from (Xu et al., 2019)). (E) Mechanical properties. The example shows a mechanically flexible neural implant consisting of soft platinum-silicone composited electrodes (lower right) and micro-cracked gold film (upper right) interconnect on a silicone substrate (reprinted with permission from (Minev et al., 2015)). (F) Optical transparency. The example shows a transparent ITO ECoG implant combined with optical stimulation (reprinted with permission from (Kwon et al., 2013))
Figure 2. Examples of electrode materials. (A) The electrodes of the neurophysiological implants (left) are made of Au/Pt alloy as indicated in the SEM image (right) (reprinted with permission from (Zhao et al., 2016)). (B) Transparent graphene as the electrode material (lower left) on the μΕCoG array (right) for the neurophysiology signal recording and imaging (upper left) (reprinted with permission from (Park et al., 2018)). (C) Thin-film glassy carbon recording electrodes on flexible polyimide (left). The SEM image (right) shows the surface morphology of the glassy carbon (reprinted with permission from (Vomero et al., 2017))
Figure 3. (a) Photo of a fabricated microelectrode probe. Microscope images of the ITO electrodes without (b) and with PEDOT:PSS coating (c)
Figure 4. Fabrication steps: (a) Depositing of 500 nm Cu. (b) Patterning the Cu layer. (c) Patterning the ITO layer. (d) Depositing 2 μm Parylene C as the insulation layer. (e) Etching the Parylene C away to expose the contact pads and microelectrodes. (f) Photolithographing the probe to only expose the microelectrodes. (g) Spincoating PEDOT:PSS on the microelectrodes. (h) Rinsing off the photoresist to only remain the PEDOT:PSS on the microelectrodes
Figure 5. (a) Impedance modulus and (b) phase versus frequency for plain ITO and PEDOT:PSS coated ITO microelectrodes, respectively

Figure 6. (a) Average 1 kHz impedance of the plain and PEDOT:PSS coated ITO microelectrod with 10 μm, 37 μm, 50 μm and 80 μm diameters (n=5). (b) Impedance changes of the pure IT and PEDOT:PSS coated ITO electrodes with different diameters, measured after soaked in roctemperature saline for 0 weeks, 1 week, 2 weeks, 3 weeks and 4 weeks
Figure 7. Impedance magnitude (upper curves, high-to-low curves) and phase changes (low curves, low-to-high curves) during 4 weeks for the PEDOT:PSS coated ITO microelectrodes and for the pure ITO electrodes (b)
Figure 8. Surface roughness changes a before and b after spin-coating PEDOT:PSS layer Atomic force microscopy (AFM). The average roughness (Ra) and peak-to-peak mean roughned depth (Rt) without the PEDOT:PSS film is 0.85 nm and 12.02 nm, while Ra and Rt. with the PEDOT:PSS film is 3.33 nm and 39.15 nm
Figure 9. (a) CVs of the plain ITO and PEDOT:PSS coated ITO WEs versus Ag/AgCl RE, showing that the PEDOT:PSS coated ITO electrode exhibits larger charge storage capacity. (b) CVs of the plain ITO and PEDOT:PSS coated electrode for 10 cycles, demonstrating the stability of the IT and the PEDOT:PSS coating in saline.
Figure 10. Optical transmittance of different thin films.
Figure 11. Equivalent circuit model of (a) the pure ITO and (b) the ITO-PEDOT:PSS electrodelectrolyte interface.
Figure 12. (a) Equivalent admittance (blue shade) of the multilayer PEDOT:PSS-ITO-Ag-ITO the film coatings. Treating as a virtual reference plane from the substrate. (b) Admittance loci with example of PEDOT:PSS (30.5 nm)-ITO (24 nm)-Ag (9.45 nm)-ITO (20 nm) assembly achieving the highest transmittance at the preferred 550 nm wavelength.
Figure 13. Temperature dependence of optical and electrical properties of sputtered ITO and a thin films. Transmittances of 100 nm ITO deposited under sputtering temperatures of 22°C, 69°C, 116°C, and 140°C on a glass slides and b Parylene C coated glass slides. c Sheet resistance of 100 nm ITO deposited under different sputtering temperatures on glass slides and Parylene coated glass slides, respectively. Transmittances of d Ag (9.45 nm) and e ITO (24 nm)-Ag (9.5 nm)-ITO (20 nm) deposited under the sputtering temperature of room temperature and his temperature (116°C) on glass slides. f Sheet resistances of ITO (24 nm)-Ag (9.5 nm)-ITO (20 nm) at room temperature and high temperature (116°C) on glass slides, respectively. High-resolution TEM images of g polycrystalline structure of high-temperature ITO, h amorphous structure room-temperature ITO. X-ray diffraction patterns of i high-temperature ITO and j room temperature ITO.

Figure 14. Concept diagrams of transparent and ultra-flexible PEDOT:PSS/ITO/Ag/ITO or Parylene C, designed for achieving the lowest reflectance
Figure 15. Equivalent circuit of the PEDOT:PSS-ITO-Ag-ITO assembly for the overall conductance calculation. Each layer of the thin film acts as a resistor and then is connected in parallel to form the total resistance. The measured sheet resistance of 20 nm ITO, 9.45 nm Ag, 24 nm ITO and 30.5 nm PEDOT:PSS was 305.2 $\Omega$ /sq, 10.28 $\Omega$ /sq, 254.2 $\Omega$ /sq, and >1000 $\Omega$ /sc (beyond the range of four-point probe), respectively
Figure 16. Thin films of PEDOT:PSS-ITO-Ag-ITO on 10 $\mu$ m Parylene C showing (a) excellent transparency and (c) ultra-flexibility. (b) The transparency before (right) and after (left) adding the PEDOT:PSS coating.
Figure 17. (a) Transmittances of the combined PEDOT:PSS-ITO-Ag-ITO films compared with the equivalent thickness ITO on the glass substrate and Parylene C substrate, respectively. (b) The peak transmittances of combined PEDOT:PSS-ITO-Ag-ITO films on Parylene C at wavelengths of 470 nm, 550 nm, and 630 nm, respectively, to confirm the tunable peak transmittance by stimulating the coatings admittance loci.
Figure 18. (a) Average sheet resistances (n=5) of PEDOT:PSS-ITO-Ag-ITO and the equivalent thickness ITO on the Parylene C substrate with neglectable standard deviation to confirm the uniformity of the combined films using the four-point probe measurements. (b) The transmittance and (i) the transparency before (right) and after (left) adding the PEDOT:PSS coating
Figure 19. (a) Electrochemical impedance magnitudes and (b) phases of the bare ITO, ITO-Ag-ITO and PEDOT:PSS-ITO-Ag-ITO versus the frequency, respectively
Figure 20. (a) CVs of the plain ITO and PEDOT:PSS-ITO-Ag-ITO WEs versus Ag/AgCl RE showing that the PEDOT:PSS-ITO-Ag-ITO electrode exhibits larger charge storage capacity. (b) CVs of the PEDOT:PSS-ITO-Ag-ITO electrode for 10 cycles, demonstrating the stability of the multilayered structures in saline.
Figure 21. Sheet resistance changes (n=5) of the combined films in air and in saline at 37°C for 12 weeks with measurements every week.
Figure 22. The peeling-off methods83
Figure 23. Photos of 100 1 mm × 1 mm blade-scratched squares with (a) no peel-off test, (b) one-time peel-off test, (c) 10-time peel-off tests, (d) 50-time peel-off tests, (e) Parylene C delamination after 50-time peel-off tests and (f) delamination of bad quality ITO after one-time peel-off test

Figure 24. Sheet resistances of the only ITO thin films with the same total ITO thickness within the total 1000 bending cycles under (a) 3 mm bending diameters and (b) 6 mm bending diameters, respectively.
Figure 25. Sheet resistances of combined thin films with the same total ITO thickness within the total 1000 bending cycles under (a) 3 mm bending diameters and (b)6 mm bending diameters, respectively.
Figure 26. Young's modulus of (e) the only Parylene C film and (f) the combined thin films on Parylene C
Figure 27. Hexagon chart of PEDOT:PSS-ITO-Ag-ITO, ITO, ultrathin metal, graphene, and PEDOT:PSS with six properties: conductivity, transparency, flexibility, stability, biocompatibility and electrochemical properties.
Figure 28. μECoG array fabrication steps: (1) Deposit Parylene C. (2) Pattern the photoresist. (3) Deposit ITO-Ag-ITO thin films. (4) Wash off photoresist and pattern the ITO-Ag-ITO layer. (5) Deposit the second Parylene C layer. (6) Etch Parylene C selectively to exposure the electrode sits and contacts. (7) Pattern another layer of photoresist. (8) Deposit Cu. (9) Wash off photoresist and pattern Cu over the contact areas. (10) Pattern another layer of photoresist. (11) Deposit PEDOT:PSS. (12) Washing off photoresist to obtain the PEDOT:PSS patterns on the electrode sites. (13) Release the μECoG array from silicon substrate. (14) Flexibility of the released μECoG array
Figure 29. The prototype of fabricated transparent and flexible μECoG microelectrodes arrays and their electrochemical impedance and SNR behaviours. (a) The transparency and (b) the flexibility of an as-fabricated μECoG microelectrode array without (c) and with (d) PEDOT:PSS coating
Figure 30. (a) Concept diagram of transparent µECoG array. (b) Concept diagram of PEDOT:PSS-ITO-Ag-ITO multilayer structure of microelectrodes
Figure 31. The prototype of fabricated transparent and flexible μECoG microelectrodes arrays and their electrochemical impedance and SNR behaviours. (a) The transparency and (b) the flexibility of an as-fabricated μECoG microelectrode array without (c) and with (d) PEDOT:PSS coating
Figure 32. (a) Impedance magnitude and (b) phase changes of the PEDOT:PSS-ITO-Ag-ITO multilayered μECoG microelectrodes during 4 weeks soaking in room temperature saline. (c) Zoom-in impedance magnitudes at 1 kHz frequency over 4 weeks. (d) Average 1 kHz impedance changes of PEDOT:PSS-ITO-Ag-ITO microelectrodes, measured after being soaked in saline for

0 week, 1 week, 2 weeks, 3 weeks, and 4 weeks (n=10)
Figure 33. Fluorescent and bright-field images of mCherry-labelled rat brain section and <i>in vivo</i> recording results of light-evoked field potentials. Leica mCherry fluorescent images (a) (c) and bright-field images (b) (d) with and without the transparent µECoG array attached on104
Figure 34. (a) SNRs of the $\mu$ ECoG microelectrode array (n=10) under no light, ~470nm blue, ~530nm green, ~580nm yellow, and ~660nm red light illumination, respectively. (b) Optical powers of the blue LED (V=3.3V), green LED (V=3.3V), yellow LED (V=1.8V), and red LED (V=1.8V), respectively (n=10)
Figure 35. (a) (b) Images of the <i>in vivo</i> test with the first version of array design. <i>In vivo</i> test data of (c) (d) signal amplitudes with visual stimulation (up and left) and without visual stimulation (down and right)
Figure 36. (a) Image of a transparent μECoG array placed on the brain tissue of the rat during the <i>in vivo</i> animal experiments. (b) Zoom-in microscope image shows the exposed brain tissue with the array attached.
Figure 37. <i>In vivo</i> test data of e signal amplitudes of left and right V1 with the strong light stimulations, medium light stimulations, and without visual stimulation
Figure 38. <i>In vivo</i> test data of f instantaneous phases of left and right V1 with the strong light stimulations, medium light stimulations, and without visual stimulation
Figure 39. <i>In vivo</i> test data of g PSD spectrograms of left and right V1 with the strong light stimulations, medium light stimulations, and without visual stimulation
Figure 40. Six photolithography masks for fabricating 120-channel transparent microelectrodes array for neurophysiology recording with PEDOT:PSS-ITO-Ag-ITO multilayer structure116
Figure 41. 3D view of design PCB interface for connecting the 120-channel microelectrode array and Intan recording headstages with Altium Designer
Figure 42. Concept diagram of 120-channel neuro-electrophysiology recording system for <i>in vivo</i> animal experiment
Figure 43. (a) Single ITO electrochemical sensor design with WE and CE. (b) Test setup with Ag/AgCl RE and magnetic stir bar at the bottom of the beaker
Figure 44. (a) Photolithography masks. (b) Fabricated ITO-based transparent electrochemical

ensors. (c) Various WE diameters on the wafer123
igure 45. (a) (b) (c) (d) DPSV of low concentration (LC) CuCl <sub>2</sub> and high concentration (HC) uCl <sub>2</sub> with 0.125mm diameter and 1mm diameter WE
igure 46. (e) (f) (g) (h) DPSV of low concentration (LC) MnCl <sub>2</sub> and high concentration (HC) InCl <sub>2</sub> with 0.125mm diameter and 1mm diameter WE
igure 47. 10-time DPSV repeatability tests with the low concentrations (LC) of (a) 1 μM, (b) 10 M, (c) 50 μM, and (d) 100 μM MnCl <sub>2</sub> with 1mm diameter WE. After each DPSV, a cleaning rocedure was processed before the next time DPSV
igure 48. 10-time DPSV repeatability tests with the low concentrations (LC) of (a) 1 $\mu$ M, (b) 10 M, (c) 50 $\mu$ M, and (d) 100 $\mu$ M MnCl <sub>2</sub> with 0.125 mm diameter WE. After each DPSV, a cleaning rocedure was processed before the next time DPSV. Blue lines show each time the peak current agnitude and the trend during the 10-time DPSV repeatability tests
igure 49. (a) Peak current magnitudes and standard deviations (STDs) of 0.125mm diameter WE nder different MnCl <sub>2</sub> concentrations. (b) DPSV of single use 0.125mm diameter WE sensors for ach concentration. (c)Linear fitting of the peak current magnitudes under different concentrations with 0.125mm diameter
igure 50. (a) SEM image of ITO sensor. (b) The zoom-in ITO WE surface before the 10-time consecutively DPSV. (c) The zoom-in ITO WE surface after the 10-time consecutively DPSV. A leaning procedure was processed after each DPSV and before the next time DPSV. (d) EDS of TO WE surface before 10-time consecutively DPSV and after 10-time consecutively DPSV in InCl <sub>2</sub> and CuCl <sub>2</sub> solution, respectively.
igure 51. (a) 0.125mm diameter WE diamond sensors to measure DPBS, 500 nM, 1 μM, 50 μM, nd 100 μM CuCl <sub>2</sub> . (b) 0.125mm diameter WE diamond sensors to measure DPBS, 1 μM, 10 M, 50 μM, and 100 μM MnCl <sub>2</sub> 132

#### **KEY TO ABBREVIATIONS**

ITO Indium-tin-oxide

PEDOT:PSS poly-(3, 4-ethylene dioxythiophene)/poly(styrene sulfonate)

SNR Signal-to-noise ratio

DPSV Differential Pulse Stripping Voltammetry

ECoG Electrocorticogram

HC High Concentration

LC Low Concentration

MEA Microelectrode Array

ChR2 Channelrhodopsin-2

ECoG Electrocorticogram

EEG Electroencephalogram

LFP Local Field Potentials

PPy Poly(pyrrole)

ROS Reactive Oxidative Species

CP Conducting Polymer

ISO International Organization of Standard

PEG Polyethylene Glycol

PEGMA PEG Methacrylate

BDD Boron-doped Polycrystalline Diamond

Si NM Silicon Nanomembrane

SiO<sub>2</sub> Silicon Dioxide

PBS Phosphate-buffered Saline

DI De-ionized

PI Polyimide

SMP Shape-memory Polymer

PEC Photoelectrochemical

PET Polyethylene Terephthalate

2D Two Dimentional

3D Three Dimentional

IrOx Iridium Oxide

CMOS Complementary Metal-oxide-semiconductor

FET Field-effect Transistor

IZO Indium-doped Zinc Oxide

PANi Poly(aniline)

PT Poly(thiophene)

CVD Chemical Vapor Deposition

CF Carbon Fiber

CNT Carbon Nanotube

CFME Carbon Fiber Microelectrode

CNF Carbon Nanofiber

COC Cyclic Olefin Copolymer

fMRI Functional Magnetic Resonance Imaging

SWCNT Single-walled Carbon Nanotube

MWCNT Multi-walled Carbon Nanotube

BBB Blood-brain Barrier

GC Glassy Carbon

EIS Electrochemical Impedance Spectroscopy

CV Cyclic Voltammetry

AFM Atomic Force Microscopy

UV-Vis Ultraviolet-visible

UV Ultraviolet

PR Photoresist

IPA Isopropyl Alcohol

WE Working Electrode

RE Reference Electrode

CE Counter Electrode

CSC Charge-storage Capacity

TEM Transmission Electron Microscopy

LED Light Emitting Diodes

IACUC Institutional Animal Care and Use Committee

AAV Adeno-associated Virus

BSE Bovine Spongelike Encephalitis

CJD Creutzfeldt-Jakob Disease

SEM Scanning Electron Microscopy

IBAD Ion-beam Assisted Deposition

PVD Physical Vapor Deposition

#### **CHAPTER 1: Introduction**

Neurological disorders are central and peripheral nervous system diseases, including Parkinson's disease, Alzheimer's disease, epilepsy, etc., affecting hundreds of millions of people worldwide [1]. Medical treatments conventionally used are medication [2] and electrical stimulation, also called deep brain stimulation [3]. However, they all have their own disadvantages. For example, taking medications always has side effects, including fatigue, loss of coordination, dizziness, speech problems, depression, severe rash, etc. For the electrical stimulation, because two long electrodes need to be inserted into the deep brain, they do damage to the tissue. In addition, this method has non-cell-type specificity since the surrounding neurons will be electrically stimulated. Some neurons not expected to be stimulated are stimulated and can cause some side effects, including balance and speech problems, jerky movements, weight gain and depressed mood. Low spatial precision is another disadvantage of this delivery approach because after the electrical stimulation, current delivered to motor circuits could interfere with other motor functions and spread to nearby cognitive pathways [4] [5]. Optogenetics is a promising neuromodulation technique being studied to address these challenges [6] [7] [8]. Optogenetics utilizes light to excite or inhibit the activity of genetically targeted neurons, expressing light-sensitive opsin proteins [9] [10]. To fully realize the potential of the optogenetics tools, neural interface devices with both recording and stimulating capabilities are vital for future engineering development, and improving their spatial precision is a constant topic of the research [11] [12].

Many researchers have designed and fabricated different types of electrophysiological recording microelectrodes with different materials on the various substrates [13] [14] [15] [16].

Among them, transparent microelectrodes arrays are promising due the high light transmittance rate, making more light to go through the recording electrodes results in more physiological signals detected [14] [17]. In addition, transparent microelectrodes have the potential to achieve the simultaneous process of electrophysiological recording and imaging capture [17]. Conventional transparent recording microelectrodes made of a single material, such as indium tin oxide (ITO), ultrathin metals, graphene and PEDOT:PSS, have limitations to possess the desired combination of excellent electrical, optical, mechanical, and biocompatible properties. ITO has been used in making transparent recording microelectrodes because of its relatively high transmittance over the entire visible spectrum [18], good biocompatibility [19] and relatively good electrical conductivity. However, the mechanical flexibility of ITO remains a challenge due to its high Young's modulus, causing brittleness [20], especially when thicker ITO (~100 nm) is required for achieving both high transmittance and feasible conductivity. Moreover, ITO electrodes, when scaled down to micron dimensions, face a critical problem of an increased electrochemical impedance, which would lead to undesirable electrochemical reactions with the brain tissue [21] and poor recording quality due to noisy, ion-based electric fluctuations of the surrounding media [22]. While having higher conductivity (in the range of ohms/sq) than ITO, ultrathin metals suffer from low transmittance ~30-70 % even with ~3-7 nm thickness [23]. Therefore, it is difficult to simultaneously achieve high transparency and high conductivity of ultrathin metals [24]. Graphene is also considered as an optimal material for transparent µECoG array due to its broad-spectrum transparency, excellent conductivity, good biocompatibility and flexibility [25]. However, growing high-quality graphene over large areas requires either high temperatures of over 1000°C

or specific substrate materials, which are incompatible with polymer materials. In addition, the graphene transfer method has been utilized to obtain four-layer graphene films to reduce the electrical resistance due to the relatively high sheet resistance of the single layer, which requires well-developed skills hence reduces the yield and reproducibility [17]. PEDOT:PSS as an attractive conductive polymer material that has been successfully used in fabricating microelectrodes for neural interface applications due to its outstanding biocompatibility, excellent stability, transparency, flexibility and simple utilization with low-cost spin-coating and ink-jet printing techniques [26] [27]. However, it is limited by its relatively low electrical conductivity compared to other transparent conducting materials, making it unsuitable for use independently in high-density electrode arrays.

Ledochowitsch et. al showed in their preliminary work that large bond pads broke along stress lines at the edge of plasma-etched vias for an ECoG array using ITO as the conductor for all electrodes [28]. Later, Kwon et al. reported an opto-μECoG array as a hybrid neural interface [14]. The authors deposited 100 nm ITO on the 10 μm Parylene C. Taking into account the brittleness of ITO, the authors did the metallization of both ITO electrode and ITO-Au interconnection. However, the transmittance at the wavelength of 470 nm was only ~55% which is unacceptably low for light to transfer through the μECoG microelectrodes [14]. Park et al. proposed a graphene-based carbon-layered electrode array for neural imaging and optogenetic applications. This graphene-based electrode array showed better flexibility for the replacement of ITO in neural interfacing devices [17] [29]. However, during the fabrication, four graphene monolayers were transferred and stacked sequentially onto the wafer surface via using the wet transfer technique,

making it difficult for fabricating large-scale and uniform graphene thin films [17]. To systematically study the electrophysiology of neural systems, microelectrode arrays (MEAs) provide a noninvasive way to record changes in the cells [15] [30]. Conventional MEAs are made by stable metals, such as gold and platinum, as researched by Kim et al [31]. However, when it comes to the field of optogenetics, the opaque properties of these MEAs make it difficult to perform the light stimulation, electrophysiological recording and cell imaging at the same time. Based on MEAs, Pas et al. coated PEDOT:PSS on the MEA device to significantly increase the single-unit activity recordings and maximize the functionality of these planar MEAs as effective tools to study neural networks [32]. In addition, a single layer of PEDOT:PSS has been shown to electrically stimulate the brain while simultaneously reaping the benefits of optical imaging [33]. However, PEDOT:PSS is generally coated as a supplementary material to promote the functions of electrophysiological recording electrodes [34] [35] [36] due to the low electrical conductivity and the bad adhesion to the surface after absorbing moisture, especially for the thick PEDOT:PSS.

To address the above challenges, my research topic is focused on designing and characterizing the microelectrodes arrays with transparent multilayered materials for the electrophysiological recording. In Chapter 3, a probe consisting of 6 transparent ITO microelectrodes with PEDOT:PSS spun on was fabricated. This microelectrodes array exhibited significantly improved impedance and charge storage capacitance compared to the single ITO microelectrodes due to the improvement of surface roughness after spin-coating PEDOT:PSS. Furthermore, the PEDOT:PSS coating increases the optical transmittance in the visible spectrum by reducing the reflectance at the air-substrate interface. However, for this microelectrode array, the material of the substrate is

polyethylene terephthalate (PET), which is not flexible enough to be attached to the soft brain tissue, causing brain tissue damage and bad connection between the brain and the microelectrodes. In addition, to make the electrophysiological recording electrodes to be specifically utilized in the field of the optogenetics, for the next chapter, an ultra-flexible, conductive and transparent thin film using a PEDOT:PSS-ITO-Ag-ITO multilayered structure on Parylene C was designed and fabricated for achieving significantly higher sheet conductivity, reduced electrochemical impedance, high transmittance, good stability, adhesion and flexibility at the same time. Furthermore, the peak transmittance of this multilayered structure is tunable for different optogenetics applications. For example, the transparent recording microelectrodes with the peak transmittance under 470 nm could be used to receive more neuron signals compared with other opaque or low transmittance microelectrodes after activating the channel rhodopsin (ChR2) with the blue light. Chapter 5 described the design and fabrication of the micro-electrocorticogram (µECoG) arrays based on this PEDOT:PSS-ITO-Ag-ITO multilayered structure. Nowadays, researchers used optogenetics combined with µECoG recording electrodes as innovative optoelectronic neural interface tools to explore the pathology of those nervous system diseases. The µECoG arrays with the optogenetic tools could achieve the no-tissue damage, genetically targeted cells stimulation, and better spatial and temporal stimulation resolution. In addition, the substrate chosen was Parylene C to make the whole µECoG arrays more flexible and better attached to the brain tissue. *In vivo* experiments utilizing the designed two microelectrode arrays were done to prove the efficacy for electrophysiology recording. More in vivo animal experiments are needed to study the feasibility of this µECoG array. In addition, in vitro experiments,

including the fluorescent light transmittance, electrochemical impedance, stability, and signal-tonoise ratios (SNRs) were also discussed in Chapter 5.

In Chapter 6, firstly, the transparent and flexible 120-channel µECoG array was designed for achieving the higher resolution compared to the previous 32-channel µECoG array. PEDOT:PSS-ITO-Ag-ITO multilayered structure was utilized in this project. The other subsection of this chapter was to fabricate an ITO-based transparent, flexible, and miniaturized electrochemical biosensor for continuous and quantitative monitoring of the concentrations of copper (Cu) and manganese (Mn) ions in bodies and soil environment. Prion diseases, such as Creutzfeldt-Jakob Disease (CJD) and Bovine Spongiform Encephalopathy (BSE), are caused by abnormal folding of proteins and can cause asymptotic neurological changes and death. Over the years, researchers found that Mn levels in the brains of patients with Creutzfeldt-Jakob disease are 10 times higher than those in the normal brain. Besides, high level of Cu ions in the bodies also has been found to intensify those prion diseases in recent research. The exceeded Cu and Mn ions in the soil environment will eventually flow through the food chain into humans and animals, aggravating the prion diseases. Therefore, it is urgent to design an electrochemical sensor for continuous and quantitative monitoring of the concentrations of Cu and Mn ions in bodies and the soil environment with high sensitivity and accuracy. This chapter showed the potential to use ITO material for Cu and Mn ions measurement.

#### 2.1 Introduction

Neurological disorders and diseases in the central and peripheral nervous systems, such as Parkinson's disease, Alzheimer's disease, and epilepsy, are affecting hundreds of millions of people worldwide [1], [37], [38]. Neurophysiology recording electrodes act as a seamless interface between the nervous system and the outside world and help diagnose these neurological diseases. Several types of neural signals could be measured from the brain using electrodes [39], including electroencephalogram (EEG) (10-400 μVpp; 1 mHz-200 Hz) [40], electrocorticogram (ECoG) (10-1000 μVpp; 1 mHz-200 Hz) [41], [42], in addition to local field potentials (LFPs) (0.5-5 mVpp; 1 mHz-200 Hz) and action potential spikes (50-500 μVpp for extracellular; 10-70 mVpp for intracellular; 100 Hz-10 kHz) [43], [44]. EEG is noninvasive but suffers from low spatial resolution and poor SNR because of signal attenuation through the scalp and skull. Mechanical disturbances and electromyographic activities also incur the artifacts that further influence the spatial and temporal resolutions of EEG recording [45]. Unlike EEG, ECoG directly measures the signals from the cerebral cortex via neurophysiological implants without any internal and external source noises due to the scalp and skull, leading to lower tissue interference, greater precision, higher sensitivity, and reduced noise interference. Although some special ECoG arrays, such as 'NeuroGrid', have been shown to be capable of recording spike activity and LFPs [46], almost ECoG can only gather the electrophysiological signals from the superficial surface of the cerebral cortex and is incapable of capturing spikes from individual neurons. Therefore, penetrating electrodes suitable for recording LFPs and action potentials with high spatiotemporal resolution have been widely used in the neuroscience community [47]. Despite recent advances in electrode technologies, all existing electrode implants are still suffering from poor long-term stability and crosstalk, due to long-standing challenges such as material biocompatibility, hermetic packaging, the relatively large physical dimensions of the devices, as well as mechanical mismatch between the brain tissue and the implant [48]. Similarly to the central nervous system, for the peripheral nervous systems, surgically implanted neural electrodes could be categorized into regenerative electrodes, intra-fascicular electrodes, inter-fascicular electrodes, and extra-neural electrodes [49]. These electrodes have more strict requirements for some material properties, such as flexibility and biocompatibility [49]. Indeed, careful selection and design of electrode and packaging/substrate materials are significantly essential to improve the recording quality and longterm stability of the electrode implants [50]. Therefore, to thoroughly study the electrical activity of neuronal circuits underlying various disorders, developing innovative neural recording devices have been a long-standing interest of many scientists, intending to achieve the best combination of excellent electrical properties, high spatiotemporal precision, prominent biocompatibility, outstanding long-term stability, and safety of the electrode devices.

To date, significant research has been devoted to the design and fabrication of implantable neural recording electrodes with different materials on various substrates. The materials of these devices could be classified into two broad categories: electrode materials as well as packaging and substrate materials. While silicon-based materials, as well as common metallic materials (e.g.,

platinum or iridium) and their derivatives (e.g., platinum black and iridium oxide), are widely used in electrode manufacturing, they are still antagonistic to the soft, ionic, wet, and dynamic nature of the biological tissue, with their hard, electronic, dry, and static nature. Non-conventional conducting materials that were not initially developed for neural implants have received significant attention and have been studied for neurophysiological recording in recent years because of their favorable properties and manufacturing advantages. Examples of these emerging electrode materials include graphene [29], [51], ITO [52], carbon-polymer hybrid nanostructures [53], [54]. The design consideration of neural stimulation electrodes is similar to that of neural recording electrodes, concerning biocompatibility, mechanical properties, electrical properties, and stability [55]. For example, platinum black and Ir/IrOx are also widely used as stimulating electrodes [56], [57]. Large charge storage capacity is specifically required for simulating electrodes to achieve better stimulating performance [58]. Neural stimulators also have the same strict requirements on hermeticity, long-term stability, and biocompatibility of device package [59], [60]. Many materials that have been utilized in neural stimulating probes include but are not limited to: ceramics, glass, epoxy, silicone, and so on [55], [59], [61].

To draw a clear picture and guide the material design for future device development, this chapter shows the current materials for the fabrication of neural recording implants that were reported in the literature in the most recent years. In the following sections, Section 2 discusses several important material properties, including electrical properties, mechanical properties, stability, biodegradability/bioresorbability, biocompatibility, and optical properties, as well as the critical

impact of these properties on the performance of electrode implants. Section 3 provides a detailed discussion of various electrode materials in three different categories: inorganic materials (e.g., metals and semiconductors), organic materials (e.g., poly(3,4-ethylene dioxythiophene):poly(styrene sulfonate (PEDOT:PSS) and poly(pyrrole) (PPy)), and carbon-based materials (e.g., graphene and carbon nanostructures). Approaches to improve the recording performance of the electrode materials are also included.

#### 2.2 Key Challenges of Neural Implants

## 2.2.1 Tissue Responses

Before selecting candidate materials for neural electrode implants, it is essential to understand the biological response to foreign objects, e.g., neural implants. The inflammatory response is usually caused by tissue injured during the implantation surgery or the existence of the implants in the body. Inflammation achieves the purpose of containing, neutralizing, diluting, or isolating the harmful substances through a series of complex physiological reactions [62]. These inflammatory reactions will significantly affect the functionality and stability of implanted devices. First, acute inflammation will occur in the first few days of implantation. A large amount of blood will flow to the damaged tissue through the dilated blood vessels, and then a blood clot will be formed to close the wound [62]. Then the tissue fluid containing water, salt, and protein will form edema [63]. At this stage, the implants have to overcome the contamination of blood and tissue fluids that may cover the implants and cause device malfunction. Similarly, the extrusion and tissue deformation that may be caused by edema also require a certain strength of the inserted

implant. This means that the electrode, package, or substrate materials must have a certain mechanical strength. The tissue environment is moist and chemically rich, which is not an ideal environment for implants [64]. Moreover, the immune response will release reactive oxidative species (ROS), which attack and degrade the implants [65], [66]. With the continual presence of the implant, the inflammatory response will be transformed into chronic inflammation. A major feature in this phase is the regeneration of damaged epithelium and vascular tissue [67]–[69], which may encapsulate the implants and consequently degrade the recording stability and accuracy of the electrodes. The immune response of the tissue does not stop at this phase, so the implant still faces the attack of ROS. Once a foreign object is implanted into the body, a sequence of events (e.g., inflammation and foreign body response) occurs in the surrounding tissue and ultimately ends at the formation of foreign body giant cells at biotic-abiotic interfaces [70]. The intensity of the response is directly related to the properties of the implant [62], such as size, shape, topography, and chemical and physical properties of the selected material. As the final stage of the inflammatory response, tissues try to wrap the implants with a vascular, collagenous fibrous capsule with a thickness of 50-200 µm to isolate foreign objects [71]. This fibrous wall will undoubtedly affect the electrical coupling between the implant and the targeted neurons, which may cause signal degradation and ultimately implant failure.

#### 2.2.2 Surgical Challenges

Before the neurophysiology recording implants are surgically implanted into the body [72], sterilization is a significant and indispensable step to reduce the microbial contaminants (e.g., viruses) by 6 orders of magnitude [73], and thereby reduce the intensity of inflammation. Various

sterilization methods have been explored to suitably match various neurophysiology recording implants [73]. Nowadays, there are a great number of sterilization methods compliant with biomedical device regulation [74], including chemical sterilization (ethanol 70%), dry heating (160-190 °C), autoclaving (120-135 °C), ethylene oxide gas, hydrogen peroxide gas plasma, peracetic acid and UV radiation. High temperatures in dry heat and autoclaving sterilization will accelerate the oxidation and corrosion speed of the electrode materials, and hence can destroy the functionality of the whole implants, especially for easily-oxidized materials, such as silver thin films and silver nanowires [75], [76]. For packaging materials, high temperature and liquid uptake are the main concerns during these sterilization procedures [64], [77]. In particular for biodegradable packaging materials, dry heat and autoclaving sterilization may cause partial denaturation to collagen [78], morphology change to silk [79], and melting and degradation to (poly(lactic-co-glycolic acid) PLGA [80]. The sterilization process has less impact on synthetic polymer packaging materials than biodegradable materials, but it is still worthy of note. For instance, significant delamination of Parylene C encapsulation has been revealed after the steam sterilization process because of the insufficient adhesion strength between Parylene C and encapsulated device [81]. In addition, because its glass transition temperature is around 90 °C, high-temperature may cause degradation in the mechanical and optical properties of Parylene C. Ceramic materials have relatively broad options of sterilization methods due to their low watervapor permeability and high-temperature resistance [64]. While ethylene oxide sterilization can be operated at relatively low temperatures, the permeability of polymers can allow liquid stored in the material and a degassing step is required [64]. In addition, ethylene oxide is a central nervous

inhibitor, stimulant and protoplasmic toxin [82]. Improper exposure of neural implants to ethylene oxide can cause acute poisoning and chronic effects, such as severe headache, loss of consciousness, neurasthenic syndrome and dysfunction of the vegetative nerve with long-term light exposure [83]. Unlike ethylene oxide gas, hydrogen peroxide gas plasma has the benefit of non-toxic final decomposition products [84]. However, because of the oxidation reaction during the sterilization by hydrogen peroxide gas plasma [84], the materials selected must be resilient to changes in electrical conductivity caused by oxidation.

#### 2.3 Key Characteristics of Electrode Materials

## 2.3.1 Electrical Properties

For electrophysiology recording, the electrode/electrolyte boundary is comprised of electrochemical reactions (Faradic) and double-layer charging (capacitive) [85], [86]. Electrochemical impedance (typically at 1 kHz) is a critical factor in benchmarking the performance of the recording electrodes [87]. The targeted impedance range of microelectrodes is from  $\sim 0.1 \text{ M}\Omega$  to  $2 \text{ M}\Omega$  with the proper recording system utilization [88]. Although some studies indicate the impedance does not have a major impact on the signal quality [89], most studies state that electrochemical impedance greatly affects the signal recording quality [30], [90], [91]. The design of electrodes present tradeoffs in dimensions, electrochemical impedance, and background noise of recording. Miniaturized electrodes with diameters of 4  $\mu$ m to 100  $\mu$ m allow for single-unit recording with high spatial resolution and minimal invasiveness, but at the expense of increased electrochemical impedance that could cause signal quality reduction and background

Johnson noise increase. In particular, Johnson noise, also known as thermal noise, is proportional to the square root of the impedance of the electrodes [92], [93], as given by the following general equation 1

$$V_{noise} = \sqrt{4kTRe\{Z\}\Delta F}$$
 (1)

Where k is Boltzmann's constant, T is the temperature value,  $Re\{Z\}$  is the resistive component of the electrode impedance, and  $\Delta F$  is the frequency band [94]. The most common solution to this challenge is to increase the effective surface area of microelectrodes by surface modification with electrically conducting polymers, nanomaterials, or nanostructures [95], [96], which will effectively reduce the impedance while keeping device dimensions at a cellular scale to achieve high recording resolution, as shown in Figure 1A. Conducting polymers (CPs), such as PPy and poly (3,4-ethylenedioxythiophene) (PEDOT), has also shown promise in improving ionic-to-electronic charges transfer at the interface between the tissue and the recording site [97], [98], therefore increasing the charge capacity of the microelectrodes. Since the insulation layer is a part of the recording system, once it has been damaged due to material degradation or insulation

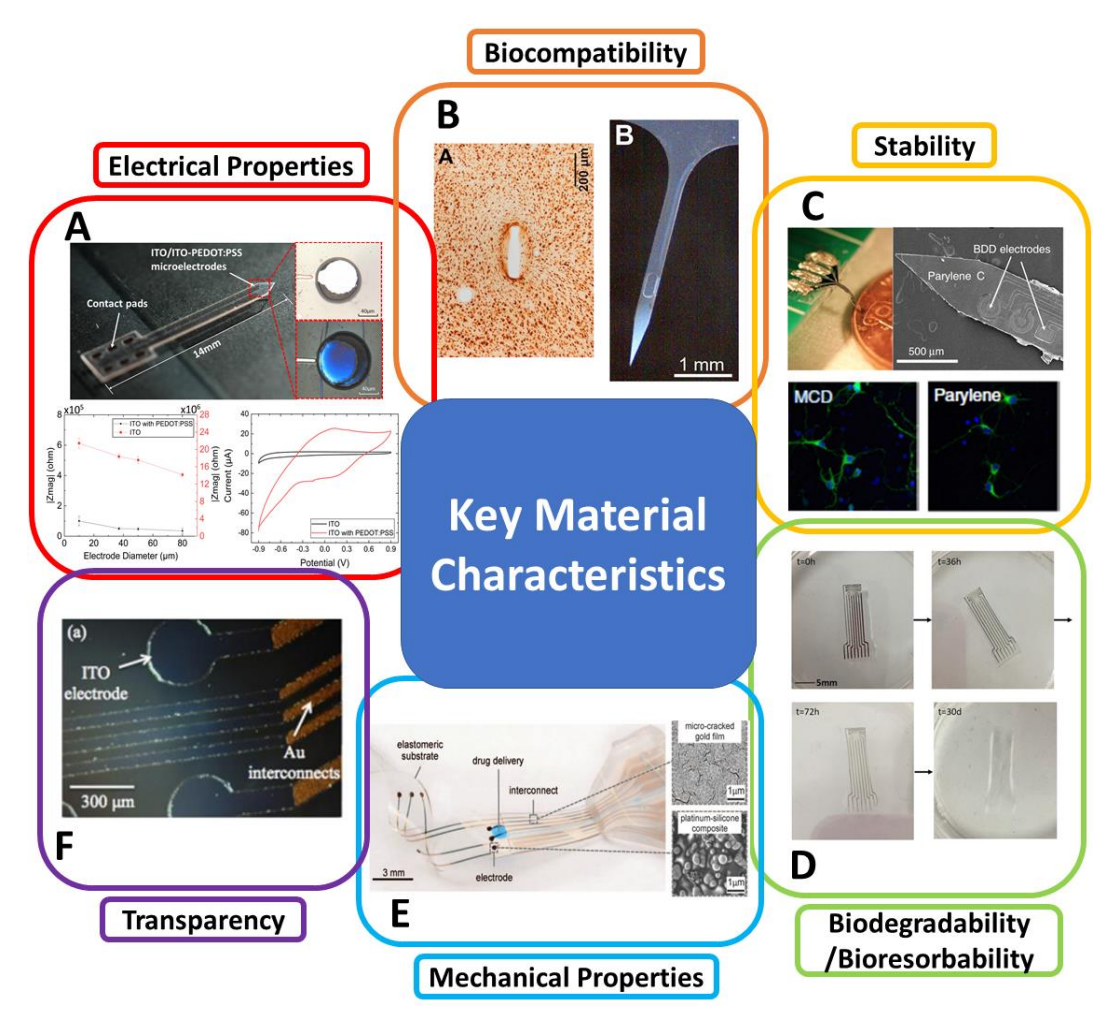


Figure 1. Key material characteristics of neural recording implants. (A) Electrical properties. The example shows a neural recording probe (upper) with ITO (white) /ITO-PEDOT:PSS (blue) microelectrodes. The added PEDOT:PSS has been proved to improve electrochemical impedance (lower left) and charge storage capacity (lower right) due to the increased surface roughness (reprinted with permission from (Yang et al., 2017)). (B) Biocompatibility. The example shows the neuronal preservation and the severity of astrogliosis (left) around implanted SU-8 devices (right) (reprinted with permission from (Márton et al., 2020)). (C) Stability. The example shows an electrode array made of mechanically and chemically stable, boron-doped polycrystalline diamond (BDD) (upper). Morphological response of rat cortical neurons on the Parylene C and microcrystalline diamond (MCD) substrates (lower) appeared similarly to the control substrate (reprinted with permission from (Fan et al., 2020)). (D) Biodegradability and bioresorbability. The example indicates patterned molybdenum (Mo) electrodes on the resorbable substrate (PLLA/PCL) (reprinted with permission from (Xu et al., 2019)). (E) Mechanical properties. The example shows a mechanically flexible neural implant consisting of soft platinum-silicone composited electrodes (lower right) and micro-cracked gold film (upper right) interconnect on a silicone substrate (reprinted with permission from (Minev et al., 2015)). (F) Optical transparency. The example shows a transparent ITO ECoG implant combined with optical stimulation (reprinted with permission from (Kwon et al., 2013)).

delamination, the electrical properties of the entire system will also change. Delamination changes the properties of the electrode by expanding the geometric area of the exposed conductor, in turn, this averages the recorded potentials across an increased electrode surface area and attenuates the neural signal [99]. Besides, an increase in the surface area will cause abnormal impedance change of the electrode during long-term implantation [50], which will further deteriorate the recording quality.

### 2.3.2 Biocompatibility

The biocompatibility of a recording electrode implant depends on various factors, including electrode materials, device geometry, and surrounding environments. From the material standpoint, biocompatibility can be defined as the "ability of a material to perform an appropriate host response in a specific application" [100]. An ideal biomaterial for neural recording implants should be non-cytotoxic in vivo and release no substances or substances at only low, non-toxic concentrations. The tissue should produce minimal glial encapsulation surrounding the implant and only mild foreign body reaction without evidence of necrosis or implant rejection [101], [102], as shown in Figure 1B. Evaluation of material/device biocompatibility is critical and may include the tests of cytotoxicity, acute/chronic systemic toxicity, sub-acute/sub-chronic toxicity, genotoxicity, hemocompatibility, toxicokinetic sensitization, irritation, studies. and immunotoxicology [103]. Since the same material may respond differently to different biological environments, the International Organization of Standard (ISO) enacts various test and evaluation protocols to evaluate the materials' biocompatibility, considering various body contact types,

contact time, environments of intended use (*in vitro*, *ex vivo*, or *in vivo*), and test methods as mentioned in [104], [105].

## 2.3.3 Stability

Material stability is another important consideration of neural recording implants [106]–[109]. The fabrication imperfection of the electrode or the packaging materials, such as unavoidable pinholes and defects, could cause the oxidation and delamination of the materials, and hence, shorten the longevity of the implants in liquid environments with a high concentration of ions, such as cerebrospinal fluid [110], [111]. The heterogeneous junction where an electrode interfaces with an adhesion-promoting layer (e.g., Ti or Cr) or the heterogeneous alloys is also a potential risk of electrode reliability. The two different metals can form a short circuit galvanic cell in the tissue fluid that accelerates the corrosion of one of the metals and weakens the metal-to-metal bonding strength [112]. Therefore, higher atomic weight transition metals with high corrosion resistance, such as platinum and iridium, were selected as the primary electrode materials [65], [113], [114]. Homogenous alloys with multiple metal elements can also improve corrosion resistance [99]. Surface modification of electrodes with electrodeposited CPs is another method to slow down metal corrosion and improve device stability [115], [116]. For example, electrodeposited PEDOT is quite chemically stable in the damp, oxygen-rich environments because PEDOT can be further polymerized by the oxygen and protect the metal electrodes from direct exposure to reactive, oxygenated solution [117], and therefore, prevent the metals from corrosion [118], [119]. However, further polymerization could cause the increased electrochemical

impedance of the whole electrodes due to cracking or delamination of the PEDOT layer [99], [120].

Biofouling also contributes to the instability of the neurophysiological recording implants. Biofouling leads to the encapsulation of electrodes by protein and glial cells, especially on those with high electrochemical surface areas, and therefore, restricts ionic diffusion at the electrodeelectrolyte interface [121], [122]. In addition, the tissue response persistently promotes the degradation of electrode materials and insulation. To minimize electrode biofouling, significant efforts have been made on surface modification or functionalization to alter the chemical terminations, morphology, and wettability of the electrode surface [99]. Several hydrogel and polymer coatings, such as polyethylene glycol (PEG) and PEG methacrylate (PEGMA), have been utilized to improve the hydrophilicity of the electrode surface [123]–[125]. With large amounts of water in their structures, these materials are highly hydrated to increase the energetic penalty of removing water for protein and microorganism attachments. Engineered antifouling electrode materials, such as sp3 carbon-enriched, boron-doped polycrystalline diamond (BDD), also show the advantages of improved biocompatibility and reduced biofouling compared to conventional electrode materials [126], [127], as shown in Figure 1C. Morphological response of rat cortical neurons on the Parylene C and microcrystalline diamond (MCD) substrates (lower) appeared similarly to the control substrate. Moreover, nanostructured surfaces with low friction and low surface energies can effectively decrease cell attachment onto the implant surface, and hence, reduce the possibility of biofouling formation [128], [129].

# 2.3.4 Biodegradability/Bioresorbability

In contrast to stability, biodegradability is another prevailing topic that has been extensively studied in neural implants [41]. Unlike the aim of the stability to keep the implant devices in vivo for long-term detection, biodegradability requires the implants to be biodegradable and bioresorbable after a certain period (days to weeks) in order to avoid secondary damage to surrounding tissues during implant removal [130]. Some inorganic materials, including metals (e.g., gold nanoparticles (GNPs)), semiconductors (e.g., silicon nanomembranes (Si NMs)), and dielectrics (e.g. silicon dioxide (SiO<sub>2</sub>)), have shown outstanding degradation behavior [131], [132]. Combining those materials with biodegradable organic materials enables high-performance and less-invasive implantable devices [108]. Despite studies on biodegradable bulk materials, recently, special attention has been paid to engineering multi-functional thin-film materials that combine degradability with other desired properties (electrical, optical, mechanical) and can be dissolved in the phosphate-buffered saline (PBS) in 30 days [133]–[135], as shown in Figure 1D. However, the biodegradation performance of most thin-film degradable materials has only been tested in deionized (DI) water or saline solution (0.9% NaCl) [136], [137]. Since the *in vivo* environments are much more complicated than the *in vitro* environments due to the presence of biological molecules, such as proteins and cells, in vivo evaluation of these materials must be conducted to understand better their degradation rate and safety in living tissues [138], [139].

## 2.3.5 Mechanical Properties

Mechanical properties of the neural implants are extremely important for in vivo applications.

The Young's moduli of traditional solid materials (silicon, glass, and metal) range from 50 GPa to 200 GPa, orders of magnitude higher than those of the nervous tissues that are typically 3.15 - 10 kPa [140]. The mechanical property mismatch between the soft tissue and the stiff implants induces reoccurring electrode movement from the target neurons in response to natural body motions [141], resulting in unreliable recording from the same neurons for an extended period. In the long term, the presence of stiff implants elicits the effect of tissue staining at the implant site due to inflammatory response, and consequently neuronal degeneration and glial scar formation near the electrodes that prohibit the transmission of neural signals [86], [92], [93], [142]. Moreover, the stress induced by the micromotions of surrounding tissues can cause mechanical damage to the implants, such as cracks or delamination of the electrode materials, and then permanent device failure [140], [143], [144]. Compared to solid materials, soft materials, such as silicone, Parylene C (PA), SU-8, and polyimide (PI), with Young's moduli of 1-10 GPa, are more compliant with the soft tissue to form a conformal contact [140], [145], [146], as shown in Figure 1E. PDMS can achieve even lower Young's modulus of 1 MPa, becoming one of the softest prevailing packaging and substrate materials for neural implants [147].

Besides the above materials with consistent mechanical properties, shape-memory materials can be deformed from the initial shape under external stimuli, such as temperature, humidity, etc. [148]. Before and during implantation, devices made of shape-memory materials are stiff enough to penetrate the target tissue [149], [150]. Once adapted to the physiological conditions, the implanted devices can be programmed to snake around and climb nerves [151]. For example, Zhao et al. reported a 16-electrode microwire electrode arrays made of a shape memory metallic alloy [152],

nitinol, which an equiatomic alloy of nickel and titanium exhibits a shape memory effect caused by a thermally-induced phase transition [153]. The device can conform to the brain vasculature with minimized damage to the blood vessels during implantation. Shape-memory polymers (SMPs), such as thiol-ene/acrylate-based SMPs [154], [155], provide good elasticity and the diminished rigidity and mechanical mismatch with the soft tissue, suitable for use in manufacturing surgical devices and medical implants. The shape-memory effect of these materials is induced by the cross-links of polymeric chains and the corresponding external stress at the transition temperature [148].

### 2.3.6 Optical Transparency

Optical transparency of an electrode implant allows one to combine electrophysiological recording with other modalities, such as high-resolution optical imaging and optogenetics [130]. To date, high-resolution, systematic electrophysiological recording on optically scanned tissue surfaces of the brain has not been implemented, because conventional opaque electrode materials do not satisfy the optical qualification of high-resolution imaging [156]. Optogenetics applications also require high transmittance of the materials over a broad spectrum or under the specifically targeted wavelength for activating or inhibiting the genetically modified neurons with the minimum optical propagation loss [41]. With a unique combination of electrical conductivity, broadband transparency, and biocompatibility, several transparent conducting materials, such as ITO (Figure 1F), graphene, and PEDOT:PSS, have been explored as electrode materials [157]. These materials also provide sufficiently wide bandgaps to limit photoelectrochemical (PEC)

artifacts that arise from photo illumination of electrodes during opto-stimulation and two-photon imaging [51], [158], [159]. In addition, Au nanomesh electrodes [160] or PEDOT:PSS-coated Au [161] microelectrodes have been proven to achieve low electrochemical impedance and some degree of optical transparency, capable of electrophysiological recording in the brain. To realize fully transparent neural recording implants, polymers, such as PET, Parylene C, and PDMS, usually act as transparent substrate and encapsulation of the electrodes [162], [163].

### 2.3.6.1 Opto-neurostimulators

To date, a wide variety of optical stimulators have been reported and can be classified into two primary categories: single-channel and multi-channel stimulators. Different configurations of multi-channel opto-neurostimulators have previously been reported, which typically consist of individual optical fibers and waveguides separately coupled to different light sources [164], or an array of microscale light emitting diodes (μ-LEDs) directly assembled on solid or flexible substrates [13], [165], [166]. Particularly, multi-channel LED-based neurostimulators have become prevalent because of their low power consumption, illumination stability, fast switching ability [167], and the possibility of miniaturization towards a fully implantable neural interface. The primary advantage of these multi-channel stimulators is to offer spatially controlled, optical stimulation with high spatial resolution. While they have moved the field forward, development of such multi-channel devices requires complex and expensive microfabrication and integration technologies [168].

Single-channel opto-neurostimulators provide unique advantages over multi-channel devices,

such as low power consumption, miniaturized dimensions, fabrication simplicity, and low cost. Over the last decade, great efforts have been made to develop various single-channel optoelectronic devices that are light-weight and compact. However, these devices are not yet commercially available for chronically reliable, optical stimulation in neuroscience and clinical research [169]. An ideal single-channel optical neurostimulator should enable precise manipulation of the target neurons with minimal power consumption. Miniaturization of the devices is imperative to reduce surgical invasiveness as well as tissue inflammation and damage. In addition, the device should ideally be constructed and packaged with biocompatible and mechanically flexible materials that ensure minimum tissue damage while simultaneously protecting the functioning electronics from the corrosive biological environments over the long term. For behavioral experiments particularly, an un-tethered device would be desired to enable free movement of the experimental subjects and prevent unwanted interference to the experimental outcomes. All these considerations place unique constraints on the light sources, materials, and system architecture of single-channel optical neurostimulators.

#### 2.4 Electrode Materials

### 2.4.1 Inorganic Materials

Recently, much attention has been devoted to investigating innovative electrode materials to improve electrical, mechanical, and optical properties, as well as stability, biocompatibility, or biodegradability of recording electrodes [48]. This section classifies the electrode materials into

inorganic, organic, and carbon-based materials, and discusses the advantages, disadvantages, and applications of each specific material in detail.

#### 2.4.1.1 Metals

Metals are the most prevailing and common electrode materials for neural recording for nearly 50 years [170]. Widely used metal electrode materials, such as gold (Au), platinum (Pt), iridium (Ir), tungsten (W), and tantalum (Ta), offer a great number of desirable properties, including chemical inertness, high electrical conductivity, and excellent biocompatibility in biological environments [130], [171], [172]. Au/Pt and Ir/Pt have been used as the electrode materials for "Utah array" and "Michigan Probe", two of the most popular neural interface electrodes [173], [174]. However, these materials suffer from limited electrochemical conductivity and injection charge density, especially when the electrode is shrunk to a micrometer scale for better spatial resolution [148].

To address the impedance-size trade-off in microelectrodes, three dimensional (3D) nanostructured Au microelectrodes have been developed wherein nanoporous structures were created on the microelectrode surface to achieve larger surface area and therefore lower impedance [175]. The nanotopography of such nanoporous structures also improves *in vivo* stability of electrode implants by reducing the incidence of glial scar encapsulation while maintaining high neuronal coverage. Surface modification with Au nanorods, nanoflakes, or nanopillars is another option to increase the effective recording area without change to the overall electrode dimensions [176]–[178]. For example, Nick et al. fabricated Au nanopillars on the microelectrodes, showing

a reduction of 1-kHz impedance by up to 89.5 times and dramatic impedance decrease over 1 Hz to 100 kHz [178]. With a determined diameter, a larger high-aspect ratio of the nanopillars results in lower impedance of the electrode. Similarly, Zhou et al. integrated an Au-nanorod array on flexible thin-film microelectrodes using locally patterned anodized porous alumina as a template [176]. The interface impedance of this 3D electrode was 25 times smaller than that of conventional two dimensional (2D) planar microelectrodes under the same dimensions. Moreover, 3D electrodes modified with Au nanoflakes have also been reported by Kim et al., demonstrating a maximum impedance reduction factor of 57.9 with an electrode diameter of 5 μm [177].

An alternative nanostructure for electrode surface modification is Pt black, a nanoparticulate-like Pt formed from electroplating. Zhang et al. show that, with Pt black, the 1 kHz impedance of a 100- $\mu$ m diameter electrode wire decreased from 16.6 k $\Omega$  to 3.5 k $\Omega$  and the charge injection limit increased from 0.286 mC/cm² to 1.906 mC/cm² [56]. Furthermore, alloys with two or more metals have been investigated for nanoparticle synthesis to improve the stability of metallic nanoparticles. One example is the bimetallic Au/Pt alloy nanoparticle modified Au microelectrode, which exhibits an average 1 kHz impedance of 0.23 M $\Omega$  with a recording site of 20- $\mu$ m diameter [30], as shown in Figure 2A.

Ir/IrOx (iridium oxide) is another prevailing electrode material and often used in the format of either a bulky wire or a thin film coating [179]–[182]. Ir wires are very stiff and highly resistant to corrosion [183], whereas IrOx thin films are unstable and prone to degradation as electrode dimensions decrease and charge densities increase [143]. However, untreated Ir electrodes suffer

from limited charge injection capacity. Ir alloys, such as PtIr, exhibit significantly improved mechanical and electrochemical properties [99]. Cassar et al. electrodeposited a PtIr coating (EPIC) on the tip of 75- $\mu$ m-diameter microwire electrodes, resulting in reduced electrochemical impedance from  $534 \pm 57 \text{ k}\Omega$  to  $80 \pm 18 \text{ k}\Omega$  and improved SNR [184].

### 2.4.1.2 Semiconductors

Semiconductors can be readily configured into various electronic elements (e.g., sensors, transistors, switches, etc.) with desired properties (e.g., signal transduction, amplification, multiplexing, etc.) to achieve a complex, integrated biointerface system [185], [186]. Organic semiconductors provide unique advantages of mechanical compliance, biodegradability, and stretchability. Contrastly inorganic semiconductors are more rigid but provide faster response, higher sensitivity, better accuracy, and lower power consumption of biological sensing than organic semiconductors because of high charge carrier mobilities in inorganic materials [187]. Moreover, advancement in modern semiconductor technologies allows precise batch fabrication of high-performance inorganic semiconductor devices in various architectures at submicron or even nanometer scale, matching the size of subcellular and molecular targets.

Silicon (Si) is the most commonly used semiconducting material in neurophysiological implants. The well-developed microfabrication and photolithography techniques for complementary metal-oxide-semiconductor (CMOS) integrated circuits enable the design and fabrication of high density, high-channel-count multielectrode arrays, capable of mapping activity from large-scale neural networks with high spatiotemporal resolution [47]. As the current state of the art, the Neuropixel

Si probe developed by Jun et al. integrates 960 recording sites (384 configurable recording channels) on a  $70 \times 20 \,\mu m$  shank, weighs only  $\sim 0.3 \, g$ , and provides on-chip signal amplification and digitization [188]. Each probe enables stable and chronic recordings from more than 100 neurons for over 150 days while maintaining a large signal to noise ratio[188].

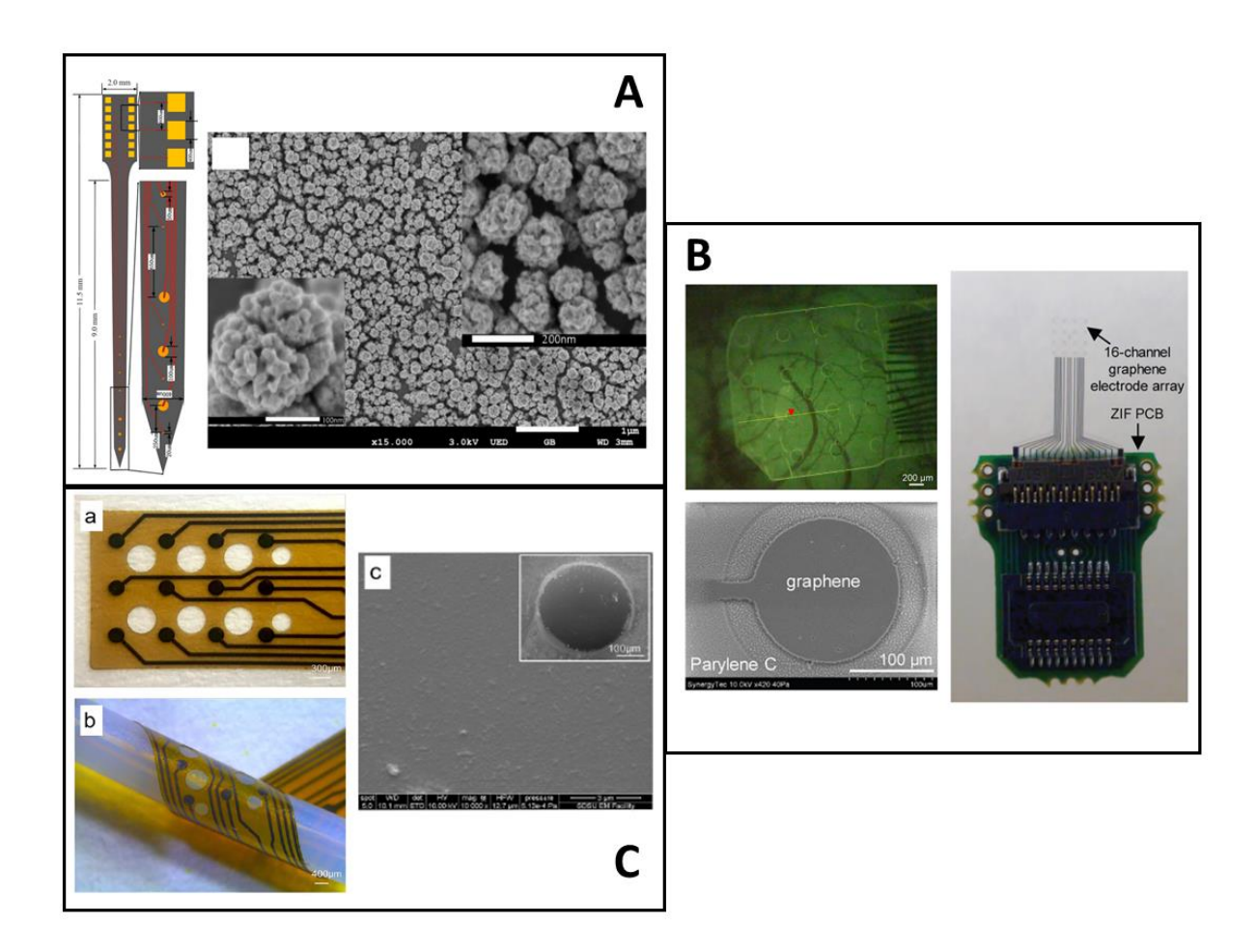


Figure 2. Examples of electrode materials. (A) The electrodes of the neurophysiological implants (left) are made of Au/Pt alloy as indicated in the SEM image (right) (reprinted with permission from (Zhao et al., 2016)). (B) Transparent graphene as the electrode material (lower left) on the μΕCoG array (right) for the neurophysiology signal recording and imaging (upper left) (reprinted with permission from (Park et al., 2018)). (C) Thin-film glassy carbon recording electrodes on flexible polyimide (left). The SEM image (right) shows the surface morphology of the glassy carbon (reprinted with permission from (Vomero et al., 2017)).

With high sensitivity to changes in electric potentials and surface charges, Si-based nanostructure materials are also used to make low impedance microelectrode interface for neurophysiology recording [175], [187]. For example, Si nanowires have been utilized as low impedance nanoelectrodes to intracellularly record action potential from cultured neurons with high precision [189], [190]. In addition, a forest of randomly oriented gold coated-Si nanowires has been shown to achieve noninvasive extracellular recording of astrocytes by mimicking the properties of astrocytes in vivo [191]. Compared to bulky materials, improved stretchability and bendability can be achieved with Si nanowires. Similarly, an amorphous atomic structured Si material has been proposed to create mesostructures with fibrils and voids, with an average Young's modulus of 2-3 orders smaller than that of the single-crystalline Si [188]. As key building blocks, nanowires can also be integrated with microporous gel-based scaffolds, yielding highly sensitive and flexible 3D neural probes for mapping the propagation of the action potential [192]. These 3D electrodes offer excellent spatial resolution and stability with little immune response to chronic implantation. In addition, Si nanowires can be configured into field-effect transistors (FETs), capable of sensing neurophysiological signals at a faster switching speed. Unlike faradaic measurement of neural signals through electrodes, the charge carrier density of FETs can be modulated as a function of LFP in surrounding tissues, allowing spikes tracking along neurites and neural networks with single-cell resolution and reasonably high sensitivity [193]–[195]. Recently, Yu et al. reported a flexible and bioresorbable neural electrode array based on Si NMs [196]. With biodegradable SiO<sub>2</sub> insulation and PLGA substrate, the whole device was able to degrade in PBS (pH=10) within 15 days.

ITO is a well-known n-type semiconductor material that is often utilized in transparent microelectrodes. ITO has high conductivity, excellent transparency over the entire visible spectrum due to a large bandgap of around 4 eV, as well as confirmed biocompatibility [197]. ITO can be grown on either solid or flexible substrates using well-developed physical vapor deposition techniques (e.g., sputtering). However, similar to metals, ITO electrodes suffer from increased electrochemical impedance when the electrode size decreases, leading to undesirable electrochemical reactions with the brain tissue and poor recording quality due to increased thermal noise and ion-based electric fluctuations of surrounding media [159]. In addition, ITO is relatively brittle, making it unsuitable for use in large patterns (e.g., pads or interconnection wires) on flexible substrates [166]. Other semiconducting materials, such as germanium (Ge), silicon germanium alloy (SiGe), indium-doped zinc oxide (IZO), indium-gallium-zinc oxide (a-IGZO), and zinc oxide (ZnO), has also been investigated as recording electrode materials because of their desired electrical, mechanical, optical, biocompatible, and stable/biodegradable properties [198]— [203].

# 2.4.2 Organic Materials

Given the same device dimensions, organic materials offer lower Young's moduli than inorganic materials, reducing potential adverse outcomes including inflammation response, glial scar encapsulation, unstable neural recording, and mechanical failure of implants [107]. Organic materials also provide significant advantages of easily modifiable surface structures, mixed ionic and electronic charge transport, less biofouling/surface oxides, and the wide option of biocompatible materials [103].

# 2.4.2.1 Conducting Polymer (CP)

CPs, as organic polymers, consist of monomeric compounds linked in chains of alternating single and double bonds, and doped with a stabilizing counter-ion. CPs have the mechanical properties matched with those of biological tissues. Because conjugated polymers have narrower band gaps, electrons can move easily between the conducting band and valence band. CPs can transduce ionic currents to electronic currents through redox reaction in bulk and volumetric charging, resulting in low impedance and high charge storage capacity [204], [205]. Due to the diversity and adaptability of synthetic processes, the ionic-electronic transport and biochemical surface characteristics are tunable for improving the performance and stability/biodegradation of CPs [206]. Furthermore, dopants, such as small cations/anions (Na<sup>+</sup>, Cl<sup>-</sup> and ClO<sup>4-</sup>) and large polymeric species (polystyrene sulfonate and polyvinyl sulfonate), can be utilized to improve the electrical conductivity of organic materials by adding electrons to the conduction band (n-doping) or removing electrons from the valence band (p-doping) [207].

PEDOT:PSS is a prevailing class of CPs for neural interfacing applications. PEDOT:PSS possesses many desirable properties, including high biostability, outstanding biocompatibility, and excellent electrochemical properties. Studies show that, with the same electrode area, the electrochemical impedance of microelectrodes is an order of magnitude lower than that of Pt microelectrodes [208]. Khodagholy et al. proposed a PEDOT:PSS-based, high-density NeuroGrid that consists of patterned PEDOT:PSS electrodes with the neuron-size density, capable of simultaneously recording LFPs and action potentials in anesthetized and awake human subjects [46], [209]. The enhancement in electrochemical conductivity of PEDOT:PSS-coated electrodes

can be attributed to the increased surface roughness of the electrode, as confirmed by Yang et al. [159], [210]. Their studies show that the average surface roughness (Ra) of the PEDOT:PSS coated electrode increased from 0.85 nm to 3.33 nm, resulting in dramatically improved charge storage capacity and impedance by several orders of magnitude. Similarly, Pranti et al. reported that electropolymerization of 1 µm thick PEDOT:PSS on Au microelectrodes increased the electrode surface area, and the corresponding electrochemical impedance was reduced by ~99% [211]. Besides planar films, ordered PEDOT nanostructures can be self-assembled on the electrode surface with surfactant molecules as a template to further reduce the electrode impedance [212]. Abidian et al. also reported that PEDOT-based nanotubes enable ~8 times lower impedance and much higher charge capacity density than planar PEDOT films, mostly due to the increased surface area [213]. PEDOT:PSS can be applied by spin-coating or ink-jet printing in a low-cost and rapid fashion, but at the expense of poor adhesion with underlying electrode materials. Electrodeposition techniques, such as electroplating, can improve the bonding strength at the PEDOT-electrode interface, preventing potential risk of PEDOT delamination in the biological environment [213]. A recent study by Boehlet et al. also demonstrates that pre-treating the smooth Pt electrode with porous Pt structures before the PEDOT deposition can enhance the adhesion between PEDOT and Pt. The PEDOT film deposited on the porous Pt substrate shows no delamination after more than 100 days in accelerated aging tests in PBS [214].

Several other CPs, such as PPy, poly(aniline) (PANi), poly(thiophene) (PT), and some of their derivatives [215]–[217] are also alternative candidates. PPy has outstanding water solubility [216],

good conductivity of 40-200 S/cm [218], low Yong's moduli of 2400 Pa for thin films (15-35 µm thick) [219], and 430-800 MPa for nanocomposites [220]. PPy can be electrodeposited in situ on the electrode surface with different dopants. PANi has an electrical conductivity of 5 S/cm [218] and is primarily used as a coating material on electrodes instead of a standalone electrode material due to its relatively small Young's modulus (2-4 GPa) [221]. Nanostructured PANi can be synthesized by chemical oxidative or electrochemical polymerization in an aqueous solution that contains a variety of surfactants to precisely tailor the structure of the film at small length scales for increased effective surface area [212], [215]. Functionalized PT copolymer, with precisely tunable electrical, optical, mechanical, and adhesive properties, is also applicable for neural recording electrodes [217]. For PT, the maximum conductivity is 10 - 100 S/cm, and Young's modulus of thin films is ~3 GPa [222].

### 2.4.3 Carbon-based Materials

Carbon-based materials, such as graphene, carbon nanofibers, carbon nanotubes, are another promising class of electrode materials. Carbon-based materials have high biocompatibility and valuable mechanical properties, such as high tensile strength, and can be prepared by various approaches, including chemical vapor deposition (CVD), electrospinning, and exfoliation.

### 2.4.3.1 Graphene

Graphene, a 2D single-layer sheet of carbon atoms in a hexagonal arrangement, has a great number of outstanding properties: ~90% optical transmittance [17],  $76\Omega/\Box$  sheet resistance (for a 4-layer structure), 200000 cm<sup>2</sup>/V·s electron mobility [223], and ~5 × 10<sup>3</sup> W/m·K thermal conductivity [224]–[226]. The remarkable biocompatibility makes graphene an appropriate choice

for neural interface applications [29], [227]. Moreover, the outstanding transparency of the graphene microelectrode enables simultaneous neurophysiological recording, light stimulation, and optical imaging of living tissues [17]. Despite many benefits, graphene has a large Young's modulus (~1.0 TPa) [140], [228] and a large impedance (~2 M $\Omega$  for 100  $\mu$ m  $\times$  100  $\mu$ m microelectrodes) at the graphene-electrolyte interface, possibly due to the intrinsic hydrophobicity of graphene [229]. The comparatively low double-layer capacitance of single- or few-layered graphene could cause considerable thermal noise and low SNR of neural recording. Therefore, it is critical to reduce the mechanical mismatch between graphene electrodes and surrounding tissues as well as to improve the electrical properties of hydrophobic graphene. Small area graphene can be prepared using mechanical exfoliation, which is tedious and time-consuming. CVD allows growing high-quality graphene over large areas at either high temperatures of over 1000 °C or on specific substrates in a specific gas mixture, but is incompatible with polymer materials [230]. Significant efforts have been made in recent years to transfer CVD graphene from rigid substrates onto soft substrates. For example, Park et al. transferred and stacked four graphene monolayers sequentially onto a flexible PA film [17] as the electrode material. Later, the same group reported a transparent carbon-layered 16-channel array[157], as shown in Figure 2B. It succeeded in simultaneous in vivo recording of light-evoked neural signals in conjunction with fluorescence imaging. Similarly, Chen et al. transferred graphene onto SU-8 and demonstrated that introducing hydroxyl groups on the graphene surface by a mild stream plasma treatment can effectively increase the water contact angle from  $91.1^{\circ} \pm 5.6^{\circ}$  to  $41^{\circ} \pm 4.7^{\circ}$  [229]. The increase in graphene hydrophilicity leads to impedance reduction from 7216  $\Omega/\text{mm}^2$  to 5424  $\Omega/\text{mm}^2$  and SNR

improvement from  $20.3 \pm 3.3$  dB to  $27.8 \pm 4.0$  dB. Besides electrode configurations, Kireev et al. developed graphene-based FETs on flexible polyimide-on-steel and found that the device did not show significant loss in recording capability after up to 1000 cycles of mechanical bending [230]. 2.4.3.2 Carbon Nanostructures

3D carbon nanostructures, such as carbon fibers (CFs) and carbon nanotubes (CNTs), can be utilized as a standalone electrode or as a surface coating to improve the surface area and electrochemical impedance [48], [175], [231]–[233]. Standalone carbon fiber microelectrodes (CFMEs) are typically constructed by insulating carbon nanofibers with pulled glass pipettes [234] or PA [235]–[239] followed by opening the electrode tip with chemical etching, plasma removal, or laser cutting. Recently Patel et al. assembled 16 CFMEs to form a multichannel CFME array, capable of chronic recording of single unit activity for one month [236]. Such CFMEs electrodes can be functionalized with electrodeposited PEDOT [236], [239] or IrOx [237], [238] to further improve their impedance and charge capacity density. An alternative method to fabricate CF electrodes is thermal drawing [53], by which carbon nanofiber (CNF) composites were unidirectionally aligned in cyclic olefin copolymer (COC) as a recording electrode. The asfabricated fiber had overall dimensions of less than 100 x 100 µm<sup>2</sup>, including a single recording site of CNF composite with a size ranging from  $18 \times 11.3 \,\mu\text{m}^2$  to  $35.2 \times 20.1 \,\mu\text{m}^2$ , and dramatically reduced impedance magnitude by 2 orders compared to the conventional polymer electrodes [53]. Alternatively, Yu et al. demonstrated in situ growth of vertically aligned carbon nanofibers on prepatterned Ni catalyst using direct current catalytic plasma-enhanced CVD. The array consists of 40 electrodes in one line with 15 μm spacing along a complete length of 600 μm. The conical shape

of the CNFs facilitates the penetration of the electrodes into the interior of the tissues or individual cells to improve electrical coupling [240]. Besides pure CNFs, Saunier et al. reported a composite PEDOT:CNF material combining PEDOT with CNFs through electrochemical deposition. The PEDOT:CNF modified microelectrode demonstrates low specific impedance of 1.28  $M\Omega \cdot \mu m^2$  at 1 kHz and charge injection limit of 10.03 mC/cm², suitable for multifunctional electrophysiological recording and neurotransmitter sensing. Moreover, CNF has magnetic susceptibility close to water and tissues, making it compatible with high field functional magnetic resonance imaging (fMRI) to enable high-resolution electrophysiological measurements and anatomical studies of large-scale neural networks without electrode interference with MRI images [241].

Unlike the CNFs, CNTs have smaller sizes with higher density and can be divided into single-walled carbon nanotubes (SWCNTs) and multi-walled carbon nanotubes (MWCNTs) [48]. SWCNT is a single graphite sheet wrapped into a cylindrical tube, while the MWCNTs nest several SWCNTs together concentrically, looking like rings of a tree trunk [242]. Perfect SWCNTs have outstanding mechanical properties and electrical properties, quite similar to the perfect MWNTs due to the weak coupling of nanotubes in MWNTs [243]. Additionally, the rolling direction of the SWCNTs decides the properties that are more like metals or semiconductors [244]. For use in neural electrode implants, CNTs can be electrochemically coated on the conventional tungsten and stainless steel wires under ambient environments at low temperatures to improve the impedance and charge transfer properties of the electrodes [245]. Furthermore, the tungsten wires can be

etched electrochemically to obtain pure carbon nanotube probes as intracellular recording electrodes [246]. Besides electrochemical deposition, CVD methods can synthesize CNTs directly on the tip of quartz-insulated platinum/tungsten electrodes [247]. Compared to electrochemically deposited CNTs, the chemical vapor deposited CNTs show remarkable mechanical toughness and stability over time. The CVD-CNT-coated microelectrodes can retain unaltered impedance values after one-year storage or after being subjected to a million current pulses at charge injection limit. CNT can also be integrated with flexible polymer substrates to implement flexible CNT electrodes. For example, Lin et al. embedded pre-patterned CNT structures into a PA film to create a flexible CNT electrode array with significantly reduced mechanical rigidity and low impedance for the high-quality recording of spontaneous spikes from the crayfish nerve cord [248]. Similar to graphene, studies show that the electrical properties of the CNT-based electrodes can be improved by tuning the hydrophilicity of CNTs. For example, plasma/UVO3 treatment of < 10s can alter the surface wettability of CNT from superhydrophobicity to superhydrophilicity, mainly due to the formation of -OH terminations [249]-[251]. Amino-functionalization of the MWCNTs surface with a 2wt% 1,4-diaminobutane solution can also improve the hydrophilicity of the surface, lasting for at least six months in the air [252]. While widely used in neural electrode implants, the cytotoxicity of these nanostructures is still a big concern, since the nanomaterials can penetrate through the blood-brain barrier (BBB) and cause irreversible cell death and damage to the brain [106], [253].

### 2.4.3.3 Glassy Carbon

Glassy carbon (GC) offers a wide range of mechanical, electrical, and electrochemical properties, which can be specifically tailored with different pyrolysis temperatures under different fabrication conditions to match the properties of the target tissue [184]. Because flexible polymer substrates are unable to tolerate high pyrolysis temperatures, pattern transfer techniques are often used to fabricate GC based, flexible ECoG microelectrode arrays on polyimide substrates [254], [255], as shown in Figure 2C. Furthermore, coating GC based microelectrodes with CPs, such as PEDOT:PSS, helps to reduce the impedance magnitude of a 60- $\mu$ m-diameter electrode by at least 2 orders [254]. Most recently, Chen et al. designed and fabricated a cone-shaped glassy carbon neural electrode array using 3D printing and chemical pyrolysis technologies [256]. The electrode had a 0.78 mm<sup>2</sup> recording area exposed at the tip, and the corresponding impedance, capacitance, and SNR are 7.1 k $\Omega$ , 9.18 mF/cm<sup>2</sup>, and 50.73  $\pm$  6.11, respectively [256].

### 2.4.3.4 Diamond

In recent years, diamond has emerged as a promising electrode material for neurophysiological recording and neurotransmitter sensing. Boron-doped polycrystalline diamond (BDD) offers unique properties, including wide aqueous potential window, chemical inertness, capability for surface modification, tunable electrical conductivity, and biocompatibility [257]–[260]. Despite the many benefits of this material, the mechanical property mismatch between BDD (Young's module of ~103 GPa) [261] and soft tissues is a major obstacle that impedes the development of BDD into fully implantable electrochemical devices. Compared to other semiconducting materials, diamond processing and patterning are more difficult due to its extreme mechanical hardness, lack

of ductility, and weldability [262]. Therefore, attempts have been made to develop new material synthesis and processing methods to fabricate diamond-based electrodes with improved flexibility. For example, Fan et al. demonstrated a wafer-scale fabrication method to transfer large-scale, prepatterned BDD microelectrode arrays from a solid silicon substrate onto a flexible PA substrate [127], [263]. The electrodes made of the BDD growth side exhibited a rougher topology, a higher sp3 content, and a large grain size than the nucleation side, enabling a wide working potential window, a low background noise, a resistance to chemical fouling, and a reduced electrochemical impedance [127].

#### 2.5 Conclusion

Investigation of the novel electrode materials is, at present, one of the most prevailing topics in developing advanced neural recording electrodes, as evident by continuous growth in literature. Electrodes are the most significant element that directly influences the quality of neurophysiology recording. With recent advancements in material science and engineering, implantable electrode interfaces capable of recording neural activity with high spatiotemporal resolution can now be achieved. This chapter showed typical electrode materials associated with the state-of-the-art electrode devices, as guidance for future device development. Tables 1 summarizes the main properties of the selected electrode materials. In particular, Table 1 lists the properties of various electrode materials discussed in this chapter, including their electrical properties, biocompatibility,

stability, biodegradability and bioresorbability, mechanical flexibility and bendability, Young's modulus and broad-band optical transmission.

With the trend of further miniaturization in large-scale, high-density recording electrodes, many challenges remain unsolved, mostly related to stability, high fidelity of recording, and minimal foreign-body immune responses. Additional studies by some groups are being done on new electrode materials (e.g., diamond and MXenes) that were not originally used in neural interfaces [264], [265]. For example, Driscoll et al. purposed flexible Ti<sub>3</sub>C<sub>2</sub> MXene microelectrode arrays for *in vivo* micro-ECoG recording with the benefits of significantly high volumetric capacitance, electrical conductivity, surface functionality, and sensitivity [265]. While significant progress has been made, comprehensive evaluation of their functionality, long-term stability and biocompatibility is needed to fully realize the true potential of these new materials for use in neural recording interfaces.

Besides new electrode materials (e.g., diamond and MXenes), one research area that has received much recent attention is to design and develop composite materials that combine the unique advantages of different existing materials while eliminating their major drawbacks. The use of composite materials in electrode structuring has the potential to bring disruptive changes to single material designs. For example, Pal et al. demonstrate a flexible bio-sensor that combines PEDOT:PSS sensing elements on a fully biodegradable and flexible silk protein fibroin support to achieve excellent electrochemical activity and stability over days [266]. Composite electrode materials can be prepared by in situ electrodeposition or multilayered assembly of inorganic and/or

organic conducting materials on planar substrates to achieve the desired electrochemical, biological, optical, and mechanical properties. Recently, with their tunable composites, configurations, and density, 3D nanostructured materials represent novel electrode materials to further improve the electrochemical impedance and the capacity of the injection charge density, two important factors that determine the SNRs and recording quality of the electrodes. While promising, the *in vivo* evaluation of these composite materials is incomplete, preventing their applications in chronic neural interfaces.

Recently, transparent neurophysiology recording electrodes are getting attention because their high potential to work with capabilities of imaging and optogenetics technology. For optogenetics, this innovative technology uses light to activate or inhibit the genetically-modified neuron. Therefore, the more transparent the electrodes, the more light will go through the electrodes and finally arrive at the neuron, leading to the minimum optical propagation loss and higher sensitivity. In addition, high-resolution imaging could be achieved along with recording function compared to the opaque materials. Several transparent materials, such as ITO, graphene, and PEDOT:PSS have been under research [17], [166]. Those materials have their own property limitations in six key material characteristics that were discussed in the previous section. Therefore, finding and building up new transparent electrodes with excellent characteristics combination are urgent to solve the existing challenges of those transparent materials.

Table 1. Summary of various electrode materials with key properties

Electrode materials		Electrical properties (impedance @1kHz)	Biocompatibilit y	Stability	Biodegradability /Bioresorbability	Mechanical flexibility/be- ndability	Young's modulus	Optical Transmission (400-700nm)	Reference
GNPs	Nanopillars	$13.1\pm2.7$ kΩ - $1172.3\pm241.6$ kΩ (0 - 22.5 μm height)	Cytotoxic (depend on the size of GNPs)	14 days in vitro	Biodegradable	Bendable	1-10 GPa	Opaque	[178]
	Nanorods	1.847 kΩ (10000 μm <sup>2</sup> area)		20 times (agarose gel insertion)					[176] [176] [177] [267]
	Nanoflakes	11.9±1.47 kΩ - 249±28.1kΩ (5 - 50 $\mu$ m diameter)		A month					[207]
Pt black		3.5 k $\Omega$ (4 mm length, ~100 $\mu$ m diameter)	Biocompatible	3 days in vivo	N/A	Bendable	N/A	Opaque	[56] [268] [269]
Au/Pt alloy		0.23 MΩ (20 nm diameter)	Biocompatible	7 times (ultrasonic treatments)	N/A	N/A	113.8 GPa	Opaque	[30]
Ir/Pt alloy		$80{\pm}18~k\Omega$ (13 mm length, 75 $\mu m$ diameter)	Biocompatible	12 weeks in vivo	N/A	Bendable	185.5-189.6 GPa	Opaque	[184]
Si nanowires		$\sim$ 20 M $\Omega$ (100 nm - 200 nm tip diameter)	Biocompatible	8 days (rodent neurons)	Biodegradable	N/A	60-240 GPa	Transparent	[190] [270] [271]

Table 1 (cont'd)

Si NMs	$\sim 50 \text{ k}\Omega$ - $\sim 250 \text{ k}\Omega$ (200 <sup>2</sup> - 500 <sup>2</sup> μm <sup>2</sup> )	Biocompatible	A month in vivo	Bioresorbable	Flexible	3.25 -180 GPa (2 nm - 25 nm thickness)	Transparent	[196] [272]
ITO/PEDOT:PSS	$\sim 40 \text{ k}\Omega$ - $\sim 100 \text{ k}\Omega$ (10 - 80 μm diameter)	Biocompatible	4 weeks in vitro	N/A	Flexible	~77 GPa (on glass)	Transparent(> 80 %)	[159] [273]
PEDOT:PSS/nanostruct ur-ed Pt	9.2 kΩ (500 μm diameter)	Biocompatible	1500 CV cycles	N/A	Flexible	N/A	Opaque	[214]
PPy nanotubes/GNP	~5 kΩ (300 μm diameter)	Biocompatible	Stable	Biodegradable	Flexible/bend a-ble	N/A	N/A	[216]
Diamond	$\sim 207.9 \text{ k}\Omega \ (0.0079 \ \text{mm}^2 \text{ area})$	Biocompatible	Stable	N/A	Flexible (on Parylene C)	~ 10 <sup>3</sup> GPa	Opaque	[127]
Graphene	243.5 ±15.9 kΩ (~200 μm diameter)	Biocompatible	70 days in vivo	N/A	Flexible	~1 TPa	Transparent(> 90%)	[17] [274]
CNFs	~1 MΩ (2 cm length, $25.7 \times 16.6 \ \mu\text{m}^2)$	Biocompatible	4 weeks in vivo	Unbiodegradable	Flexible	6-207 GPa	N/A	[53] [275] [276]
CNTs	~64.5 Ω mm <sup>-2</sup>	Biocompatible	Stable	Unbiodegradable	Flexible	530- 700GPa	Transparent (~60%)	[250] [276] [277]
Glassy carbon	$11.0 \pm 5.4$ kΩ (300 μm diameter)	Biocompatible (12 days)	Stable	N/A	Flexible	20 GPa	Opaque	[278] [254]

# CHAPTER 3: Characteristics of Transparent, PEDOT:PSS Coated ITO Microelectrodes

This chapter covers preliminary work of our research on electrochemical and optical characteristics of flexible, transparent microelectrodes, which consist of thin PEDOT:PSS spun onto ITO electrodes for potential applications in biomedical optoelectronic devices. Although PEDOT:PSS-ITO combined films have been extensively investigated for applications in optical devices, such as solar cells and LEDs, PEDOT:PSS-ITO films for use in electrophysiological recording have not been well-characterized yet. Therefore, this chapter reports on electrochemical and optical characteristics of flexible, transparent microelectrodes, which consist of thin PEDOT:PSS spun onto ITO electrodes for potential applications in biomedical optoelectronic devices. In this work, PEDOT:PSS coated ITO microelectrodes with various diameters of 10 µm, 37 µm, 50 µm and 80 µm were microfabricated and characterized, and their properties were compared with plain ITO microelectrodes. Experimental results demonstrate that PEDOT:PSS coated ITO electrodes exhibit decreased electrochemical impedance, well-performed stability in saline, and increased charge storage capacity while preserving excellent optical transparency and mechanical flexibility. The experimental results were fit to equivalent circuit models to extract the interface capacitance, charge transfer resistance and solution resistance at the electrode-electrolyte interface.

# 3.1 Introduction

Optogenetics is a revolutionary neuromodulation technique that utilizes light to excite or inhibit the activity of genetically targeted neurons, expressing light-sensitive opsin proteins [279]. To fully realize the potential of the optogenetics tools, neural interface devices with both recording and stimulating capabilities are vital for future engineering development, and improving their spatial precision is of high interest. While ITO has been used in making transparent recording microelectrodes for optogenetics applications [166], it contains expensive rare elements and has poor mechanical flexibility. Moreover, ITO electrodes, when scaled down to micron dimensions, face a critical problem of increased electrochemical impedance, which would lead to undesirable electrochemical reactions with the brain tissue [21] and poor recording quality due to noisy, ionbased electric fluctuations of the surrounding media [22]. Thus, there is an urgent need to develop low-impedance, transparent microelectrodes as a neural recording interface in combination with optogenetics. PEDOT:PSS, as one of the most prevalent conducting polymers (CPs), has been demonstrated with many desirable properties for electrophysiological recording, including high biostability, outstanding biocompatibility, and simple utilization with low-cost spin-coating and ink-jet printing techniques [26] [27]. However, PEDOT:PSS has seldom been used independently as a transparent electrode because of its limited electrical conductivity. PEDOT:PSS can only achieve a sheet resistance of ~40 ohms/sq even when doped with solvents, such as H<sub>2</sub>SO<sub>4</sub>, which is significantly higher than the ITO sheet resistance of ~10 ohms/sq [280].

To address the above challenges, I proposed a combined ITO-PEDOT:PSS electrode configuration by spinning thin PEDOT:PSS films on ITO microelectrodes, for applications in low-

impedance neural recordings. PEDOT:PSS coated ITO microelectrodes with different diameters were microfabricated and characterized experimentally, and their properties were compared with plain ITO microelectrodes. In particular, electrochemical impedance spectroscopy (EIS) was used to analyze the frequency-dependent impedance of the microelectrodes in a 0.9% NaCl (saline) solution. Equivalent circuit models were applied to fit the experimental results into parameters representing macroscopic physical quantities related to electrode-electrolyte interface impedance. Cyclic voltammetry (CV) was used to quantify the charge storage capacity of the microelectrodes. Atomic force microscopy (AFM) and ultraviolet-visible (UV-Vis) spectroscopy were used to study the sample's surface morphology and optical transmittance, respectively.

# 3.2 Materials and Methods

### 3.2.1 Design and Fabrication of Microelectrode Probes

Each probe under test consisted of 6 transparent microelectrodes distributed uniformly along the tip of a single shank, and interconnection wires and contact pads made out of copper (Figure 3a). To fabricate the ITO electrode probe, first, 500 nm copper was thermally evaporated (Edward Auto306, Edwards, UK) on an ITO coated PET substrate (639303, Sigma-Aldrich). The copper was patterned using ultraviolet (UV) photolithography and then etched in copper etchant. Next, photoresist (PR) was spun on the substrate and photolithographically patterned to form a mask for chemical etching of ITO in 5% hydrochloric acid. After ITO electrodes were constructed, 2 μm Parylene C was deposited (PDS 2010, Specialty Coating System, Inc) on the substrate as an insulation layer. Then Parylene C on the contact pads and ITO electrodes was

removed completely using oxygen plasma dry etching (RIE-1701 plasma system, Nordson March, Inc). Prior to PEDOT:PSS coating, a PR layer was patterned to expose only the ITO electrode sites. PEDOT:PSS (768642, Sigma-Aldrich) was spun on the top of the substrate with

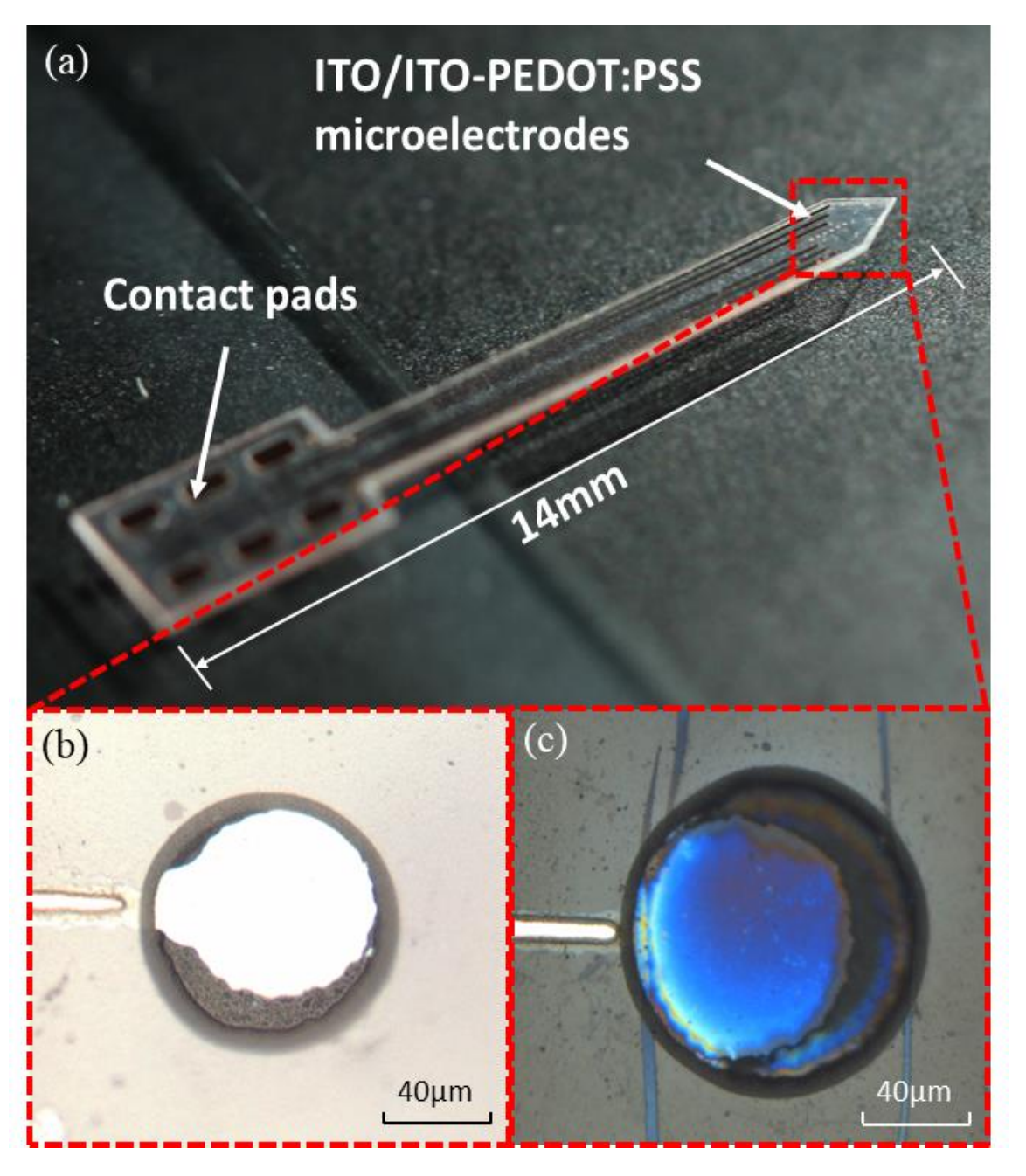


Figure 3. (a) Photo of a fabricated microelectrode probe. Microscope images of the ITO electrodes without (b) and with PEDOT:PSS coating (c).

500 rpm spin speed for 30 s and then 4000 rpm for 120 s, followed by baking on a hotplate at 100°C for 30 mins. Finally, the PR was rinsed off with acetone, isopropyl alcohol (IPA) and deionized (DI) water to remove unwanted PEDOT:PSS, leaving PEDOT:PSS on top of the ITO microelectrodes. Figure 3b and 3c show examples of the fabricated ITO microelectrodes before and after the PEDOT:PSS treatment. The whole fabrication steps were concluded in Figure 4.

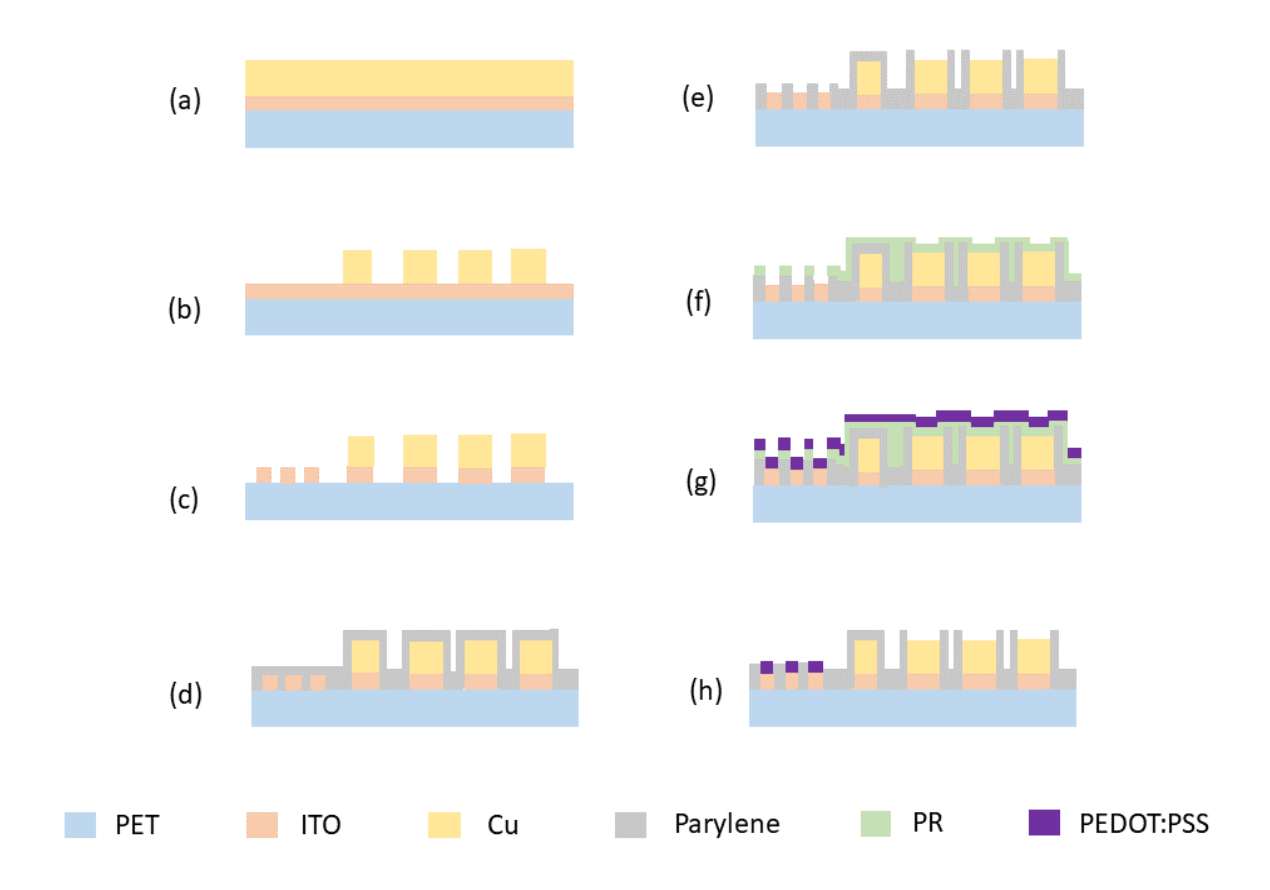


Figure 4. Fabrication steps: (a) Depositing of 500 nm Cu. (b) Patterning the Cu layer. (c) Patterning the ITO layer. (d) Depositing 2 µm Parylene C as the insulation layer. (e) Etching the Parylene C away to expose the contact pads and microelectrodes. (f) Photolithographing the probe to only expose the microelectrodes. (g) Spincoating PEDOT:PSS on the microelectrodes. (h) Rinsing off the photoresist to only remain the PEDOT:PSS on the microelectrodes.

# 3.2.2 Testing Methods

To fully understand the electrochemical properties of the transparent microelectrodes, EIS measurements were performed using a potentiostat (Electrochemical Analyzer, CH Instruments, Inc.) in a three-electrode cell [281], with the ITO or PEDOT:PSS coated ITO microelectrode as the working electrode (WE), an Ag/AgCl electrode as the reference electrode (RE), and a platinum electrode as the counter electrode (CE). The tests were conducted in physiological saline solution at room temperature. The electrochemical impedance of the microelectrode was measured from 0.1 Hz to 100 kHz when a 5 mV RMS sinusoid waveform was applied to the WE. Using the above three-electrode setup, CV of the microelectrode were measured at a 100 mV/s sweep rate in a potential range of -0.9 V to 0.9 V. Multiple CV scans were done in experiments before data collection to clean the electrode surface and allow the system to settle. Besides electrochemical measurements, an atomic force microscope (AFM) (5100N, Hitachi, Inc) was used to compare the surface morphology of the ITO microelectrodes with and without the PEDOT:PSS coating. Thin film optical transmittance was quantified by UV-Vis spectroscopy (Lambda 900, Perkin Elmer) in a wavelength range of 310-750 nm. The PEDOT:PSS film thickness was measured by a profilometer (Nanomap-500LS, Aeptechnology, Inc.), and the sheet resistance of the pure ITO and PEDOT:PSS coated ITO films was detected by a four-point probe station (Lucas Signatone SP4, Signatone).

# 3.3 Results and Discussion

# 3.3.1 Electrochemical Impedance

The average thickness of the PEDOT:PSS coating was 103 nm (n=5). The sheet resistance was

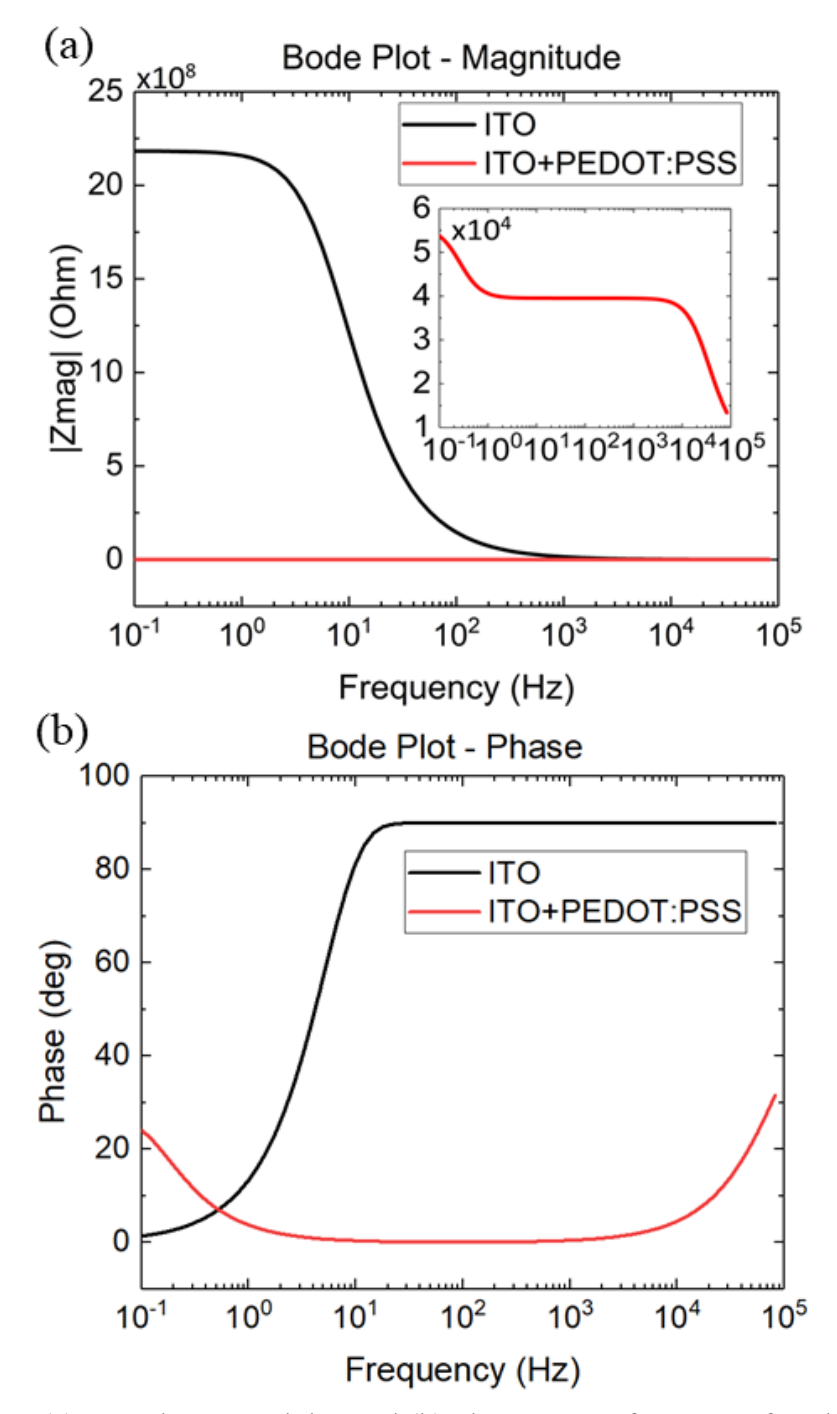


Figure 5. (a) Impedance modulus and (b) phase versus frequency for plain ITO and PEDOT:PSS coated ITO microelectrodes, respectively.

59.96 ohm/sq and 56.35 ohm/sq (n=5) for the PEDOT-PSS coated ITO and pure ITO film, respectively, which were consistent with the values provided by Sigma-Aldrich. The PEDOT:PSS coated ITO film exhibits a slightly higher resistance than the pure ITO film. For the EIS measurements, four different diameters of the ITO electrodes with and without the PEDOT:PSS coating were tested: 10 µm, 37 µm, 50 µm and 80 µm. These diameters were chosen to match the size of neuron cell body for single unit recording, which typically varies from 4 µm to 100 µm in diameter [282]. The Bode plots in Figure 5a and 5b show the typical electrode impedance magnitude and phase versus frequency, respectively. The impedance of the PEDOT:PSS coated ITO electrode was highly resistive over a wide frequency range of 1 Hz - 10 kHz, suggesting that charge transfer is attributed to reversible faradaic reactions. The PEDOT:PSS coating effectively reduced the overall electrochemical impedance of the microelectrodes in a wide frequency spectrum, in consistence with other reports [283]. Figure 6a showed that the average impedance at 1 kHz decreased when the electrode area increased for both the plain and PEDOT:PSS coated ITO microelectrodes. The impedances of the PEDOT:PSS coated microelectrodes were consistently two orders of magnitude lower than those of the plain ITO microelectrodes.

This reduction in impedance is mainly attributed to the increase in the surface roughness of the microelectrodes after the PEDOT:PSS coating, as indicated in the AFM images in Figure 8. The average roughness ( $R_a$ ) and peak-to-peak mean roughness depth ( $R_t$ ) of the PEDOT:PSS-ITO film is 3.33 nm and 39.15 nm, respectively, while  $R_a$  and  $R_t$  of the ITO film is 0.85 nm and 12.02 nm, respectively. The rough surface provides a large effective surface area of the electrode when

exposed to the electrolyte, allowing more charge to flow across the electrode-electrolyte interface.

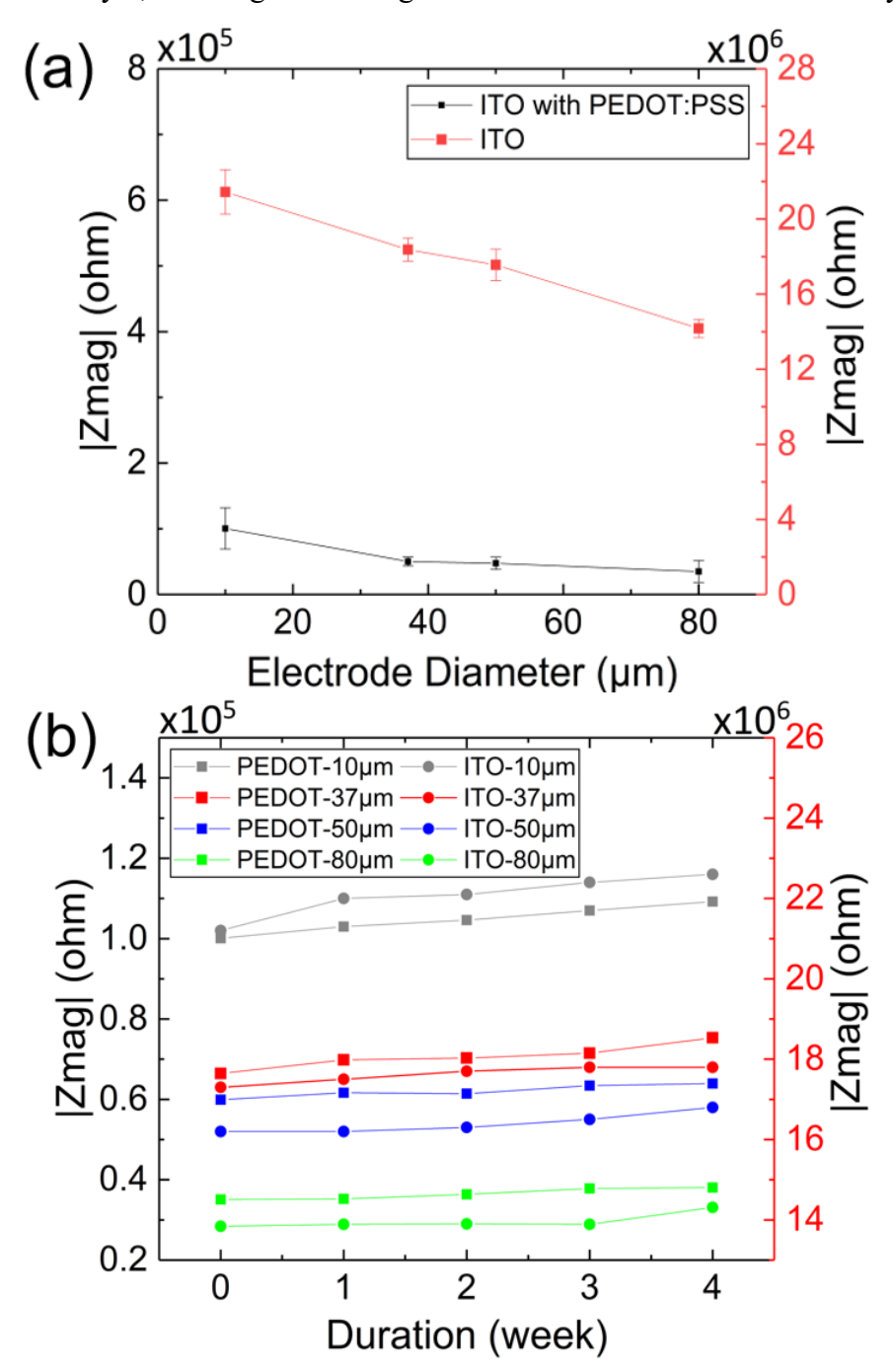


Figure 6. (a) Average 1 kHz impedance of the plain and PEDOT:PSS coated ITO microelectrodes with 10  $\mu$ m, 37  $\mu$ m, 50  $\mu$ m and 80  $\mu$ m diameters (n=5). (b) Impedance changes of the pure ITO and PEDOT:PSS coated ITO electrodes with different diameters, measured after soaked in room temperature saline for 0 weeks, 1 week, 2 weeks, 3 weeks and 4 weeks.

Consequently, the PEDOT:PSS coating reduced the impedance of the electrode.

To evaluate the stability of the microelectrodes, the devices were kept in saline at room temperature for up to 4 weeks, and their impedance and phase changes were monitored weekly

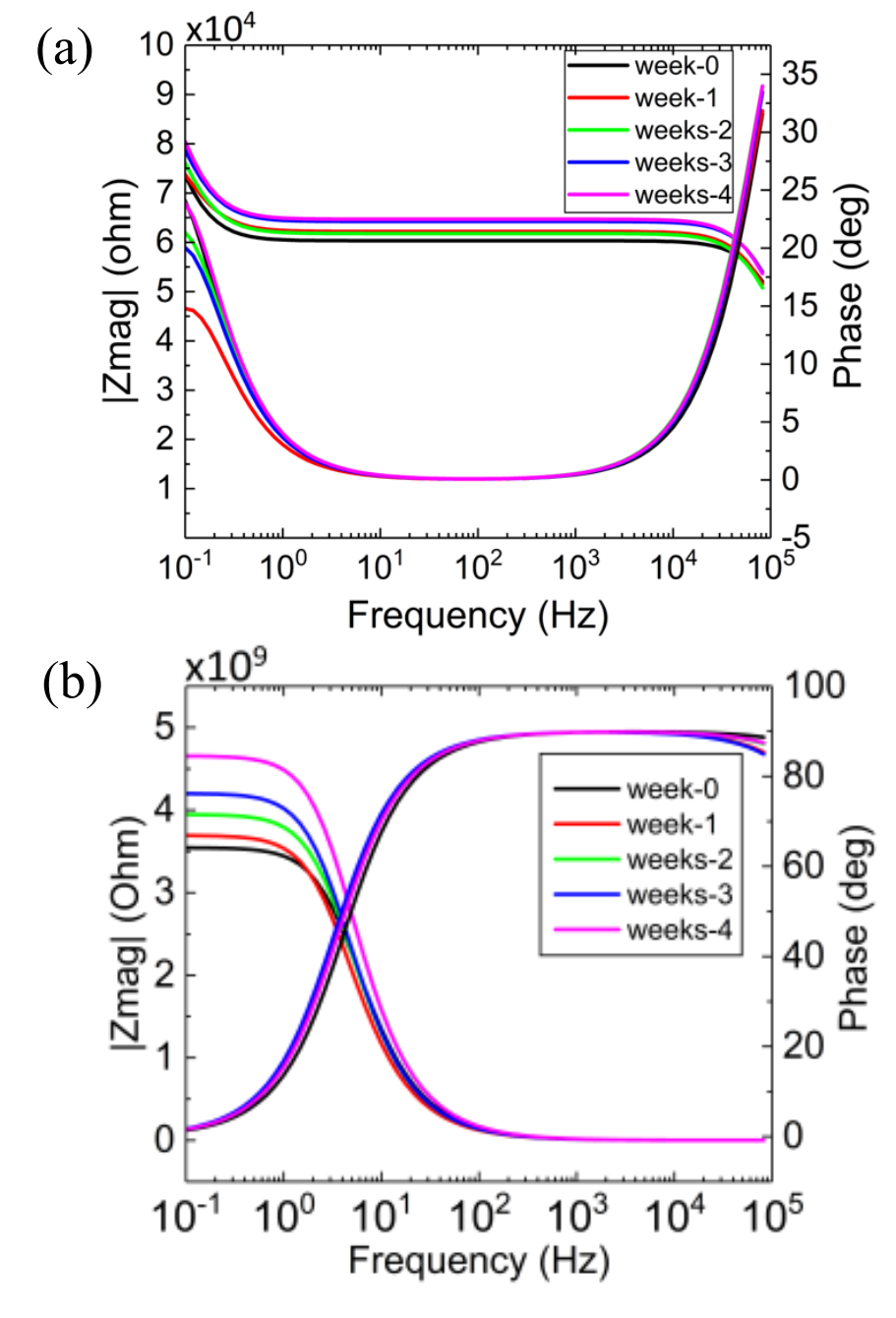


Figure 7. Impedance magnitude (upper curves, high-to-low curves) and phase changes (lower curves, low-to-high curves) during 4 weeks for the PEDOT:PSS coated ITO microelectrodes (a) and for the pure ITO electrodes (b).

and plotted in Figure 6b and Figure 7a & 7b. Our results show that the PEDOT:PSS coated ITO electrodes exhibited good stability over four weeks with an overall impedance increase of less than 7.23%, which is slightly higher than the ITO electrodes (with an impedance increase of 3.62%). The increase in impedance magnitude may be due to PEDOT:PSS reaction with oxygen and moisture. PEDOT:PSS absorbs water upon exposure to air, creating an aqueous acid environment that facilitates etching of the ITO [284]. Indium etch products will then be transported throughout the PEDOT:PSS film, thereby weakening the stability of the ITO-PEDOT:PSS interface and slowly increasing impedance. The impedance magnitude of week 2 was slightly lower than week 1, possibly because the Parylene C layer was a little detached from the substrate, leading to more ITO electrode exposure in the saline solution during the electrochemical testing which counteracted the influence from oxygen and moisture. Of note is that exposing the device to saline had minimal impact on the impedance phase within the frequency range of interest (100 Hz - 10 kHz) [285]. Visual inspection did not observe any signs of major physical damage and delamination of the PEDOT:PSS coating.

## 3.3.2 Charge Storage Capacity

Figure 9a plots the CV scans of both the plain and PEDOT:PSS coated ITO electrodes. For the PEDOT:PSS coated devices, the larger area under the CV curve indicates a larger cathodic charge storage capacity, as compared to the plain ITO electrode. The charge storage density (CSC) of the films was calculated from the CV curves using Equation 2

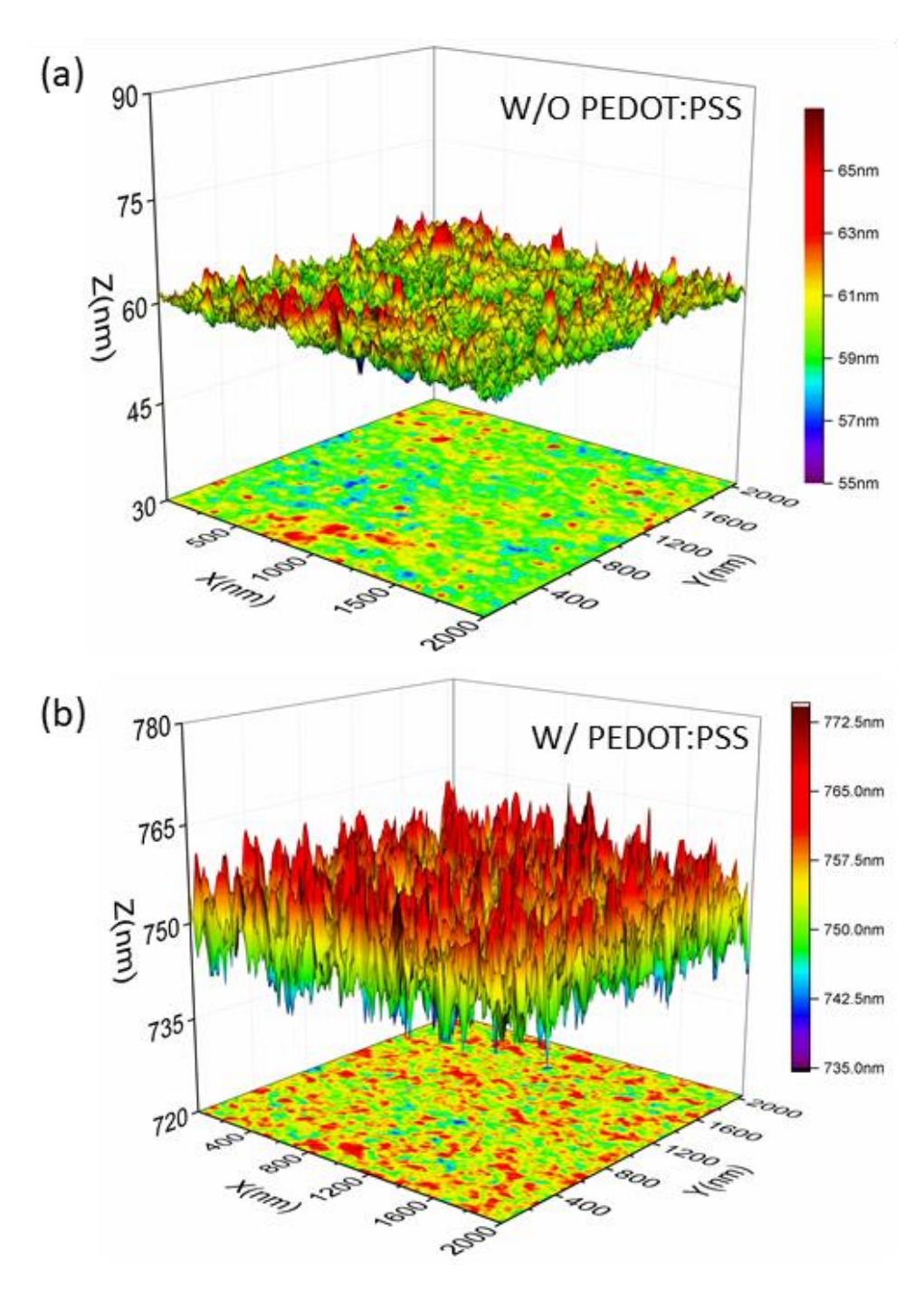


Figure 8. Surface roughness changes a before and b after spin-coating PEDOT:PSS layer by Atomic force microscopy (AFM). The average roughness (Ra) and peak-to-peak mean roughness depth (Rt) without the PEDOT:PSS film is 0.85 nm and 12.02 nm, while Ra and Rt. with the PEDOT:PSS film is 3.33 nm and 39.15 nm.

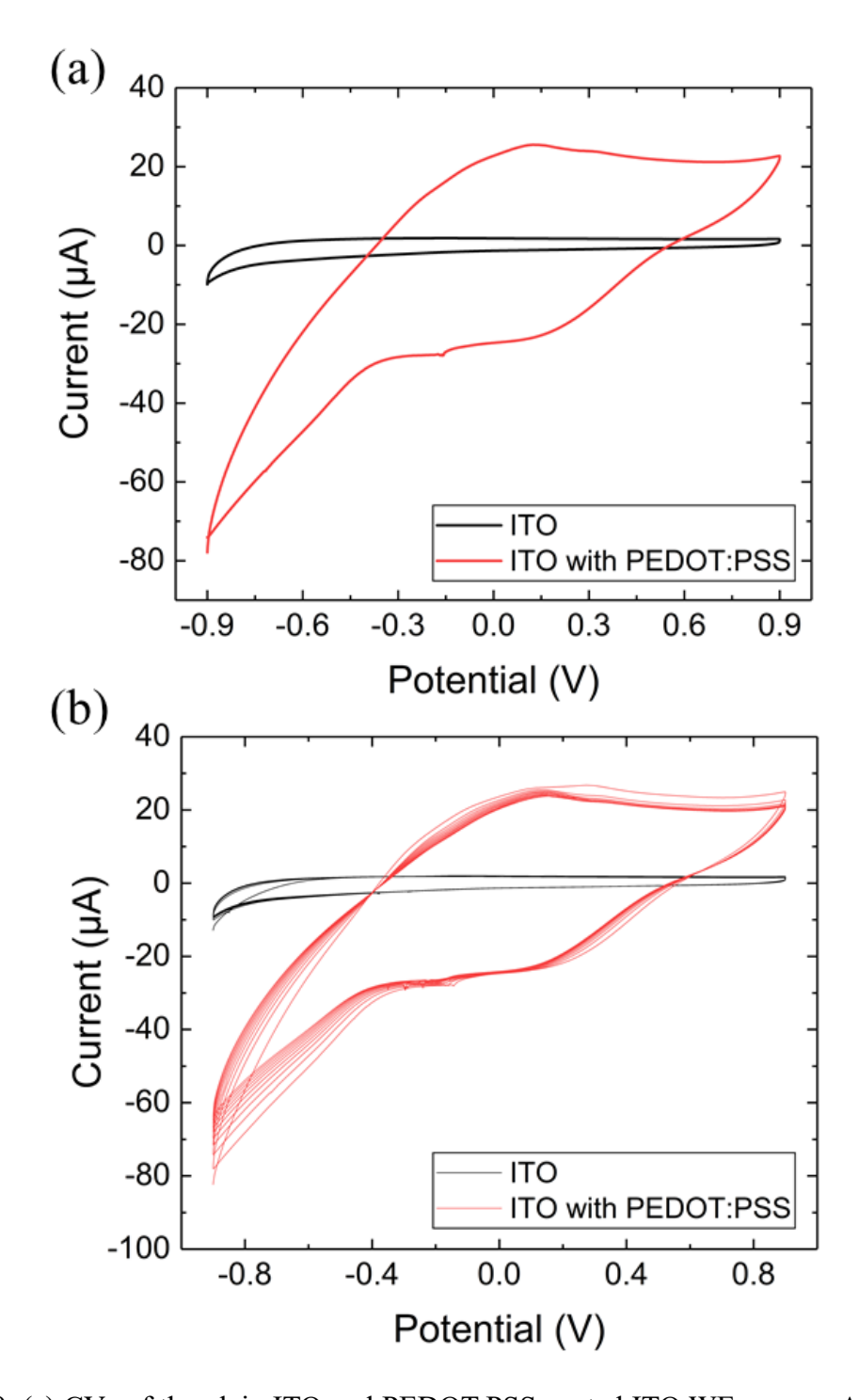


Figure 9. (a) CVs of the plain ITO and PEDOT:PSS coated ITO WEs versus Ag/AgCl RE, showing that the PEDOT:PSS coated ITO electrode exhibits larger charge storage capacity. (b) CVs of the plain ITO and PEDOT:PSS coated electrode for 10 cycles, demonstrating the stability of the ITO and the PEDOT:PSS coating in saline.

$$CSC = \int_{V_1}^{V_2} I(V)dV \tag{2}$$

where  $V_1$  is the beginning of CV cycle,  $V_2$  is the end of CV cycle and I is the current under each potential. The charge storage capacity of the electrodes calculated from these CV curves was 58.06  $\mu$ C/cm<sup>2</sup> for the plain ITO electrode and 582.45  $\mu$ C/cm<sup>2</sup> for the PEDOT:PSS coated ITO electrode. Our result is consistent with those from previous studies [286], where PEDOT:PSS films had been shown to have enhanced the charge storage capacity due to the increased effective surface area. Figure 9b shows the CV scans of the PEDOT:PSS coated electrode for 10 consecutive cycles, indicating the excellent short-term stability of the PEDOT:PSS coating in room temperature saline solution.

### 3.3.3 Optical Transmittance

Figure 10 shows the optical transmittance of different substrates: pure PET, ITO-PET, ITO/PET with PEDOT:PSS, and ITO-PET with PEDOT:PSS stripped. It can be seen that the PEDOT:PSS coating significantly improves the optical transmittance throughout the visible range of 400-700 nm. Because the refractive index of the PEDOT:PSS (1.334) is much smaller than that of the ITO (1.972), the overall reflective loss at the air-PEDOT:PSS and PEDOT:PSS-ITO interface is lower than that at the air-ITO interface, based on the Fresnel equations [287]. Since PEDOT:PSS has a very small absorption coefficient in UV-Vis region [288], the transmittance improvement of the PEDOT:PSS coated ITO is mainly attributed to the decrease in reflectance at the air-substrate

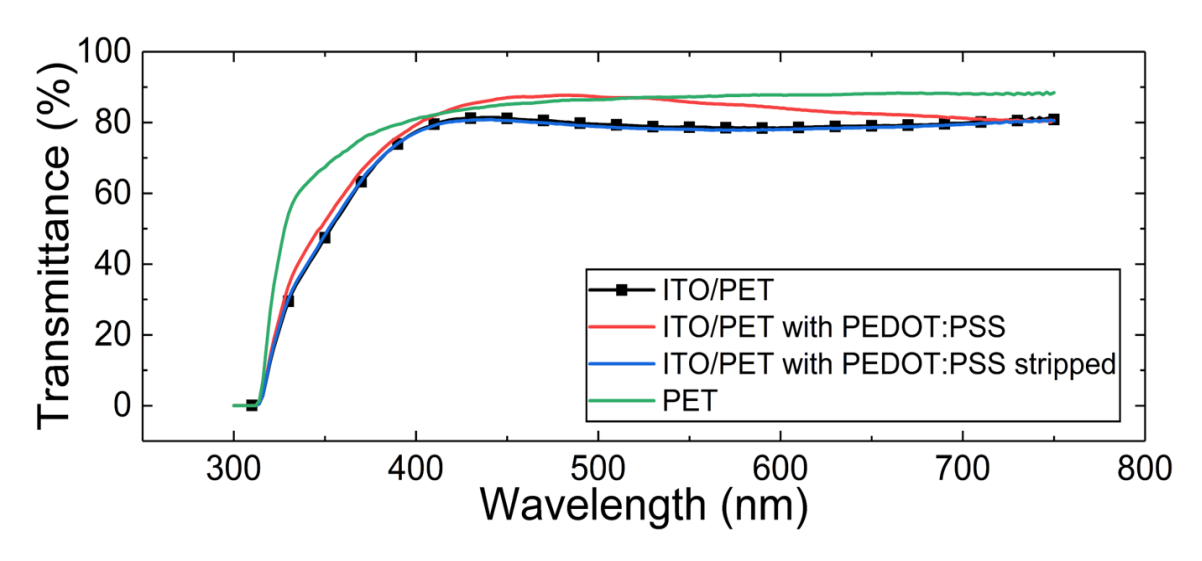


Figure 10. Optical transmittance of different thin films.

interface. A quarter-wave effect may also contribute to the increase in transmittance:  $nd= \lambda/4$ , where n and d are the refractive index and thickness of the film, respectively, and  $\lambda$  is the wavelength [287]. At visible wavelengths, the thickness of our PEDOT:PSS film (103 nm) fits the quarter-wave situation, where the PEDOT:PSS film acts as an antireflective layer, allowing more light to be transmitted through the substrate. Both the PEDOT:PSS coated ITO and pure ITO films show strong absorption at 310-400 nm.

### 3.3.4 Equivalent Circuit Model

I studied the physical processes contributing to the electrode impedance using equivalent circuit models. The circuit model in Figure 11a obtained from [289] was used for the plain ITO electrode, which consists of a constant phase angle impedance  $Z_{CPA}$ , shunted by a charge-transfer resistance  $R_c$ , in series with the solution resistance  $R_s$ . After the ITO surface was covered with PEDOT:PSS, the device was modeled by the circuit in Figure 11b, where an additional  $Z_{CPA}$ - $R_c$  circuit element was used. The first  $Z_{CPA}$ - $R_c$  parallel element represents the electron transfer occurring at the ITO-PEDOT:PSS interface while the second  $Z_{CPA}$ - $R_c$  element represents the charge transfer reaction at

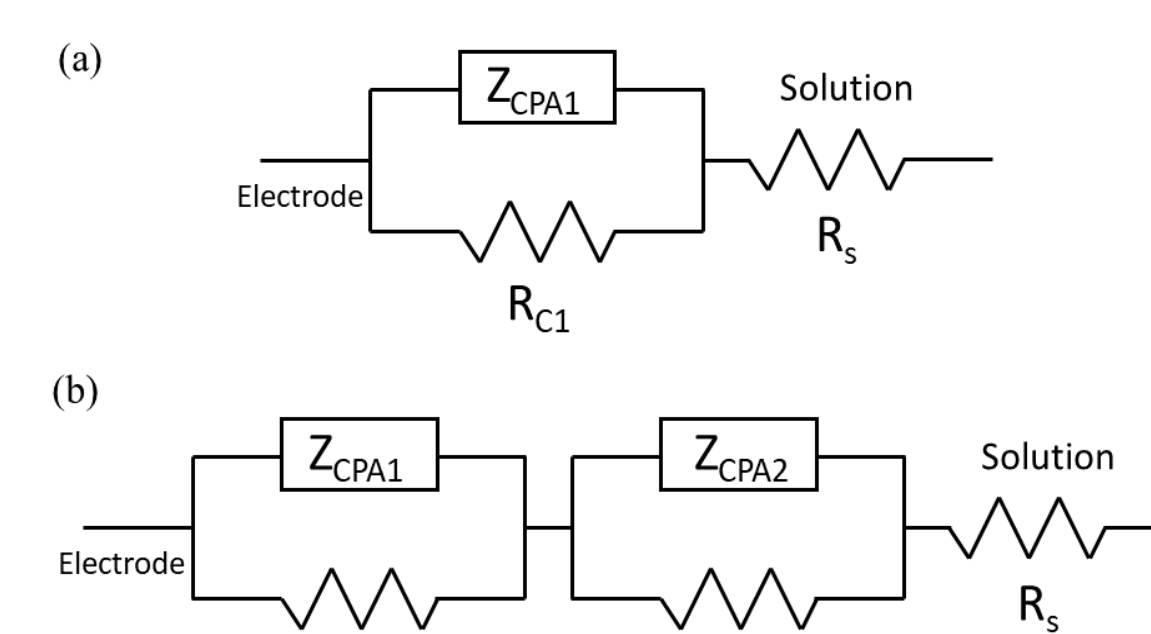


Figure 11. Equivalent circuit model of (a) the pure ITO and (b) the ITO-PEDOT:PSS electrode-electrolyte interface.

 $R_{c1}$ 

the PEDOT:PSS-electrolyte interface. The two parallel circuit elements were put in series with the solution resistance R<sub>s</sub>. The Warburg impedance was not included in this study because it did not have a significant contribution to the overall impedance in our experiment [290]. The constant phase angle impedance, which is a measure of the non-faradaic impedance, can be calculated by the empirical relation:

 $R_{c2}$ 

$$Z_{CPA} = \frac{1}{(j\omega Q)^n} \tag{3}$$

where Q is a measure of the magnitude of  $Z_{CPA}$ , n is a constant  $(0 \le n \le 1)$  representing inhomogeneity in the surface, and  $\omega = 2\pi f$ . When n = 1,  $Z_{CPA}$  corresponds to an interface capacitance that acts as a purely capacitive impedance element [22]. The solution resistance  $R_s$  is

Table 2. Summary of the fitted values by utilizing the equivalent circuit models

Materials	Diameter [μm]	Z <sub>CPA1</sub> [Ohm]	R <sub>C1</sub> [Ohm]	Z <sub>CPA2</sub> [Ohm]	R <sub>C2</sub> [Ohm]	R <sub>S</sub> +R <sub>W</sub> [Ohm]	Total Impedance
ITO	80	4.67E+10	1.25E+10			1.34E+04	9.86E+09
	50	8.61E+10	1.14E+10			1.19E+04	1.01E+10
	37	9.06E+10	1.17E+10			2.49E+04	1.03E+10
	10	9.34E+10	2.88E+10			1.52E+04	2.20E+10
ITO- PEDOT:P SS	80	3.54E+10	3.53E+04	6.08E+04	1.04E+04	1.88E+04	6.29E+04
	50	3.04E+10	4.16E+04	1.66E+04	3.67E+04	2.26E+04	7.56E+04
	37	4.23E+10	4.97E+04	1.57E+04	2.67E+04	1.62E+04	7.59E+04
	10	3.27E+10	5.77E+04	2.55E+04	2.86E+04	1.53E+04	8.64E+04

the resistance between the working electrode and the reference electrode. The charge transfer resistance arises from the low-field approximation of the Butler-Volmer equation, which reduces to Ohm's law.

Table 2 shows the fitted values based on the above models. The impedances of the interface capacitance were calculated using Eq. 3 at an angular frequency of 1 s<sup>-1</sup>. The fitted parasitic resistance is given as  $R_s + R_w$ , where  $R_w$  is the resistance of the wire connecting the electrode to the testing instrument. Finally, we calculated the overall impedances of each microelectrode. The results show that the PEDOT:PSS coating leads to a decrease in  $R_c$  by 6 orders of magnitude at both the ITO-PEDOT:PSS and PEDOT:PSS-solution interfaces. Compared to the ITO-electrolyte interface, the PEDOT:PSS-electrolyte interface exhibited much lower  $Z_{CPA}$  values, which were comparable to the reduced Rc values. Consequently, the total impedance magnitude of the PEDOT:PSS coated ITO microelectrode was 6 orders smaller than that of the plain ITO

microelectrode. These analytical results for the PEDOT:PSS coated ITO have not been well-concluded in electrophysical recording before our investigation, while the solar cells and LEDs have been extensively-researched [284].

#### 3.4 Conclusion

In this chapter, I fully characterized the electrochemical properties of the PEDOT:PSS coated ITO microelectrodes, which exhibit significantly decreased impedance and improved charge capacitance over the pure ITO electrodes, suitable for use in neurophysiological recording. The PEDOT:PSS coated ITO electrodes remain stable over 4 weeks in room temperature saline. The PEDOT:PSS coating results in a rougher surface morphology, which contributes to the impedance decrease and capacitance increase of the electrode. The EIS results were fitted into the equivalent circuit models, confirming that the significantly reduced impedance of the electrode was caused by the PEDOT:PSS coating. Lastly, the PEDOT:PSS coating improves the optical transmittance in the visible spectrum by reducing the reflectance at the air-substrate interface. Future work will focus on evaluating electrode functionality for *in vivo* neural recording experiments.

CHAPTER 4: A Highly Conductive, Transparent, and Anti-reflective PEDOT:PSS-ITO-Ag-ITO on Parylene C with Tunable Peak Transmittance

The previous chapter reported on electrochemical and optical characteristics of flexible, transparent PEDOT:PSS-ITO based microelectrodes for potential applications in biomedical optoelectronic devices. The PEDOT:PSS coated ITO microelectrodes exhibited significantly decreased impedance and improved charge capacitance over the pure ITO electrodes, suitable for use in neurophysiological recording. In addition, the PEDOT:PSS coating improved the optical transmittance in the visible spectrum by reducing the reflectance at the air-substrate interface. However, the PET substrate with 127 µm thickness was not flexible enough to match the low Young's modulus of the brain tissue. Meanwhile, the probe shape design of the array needs to be inserted into the brain tissue while doing the neurophysiology recording, leading to brain tissue damage. Besides, the brittle 100 nm ITO causes the problems of cracks and disconnection. For further exploring PEDOT:PSS-ITO structure and addressing those disadvantages of the design in Chapter 3, ultra-flexible, conductive, transparent thin films using a PEDOT:PSS-ITO-Ag-ITO multilayer structure on 10 µm Parylene C at room temperature were investigated as described in this Chapter. Compared to single-layer ITO of an equivalent thickness, the multilayer film exhibited significantly enhanced sheet conductivity, reduced electrochemical impedance, remarkable transmittance, excellent adhesion, and flexibility. The peak transmittance of the combined films can be tailored to a specific wavelength for particular applications, such as optogenetics. Besides Parylene C, our high-quality ITO-Ag-ITO films can be deposited on a wide variety of heat-sensitive substrates over large scales.

#### 4.1 Introduction

Transparent and flexible conductive thin films are critical components in optoelectronics, such as wearable electronics, biosensors, displays, etc. [291]. Single-layered ITO, ultrathin metals, graphene or PEDOT:PSS, as conventional transparent electrode materials, have been widely used. However, utilizing only a single material is hard to achieve the desired combination of excellent electrical, optical, mechanical, and biocompatible properties.

For example, ITO is most commonly used because of its relatively high transmittance over the entire visible spectrum [292], biocompatibility [293], and good electrical conductivity [292]. However, the mechanical flexibility of ITO remains a challenge due to its high Young's modulus [294], especially when relatively thick ITO (100 nm) is required for performing both good transmittance and conductivity. Besides, ITO microelectrodes face a critical problem of the high electrochemical impedance, which would lead to undesirable electrochemical reactions with the brain tissue [295].

Ultrathin metals enable higher conductivity (in the range of ohms) than ITO but cannot achieve high transparency and conductivity simultaneously due to their limited optical transmittance of ~50-70 % even with ~4-12 nm thickness [296]. Therefore, micro/nanostructured metals, such as nanomesh or microgrid, have been proposed as an alternative, which enables improved transmittance compared to ultrathin metal films [160], [297]. For example, Seo et al. report Au

nanomesh electrodes with over 70% transmittance at 550 nm, good flexibility, low sheet resistance of 0.9-18  $\Omega$ /sq and electrochemical impedance of 8.14  $\Omega$ ·cm<sup>2</sup> [160]. Electrodepositing PEDOT:PSS on top of Au nanomesh to make bilayer nanomesh further improves the electrical properties [35], [161], [298]. Despite its many benefits, the Au nanomesh significantly reduces the effective recording area because of the large hollow structures on the electrode.

Most recently, graphene has emerged as a promising material for making transparent electrodes on account of its broadband transparency, good conductivity, biocompatibility and flexibility [17], [29], [157]. However, it is hard to grow high-quality, large-scale graphene on the polymer substrates because either high temperatures (>1000°C) or specific substrate materials are required. To address these challenges, engineering methods have been explored to transfer graphene from rigid substrates to flexible polymer substrates [157]. However, those methods are laborious and tedious and reduce the yield and reproducibility.

As an attractive conductive polymer, PEDOT:PSS excels in the fabrication of microelectrodes for neural interface applications, owing to its outstanding biocompatibility, excellent stability, transparency, and flexibility [299]. However, compared to other transparent conducting materials, the relatively low electrical conductivity of PEDOT:PSS makes it unsuitable for use in high-density electrode arrays.

In this chapter, I fabricated and reported, for the first time, an ultra-flexible, conductive, and transparent thin film using a PEDOT:PSS-ITO-Ag-ITO multilayer structure on Parylene C for achieving significantly enhanced sheet conductivity, reduced electrochemical impedance,

remarkable transmittance, good stability, adhesion, and flexibility. The multilayer assembly was optimized to achieve the lowest theoretical reflectance by simulating the coatings admittance loci under the preferred reference wavelength. Ag was selected to be deposited between two layers of ITO for increasing the conductivity of the whole multilayer structure. Although Ag is not biocompatible, the Ag was sandwiched by two layers of ITO which avoids the direct contact with biological tissues. The ITO and Ag were sputtered consecutively at room temperature, followed by spin-coating of PEDOT:PSS. The room temperature as the sputtering temperature of ITO-Ag-ITO structure was chosen depending on our systematic study, where ITO was deposited on Parylene C coated glass slides at different temperatures, using an RF magnetron sputtering system (Denton Explorer-14, Denton Vacuum, Inc). The transmittance and sheet resistance of the combined films were measured by utilizing a Filmetrics thin film analyzer (F20-UVX, Filmetrics, Inc) and a four-point probe station (SRM-232, Bridge Technology, Inc), respectively, and the measurements were compared with those of single-layer ITO films of equivalent thicknesses. Tunable peak transmittances were confirmed by depositing different thicknesses of individual layers on Parylene C after theoretical admittance loci simulation under the preferred wavelengths. EIS of different coatings were measured in a 0.9% NaCl (saline) solution at room temperature. The adhesion between ITO and Parylene C was evaluated using Scotch tape tests for 50 times of peeling. In addition, the combined thin films were kept at 37°C in air and in saline, respectively to test the film stability over 4 weeks. The Young's modulus of the combined films was measured by an MTS nano-indenter and compared with their theoretical values.

#### 4.2 Materials and Methods

#### 4.2.1 Fabrication

### 4.2.1.1 ITO Films Deposition

Before the ITO sputtering, glass slide substrates were ultrasonically cleaned in an acetone bath for removing organic contaminants and dusts, followed by cleaning with ethanol, IPA, and DI water. 100 nm ITO films were sputtered with RF magnetron sputtering system at 22°C, 69°C, 92°C, 116°C and 140°C, respectively. Finally, the glass slides were dried in a N2 stream and baked on a hotplate at 100°C for 30 mins. For some cleaned glass slides, 10 µm Parylene C was deposited first (PDS 2010, Specialty Coating System, Inc) as the substrate for the future peel-off. Film deposition was done in a RF magnetron sputtering system (Denton Explorer-14, Denton Vacuum, Inc) with a 4-inch diameter ITO target (99.99% purity, which composited by 90% indium oxide and 10% tin oxide. The heater was turned on when the turbo pump was on to guarantee the sufficient time for the temperature to increase to the setup value. After the base pressure inside the chamber was decreased below  $2 \times 10^{-6}$  Torr, 60 sccm argon was introducing into the chamber for achieving  $3 \times 10^{-3}$  Torr sputtering pressure. Substrate rotating speed was set up at 20% for the sputtering uniformity. In addition, the pre-sputtering was run for 10 mins for getting rid of the contaminates on the target surface. During the deposition, the sputtering RF power was set up at 100 watts with the deposition time of 15 mins and 40 s for 100 nm ITO. After the sputtering, the heater was turned off immediately and the samples were taken out after the temperature decreased to the room temperature.

### 4.2.1.2 Design Methodology for Multilayer Anti-reflection Coatings

For designing multilayer anti-reflection coating, optical interference matrix is applied [287]. Under the incident light with zero-degree incident angle, the equation of optical interference matrix for N-layer anti-reflection coatings is

$$\begin{pmatrix} B \\ C \end{pmatrix} = \left\{ \prod_{j=1}^{N} \begin{bmatrix} \cos \delta_j & i \frac{\sin \delta_j}{n_j} \\ i(n_i \sin \delta_i) & \cos \delta_i \end{bmatrix} \right\} \begin{pmatrix} 1 \\ n_s \end{pmatrix} \tag{4}$$

Where Y is the optical admittance which is the ratio of the normalized tangential electric field B and magnetic field C,  $\delta_j$  is the effective optical thinckenss of  $j^{th}$  layer,  $n_j$  is refractive index of  $j^{th}$  layer,  $n_s$  is refractive index of substrate material. For this method, B and C of the incident light are well adjusted on the multilayers surface. For calculating optical admittance Y, the following equation is given:

$$Y = \frac{C}{B} \tag{5}$$

For calculating the effective optical thickness  $\delta_j$ , the below equation is used:

$$\delta_j = \frac{2\pi}{\lambda} n_j d_j \cos \theta_j \tag{6}$$

Where  $\theta_j$  is the incident light angle on the surface of  $j^{th}$  layer, and  $d_j$  is the actual thickness of  $j^{th}$  layer. For a stack of N layers of thin film, the B and C could be determined by:

$$\begin{pmatrix}
B \\
C
\end{pmatrix}
= \begin{bmatrix}
\cos \delta_1 & i \frac{\sin \delta_1}{n_1} \\
i(n_1 \sin \delta_1) & \cos \delta_1
\end{bmatrix} \begin{bmatrix}
\cos \delta_2 & i \frac{\sin \delta_2}{n_2} \\
i(n_2 \sin \delta_2) & \cos \delta_2
\end{bmatrix} \dots \begin{bmatrix}
\cos \delta_N & i \frac{\sin \delta_N}{n_N} \\
i(n_N \sin \delta_N) & \cos \delta_N
\end{bmatrix} \begin{pmatrix}
1 \\
n_S
\end{pmatrix}$$
(7)

For the PEDOT:PSS-ITO-Ag-ITO on Parylene C design in this dissertation, B and C could be calculated by the following specific equation:

$$\begin{pmatrix}
B \\
C
\end{pmatrix}$$

$$= \begin{bmatrix}
\cos \delta_{PEDOT} & i \frac{\sin \delta_{PEDOT}}{n_{PEDOT}} \\
i(n_{PEDOT} \sin \delta_{PEDOT}) & \cos \delta_{PEDOT}
\end{bmatrix} \begin{bmatrix}
\cos \delta_{ITO-1} & i \frac{\sin \delta_{ITO-1}}{n_{ITO-1}} \\
i(n_{ITO-1} \sin \delta_{ITO-1}) & \cos \delta_{ITO-1}
\end{bmatrix} (8)$$

$$\begin{bmatrix}
\cos \delta_{Ag} & i \frac{\sin \delta_{Ag}}{n_{Ag}} \\
i(n_{Ag} \sin \delta_{Ag}) & \cos \delta_{Ag}
\end{bmatrix} \begin{bmatrix}
\cos \delta_{ITO-2} & i \frac{\sin \delta_{ITO-2}}{n_{ITO-2}} \\
i(n_{ITO-2} \sin \delta_{ITO-2}) & \cos \delta_{ITO-2}
\end{bmatrix} \begin{pmatrix}
1 \\
n_{Parylene C}
\end{pmatrix}$$

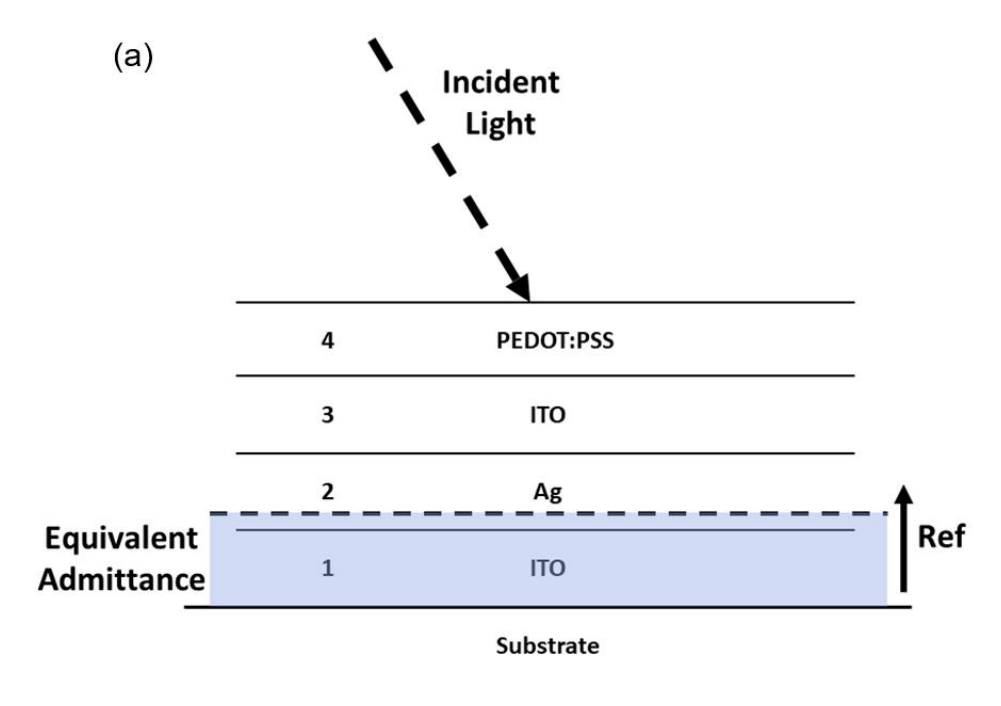
Finally, the reflectance, *R* could be calculated:

$$R = \left| \frac{n_0 - Y}{n_0 + Y} \right|^2 \tag{9}$$

where  $n_0$  ( $n_0$ =1) is the refractive index of air. Depending on the above equations [300], an Excel document was developed for thin film layer thickness optimization. Theoretical layer thickness calculation was conducted by admittance loci simulation by using this Excel, as shown in APPENDIX.

# 4.2.1.3 Fabrication of PEDOT:PSS-ITO-Ag-ITO Thin Films

The admittance loci for the coating was simulated in order to determine the optimal thickness of each layer with the lowest theoretical reflectance under preferred wavelengths, such as, 470 nm,



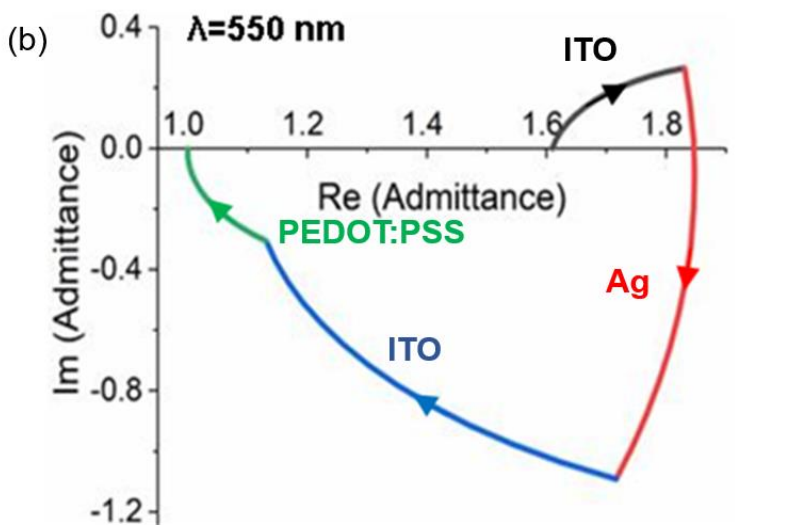


Figure 12. (a) Equivalent admittance (blue shade) of the multilayer PEDOT:PSS-ITO-Ag-ITO thin film coatings. Treating as a virtual reference plane from the substrate. (b) Admittance loci with an example of PEDOT:PSS (30.5 nm)-ITO (24 nm)-Ag (9.45 nm)-ITO (20 nm) assembly for achieving the highest transmittance at the preferred 550 nm wavelength.

550 nm and 630 nm (Figure 12). I studied in detail the transparency, conductivity, electrochemical properties, mechanical properties, and stability of the combined PEDOT:PSS-ITO-Ag-ITO film under 550 nm. Therefore, the following fabrication steps will be illustrated focusing on the combined PEDOT:PSS (30 nm)-ITO (24 nm)-Ag (9.5 nm)-ITO (20 nm) thin films under 550 nm reference wavelength. Both of the two layers of ITO were sputtered with the same steps described above. However, the deposition time was reduced to 2 mins 30 secs and 3 mins 6 secs, individually. For the Ag deposition, a 4-inch diameter Ag target (99.99% purity) was installed as another cathode in the Denton system. The base pressure, sputtering pressure and sputtering RF power were kept same with the ITO sputtering, while the deposition time changed to 22 secs for 9.5 nm thickness Ag and the substrate rotating speed increased to 70%. ITO-Ag-ITO deposition was finished step by step consecutively without pause. As the last step, 0.55% PEDOT:PSS, which was diluted from 1.1% PEDOT:PSS (768642, Sigma-Aldrich), was spun on the top of the substrate with 500 rpm spin speed for 5 secs and then 4000 rpm for 120 secs, followed by baking on a hotplate at 100°C for 30 mins. For comparison, 53.5 nm single layer ITO which had the equivalent thickness with ITO-Ag-ITO structure was sputtered under the same recipe.

### 4.2.1.4 TEM Samples Preparation and Test

The carbon grid samples were loaded in the sputtering chamber and then followed the same deposition procedures as the above described. Samples were loaded and tested individually in the TEM (JEOL 2200FS).

#### 4.2.2 Testing Methods

#### 4.2.2.1 Transmittance and Conductivity Measurements

Filmetrics thin film analyzer was utilized to measure the transmittance of ITO samples in a wavelength range of 300 nm - 800 nm (F20-UVX, Filmetrics, Inc) and four-point probe (SRM-232, Bridge Technology, Inc) was applied to measure the sheet resistances of the samples.

#### 4.2.2.2 Electrochemical Measurements

EIS and the following CV measurements were taken using a potentiostat (Electrochemical Analyzer, CH Instruments, Inc.) to analyze the electrochemical impedance in a three-electrode cell, with the microelectrode as the WE, an Ag/AgCl electrode as the RE, and a platinum electrode as the CE. The tests were conducted in physiological saline solution (0.9% NaCl<sub>2</sub>) at room temperature. The electrochemical impedance of the microelectrode was measured from 0.1 Hz to 100 kHz when a 5 mV RMS sinusoid waveform was applied to the WE. CVs of the microelectrode were measured at a 100 mV/s sweep rate in a potential range of -0.9 V to 0.9 V. Multiple CV scans were done in experiments before data collection to clean the electrode surface and allow the system to settle.

## 4.2.2.3 Peel-off Tests

Scotch tape test was processed by applying Scotch No. 810 pressure-type tape on the ITO-Parylene C samples with  $10 \times 10$  of 1 mm<sup>2</sup> squares for repeating 50 times with  $180^{\circ}$  peel-off angle to track whether there was any ITO delaminated from the Parylene C substrate. The  $10 \times 10$  of 1 mm<sup>2</sup> squares were cut by using the single edge industrial razor blades to gently cut through the

ITO layer but leave the Parylene C thin film a complete sheet. To assure that the ITO layer was completely cut through, a digital multimeter was used to measure continuity between adjacent sides of the cut.

## 4.2.2.4 Bending Tests and Young's Modulus Measurements

The bending tests were conducted under a bending curvature of 3 mm and 6 mm in diameter, respectively. The sheet resistances of the combined films with different total ITO thickness were measured every 100 bending cycles within the total 1000 bending cycles. The Young's modulus of the combined films on Parylene C and single layer of Parylene C were measured using the MTS Nanoindenter XP system, and the experimental value was compared with the theoretical values.

#### 4.3 Results and Discussion

### 4.3.1 Temperature Study of ITO

ITO must be deposited at temperatures lower than 80 - 100°C, the range of the glass transition temperature of Parylene C to avoid polymer degradation. Therefore, the influence of the processing temperature on the performance of ITO thin films was studied to lay the basis for further development of the multilayer assembly. For these experiments, ITO films with a common thickness of 100 nm were sputtered on either glass or Parylene-coated glass substrates at selected temperatures of 22°C, 69°C, 92°C, 116°C and 140°C. Figure 13a and 13b show the average transmittances (n=5) of ITO films deposited on different substrates. The ITO-on-glass samples show no significant changes in the film transmittance within a wavelength range of 300-800 nm when the sputtering temperature was lower than 92°C. As the temperature increased over 116°C,

the wavelength of the peak transmittance gradually shifted down from 441 nm to 386 nm. At 140°C, the peak transmittance increased by 2.186%, mainly due to ITO crystallization at high sputtering temperatures. The optical transparency of the ITO-on-Parylene films exhibited an inverse trend in

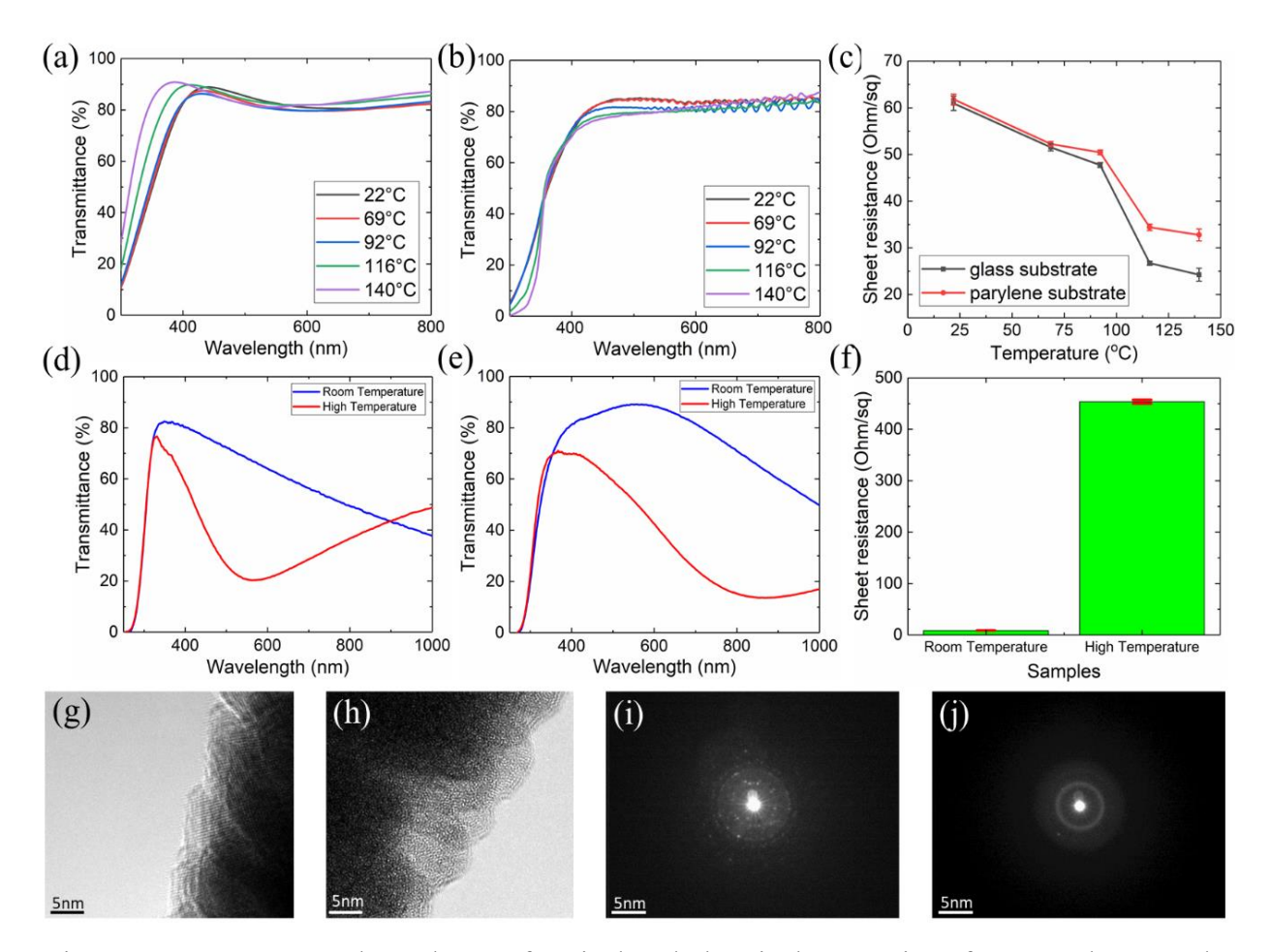


Figure 13. Temperature dependence of optical and electrical properties of sputtered ITO and Ag thin films. Transmittances of 100 nm ITO deposited under sputtering temperatures of 22°C, 69°C, 92°C, 116°C, and 140°C on a glass slides and b Parylene C coated glass slides. c Sheet resistances of 100 nm ITO deposited under different sputtering temperatures on glass slides and Parylene C coated glass slides, respectively. Transmittances of d Ag (9.45 nm) and e ITO (24 nm)-Ag (9.45 nm)-ITO (20 nm) deposited under the sputtering temperature of room temperature and high temperature (116°C) on glass slides. f Sheet resistances of ITO (24 nm)-Ag (9.5 nm)-ITO (20 nm) at room temperature and high temperature (116°C) on glass slides, respectively. High-resolution TEM images of g polycrystalline structure of high-temperature ITO, h amorphous structure of room-temperature ITO. X-ray diffraction patterns of i high-temperature ITO and j room-temperature ITO.

temperature dependence. While the peak wavelength shifted forward slightly from 493 nm to 450 nm as the sputtering temperature increased, the peak transmittance decreased from ~85% to ~78%. This reduction in transmittance could be mainly caused by oxidation degradation of Parylene C aromatic rings in air at temperatures greater than its glass transition temperature, which produces accumulated carboxylic acids in polymer chains, resulting in discoloration, cracks, and brittleness of the film. The periodic waves in Figure 13b are due to the light interference. The resistivity decreased from 6.1 x  $10^{-4} \Omega \cdot \text{cm}$  to  $2.4 \times 10^{-4} \Omega \cdot \text{cm}$  for ITO on glass and from 6.2 x  $10^{-4} \Omega \cdot \text{cm}$  to  $3.3 \times 10^{-4} \Omega \cdot \text{cm}$  for ITO on Parylene C, as shown in Fig. 1c. The resistivity of our room-temperature sputter ITO (6.1 x  $10^{-4} \Omega \cdot \text{cm}$ ) is close to that of excimer laser annealed ITO (2.5 x  $10^{-4} \Omega \cdot \text{cm}$ ) [301] and better than that of low-temperature plasma annealed ITO (2.5 x  $10^{-3} \Omega \cdot \text{cm}$ ) [302] as reported in the literature.

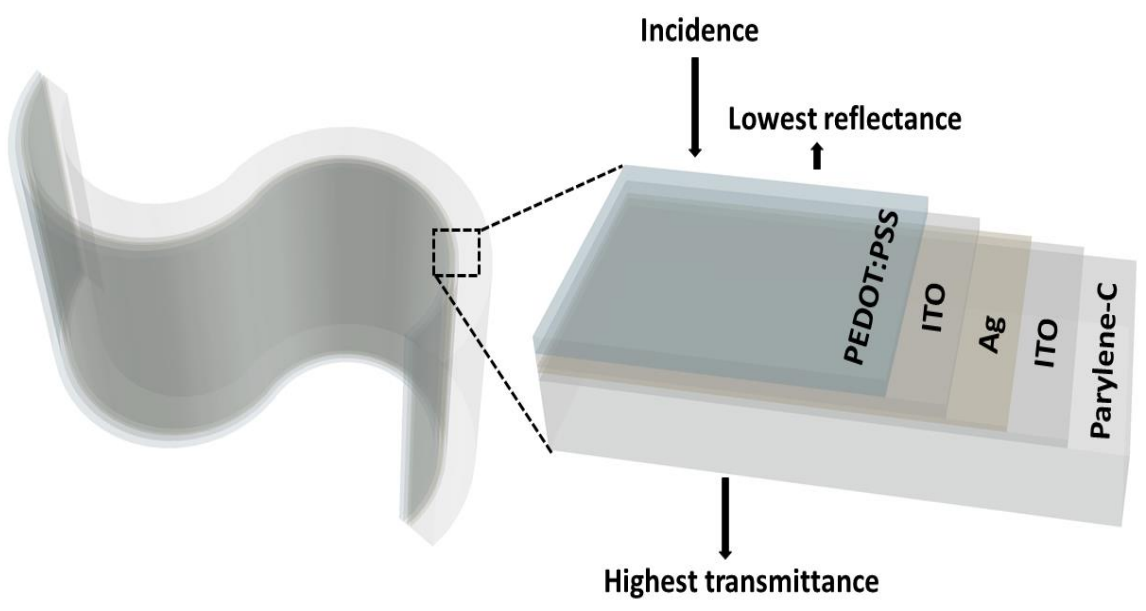


Figure 14. Concept diagrams of transparent and ultra-flexible PEDOT:PSS/ITO/Ag/ITO on Parylene C, designed for achieving the lowest reflectance.

The crystallization of the ITO films sputtered at room temperature and 110°C was analyzed using transmission electron microscopy (TEM), as shown in Figure 13g - 13j. The room temperature deposited ITO films were mostly amorphous with some degree of crystallites in small areas. When the sputtering temperature increased, the amorphous ITO films were crystallized and densified as demonstrated in Fig. 13g and 13h. The crystallization of thin ITO films can significantly improve the film quality, resulting in better optical transparency and electrical conductivity. This is consistent with our results obtained from the ITO-on-glass samples and the

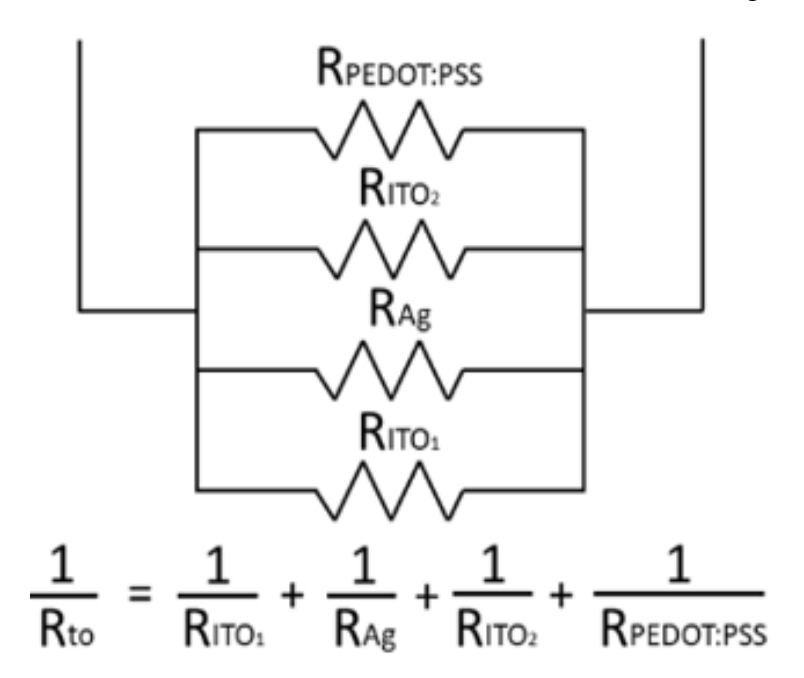


Figure 15. Equivalent circuit of the PEDOT:PSS-ITO-Ag-ITO assembly for the overall conductance calculation. Each layer of the thin film acts as a resistor and then is connected in parallel to form the total resistance. The measured sheet resistance of 20 nm ITO, 9.45 nm Ag, 24 nm ITO and 30.5 nm PEDOT:PSS was 305.2  $\Omega$ /sq, 10.28  $\Omega$ /sq, 254.2  $\Omega$ /sq, and >1000  $\Omega$ /sq (beyond the range of four-point probe), respectively.

findings of other groups [303].

Despite the good performance of the high-temperature ITO films, the overall conductance of the PEDOT:PSS-ITO-Ag-ITO assembly is a result of the parallel combination of the four individual layers (Figure 14 and Figure 15), and is dominated by the Ag layer which has the lowest sheet resistivity ( $1.59 \times 10^{-6} \ \Omega \cdot \text{cm}$ ) among these three materials [304]. Hence, the improved conductivity of high-temperature ITO does not play a significant role. As ITO and Ag were deposited consecutively in the same sputtering system, high-temperature processing may also deteriorate the quality of Ag thin films due to oxidation (Figure 13d-13f), therefore causing decreased transmittance over 400 nm wavelength. Moreover, as shown in Figure 13b, the combined ITO-Parylene C film exhibits higher transmittance between ~400 nm and ~600 nm at lower sputtering temperatures. Having considered the tradeoffs between the ITO quality and the overall performance of the assembly, room-temperature sputtered ITO was chosen as the electrode material for the following experiments.

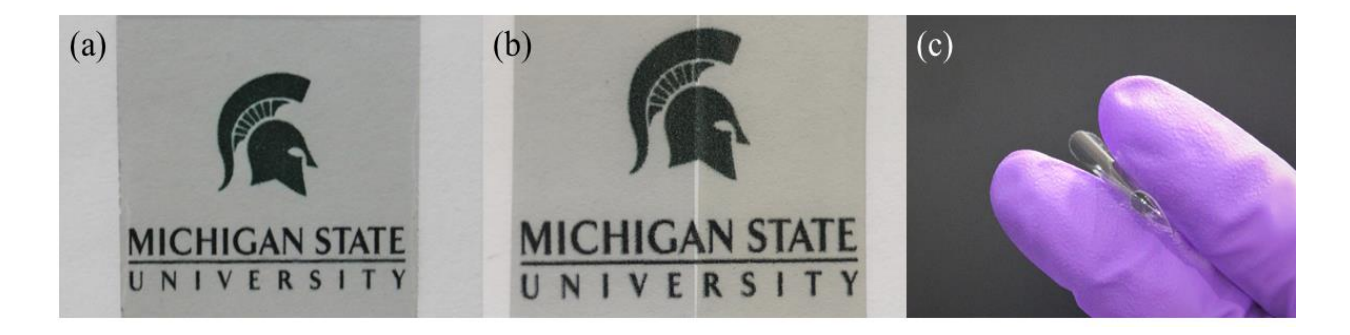


Figure 16. Thin films of PEDOT:PSS-ITO-Ag-ITO on  $10 \,\mu$  m Parylene C showing (a) excellent transparency and (c) ultra-flexibility. (b) The transparency before (right) and after (left) adding the PEDOT:PSS coating.

### 4.3.2 Conductivity and Transmittance

Figure 14 shows the concept diagram of PEDOT:PSS-ITO-Ag-ITO on Parylene C assembly.

The thickness of each individual layer was simulated using an equivalent admittance method

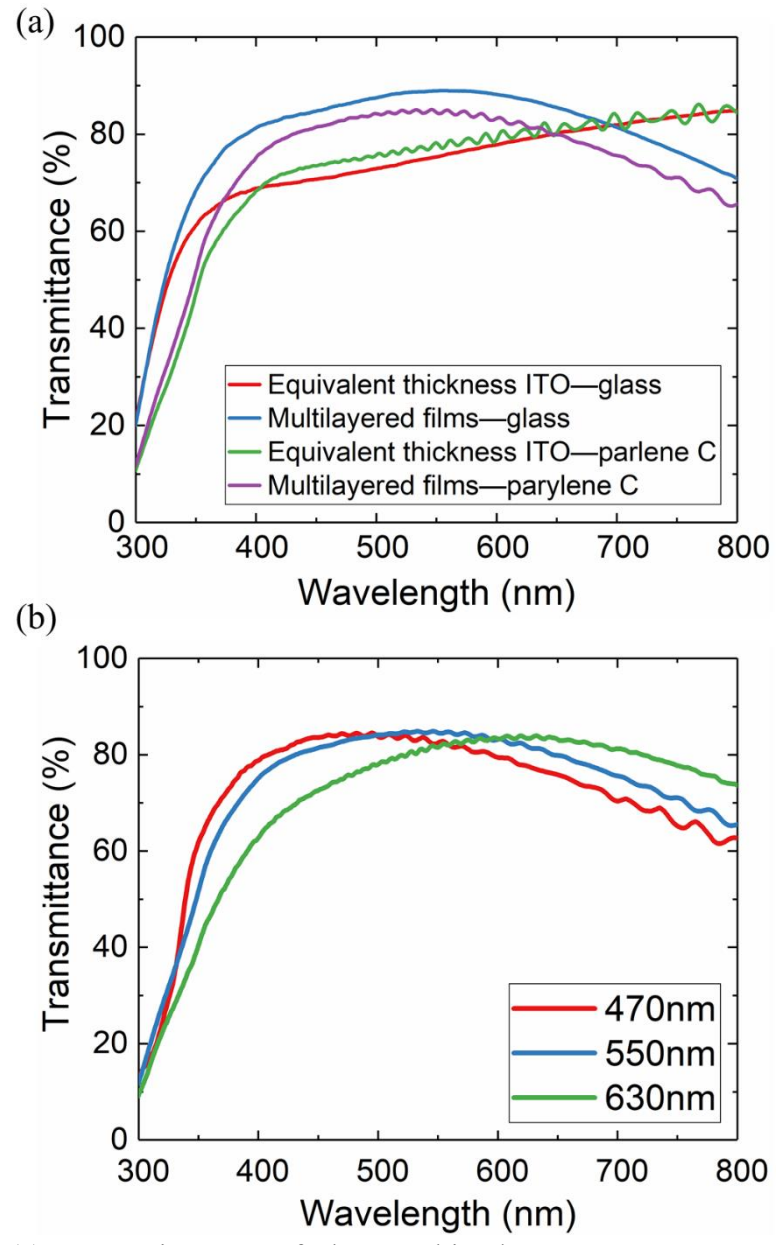


Figure 17. (a) Transmittances of the combined PEDOT:PSS-ITO-Ag-ITO films compared with the equivalent thickness ITO on the glass substrate and Parylene C substrate, respectively. (b) The peak transmittances of combined PEDOT:PSS-ITO-Ag-ITO films on Parylene C at wavelengths of 470 nm, 550 nm, and 630 nm, respectively, to confirm the tunable peak transmittance by stimulating the coatings admittance loci.

(Figure 12) [305], [306] to minimize the reflectance at inhomogeneous thin film interfaces and maximize the admittance of the combined film at the desired wavelength. Figure 16a and 16c show an example of PEDOT:PSS (30.5 nm)-ITO (24 nm)-Ag (9.45 nm)-ITO (20 nm) assemblies with peak transmittance optimized at 550 nm. Compared with single-layer ITO of equivalent thickness, the assembly had a significant increase in transmittance throughout the visible spectrum from 350 nm to 700 nm on both Parylene C and glass substrates. The peak transmittance at 550 nm was enhanced by  $\sim$ 7% from  $\sim$ 78% to  $\sim$ 85% on Parlylene C, and by  $\sim$ 14% from  $\sim$ 75% to  $\sim$ 89% on glass (Figure 17a). The four-point probe measurements were performed on five different regions over the entire substrate, confirming that the average sheet resist was significantly reduced from 147.5  $\pm$  1.53  $\Omega/\text{sq}$  (1.24 x10<sup>-3</sup>  $\Omega\cdot\text{cm}$  resistivity) to 8.81  $\pm$  0  $\Omega/\text{sq}$  (7.40 x 10<sup>-5</sup>  $\Omega\cdot\text{cm}$  resistivity) for the combined film, as shown in Figure 18a. There was no change in the sheet resistance before and after adding PEDOT:PSS to the ITO-Ag-ITO stack. Figure 17b shows that the peak transmittance of the combined film can be tuned to preferred wavelengths, such as 470 nm, 550 nm, and 630 nm, using the admittance loci simulation. This is an important quality for many optical applications, especially optogenetics that utilizes different wavelength light to activate (470 nm for channelrhodopsin) or inhibit (535 nm for halorhodopsin) the activity of light-sensitive ion channel proteins [7]. Figure 18b shows that the additional coating of 30 nm PEDOT:PSS on ITO-Ag-ITO resulted in ~2 % improvement in peak transmittance at 550 nm since the PEDOT:PSS coating acted as an anti-reflective layer. Figure 16b shows that the color of the thin films changed from light yellow (right) to light blue (left) after spin-coating PEDOT:PSS. There was a neglectable change in the film's sheet resistance before and after adding PEDOT:PSS, due to the higher

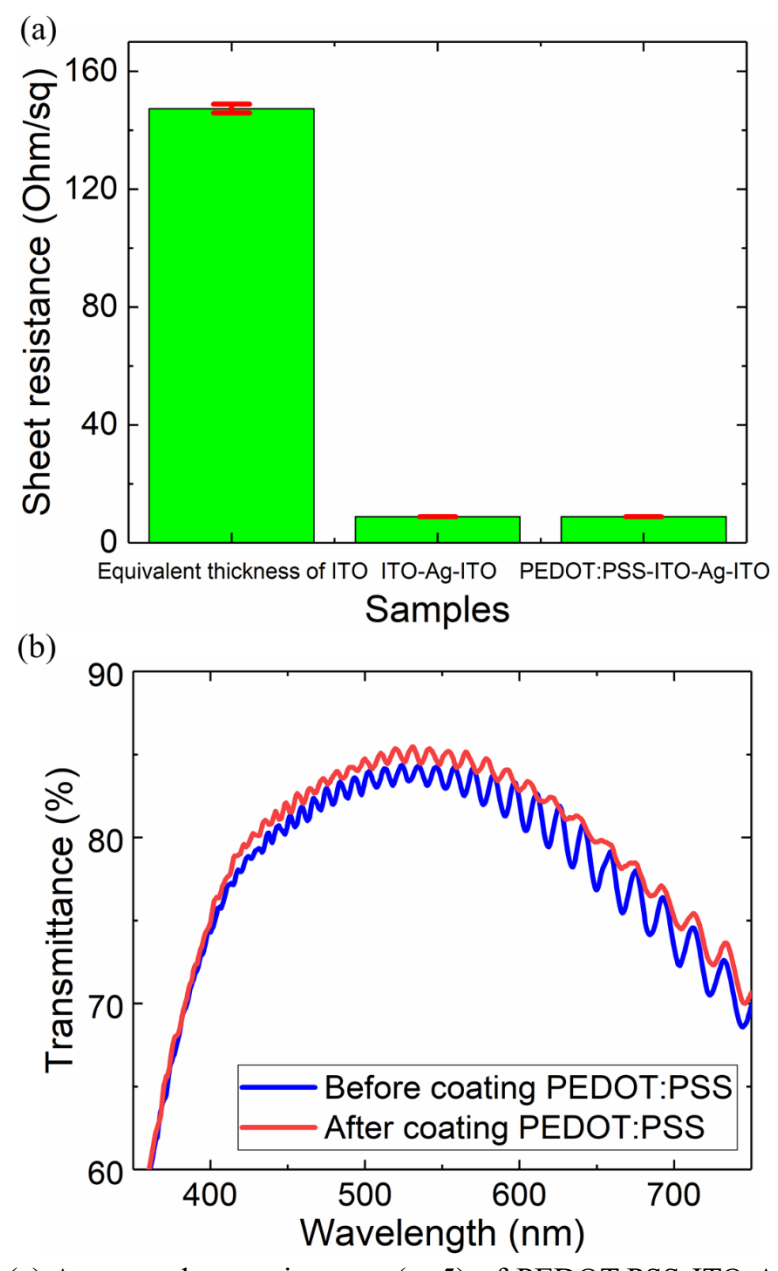


Figure 18. (a) Average sheet resistances (n=5) of PEDOT:PSS-ITO-Ag-ITO and the equivalent thickness ITO on the Parylene C substrate with neglectable standard deviation to confirm the uniformity of the combined films using the four-point probe measurements. (b) The transmittance and (i) the transparency before (right) and after (left) adding the PEDOT:PSS coating.

# 4.3.3 Electrochemical Impedance and Charge Storage Capacity

Figure 19 and 19b show the Bode plots of the impedance magnitudes and phases of the ITO,

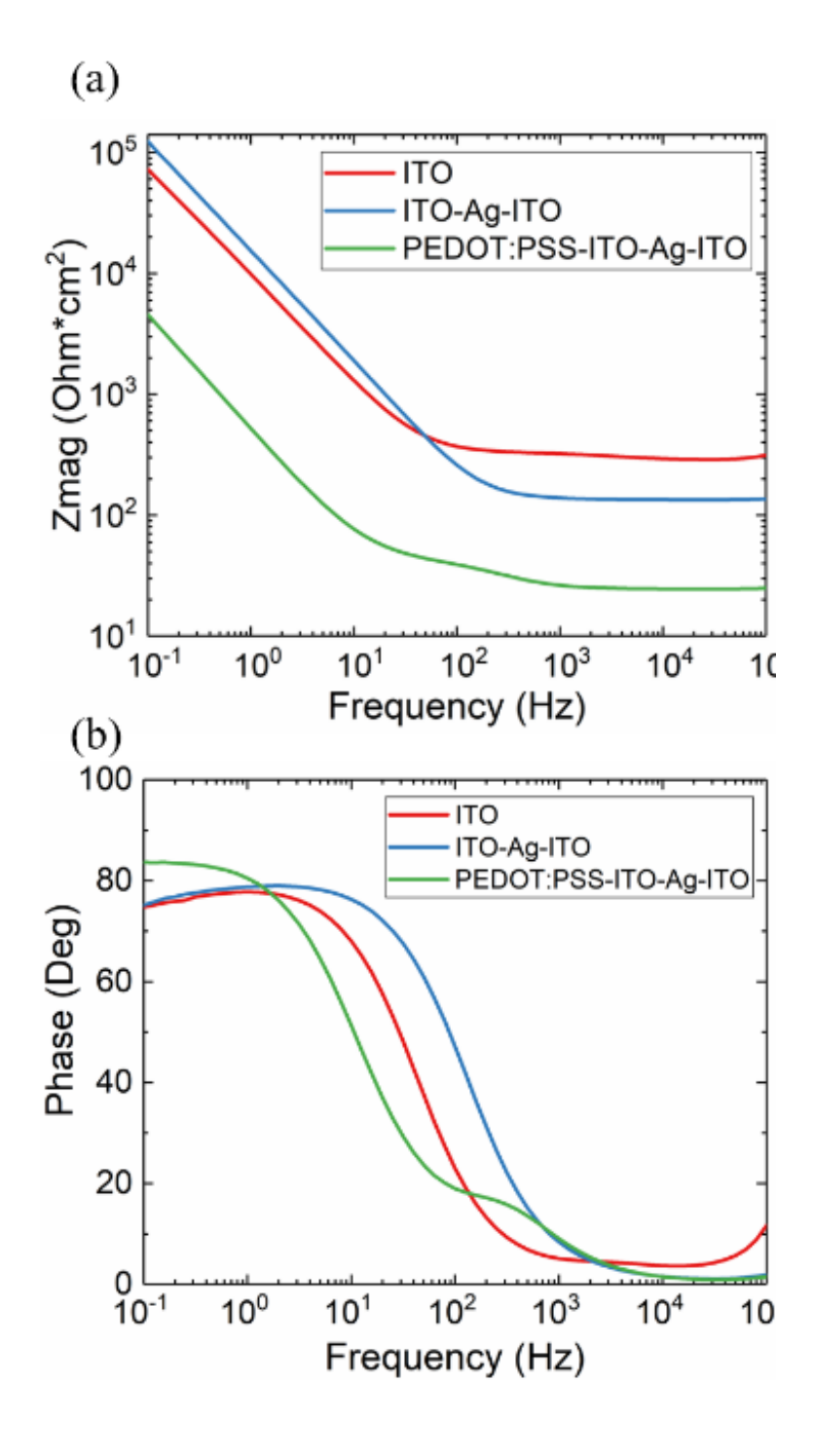


Figure 19. (a) Electrochemical impedance magnitudes and (b) phases of the bare ITO, ITO-Ag-ITO and PEDOT:PSS-ITO-Ag-ITO versus the frequency, respectively.

ITO-Ag-ITO and PEDOT:PSS-ITO-Ag-ITO versus frequency, respectively. These EIS and the following CV measurements were performed using a potentiostat (Electrochemical Analyzer, CH Instruments, Inc.) to analyze the electrochemical impedance in a three-electrode cell. The ITO-Ag-ITO structure effectively reduced the overall electrochemical impedance over a wide frequency range of 0.1 Hz - 100 kHz, while the coating of PEDOT:PSS further decreased the electrochemical impedance in a wide frequency spectrum, which is consistent with other reports [283]. The electrochemical impedance of the total combined film at 1 kHz decreased by at least one order from 322.49 Ohm·cm² to 26.29 Ohm·cm² compared with the pure ITO film. This reduction in impedance is mainly attributed to the improved conductivity of the film and the increase in the surface roughness because of the PEDOT:PSS coating, which was confirmed in Chapter 3. The rough surface provides a large effective surface area of the electrode when exposed to the electrolyte, allowing more charge to flow across the electrode-electrolyte interface.

Figure 20a plots the CV scans of both the pure ITO and PEDOT:PSS-ITO-Ag-ITO combined thin films on Parylene C substrate. For the combined thin films, the larger area under the CV curve indicated a larger cathodic charge capacity, as compared to the pure ITO film. The charge storage capacity of the films calculated from these CV curves was  $29.87~\mu\text{C/cm}^2$  for the pure ITO film and  $1259.65~\mu\text{C/cm}^2$  for the PEDOT:PSS-ITO-Ag-ITO combined film. Our results were consistent with our previous research and those from the last chapter, where the combined films had been proven to have a large degree to enhance the charge storage capacity due to the increased effective surface area. The reduced impedance and the increased charge storage capacity decided the decrease of the total impedance, indicating the less signal to noise ratio (SNR) in the future

electrophysiological signal recording. In addition, for studying the short-term stability of the combined thin films in the room temperature saline solution, 10 consecutive cycles of CV scans of the combined films were run, showing no big variations of 10 shapes in Figure 20b.

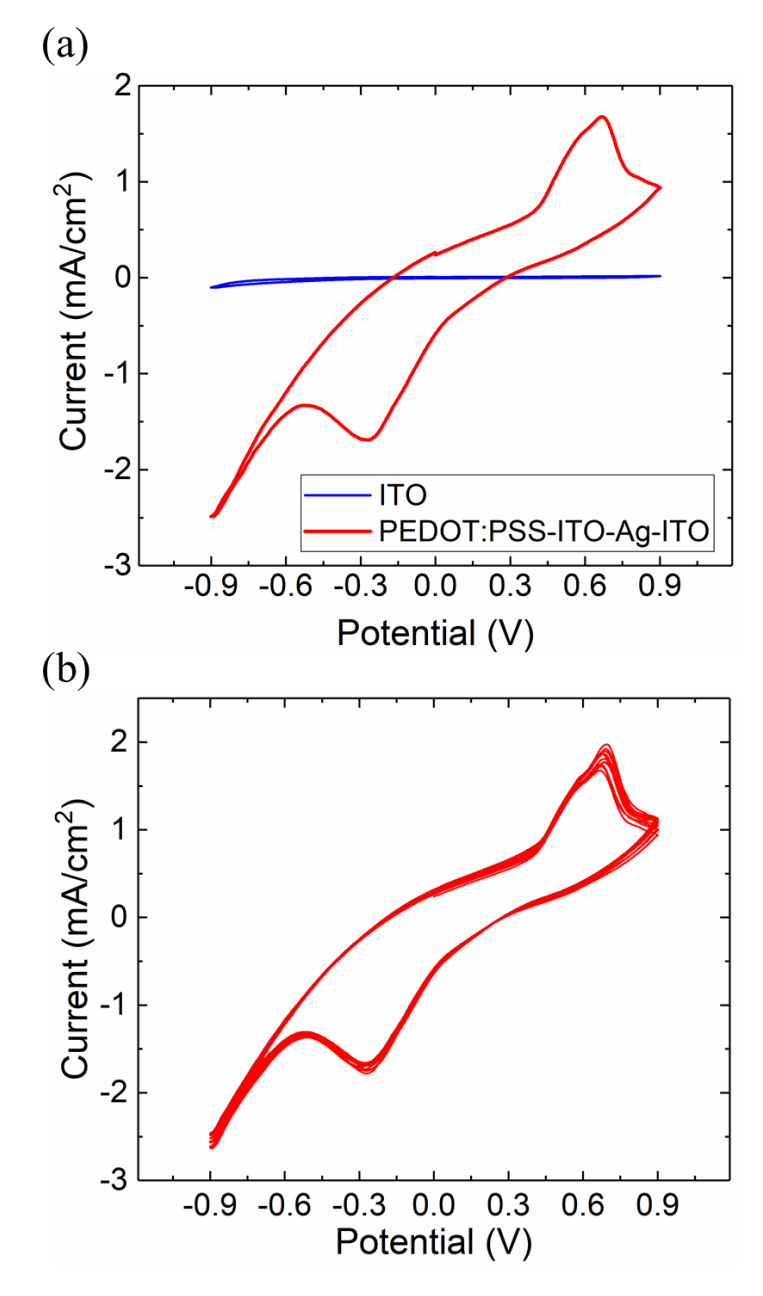


Figure 20. (a) CVs of the plain ITO and PEDOT:PSS-ITO-Ag-ITO WEs versus Ag/AgCl RE, showing that the PEDOT:PSS-ITO-Ag-ITO electrode exhibits larger charge storage capacity. (b) CVs of the PEDOT:PSS-ITO-Ag-ITO electrode for 10 cycles, demonstrating the stability of the multilayered structures in saline.

### 4.3.4 Stability

To evaluate the stability of the combined thin films, first, the CV scans of the same sample at room temperature in the saline solution were repeated for 10 consecutive cycles. No significant changes in CV curves were observed among 10 cycles, as shown in Figure 20a. Then, the long-term stability of combined films using accelerated testing at 37°C in air and saline environments was assessed, respectively. As shown in Figure 21, the combined films exhibited excellent stability with only a slight resistance increase of less than 1.25% and 2.75% after four-week exposure in air and saline, respectively. At the 12-week endpoint, the combined films tested in air still exhibited good stability with an overall resistance increase of less than 12.14%, while the samples tested in saline had a resistance increase of ~ 44.18%. The increase in sheet resistance may be due to the

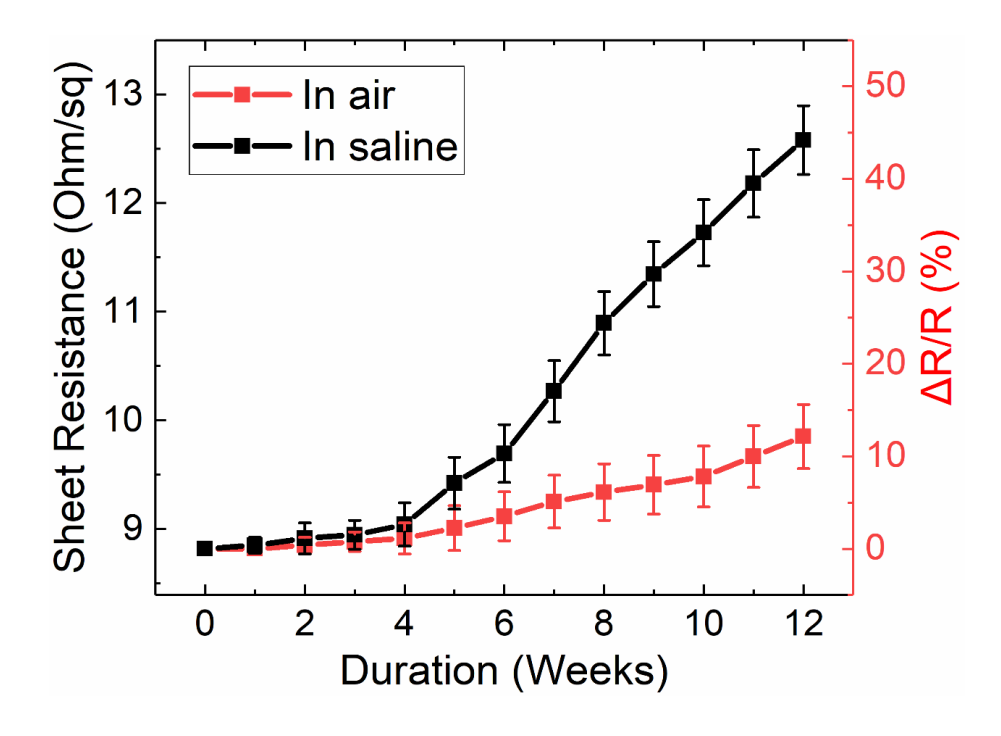


Figure 21. Sheet resistance changes (n=5) of the combined films in air and in saline at 37°C for 12 weeks with measurements every week.

reaction of Ag with oxygen and moisture. Moisture can also weaken the bonding strength at the interfaces between multilayer thin films, which will lead to delamination, and thus, accelerated degradation of the film quality. Nevertheless, because the initial sheet resistance of our combined films was only  $8.81~\Omega/\text{sq}$ , the 44.18% increase in sheet resistance to  $12.70~\Omega/\text{sq}$  was still acceptable for the intended applications in the neural recording.

### 4.3.5 Adhesion

5 samples were run the peel-off tests for evaluating the adhesion between ITO and Parylene C interface without any adhesion promoting layer, as shown in Figure 22. During 50 times of peeling,

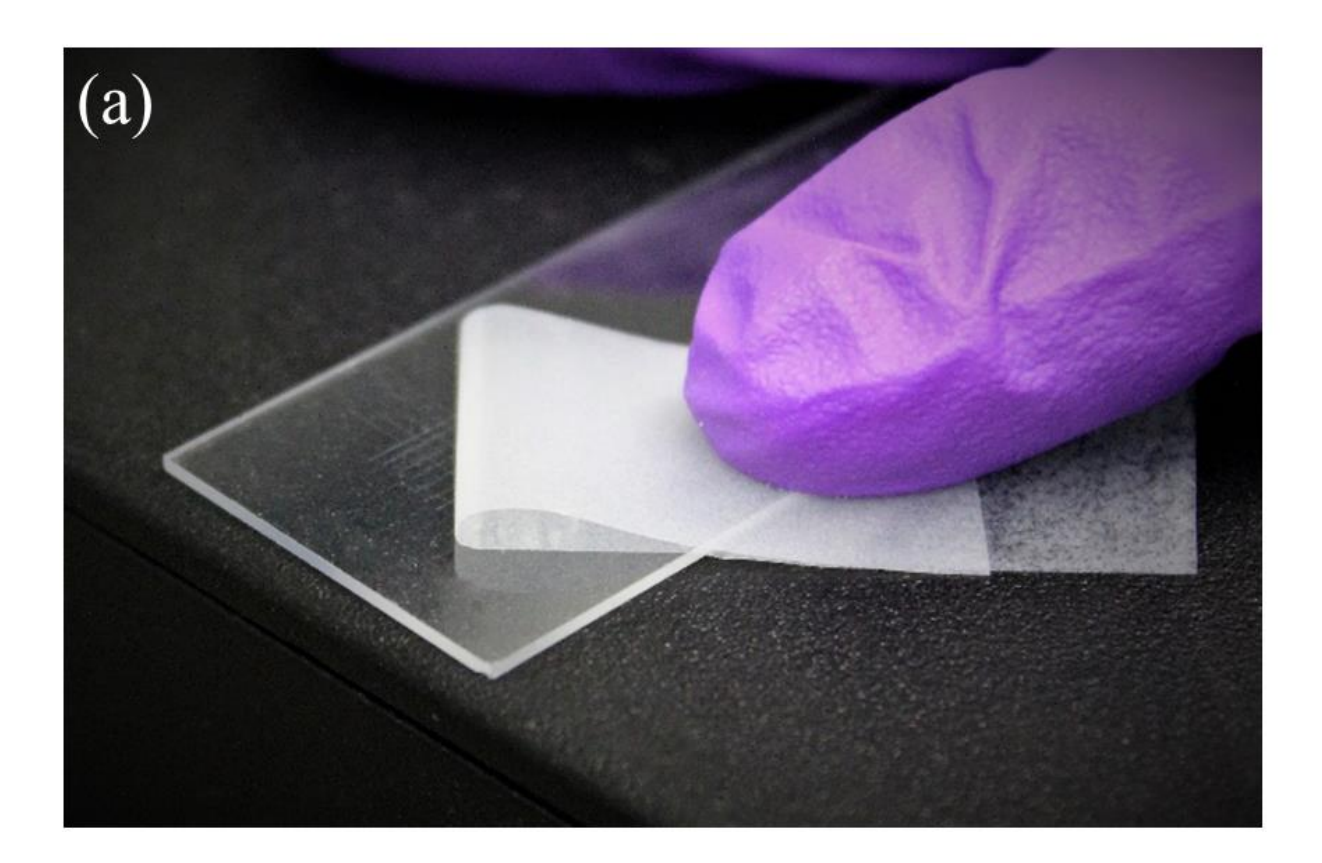


Figure 22. The peeling-off methods.

the tested sample area was recorded at 0 time, 1 time, 10 times and 50 times of peel-off, as clearly displayed in Figure 23a-e. No ITO film was delaminated from the Parylene C during the tests. For easily processing the experiments, I deposited 10  $\mu$ m Parylene C directly on the glass slides and then sputtered the ITO to run our peel-off tests. 8 %, 33 % and 53 % of the Parylene C delaminated

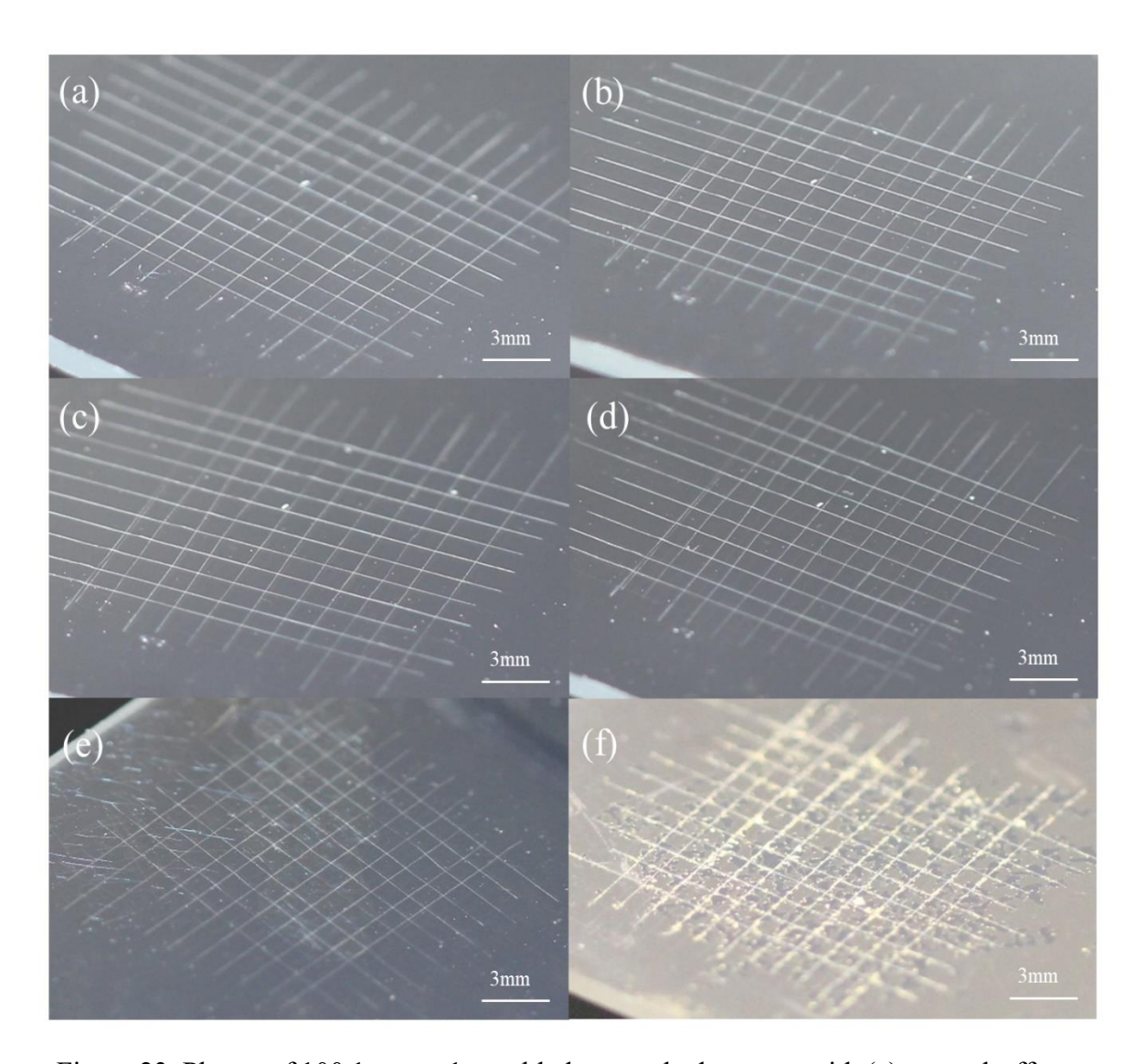


Figure 23. Photos of  $100\ 1\ mm \times 1\ mm$  blade-scratched squares with (a) no peel-off test, (b) one-time peel-off test, (c) 10-time peel-off tests, (d) 50-time peel-off tests, (e) Parylene C delamination after 50-time peel-off tests and (f) delamination of bad quality ITO after one-time peel-off test.

Table 3 Peeling test results with 5 samples

Samples	ITO Delamination	Parylene C Delamination
Sample 1	0%	0%
Sample 2	0%	0%
Sample 3	0%	8%
Sample 4	0%	33%
Sample 5	0%	53%

from the glass surface for sample 3, 4 and 5 in consecutive 50 times peel-off cycles respectively, as shown in Table 3, in consistent with previous research result that Parylene C had poor adhesion on the glass. Our peel off tests results also confirmed that the adhesion of ITO-Parylene C interface was stronger than the Parylene C-glass interface. All peel-off tests results were concluded in Table 3. In addition, control peel-off tests were processed to verify that the good adhesion of ITO-Parylene C substrate was because of our successful sputtering procedures. For ITO with bad quality on account of failed sputtering procedures, delamination and cracks were visible as shown in Figure 23f after only one-time peel off.

### 4.3.6 Bending Test

Bending tests were performed to validate the flexibility of the ITO-Ag-ITO combined thin films on the Parylene C substrate with different ITO thicknesses. Three samples were tested, including 37 nm ITO- 10 nm Ag- 33 nm ITO, 15 nm ITO- 10 nm Ag- 38.5 nm ITO, and 20 nm ITO- 9.5 nm Ag- 24 nm ITO, corresponding to the total ITO thicknesses of 70 nm, 53.5 nm, and 44 nm,

respectively. The changes in the sheet resistance of the flexible ITO-Ag-ITO thin films were measured and then normalized as  $\Delta R/R$ , where R was the initially measured sheet resistance and  $\Delta R$  was the difference in the sheet resistance before and after bending cycles. Bending curvatures with diameters of 3 mm and 6 mm were tested individually for checking how the sheet resistance changed with the different degree of bending. As shown in Figure 24a and 24b, for single-layer

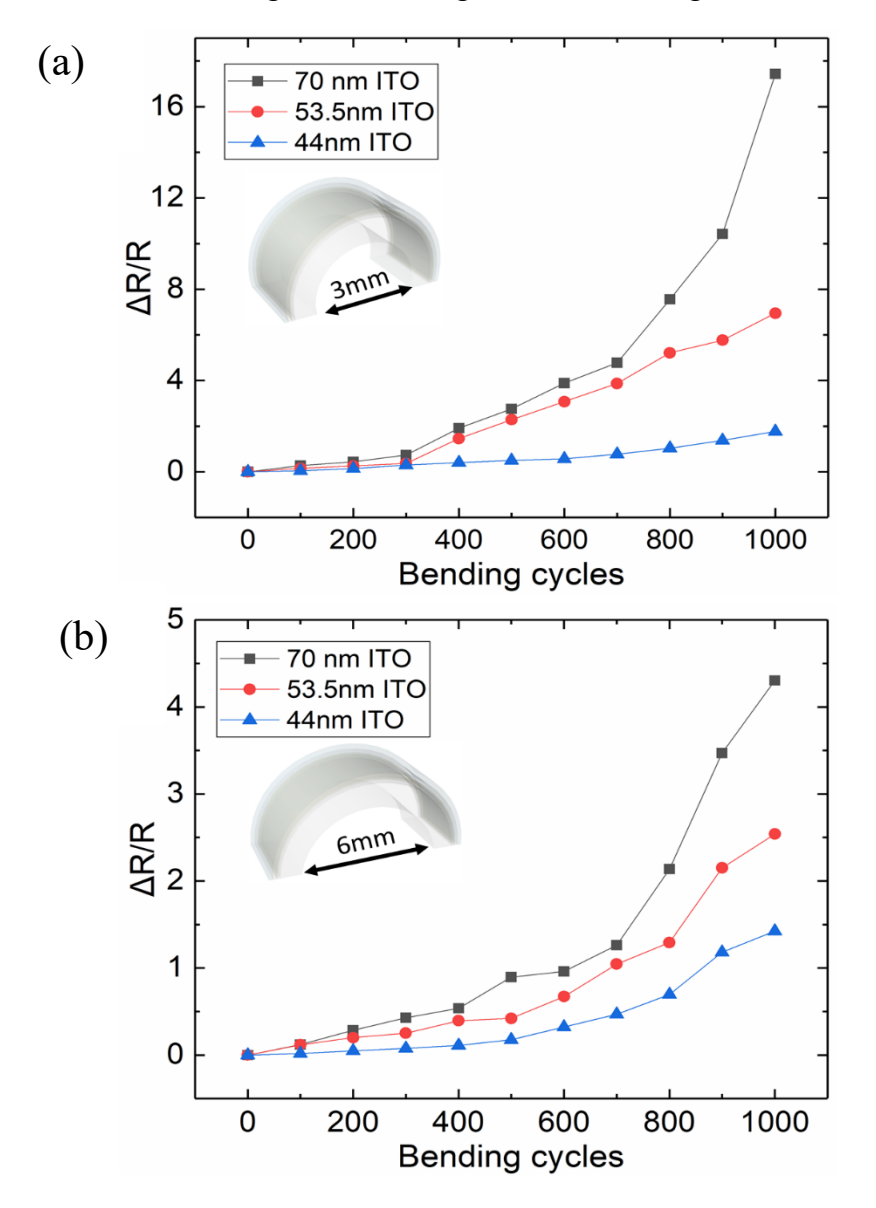


Figure 24. Sheet resistances of the only ITO thin films with the same total ITO thickness within the total 1000 bending cycles under (a) 3 mm bending diameters and (b) 6 mm bending diameters, respectively.

ITO, the films with thinner ITO are more robust to withstand bending. When combining thin ITO in the multilayer assembly shown in Figure 25a and 25b, the films with the same thickness show significantly improved flexibility and tolerance to bending cycles. The results also indicated that, for a smaller bending diameter, the changes of sheet resistance were more noticeable but still within a good tolerance range of less than 140%.

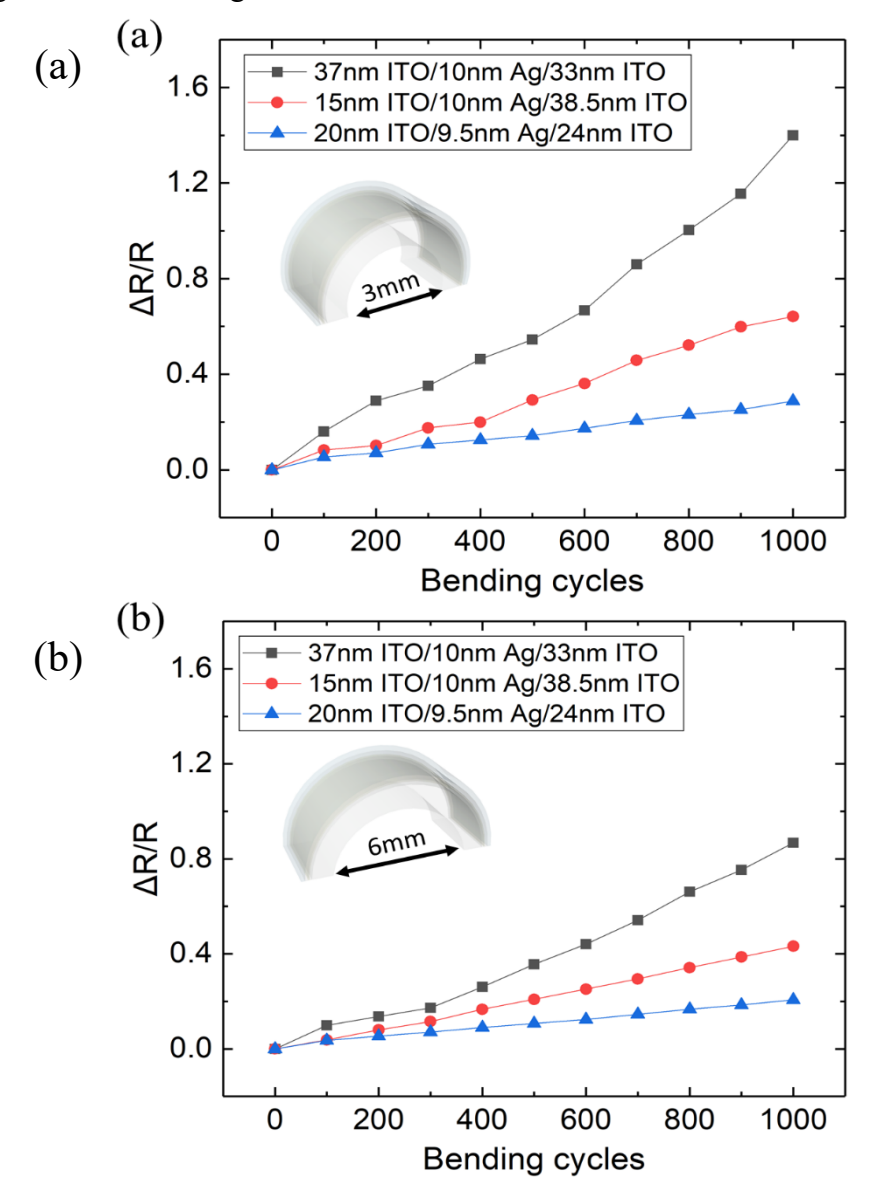


Figure 25. Sheet resistances of combined thin films with the same total ITO thickness within the total 1000 bending cycles under (a) 3 mm bending diameters and (b)6 mm bending diameters, respectively.

# 4.3.7 Young's Modulus

Furthermore, cyclic nanoindentation tests were conducted to quantify Young's modulus of the Parylene C films with and without the PEDOT:PSS-ITO-Ag-ITO coating. 36 indents were made on each sample, and Young's moduli of different samples were plotted in Figure 26a and 26b as a function of the load displacement into the surface. The pointed shapes in the curves were

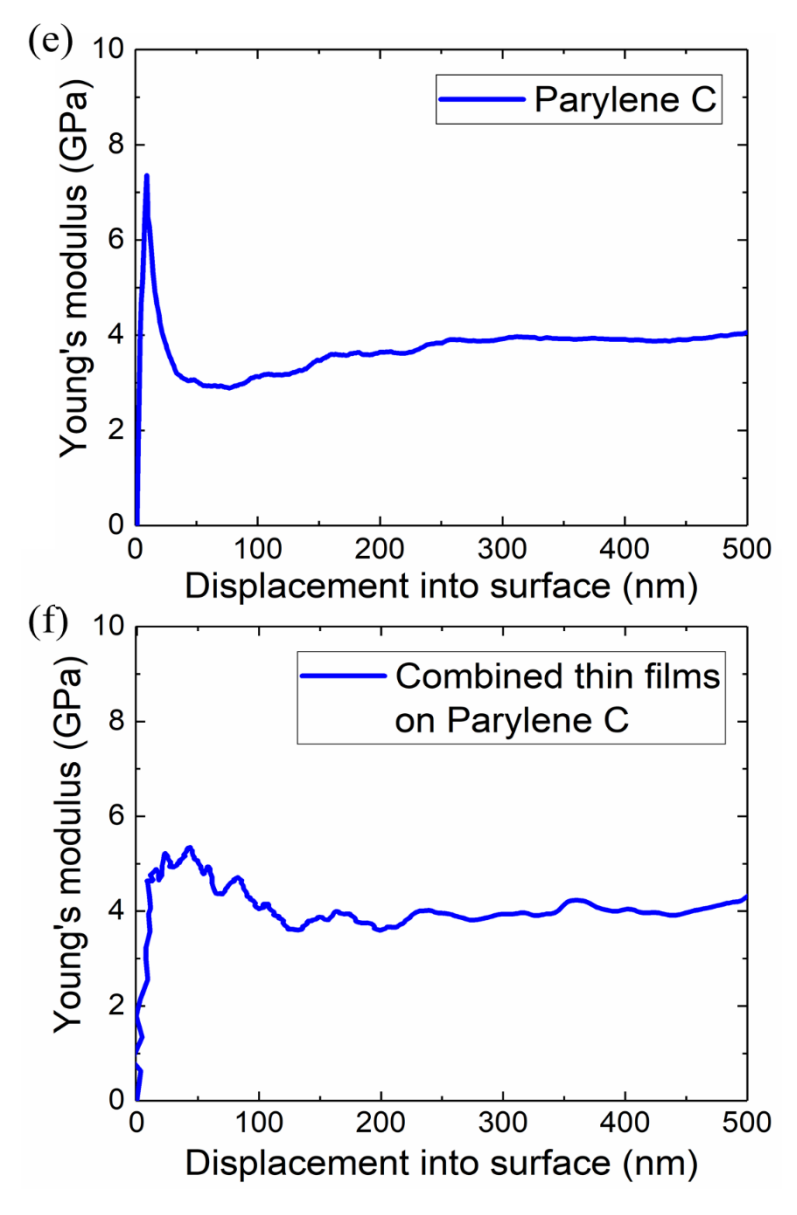


Figure 26. Young's modulus of (e) the only Parylene C film and (f) the combined thin films on Parylene C.

corresponding to the pop-in events [307]. The Young's modulus after the first pop-in remained nearly constant at 4.049 GPa for Parylene C and 4.064 GPa for the combined film after averaging all 36 indents. This result indicates that the added PEDOT:PSS-ITO-Ag-ITO coating has minimal impact on the overall Young's modulus of the combined film that is predominated by the polymer substrate. The small fluctuations in Figure 26a were due to environment interference while the fluctuations in Figure 26b were possibly associated with dislocation activities [308]. The experimental data were compared with theoretical calculations based on Equation 4 for less mixture of particle and polymer [309]:

$$\frac{1}{E_{composite}} = \frac{V_{ITO_1}}{E_{ITO_1}} + \frac{V_{Ag}}{E_{Ag}} + \frac{V_{ITO_2}}{E_{ITO_2}} + \frac{V_{Parylene}}{E_{Parylene}}$$

$$(10)$$

where E is Young's modulus and V is the volume fraction of each layer. With an assumption of the same cross-sectional area, the volume fraction was replaced by the layer thickness during the calculations. The Young's moduli of Parylene C, ITO, and Ag are 4 GPa [310], 116 GPa [311], and 85 GPa, and the thicknesses were 10  $\mu$ m, 44 nm, and 9.5 nm, respectively. The calculated  $E_{composite}$ 

is 4.021 GPa, very close to the measured Young's moduli.

#### 4.4 Conclusion

This chapter, for the first time, reported an ultra-flexible, conductive, transparent thin film using PEDOT:PSS-ITO-Ag-ITO multilayer structure on Parylene C, which exhibited significantly reduced sheet conductivity, decreased electrochemical impedance, tunable peak transmittance with higher transmittance over the pure ITO film, excellent adhesion, stability, and flexibility, suitable for use in many different biomedical applications as optoelectronics. The effects of the sputtering temperature and layer thickness on the properties of the combined thin films were studied theoretically and experimentally to achieve the desired film properties. Our combined films also show remarkably improved conductivity and transmittance as compared to the pure ITO thin film.

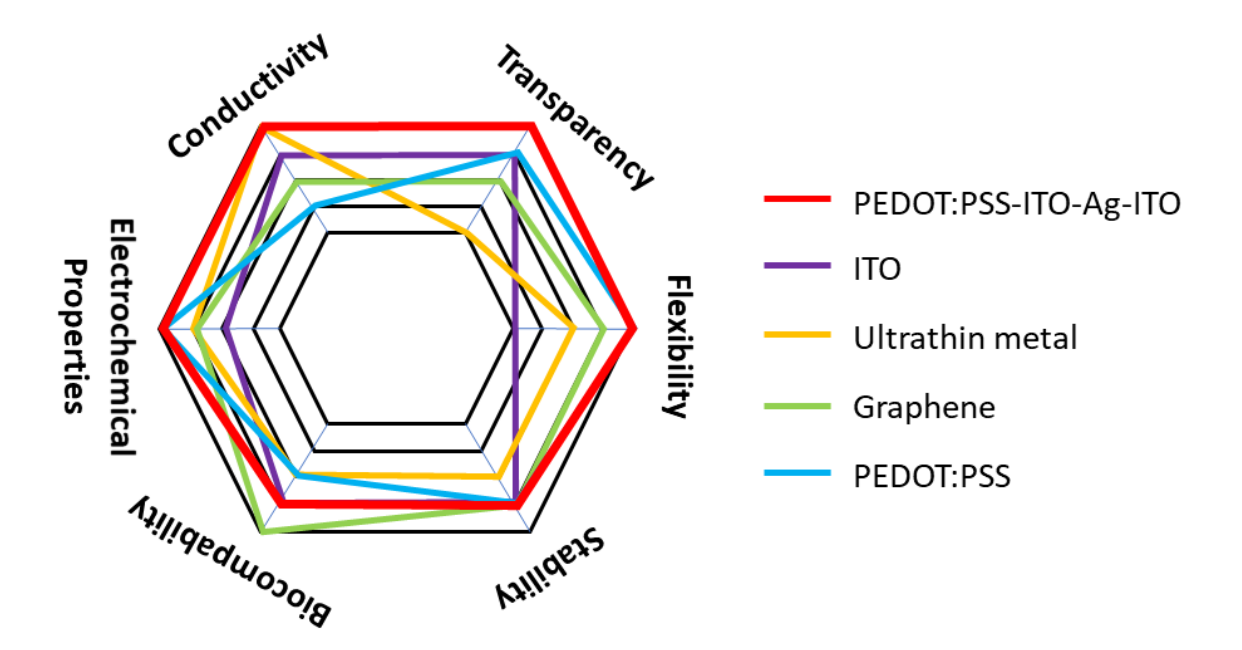


Figure 27. Hexagon chart of PEDOT:PSS-ITO-Ag-ITO, ITO, ultrathin metal, graphene, and PEDOT:PSS with six properties: conductivity, transparency, flexibility, stability, biocompatibility, and electrochemical properties.

In addition, the combined thin films remained stable over 12 weeks in both air and saline environments at 37°C. Scotch tape peeling tests confirmed the strong adhesion strength between the ITO-Ag-ITO structure and the Parylene C substrate. Finally, bending test results validate the excellent flexibility of the combined thin films and suggest that the thinner ITO coating in the multilayered structure results in better bending tolerance. The slight increase in the film sheet resistance during the bending test was believed to be mainly caused by cracks under repetitive mechanical stressing. The Young's modulus of the combined film was tested to be ~4 GPa, dominated by the Parylene C substrate. The flexibility of the combined film could be further improved by switching Parylene C to another polymeric material with a lower Young's modulus, such as PDMS. Future work will focus on utilizing this multilayer structure to fabricate electrocorticogram (ECoG) array interface to record the neurophysiology signals *in vivo*. The hexagon chart in Figure 27 compares the advantages and disadvantages of PEDOT:PSS-ITO-Ag-ITO, IITO, ultrathin metal, graphene, and PEDOT:PSS.

CHAPTER 5: A Fully Transparent, Flexible PEDOT:PSS-ITO-Ag-ITO Based Microelectrode Array for ECoG Recording

Integrative neural interfaces combining neurophysiology and optogenetics with neural imaging provide numerous opportunities for neuroscientists to study the structure and function of neural circuits in the brain. Such a comprehensive interface demands miniature electrode arrays with high transparency, mechanical flexibility, electrical conductivity, and biocompatibility. In the previous Chapter, an ultra-flexible, conductive, transparent PEDOT:PSS-ITO-Ag-ITO multilayered thin films on Parylene C has been designed and fabricated. Therefore, this chapter is focused on designing, fabricating a microscale electrocorticogram (µECoG) electrode arrays made of this PEDOT:PSS-ITO-Ag-ITO assembly on thin Parylene C films. EIS analyses was used to measure the electrical impedance of the microelectrodes with the PEDOT:PSS-ITO-Ag-ITO assembly as well as the electrochemical impedance stability over 12 weeks. The µECoG electrodes enable electrical recordings with high signal-to-noise ratios (SNRs) (~35-36 dB) under different color photostimulations, suggesting that the electrodes are resilient to photon-induced artifacts. The transmittance of the transparent microelectrodes of the µECoG array was also confirmed by attaching on a 50 µm-thick, mCherry-labelled, rat brain section. In vivo animal experiments confirm that our array can successfully record light-evoked ECoG oscillations from the primary visual cortex (V1) of an anesthetized rat.

#### 5.1 Introduction

Neurological disorders and diseases in central and peripheral nervous systems, such as Parkinson's disease, Alzheimer's disease, epilepsy, etc., affect hundreds of millions of people worldwide [37]. Besides commercially-available medications and deep brain stimulation approaches, numerous neural interface electrodes have been developed to allow researchers to stimulate and record neural activity with high temporal resolution, permitting quantitative studies of the correlation between neural function and dysfunction. However, most existing microelectrode techniques cannot achieve cell-type specific neuromodulation and high spatial resolution due to current spread in tissues.

Optogenetics, a technique that uses light to control genetically targeted neurons [312], [313], has emerged as a viable alternative that overcomes the limitations associated with microelectrode technologies [9], [313]. However, optical imaging methods have not achieved the high temporal resolution seen with microelectrodes. Leveraging the advantages of both technologies, hybrid optoelectronic neural interface tools that combine optogenetic neurostimulators with microscale electrocorticogram (µECoG) recording electrodes have been proposed by several groups [159], [314]. Although most of the existing ECoG arrays are used to only gather the electrophysiological signals from the superficial surface of the cerebral cortex, some ECoG arrays with high spatial resolution, such as 'NeuroGrid', have been proved to be capable of recording spike activity and LFPs [46]. In such devices, transparent µECoG electrodes allow more light to penetrate through the electrode array, and therefore are more beneficial than their opaque counterparts.

To date, most transparent µECoG arrays are fabricated with a single material, including ITO, ultrathin metals, micro/nanostructured metals, graphene and PEDOT:PSS. However, utilizing only a single material is hard to achieve the desired combination of excellent electrical, optical, mechanical, and biocompatible properties.

Depending on what have been explored in Chapter 4, in Chapter 5, a PEDOT:PSS-ITO-Ag-ITO multilayered structure was applied to fabricate the conductive, ultra-flexible, anti-reflective and transparent μECoG array. EIS analyses were run to test the electrochemical impedance of the microelectrodes with the PEDOT:PSS-ITO-Ag-ITO assembly. EIS measurements were conducted over 12 weeks every 3 weeks to check the stability of each different size of microelectrodes, including 25 μm, 30 μm, 36 μm, 45 μm, and 50 μm. SNRs of μECoG electrodes were measured under blue, green, yellow and red light emitting diodes (LEDs) and compared with no LED light, confirming that the influence of LED light on the quality of recorded signals is neglectable. The transmittance of the transparent microelectrodes of the μECoG array was also confirmed by attaching on a 50 μm-thick, mCherry-labelled, rat brain section. *In vivo* animal experiments confirm that our array can successfully record light-evoked ECoG oscillations from the primary visual cortex (V1) of an anesthetized rat.

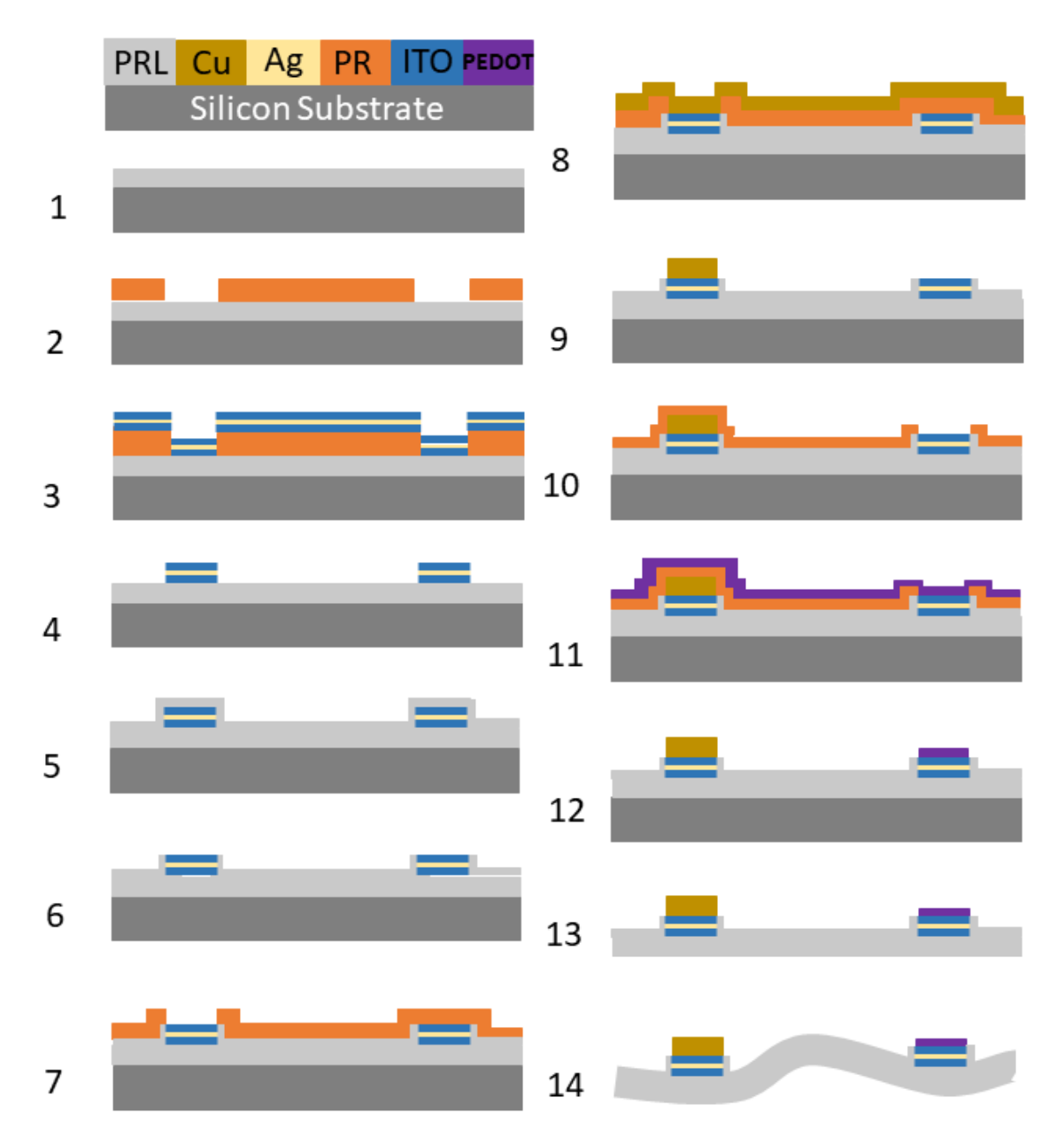


Figure 28. μECoG array fabrication steps: (1) Deposit Parylene C. (2) Pattern the photoresist. (3) Deposit ITO-Ag-ITO thin films. (4) Wash off photoresist and pattern the ITO-Ag-ITO layer. (5) Deposit the second Parylene C layer. (6) Etch Parylene C selectively to exposure the electrode sits and contacts. (7) Pattern another layer of photoresist. (8) Deposit Cu. (9) Wash off photoresist and pattern Cu over the contact areas. (10) Pattern another layer of photoresist. (11) Deposit PEDOT:PSS. (12) Washing off photoresist to obtain the PEDOT:PSS patterns on the electrode sites. (13) Release the μECoG array from silicon substrate. (14) Flexibility of the released μECoG array.

#### 5.2 Materials and Methods

# 5.2.1 Fabrication of µECoG Array

First, 10 µm Parylene C was deposited on a cleaned 3-inch silicon wafer. Then, a photoresist (PR) layer was spun on the substrate and photolithographically patterned to expose the areas of microelectrodes, interconnection wires, and contact pads. Following ITO-Ag-ITO deposition using the above method, the wafer was submersed in acetone at room temperature. With the PR mask, ITO-Ag-ITO on the undesired areas was washed off with acetone and the surface was cleaned with IPA and DI water, leaving the ITO-Ag-ITO on the electrode sites, contact pads, and interconnect wires. Next, 2 µm Parylene C was deposited on the substrate as an insulating layer, and then Parylene C on the contact pads and microelectrodes were removed completely using oxygen plasma dry etching (RIE-1701 plasma system, Nordson March, Inc). Then, 500 nm copper was sputtered and patterned only on the contact pad with a sacrificial PR mask. Then, the PR was rinsed off with acetone, IPA and DI water for copper lift off. After that, another PR mask was patterned to expose only the microelectrode sites followed by spin coating of diluted 0.55% PEDOT:PSS using the above recipe. Finally, PR was rinsed off with acetone, IPA, and DI water to remove unwanted PEDOT:PSS, leaving PEDOT:PSS only on top of the ITO-Ag-ITO microelectrodes. Instead of using plasma etching, the outer shape of the array was manually cut according to the defined outlines that we initially designed on our mask to prevent the damage of ITO from plasma over-etching. The detailed fabrication steps are shown in Figure 28.

### 5.2.2 Testing Methods

### 5.2.2.1 Electrochemical Impedance

EIS measurements were taken using a potentiostat (Electrochemical Analyzer, CH Instruments, Inc.) to analyze the electrochemical impedance in a three-electrode cell, with the microelectrode as the WE, an Ag/AgCl electrode as the RE, and a platinum electrode as the CE. The tests were conducted in the physiological saline solution (0.9 % NaCl) at room temperature. The electrochemical impedance of the microelectrode was measured from 0.1 Hz to 100 kHz when a 5 mV RMS sinusoid waveform was applied to the WE. CVs of the microelectrode were measured at a 100 mV/s sweep rate in a potential range of -0.9 V to 0.9 V. Multiple CV scans were done in experiments before data collection to clean the electrode surface and allow the system to settle.

#### 5.2.2.2 Transmittance Measurements

The mCherry fluorescent images and bright-field were taken by a THUNDER imager (3D Cell Culture, Leica, Inc).

### 5.2.2.3 Signal to Noise Ratios (SNRs) Measurements

The microelectrode array and LEDs of different colors were immersed in the saline solution with a separation distance of ~ 0.5 cm. A 1 mVpp sinusoidal waveform at 5 Hz frequency was applied at the opposite ends of the saline solution container. LEDs were kept flashing on the microelectrode panels with applied voltages of Vblue=3.3 V, Vgreen=3.3 V, Vyellow=1.8 V, and Vred=1.8 V, respectively. The whole setup was placed in a Faraday cage to minimize the environmental noises. The signals were acquired via an RHD2132 system (Intan Techonogies, Inc), and then analyzed with OriginLab and Excel to calculate the SNRs.

### 5.2.2.4 *In vivo* Animal Experiment

One male adult rat (Sprague Dawley, 435 g) was tested based on our established protocols approved by the Institutional Animal Care and Use Committee (IACUC) at Michigan State University. Following the stereotaxic surgery protocol, an adeno-associated virus (AAV) vector containing the channel rhodopsin and m-Cherry genes (AAV-hSyn-hChR2 (H134R)- mCherry; UNC Vector Core) was injected bilaterally into the rat's V1. After injection, the rats were kept in the animal facility for 4 weeks until the V1 neurons expressed channelrhodopsin-2 (ChR2). During the *in vivo* experiments, the rat was anesthetized with 2% isoflurane and oxygen (0.8L/min.) and placed in a stereotaxic apparatus. Using sterile surgical procedures, a 3-4 cm incision was made in the skin overlying the skull and a small region of bone was removed to expose the V1 areas. The µECoG array was carefully attached to the VI region using a micromanipulator.

For the first *in vivo* acute animal experiment, the rat's left eye was optically stimulated using a white LED with a light pulse duration of 20 ms at 0.5 Hz frequency, while the right eye was covered with a gauze pad. During the visual stimulation, the ECoG recording signals were simultaneously recorded through the implanted 32-channel PEDOT:PSS-ITO-Ag-ITO microelectrodes. Spontaneous ECoG activities were also recorded as control while the LED light was off.

A wireless-powered micro-LED was placed over the  $\mu ECoG$  array on the left V1 area, with a light pulse duration of 20 ms at 1 Hz frequency and with 1.5mW/mm<sup>2</sup> low light intensity or 11.8 mW/mm<sup>2</sup> high light intensity. The microelectrodes on the left panel were illuminated directly by

the micro-LED. Light-evoked ECoG activity was simultaneously recorded through the implanted microelectrodes. Spontaneous ECoG activities recorded from the left V1 when the LED light was completely off were used as a positive control, while a negative control consists of ECoG recordings from the right V1 when the left V1 underwent high optical stimulation. The recorded signals were amplified and digitalized using a commercial Intan RHD2132 system (Intan Technologies) and then analyzed using the Matlab Chronux toolbox to extract the activation energy, phase synchrony, PSD distribution from the recordings.

#### 5.3 Results and Discussion

# 5.3.1 Fabricated Microscale ECoG Microelectrode Arrays

Having characterized the performance of the combined films, a 32-channel  $\mu$ ECoG array was designed and fabricated using the multilayer PEDOT:PSS-ITO-Ag-ITO film. In the first version of the array design, 32 microelectrodes with 100  $\mu$ m diameter were distributed equally on the two 5 mm × 11 mm panels with the whole device dimension was 12 mm × 34 mm, as shown in Figure 29. However, it was hard to be attach the whole array panels on the left and right hemispheres of the rat's brain because the panel size was too large. The poor attachment of the microelectrodes with the cortex caused the poor signal recording. The *in vivo* results were shown in the following "*In vivo* Animal Experiment" section. Therefore, the improved  $\mu$ ECoG electrode array had dimensions of 16 mm × 10 mm, with two 3 mm × 3 mm panels to cover both left and right hemispheres of the primary visual cortex (V1) of the rat's brain. Each panel consisted of 16 microelectrodes with different diameters: 25  $\mu$ m, 30  $\mu$ m, 36  $\mu$ m, 43  $\mu$ m and 50  $\mu$ m. Figure 30a

gives an example of the fabricated  $\mu$ ECoG array, Figure 30c,d show the ITO-Ag-ITO microelectrodes before and after the PEDOT:PSS treatment, and Figure 30b demonstrates the flexibility of the array. Compared to the inkjet-printed PEDOT:PSS electrode with the electrochemical impedance of 12.675  $\Omega$ ·cm<sup>2</sup> at 1kHz, our PEDOT:PSS treated electrode shows 4 times lower impedance of 3.257  $\Omega$ ·cm<sup>2</sup> [315]. Recently reported electroplated PEDOT:PSS-graphene electrode indicated lower electrochemical impedance of under 0.21-0.3  $\Omega$ ·cm<sup>2</sup> [316], [317]. However, like most electroplated PEDOT:PSS, the PEDOT:PSS-coated electrode areas have low transparency or are not transparent.

# 5.3.2 Electrochemical Impedance

The stability of the µECoG electrode array was evaluated in air at room temperature for up to 12 weeks, during which impedance changes were monitored every three weeks and plotted in

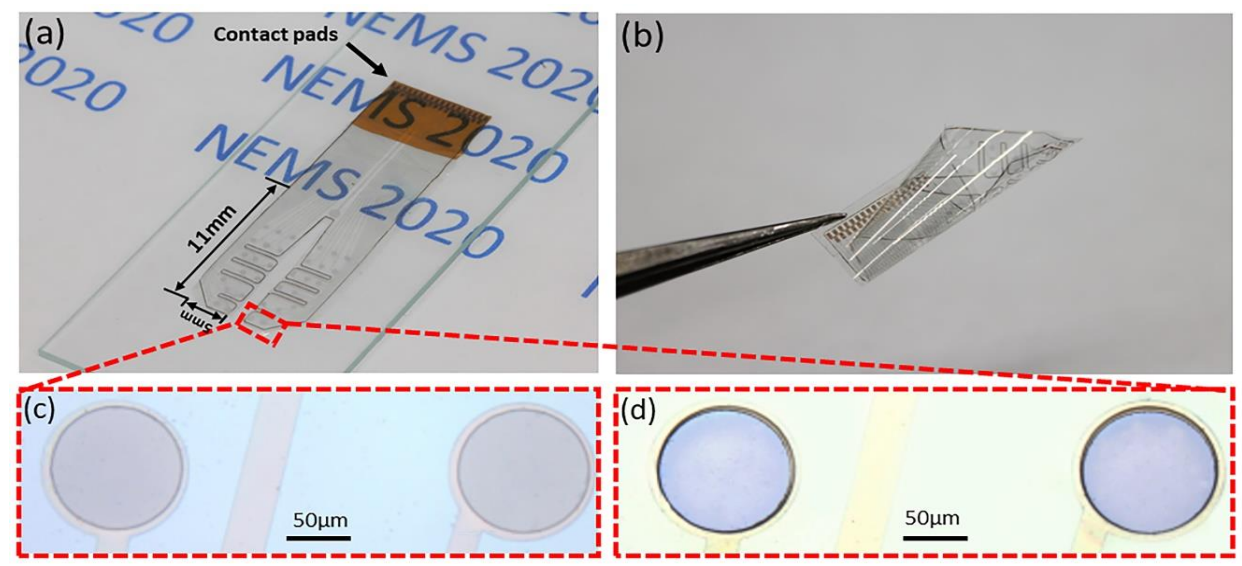


Figure 29. The prototype of fabricated transparent and flexible  $\mu ECoG$  microelectrodes arrays and their electrochemical impedance and SNR behaviours. (a) The transparency and (b) the flexibility of an as-fabricated  $\mu ECoG$  microelectrode array without (c) and with (d) PEDOT:PSS coating.

Figure 32a-d. The zoom-in results in Figure 32c show that the µECoG electrode array exhibited good stability over 12 weeks with an overall impedance increase of less than 8.47%. The average 1 kHz impedance decreased when the electrode area increased (Figure 32d). The average 1 kHz impedance changes were less than 11.8% over 12 weeks for all the electrode diameters. This impedance increase may be due to PEDOT:PSS reaction with oxygen upon exposure to air, creating an aqueous acid environment that corrodes ITO [284]. ITO etching chemical will then diffuse through the PEDOT:PSS film and weaken the stability of the ITO-PEDOT:PSS interface, thereby slowly increasing impedance. Another possible reason for the increased impedance could

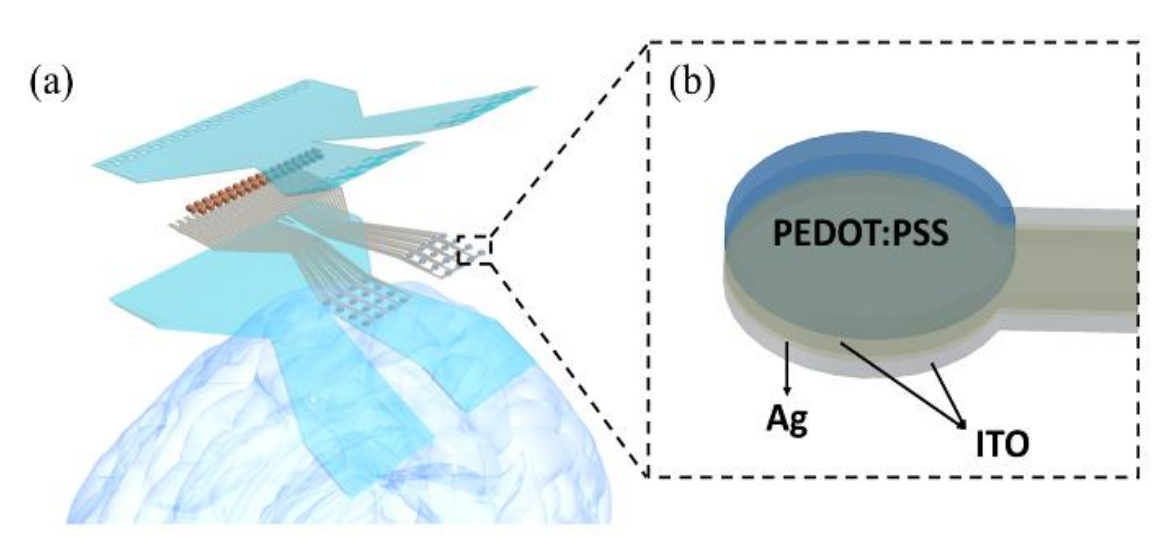


Figure 30. (a) Concept diagram of transparent μECoG array. (b) Concept diagram of PEDOT:PSS-ITO-Ag-ITO multilayer structure of microelectrodes.

be the corrosion reaction between Ag and the ionic solution that diffused through defects or pinholes in the top-most ITO layer [210].

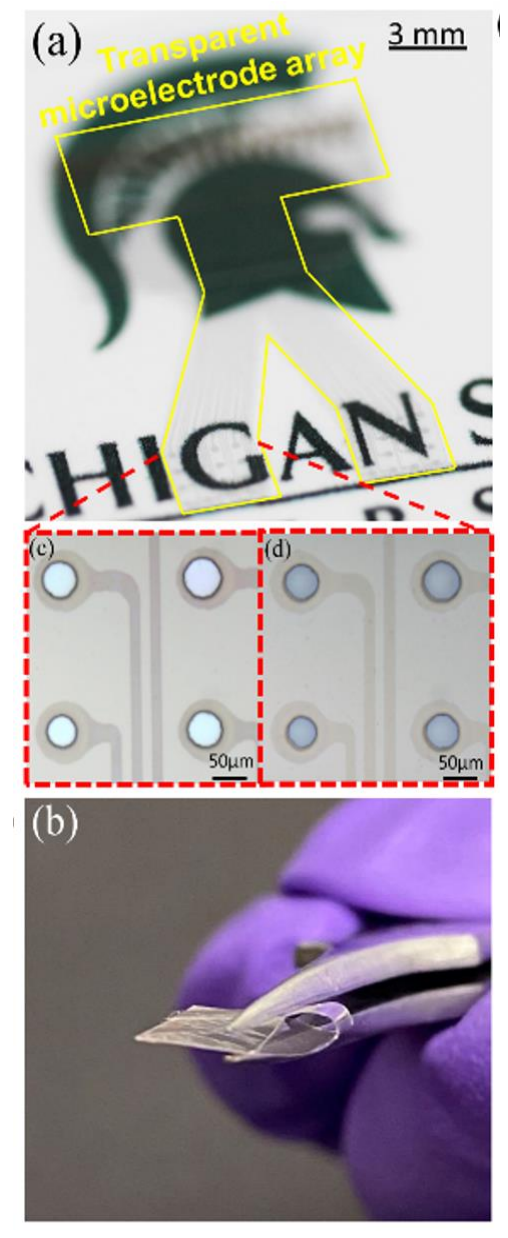


Figure 31. The prototype of fabricated transparent and flexible  $\mu ECoG$  microelectrodes arrays. (a) The transparency and (b) the flexibility of an as-fabricated  $\mu ECoG$  microelectrode array without (c) and with (d) PEDOT:PSS coating.

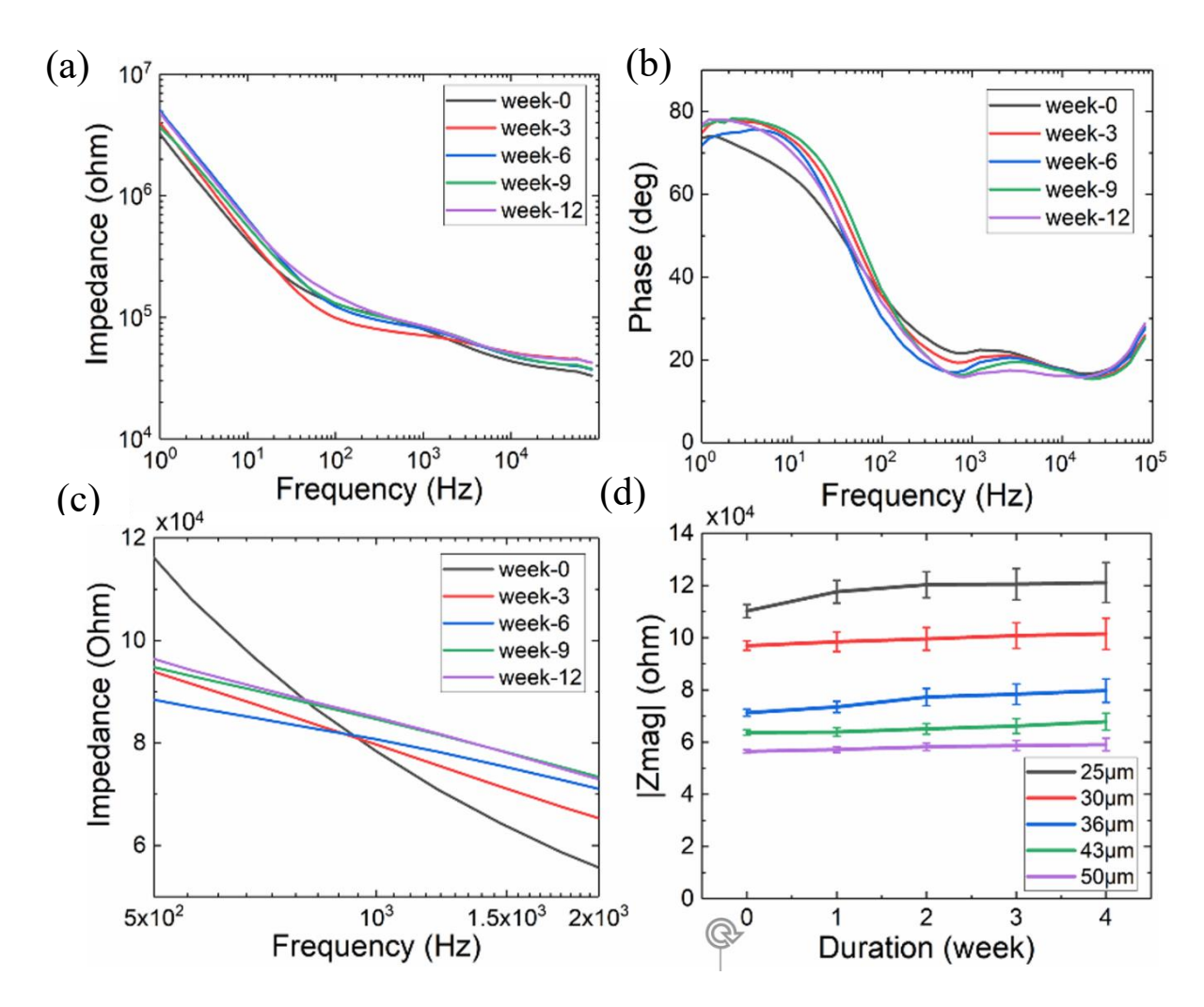


Figure 32. (a) Impedance magnitude and (b) phase changes of the PEDOT:PSS-ITO-Ag-ITO multilayered  $\mu ECoG$  microelectrodes during 4 weeks soaking in room temperature saline. (c) Zoom-in impedance magnitudes at 1 kHz frequency over 4 weeks. (d) Average 1 kHz impedance changes of PEDOT:PSS-ITO-Ag-ITO microelectrodes, measured after being soaked in saline for 0 week, 1 week, 2 weeks, 3 weeks, and 4 weeks (n=10).

### 5.3.3 Transmittance Measurements

To further evaluate the transmittance of the transparent microelectrodes of the  $\mu ECoG$  array, we placed the  $\mu ECoG$  array on a 50  $\mu$ m-thick, mCherry-labelled, rat brain section. We inspected both the fluorescent and bright-field images from the same region of the brain section with and without the electrode array in place, as shown in Figure 33a-d. We analyzed the light intensities in an

arbitrary unit of the mCherry labeled cell bodies (in red dots) within and outside of the transparent microelectrode area. The transmittance rate of the transparent microelectrodes was derived by comparing the maximum light intensities of selected labeled cell bodies via Matlab to eliminate the interference of 10 µm Parylene C. The calculated transmittance rate of the transparent microelectrode area was above 95.7%, indicating the excellent fluorescent transparency of our PEDOT-ITO-Ag-ITO thin films. Also of note is the shadowing effect of the top Parylene C

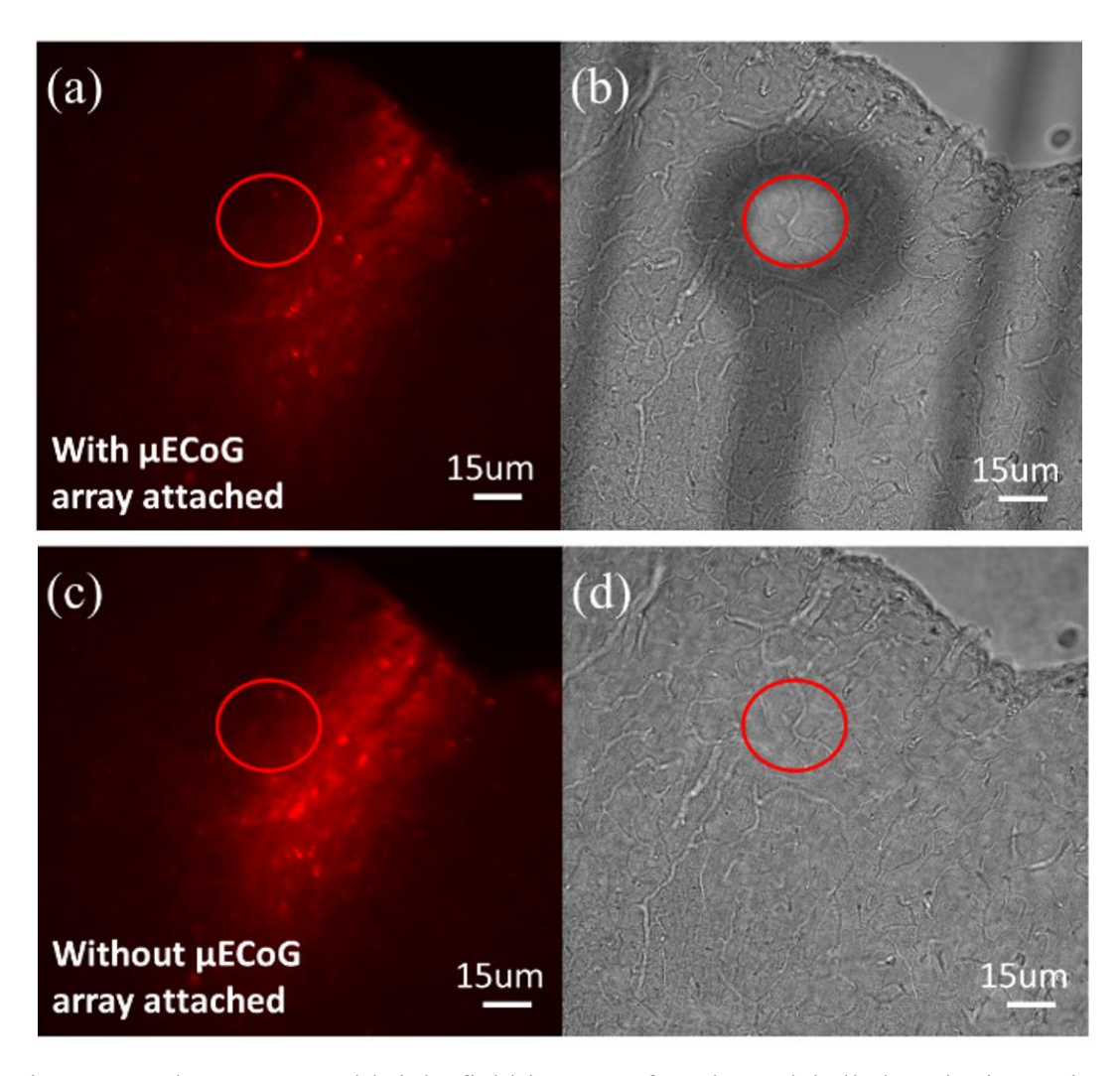


Figure 33. Fluorescent and bright-field images of mCherry-labelled rat brain section and in vivo recording results of light-evoked field potentials. Leica mCherry fluorescent images (a) (c) and bright-field images (b) (d) with and without the transparent  $\mu$ ECoG array attached on.

encapsulation over the electrode edge and trace areas under the bright field condition (Figure 33b), due to extra absorption and reflection at the top Parylene-ITO interface. This top encapsulation does not impact the transparency of the array under fluorescent imaging, as indicated in Figure 33a.

### 5.3.4 Signal to Noise Ratios (SNRs) Measurements

Increased noise and artifacts from the photoelectrochemical (PEC) effect, also known as the Becquerel effect, is a long-standing challenge for recording light-evoked neural activities in optogenetics. Therefore, we studied the effect of photon-induced artifacts on recording performance of the transparent μΕCoG electrode array. Figure 34a shows the SNRs of recordings, measured from the μΕCoG microelectrodes (n=10) in saline under room light as well as blue, green, yellow, and red LED light. For all the light conditions, the average SNRs ranged from ~35 dB to ~36 dB with variations of less than 2.7%, indicating that the PEDOT:PSS-ITO-Ag-ITO electrodes are quite resistant to photoelectrochemical artifacts. The maximum forward LED voltages applied to different color LEDs were adjusted to achieve consistent illumination. Figure 34b shows the corresponding optical powers of individual LEDs with forward voltages of V<sub>blue</sub>=3.3 V, V<sub>green</sub>=3.3 V, V<sub>yellow</sub>=1.8 V, and Vred=1.8 V, respectively, measured in the solution at a distance of 0.5 cm from the LEDs. The blue LED had the strongest optical power of 16.2 mW among all the LEDs at the high applied voltage of 3.3 V. Although the same high 3.3 V voltage

was applied on the green LED, the theoretical luminous efficacy of the green LED is much lower

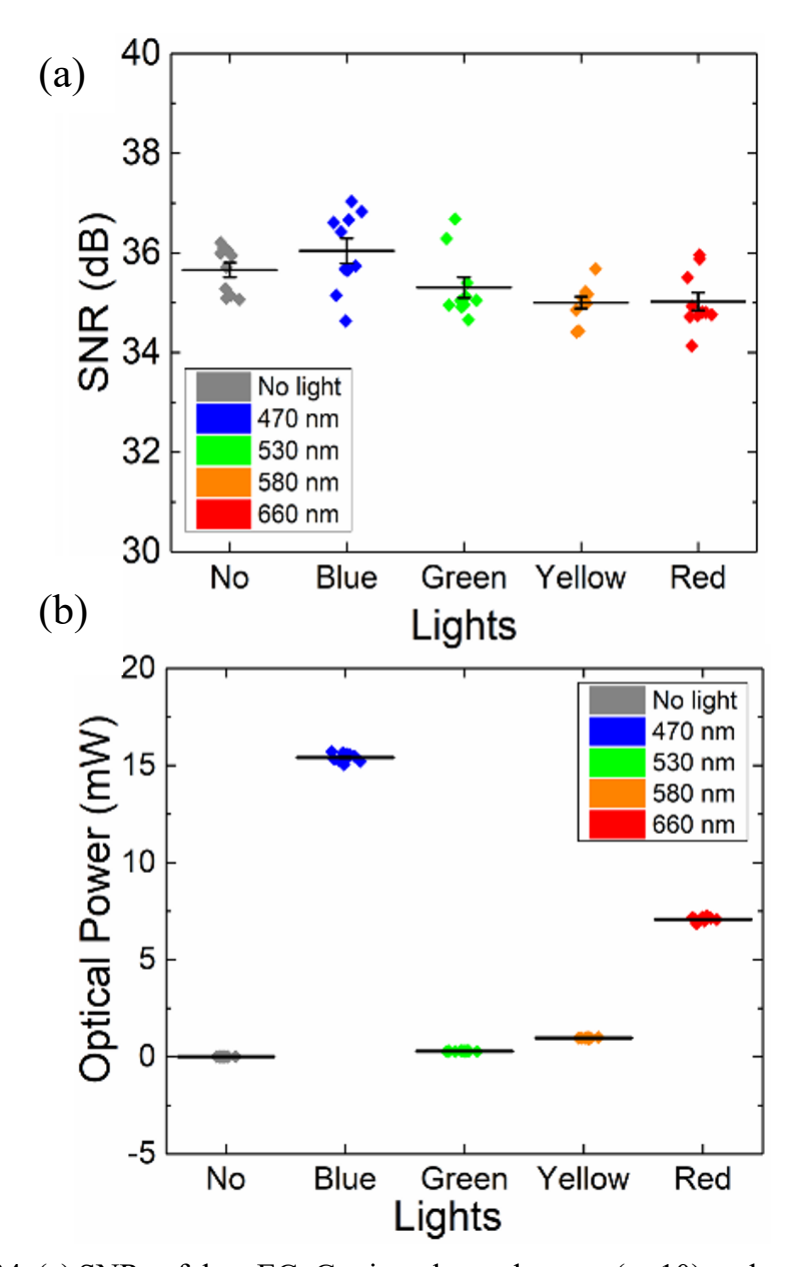


Figure 34. (a) SNRs of the  $\mu$ ECoG microelectrode array (n=10) under no light, ~470nm blue, ~530nm green, ~580nm yellow, and ~660nm red light illumination, respectively. (b) Optical powers of the blue LED (V=3.3V), green LED (V=3.3V), yellow LED (V=1.8V), and red LED (V=1.8V), respectively (n=10).

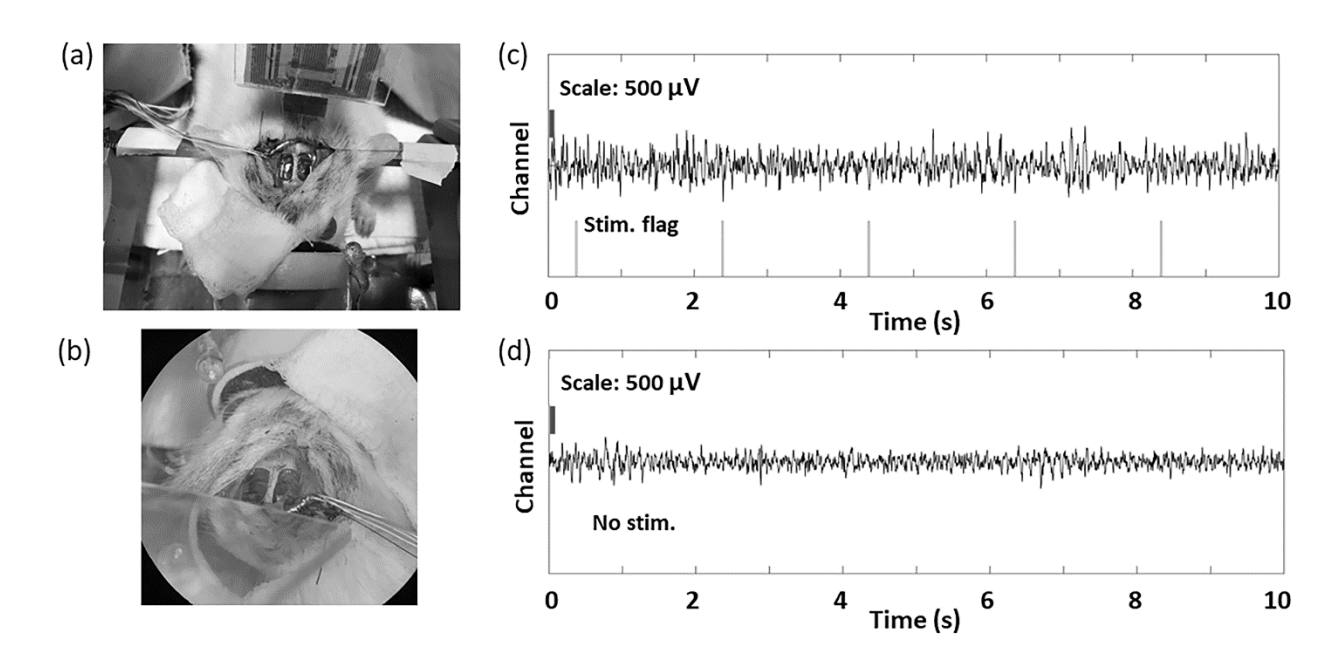


Figure 35. (a) (b) Images of the in vivo test with the first version of array design. In vivo test data of (c) (d) signal amplitudes with visual stimulation (up and left) and without visual stimulation (down and right).

than the blue one. While preliminary, these results show that optical stimulation with various light intensity and wavelengths would have minimal impact on the recording quality of our  $\mu ECoG$  microelectrodes.

#### 5.3.5 *In vivo* Animal Experiment

For the first version of the ECoG array, the animal experiment was conducted, and the two array panels were attached on both the left and right cortex. However, it was hard to adhere the whole 5 mm × 11 mm panel because of the area mismatch of the large microelectrode array panels and the rat's brain, as shown in Figure 35a and 35b. The poor adhesion caused the poor and low-resolution signal recording, as shown in Figure 35c and 35d. With the stimulation on, the recorded ECoG signals show significantly larger variations than the baseline, indicating that the optical stimulation

can efficiently evoke neural activity and our transparent microelectrode array can effectively record ECoG oscillations.

After reducing the dimension design of the array, the second *in vivo* acute animal experiments were conducted to evaluate the surgical and functionality of the devices on V1 of rats. During the *in vivo* experiments, the developed µECoG array was gently placed on both the left and right lobes of V1 (Figure 36). The left V1 was stimulated with the light stimuli under high or low intensity, while the right V1 served as a control. Light-evoked ECoG activities were recorded from both V1 lobes via the implanted microelectrodes, and the neural recordings were analyzed over a time span of 20s and compared with a baseline that was recorded when the LED stimulation was turned off. Figure 37 show that the ECoG activity evoked by the high-intensity stimulus had significantly larger energy variations compared to both the baseline and activity evoked by the low-intensity stimulus. Furthermore, Hilbert transformation was applied to extract the instantaneous phases of 150 trails of ECoG recordings within a frequency range of 1-25 Hz. As shown in Figure 38, the

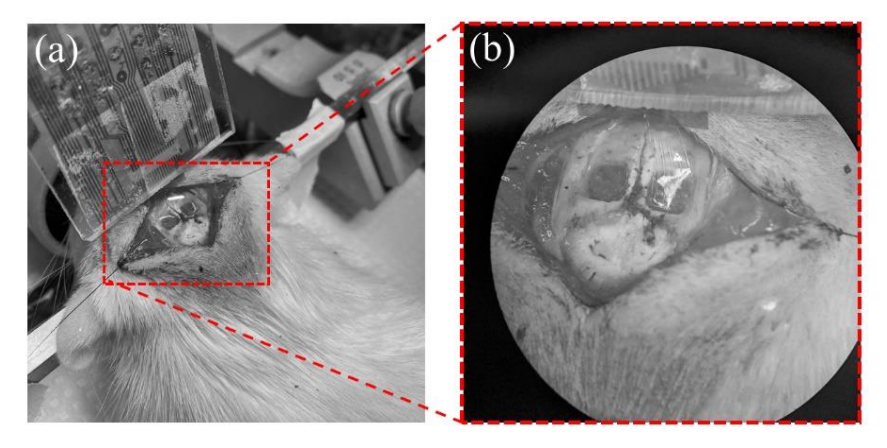


Figure 36. (a) Image of a transparent μECoG array placed on the brain tissue of the rat during the in vivo animal experiments. (b) Zoom-in microscope image shows the exposed brain tissue with the array attached.

150 trails are aligned to the concurrence of the stimulus and stacked, and the colors indicate the instantaneous phase of each trail. The baseline and control did not show significant phase synchrony, while strong and reliable phase-locked synchronization was observed across 150 trials of signals recorded with the high light stimulation. The instantaneous phase that resulted from the low-intensity stimulation showed only slight synchronization, as expected. Additionally, 150 trial ECoG recordings were averaged and mapped onto a time-frequency graph of color-coded, normalized power spectral density (PSD) distribution (Figure 39). A significant increase of PSD

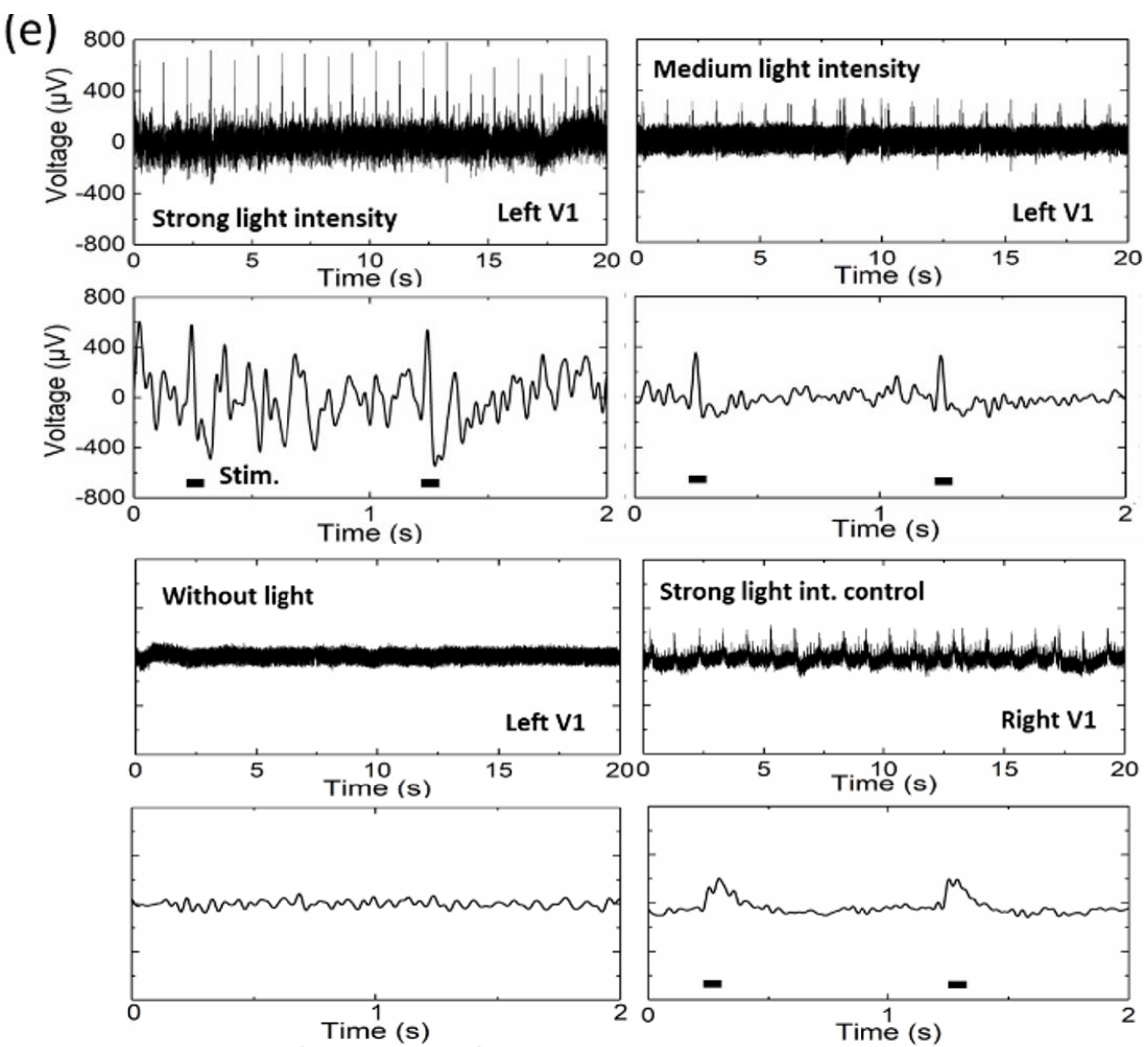


Figure 37. In vivo test data of e signal amplitudes of left and right V1 with the strong light stimulations, medium light stimulations, and without visual stimulation.

was observed in a short time window of ~200 ms following the light stimulation compared to the control baseline. Higher light intensity resulted in higher PSD compared to that seen with lower optical stimulation [318]. The control also showed increased PSD at the onset of high-intensity stimulation, which may have been caused by the electrical artifacts of the LED. These results suggest that the optical stimulation can effectively evoke neural activity and that our transparent microelectrode array can successfully record light-evoked ECoG oscillations.

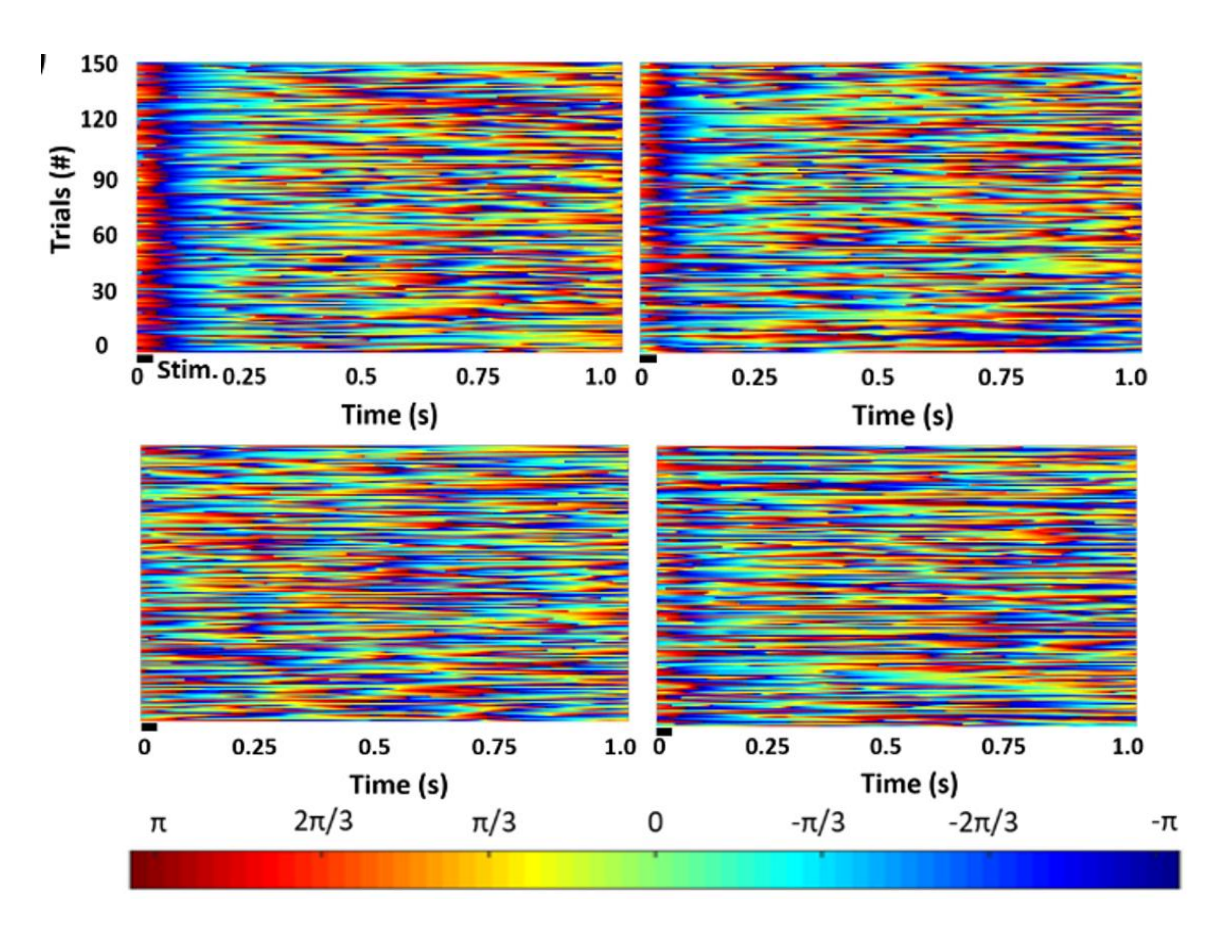


Figure 38. In vivo test data of instantaneous phases of left and right V1 with the strong light stimulations, medium light stimulations, and without visual stimulation.

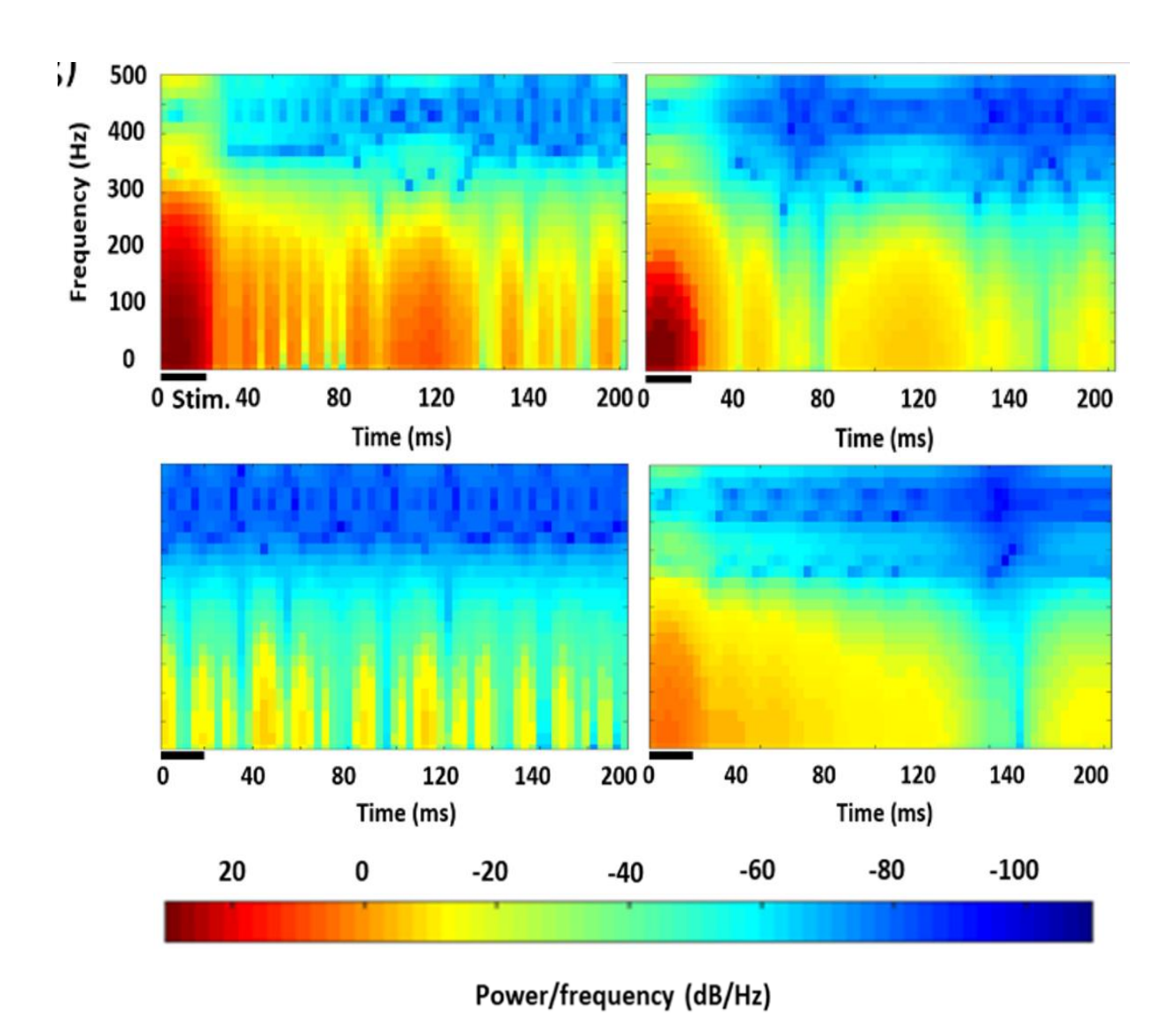


Figure 39. In vivo test data of g PSD spectrograms of left and right V1 with the strong light stimulations, medium light stimulations, and without visual stimulation.

### 5.4 Conclusion

In summary, a conductive, anti-reflective, transparent, and ultra-flexible  $\mu ECoG$  array using PEDOT:PSS-ITO-Ag-ITO multilayer thin films on Parylene C is demonstrated in this chapter. This PEDOT:PSS-ITO-Ag-ITO based  $\mu ECoG$  array exhibits significantly reduced sheet resistance, remarkable transmittance, good electrochemical impedance, increased charge storage capacity, excellent SNRs, and the capacity for *in vivo* ECoG recordings. Other recently reported

transparent ECoG arrays were compared with ours and a benchmark table was made, as shown in Table 4.

Moreover, SNRs were measured under various color LEDs, confirming the negligible photon-induced artifacts of recordings using the combined film. The optical transmittance of the transparent microelectrode array was further demonstrated under both fluorescent and bright-field illumination conditions. Finally, *in vivo* animal experiments validated the ability to use these transparent microelectrodes to record optogenetically evoked ECoG activity from the rat visual cortex.

It is worth noting that the Parylene C insulation greatly reduced the transparency of the μECoG device, particularly in the shorter wavelength range (i.e. blue light), due to the absorptive and reflective loss in Parylene layers. Future studies could fruitfully explore this issue by further Table 4 Benchmark table of transparent ECoG arrays

Materials	Transmission	1K kHz Impedance $(\Omega \text{ cm}^2)$	Ref.
Silver nanowires + indium-doped zinc oxide (IZO)	~73.8%	~45.16	47
Gold nanonetwork	87%	~18.60	48
ITO	> 80%	~65.21	16
PEDOT:PSS- Graphene	<50%	~0.21-~0.3	42,43
Carbon nanotube	> 85%	~20	49
Graphene	>90%	~22.49	22
Gold nanomesh	>70%	~8.14	17
PEDOT:PSS-ITO- Ag-ITO	89%	~0.81	Our work

analyzing and refining the dimension design of each layer to make the whole  $\mu ECoG$  device more transparent over a broad spectrum. In addition, fabricating anti-reflective moth-eye nanostructure at the backside of Parylene C could be considered to further improve the transmittance of ECoG arrays [319], as well as perform a better antibacterial effect [320]. Instead of increasing deposition temperature, the quality of the room temperature ITO could be improved with other methods, such as ion source assisted sputtering [321], which not only improves the electrical and optical properties of the ITO film but also enhances the film stability due to increased density with fewer pinholes. An alternative approach to improve the ITO film quality is low-temperature plasma annealing [302], which has been shown to enable relatively low resistivity (2.5x10<sup>-3</sup>  $\Omega$ ·cm) and high optical transmission (94%) while allowing multiple wafer processing in parallel.

Based on previous chapters, this chapter is focused on proposed future work. One is to explore the transparent  $\mu ECoG$  array with higher spatial resolution (120 channels), and the other is characterizing the potential of utilizing ITO-based electrochemical sensors for Cu and Mn ions detection.

For our previous research, we concentrated on designing antireflective, peak-transmittance-tunable, transparent PEDOT:PSS-ITO-Ag-ITO thin films and then applied this multilayered structure in the 32-channel μECoG array followed by showing the efficacy of this transparent microelectrode array. However, the diameters of those microelectrodes are ranging from 25 μm to 100 μm with the separation ~500 μm. The mismatch size of the microelectrode with the neurons could collect more surrounding neuron signals around the targeted neurons, thereby reducing the specificity of targeted neuron extracellular electrophysiology recording. Therefore, for future studies, a high spatial resolution transparent μECoG array was designed with 120 microelectrode channels and an associated 120-channel data collecting system.

The other direction is to explore the potential of utilizing ITO-based electrochemical sensors for Cu and Mn ions detection. ITO has been widely used in spectroelectrochemistry as a WE material because of its excellent conductivity and good optical transparency. In addition, ITO has a large potential window and are capable of measurements beyond +1.5 V, making it appropriate as a WE material for voltametric methods. Therefore, this subsection is focused on fabricating and

characterizing an ITO-based electrochemical sensors for Cu and Mn ions detection in bodies and the soil environment.

- 6.1 120-channel Transparent µECoG Array
- 6.1.1 Transparent µECoG Array Design

### 6.1.1.1 Mask Designs

A 120-channel transparent  $\mu$ ECoG array was designed and the masks are shown in Figure 40. The  $\mu$ ECoG electrode array was designed with dimensions of 34 mm  $\times$  24.4 mm, with a single 2.6 mm  $\times$  2 mm panel to cover one side of hemispheres of the primary visual cortex (V1). Because it is hard to design 120 interconnections on single layer, 120 microelectrodes and interconnections were split on 2 layers, for each layer with 60 channels. 2  $\mu$ m Parylene C, as an insulating layer, separated those 2 layers. The single panel consisted of the total 120 microelectrodes with the surface area of 25  $\times$  25  $\mu$ m<sup>2</sup> and a separation distance of 200  $\mu$ m.

#### 6.1.1.2 Fabrication Procedures

First, 10 µm Parylene C is deposited on a cleaned 3-inch silicon wafer by CVD. Next, a photoresist (PR) layer is spun on the substrate and photolithographically patterned to expose the areas of the first layer of microelectrodes, interconnection wires, and contact pads. Then, similarly, ITO-Ag-ITO is sputtered using the above magnetron sputtering system via the same recipe. With the PR mask, ITO-Ag-ITO on the undesired areas was washed off with acetone at room

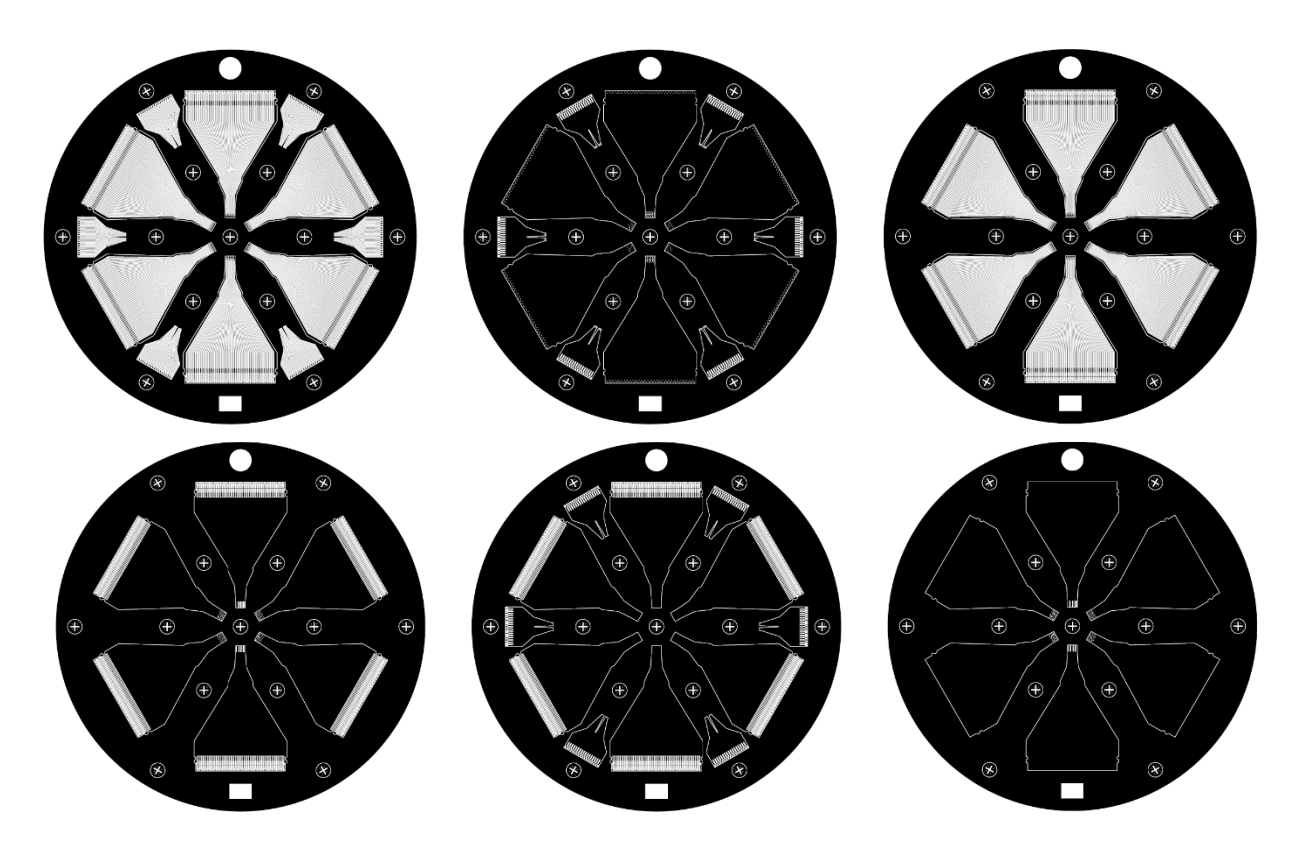


Figure 40. Six photolithography masks for fabricating 120-channel transparent microelectrodes array for neurophysiology recording with PEDOT:PSS-ITO-Ag-ITO multilayer structure.

temperature and the surface was cleaned with IPA and DI water, leaving the ITO-Ag-ITO on the electrode sites, contact pads, and interconnect wires. Next, 2 µm Parylene C was deposited on the substrate as an insulating layer, and then Parylene C on the microelectrodes and contact pads were removed completely using oxygen plasma dry etching method (RIE-1701 plasma system, Nordson March, Inc). Next, another PR layer is spun on followed by the photolithography to expose the areas of the second layer of microelectrodes, interconnection wires, and contact pads. Then, the second layer of ITO-Ag-ITO was deposited by utilizing the above method with the thickness of each layer. Later, the PR was washed off with acetone and the whole wafer is rinsed next with IPA and DI water. Afterwards, another layer of 2 µm Parylene C was deposited on the wafer as an

insulating layer, following by the oxygen plasma dry etching to get rid of the Parylene C on the contact pads and microelectrodes. After that, 500 nm copper was sputtered and patterned only on the contact pad with a sacrificial PR mask. Then, PR was rinsed off with acetone, IPA and DI water for copper lift off. Next, another PR mask was patterned to expose only the microelectrode sites followed by spin coating of diluted 0.55% PEDOT:PSS using the above recipe. Finally, PR was rinsed off with acetone, IPA, and DI water to remove unwanted PEDOT:PSS, leaving PEDOT:PSS only on top of the ITO-Ag-ITO microelectrodes. Instead of using plasma etching, the outer shape of the array was manually cut according to the defined outlines that was initially designed on masks to prevent the damage of the ITO from plasma over-etching.

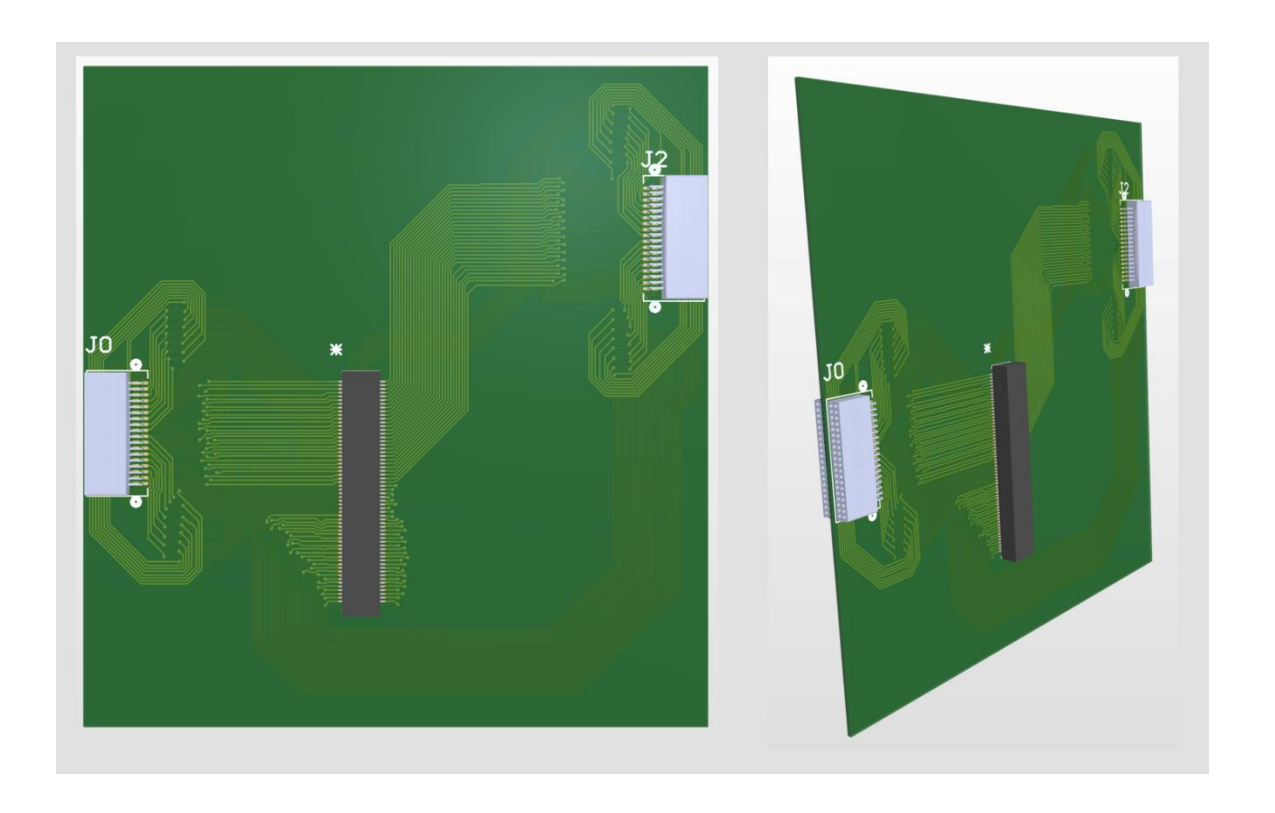


Figure 41. 3D view of design PCB interface for connecting the 120-channel microelectrode array and Intan recording headstages with Altium Designer.

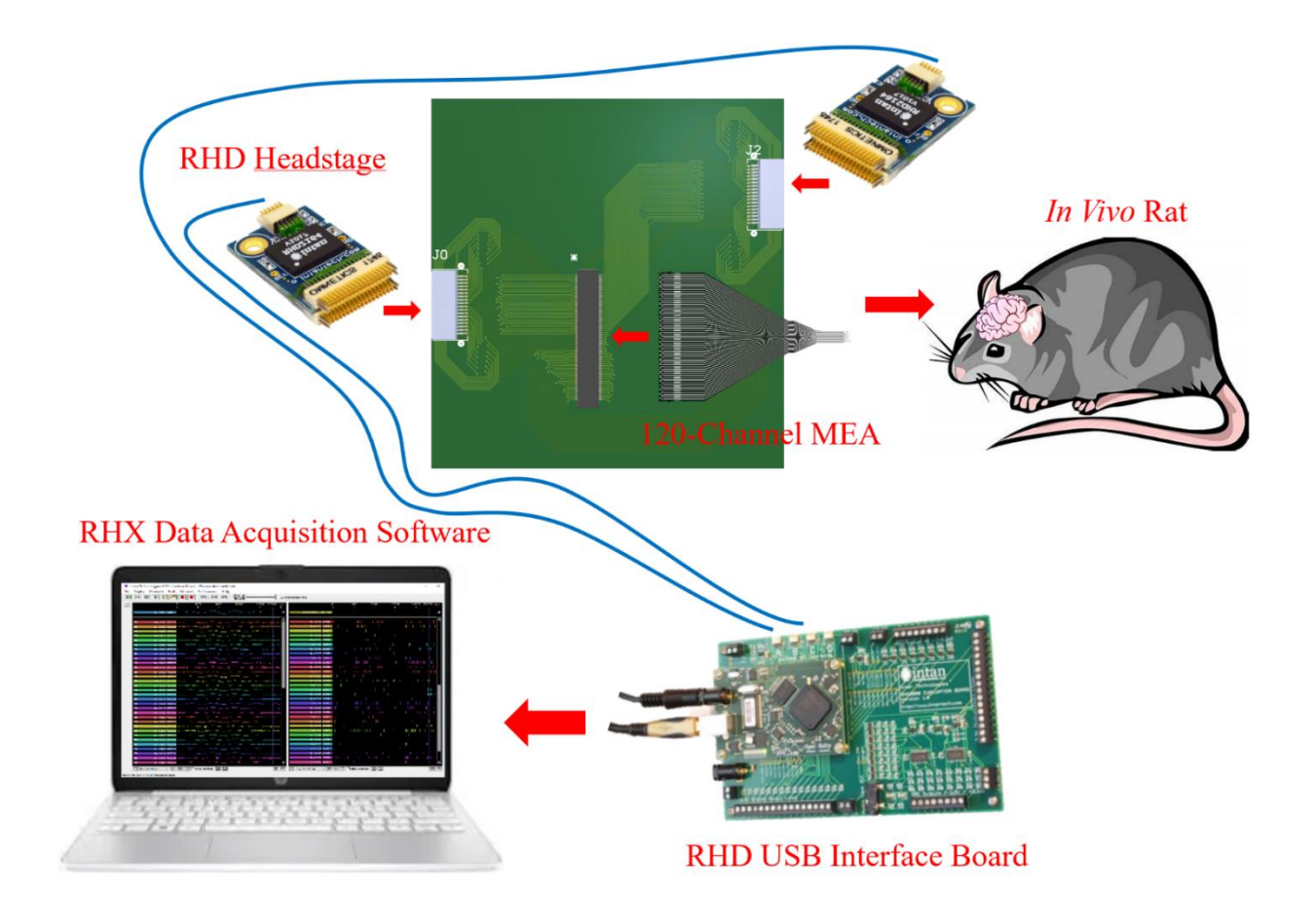


Figure 42. Concept diagram of 120-channel neuro-electrophysiology recording system for in vivo animal experiment.

### 6.1.2 Connection Part

# 6.1.2.1 PCB Design

A printed circuit board (PCB) interface was designed for connecting the microfabricated 120-channel ECoG array and RHD headstages (C3315, Intan Technologies Inc.), as shown in Figure 41. The four 36-position dual row male nano-miniature connectors (NPD-36-AA-GS, Omnetics Connector Corporation Inc.) were designed in pairs at the double sides on the edges of the PCB for two 64-channel RHD recording headstages to be convenient to be plugged in. A 120-position

ZIF connector (FH29B-120S-0.2SHW(05), Hirose Electric CO., LTD) is placed for connecting to the high spatial resolution ECoG array and wiring out to the recording headstages.

### 6.1.2.2 Recording System Setup

The whole 120-channel recording system was well designed and set up, as shown in Figure 42. When conducting the neurophysiology recording, the 120-channel µECoG array is inserted into the ZIF connector while keeping the good connection between the contact pads of connector and array. Next, two RHD recording headstages should be plugged carefully in the female connectors. Four RHD standard SPI interface cables are connecting to the RH USB interface board (C3100, Intan Technologies Inc.). The interface board is powered up and connected to the laptop. RHX data acquisition software is utilized to display and record electrophysiological signals. Then, the data can be analyzed using the Matlab Chronux toolbox to extract the activation energy, phase synchrony, PSD distribution from the recordings. The universal Intan software also can be utilized to plot the signals, probe map, and the spectrogram as well as spike sorting.

6.2 A Transparent and Miniaturized ITO-based Electrochemical Sensor for Continuous and Quantitative Monitoring of the Concentrations of Copper (Cu) and Manganese (Mn) Ions in Bodies and Soil Environment

#### 6.2.1 Introduction

Prion diseases are caused by abnormal folding of proteins and can cause asymptotic neurological changes and death [322]. The most typical prion disease that everyone is familiar with is the mad cow disease, also called bovine spongelike encephalitis (BSE) in cattle. For the case of human prion disease, in the 1980s and 1990s, more than 4 million cattle were slaughtered in the UK to this disease, and 177 people died from eating tainted beef with variant Creutzfeldt-Jakob disease (CJD), which sponges out the brain and causes it to lose function [323]. Lowering copper levels in the body can delay the onset of the disease [324]–[326]. Researchers at the Scripps Research Institute found that mice lacking a gene that encodes a copper transporter protein survived significantly longer when infected with prion disease than normal mice [327], [328]. Another metal, Manganese has been found that could replace the copper, turning normal prions into alloforms, that cannot be broke down by proteases [329]. Prion proteins associated with BSE can combine with manganese in feed to form pathogenic prions, and manganese levels in the brains of patients with CJD are 10 times higher than those in the normal brain [330]–[332]. Therefore, it is important to detect the copper and manganese levels in the human bodies and animals to prevent and postpone the prion diseases.

In recent years, with the rapid development of electroplating, chemical industry, mining and other industries, heavy metal pollution in the environment is increasing day by day. The copper and manganese ions have exceeded several times or even dozens of times of the soil background value [333]. This has been far beyond the endurance of the soil environment, which not only poses a threat to plants, animals, and microorganisms in the soil, but also poses a certain threat to the stability of the entire ecosystem and the safety of human beings. As is known to all, copper and manganese is a necessary trace element for the growth and development of animals. Excessive intake of Cu<sup>2+</sup> and Mn<sup>2+</sup> will cause certain harm to animals. The harm of Cu<sup>2+</sup> and Mn<sup>2+</sup> to an animal is mainly through the food chain into humans and animals [334]. When the body Cu content is too high, it is easy to cause harm to the organs and also facilitate the prion diseases [334]. Therefore, it is also significant to detect the Cu<sup>2+</sup> and Mn<sup>2+</sup> levels in the soil environment to tackle the root of the problem.

The task aims of this project are to develop a miniaturized electrochemical sensor for continuous and quantitative monitoring of the concentrations of Cu and Mn ions in bodies and the soil environment with high sensitivity and accuracy. In addition, the detecting and cleaning methods and recipes are well manipulated for achieving the repeatability of the sensors. Our research was focused on transparent ITO materials. ITO has been widely used in spectroelectrochemistry as a WE material because of its excellent conductivity and good optical transparency. In addition, ITO has a large potential window and are capable of taking measurements beyond +1.5 V, making it appropriate as a WE material for voltametric methods. BDD material was also used to study the

sensitivity of the devices to Cu and Mn ions when various materials are used for the electrodes.

SEM and EDS were done to find the surface changes before and after the ion detection.

#### 6.2.2 Materials and Methods

#### 6.2.2.1 Fabrication of Transparent ITO sensors

As shown in Figure 43a, the electrochemical sensor consisted of a circular working WE and a surrounding CE on a flexible and transparent polymer PET substrate. Two different conducting materials including ITO and BDD were utilized as the electrode materials in sensor fabrication. To fabricate the device, ITO or BDD were deposited on the polymer substrate and photolithography-patterned to form the WE and CE. Then another 2 µm paylene C as insulator was deposited and oxygen plasma etching was processed after the photolithography for exposing the electrode pattern areas. During the cleanroom procedures, 12 sizes WE were fabricated with the diameters scaled down from 4.5 mm to 0.0556 mm, as shown in Figure 44. After the initial

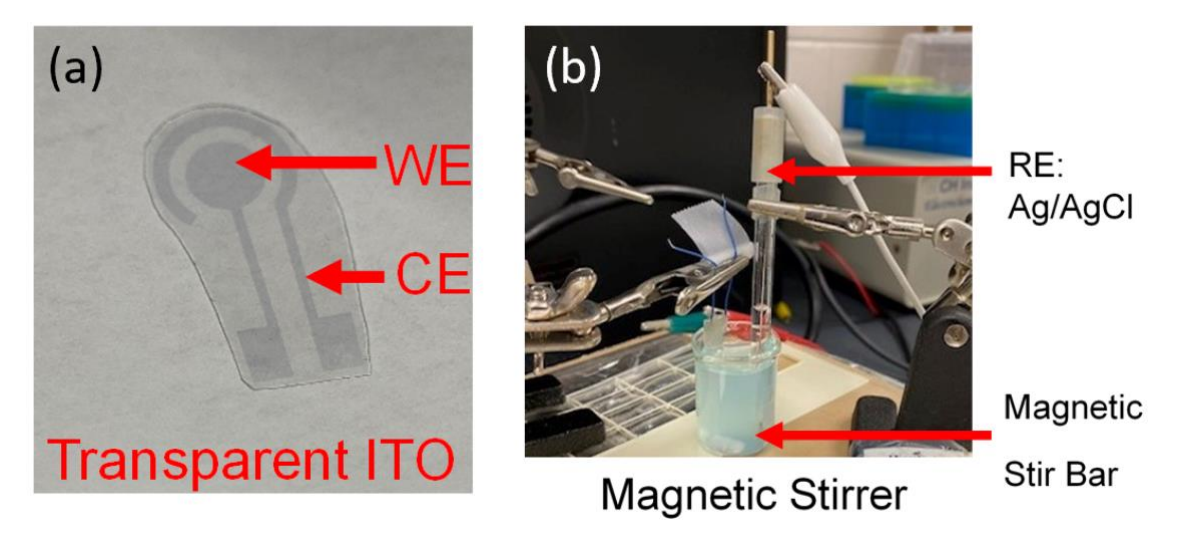


Figure 43. (a) Single ITO electrochemical sensor design with WE and CE. (b) Test setup with Ag/AgCl RE and magnetic stir bar at the bottom of the beaker.

tests with 12 different WE areas, two different device sizes were narrowed down with the WE diameters of 1mm and 0.125mm, considering the tradeoffs between miniaturization and sensing performance. After each sensor was trimmed individually, wires connected to the test instrument were soldered onto the contact pads of the sensor using low-temperature silver pastes.

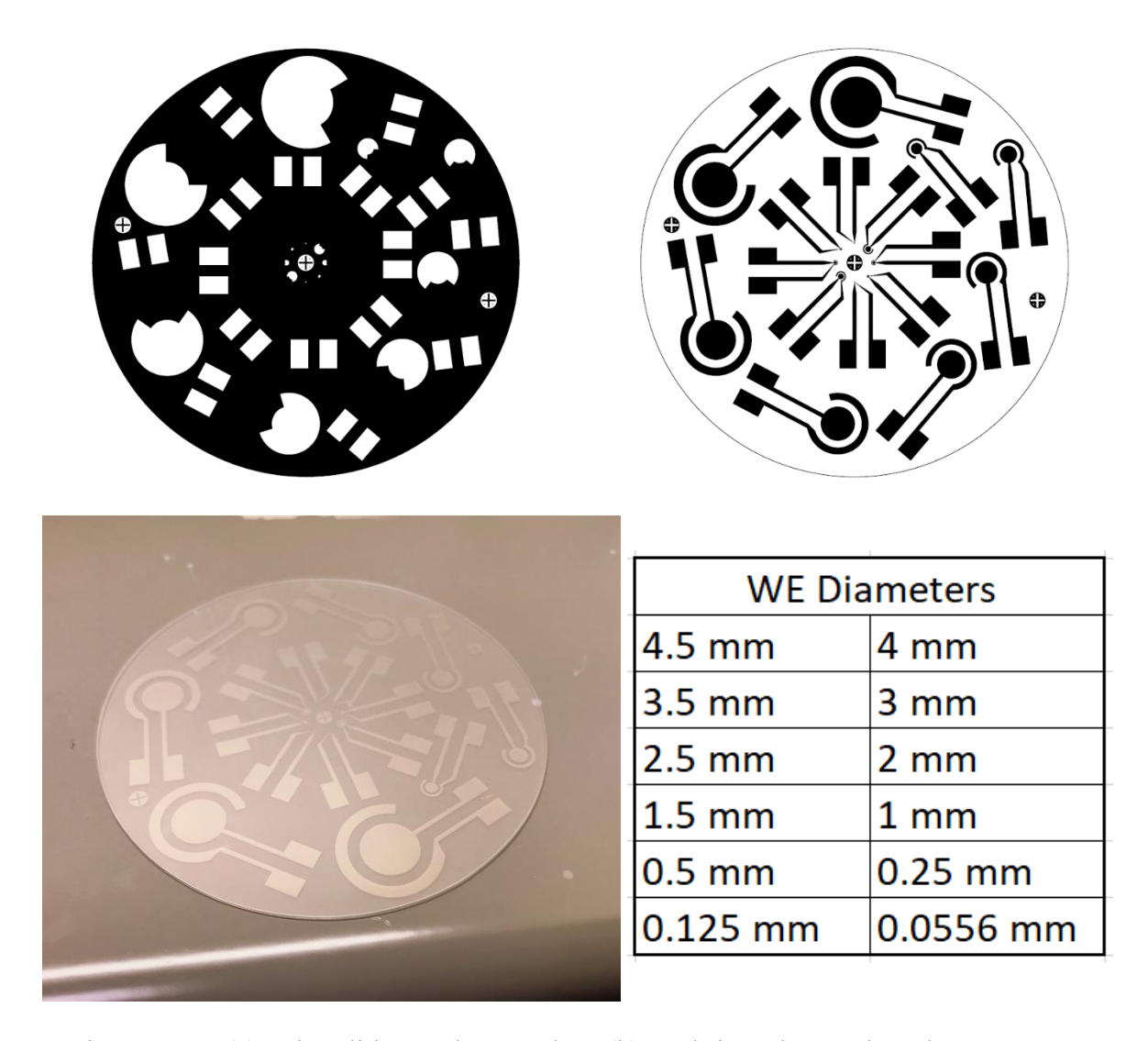


Figure 44. (a) Photolithography masks. (b) Fabricated ITO-based transparent electrochemical sensors. (c) Various WE diameters on the wafer.

### 6.2.2.2 Testing Methods

#### 6.2.2.2.1 Test Setup

A three-cell differential pulse stripping voltammetry (DPSV) was chosen to detect different concentrations of the ions due to the high sensitivity and accuracy of this scanning method, as shown in Figure 43b. An Ag/AgCl electrode served as the RE. A potentiostat (CH Instrument 620A) was used to connect the WE, CE and RE respectively with green cable, red and white cable. During the measurements, electrochemical sensors and RE were immersed in the Cu or Mn solutions. A magnetic stir bar was placed at the bottom of the beaker to well mix the solutions during the deposition steps. The whole experiment setup was placed on a magnetic stirrer.

# 6.2.2.2.2 Cu and Mn Ions Solutions Preparation

For initial studies, simulated solutions were prepared by mixing different concentrations of CuCl<sub>2</sub> and MnCl<sub>2</sub> powder in the Dulbecco's phosphate-buffered saline (DPBS), mimicking the human body environment. For CuCl<sub>2</sub> and MnCl<sub>2</sub> solutions, low concentration and high concentration groups were separated to clearly study the detection window and sensitivity of these electrochemical sensors. For the low concentration (LC) group of Cu<sup>2+</sup>, solution concentrations are 0, 500 nM, 1  $\mu$ M, 50  $\mu$ M, and 100  $\mu$ M, respectively. For the high concentration (HC) group of Cu<sup>2+</sup>, we have solution concentrations of 0, 500  $\mu$ M, 1 mM, 2.5 mM, and 5 mM. For the Mn<sup>2+</sup>, we have 0, 1  $\mu$ M, 10  $\mu$ M, 50  $\mu$ M, and 100  $\mu$ M for the low concentrations while the high concentrations are 0, 500  $\mu$ M, 1 mM, 2.5 mM, and 5 mM.

# 6.2.2.2.3 Testing and Cleaning Recipes

During the experiment, the CuCl<sub>2</sub> and MnCl<sub>2</sub> solutions were kept at room temperature and agitated using a magnetic stirrer. The DPSV scan for Cu<sup>2+</sup> started with a deposition cycle at -1V followed by a 5 secs equilibrium cycle with a scanning range of -1V to 0.5V. For Mn ions, the deposition was done at 1.2V and the equilibrium cycle was 5 secs from 1.2V to -1V. The deposition duration of the DPSV scan was adjusted to achieve the best sensitivity and repeatability. Particularly, for Cu<sup>2+</sup>, the deposition duration was 90 secs at -1V for the low concentration range (500nM-100µM) and 60 secs at -1V for the high concentration range (500µM-5mM). For MnCl<sub>2</sub>, the deposition duration was 15 secs at 1.2V for both the low concentration and high concentration groups. Between each measurement, the electrode surface was cleaned by holding the WE at 0.3V and -0.3V for 30 secs for Cu<sup>2+</sup> and Mn<sup>2+</sup>, respectively, for removing any deposit from previous measurements. For the experiment, we put the single sensor in the same concentration of Cu or Mn solutions for at least 10-time measurements to check the repeatability of our electrochemical sensors. The single sensor was also utilized to measure the peaks when the concentrations of the solution increases. After each test, we used the cleaning recipe to eliminate the ions on the WE surface and made the sensor ready for the next measurement.

#### 6.2.3 Results and Discussion

### 6.2.3.1 Cu / Mn Ions

For the sensors made of ITO, DPSV signals at each concentration of Mn<sup>2+</sup> were clearly distinguishable from the baseline and from each other, as shown in Figure 46. However, the ITO

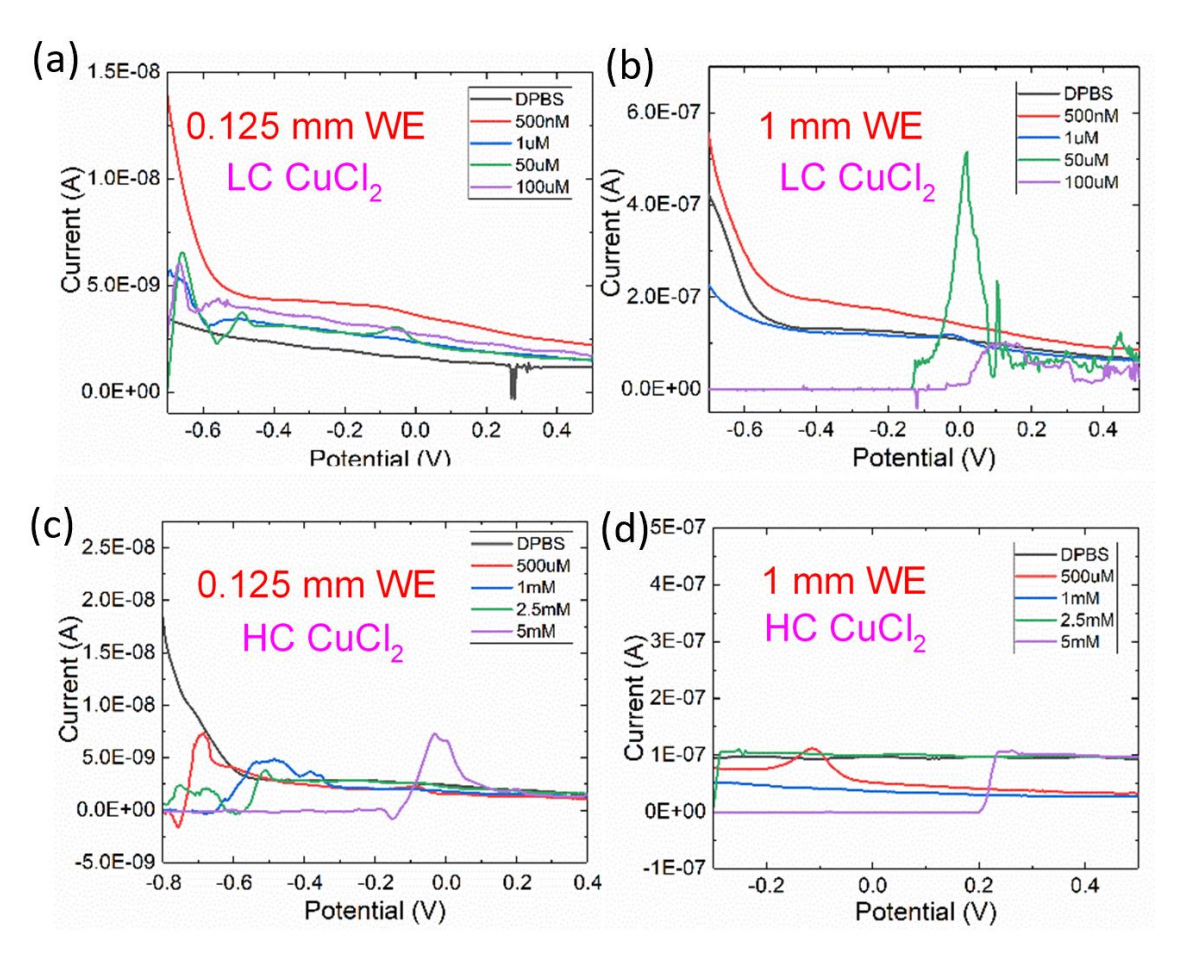


Figure 45. (a) (b) (c) (d) DPSV of low concentration (LC) CuCl<sub>2</sub> and high concentration (HC) CuCl<sub>2</sub> with 0.125mm diameter and 1mm diameter WE.

sensors were insensitive to  $Cu^{2+}$  as evident in Figure 45. In Figure 45a, the only peak we observed was under 50  $\mu$ M. It is because that the concentrations of 500 nM and 1  $\mu$ M were too low for the 0.125 mm WE to detect  $Cu^{2+}$ , while 100  $\mu$ M concentration was too high and caused too much absorption of  $Cu^{2+}$  that damaged the ITO WE. In Figure 45c, the concentrations of 500  $\mu$ m - 5 mM were all too high and the severe absorption caused the irregular shape and the shift of peaks. Similar to the 1 mm WE, the valid peak detected under LC of  $Cu^{2+}$  was 1  $\mu$ M. The concentration of 500 nM was too low for the 1 mm WE to detect  $Cu^{2+}$ , while 50  $\mu$ M and 100  $\mu$ M concentration was too high and caused too much absorption of  $Cu^{2+}$  that damaged the ITO WE. ITO

electrochemical sensors showed excellent sensitivity to  $Mn^{2+}$  compared to  $Cu^{2+}$ . Figure 46e, f showed smooth and clear peaks for both 0.125 mm and 1 mm WE under both LC and HC MnCl<sub>2</sub> solutions. According to the results of Figure 46f and 46g, the higher concentrations of the  $Mn^{2+}$  in the solution, the sharper the peak obtained, and the absolute magnitude was larger. However, in Figure 46e and 46h, under some concentrations, as the concentration increased, the peak magnitude decreased which we attribute to the absorption of the ions accumulated on the WE surface. For 0.125 mm WE, the magnitude decreased when the concentrate rises to 100  $\mu$ M. For the 1 mm WE, the magnitude decreased when the concentration changed from 500  $\mu$ M to 1 mM.

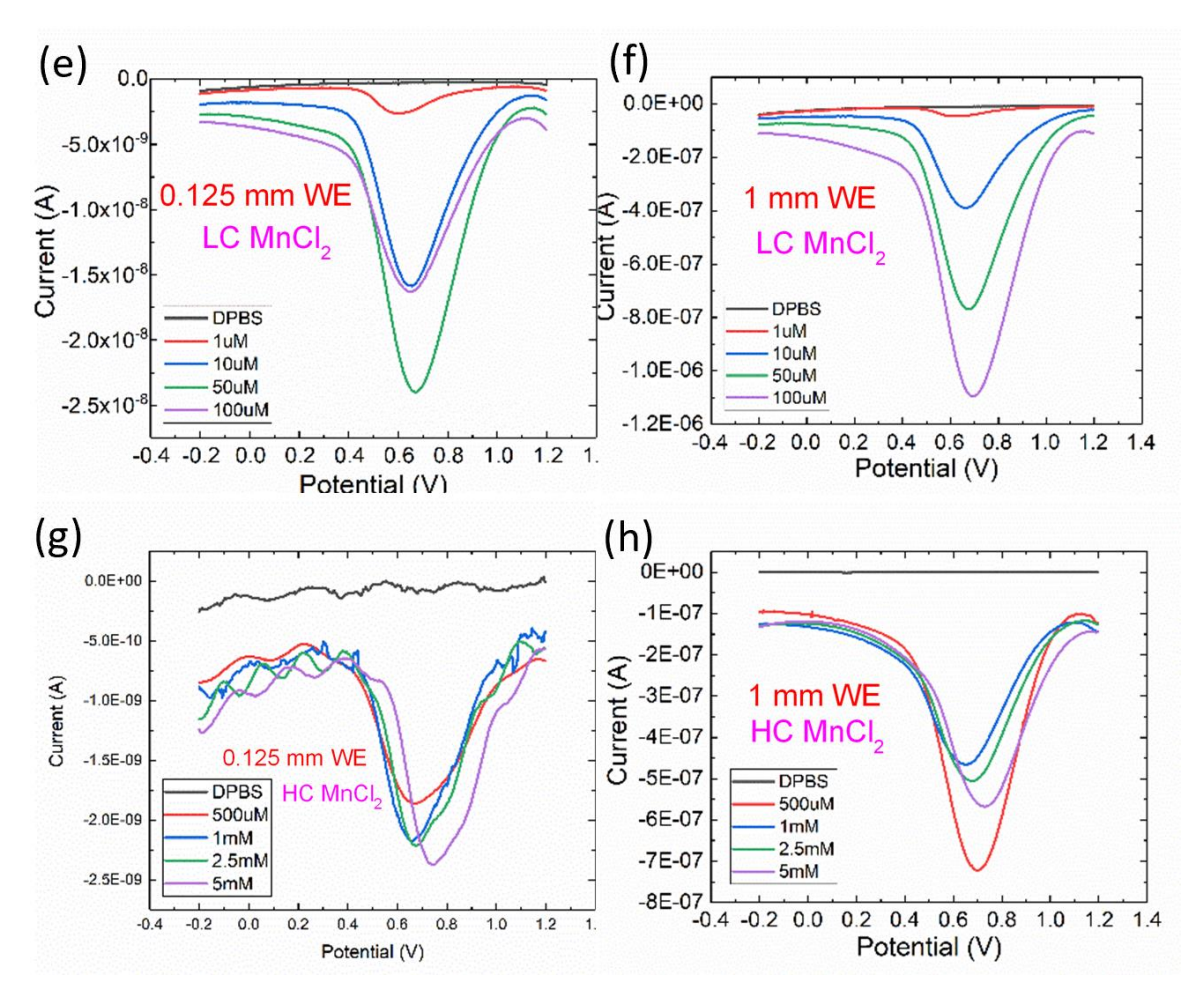


Figure 46. (e) (f) (g) (h) DPSV of low concentration (LC) MnCl<sub>2</sub> and high concentration (HC) MnCl<sub>2</sub> with 0.125mm diameter and 1mm diameter WE.

# 6.2.3.2 Linearity and Repeatability

To evaluate the reliability and repeatability of the ITO sensor, we repeated the DPSV scan for at least 10 times, using the 0.125mm and 1 mm WE sensor in  $Mn^{2+}$  solutions from  $1\mu M$  to  $100\mu M$ . The results in Figure 49a show that the DPSV signals detected from the low concentration solutions when using 0.125 mm WE did not exhibit significant difference (STDs < 5%) while the variation increased to 7.2% as the concentration increased to  $100\,\mu M$ , mainly due to the absorption

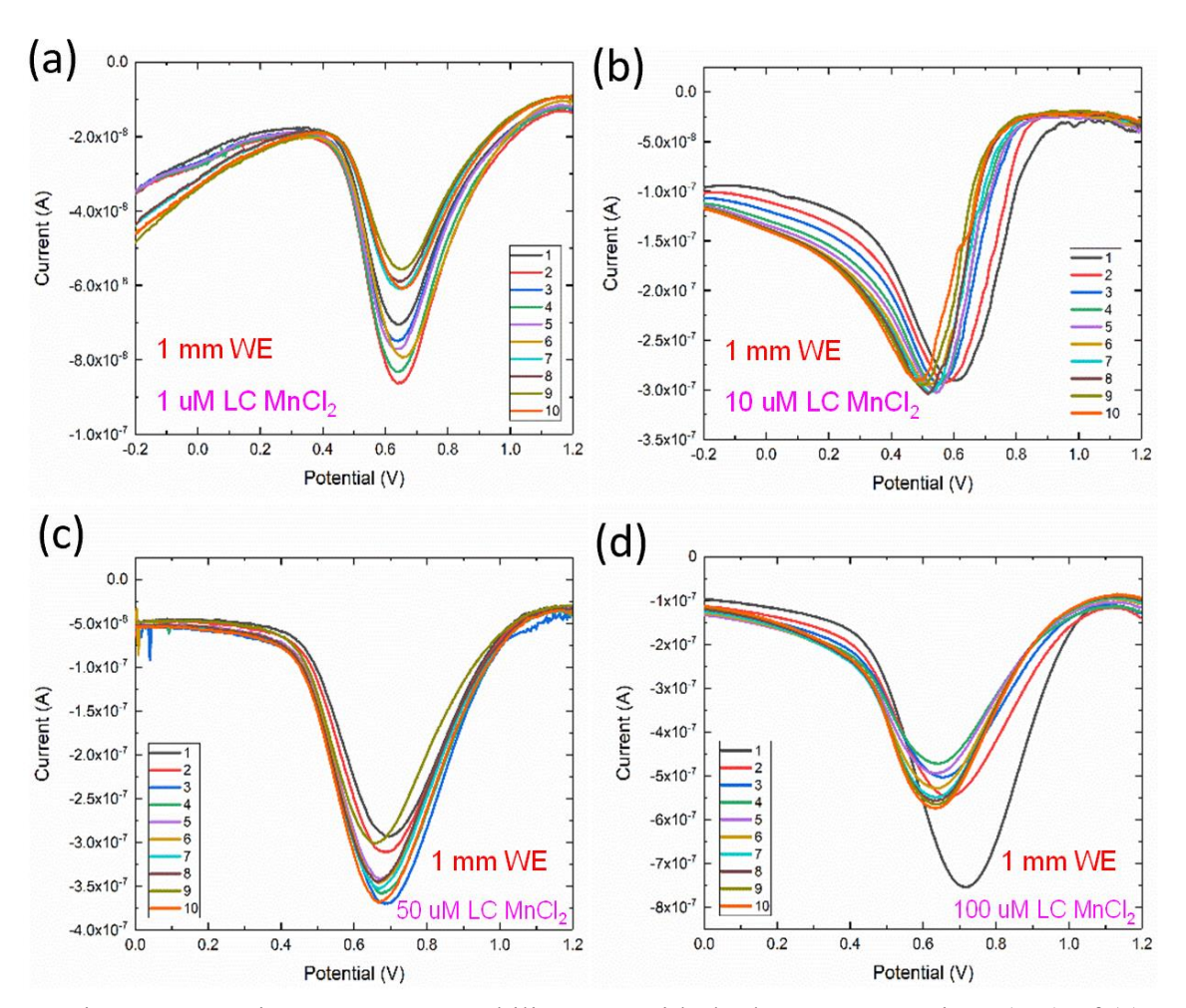


Figure 47. 10-time DPSV repeatability tests with the low concentrations (LC) of (a) 1  $\mu$ M, (b) 10  $\mu$ M, (c) 50  $\mu$ M, and (d) 100  $\mu$ M MnCl<sub>2</sub> with 1mm diameter WE. After each DPSV, a cleaning procedure was processed before the next time DPSV.

of chemicals on the electrode surface. The DPSV signals from 10 measurements were averaged and fitted to a linear curve as shown in Figure 49c for 0.125 mm WE. The sensor exhibited a good linear response with correlation coefficient,  $R^2 \approx 0.89$ . The results in Figure 47 and Figure 48 show that the DPSV signals of 1 mm WE have less repeatability and stability compared to the 0.125 mm WE. The magnitudes showed the more obvious fluctuation. Therefore, the results indicate that with smaller WE and lower concentration of MnCl<sub>2</sub>, the sensors have higher repeatability and

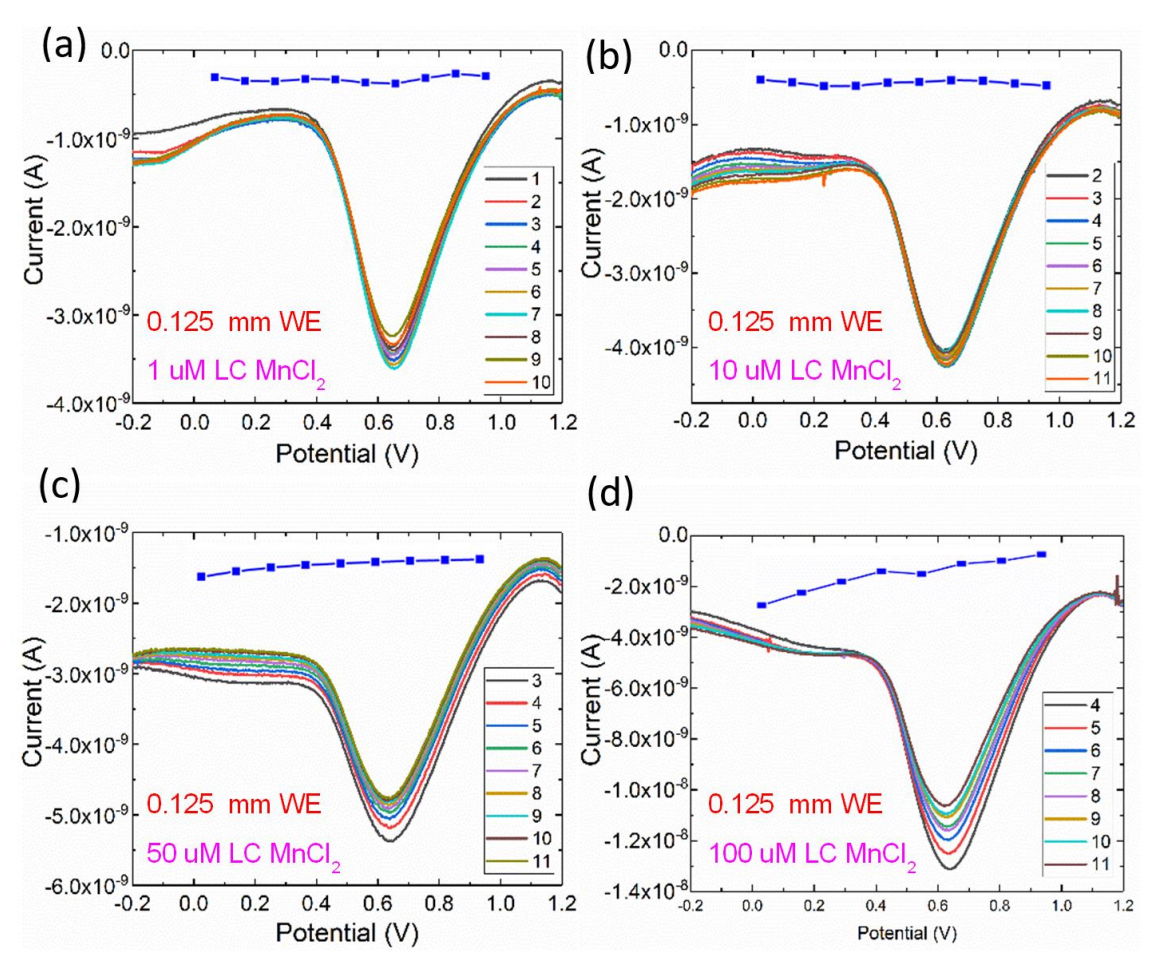
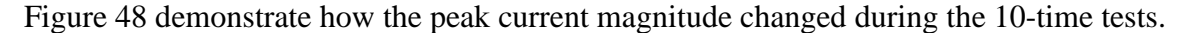


Figure 48. 10-time DPSV repeatability tests with the low concentrations (LC) of (a) 1  $\mu$ M, (b) 10  $\mu$ M, (c) 50  $\mu$ M, and (d) 100  $\mu$ M MnCl<sub>2</sub> with 0.125 mm diameter WE. After each DPSV, a cleaning procedure was processed before the next time DPSV. Blue lines show each time the peak current magnitude and the trend during the 10-time DPSV repeatability tests.

stability compared to the larger WE and higher solution concentration. The blue lines shown in



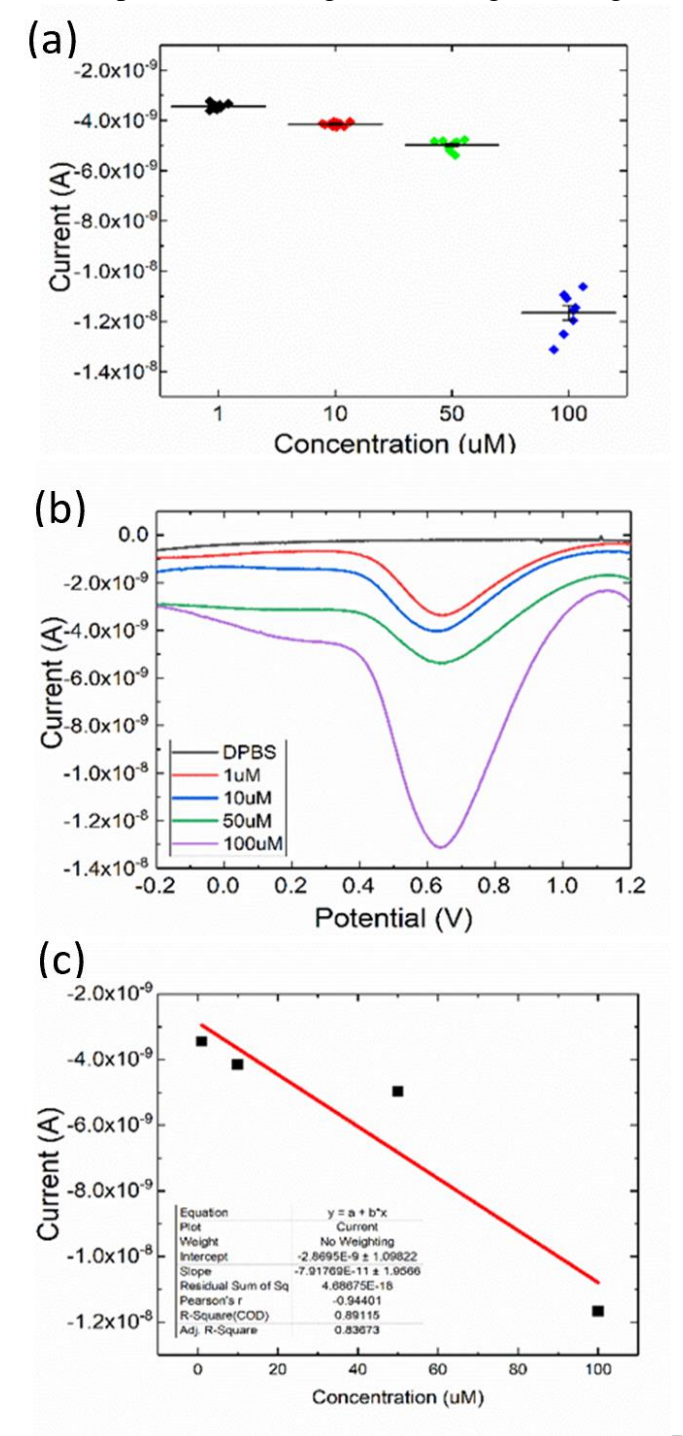


Figure 49. (a) Peak current magnitudes and standard deviations (STDs) of 0.125 mm diameter WE under different MnCl<sub>2</sub> concentrations. (b) DPSV of single use 0.125 mm diameter WE sensors for each concentration. (c)Linear fitting of the peak current magnitudes under different concentrations with 0.125 mm diameter.

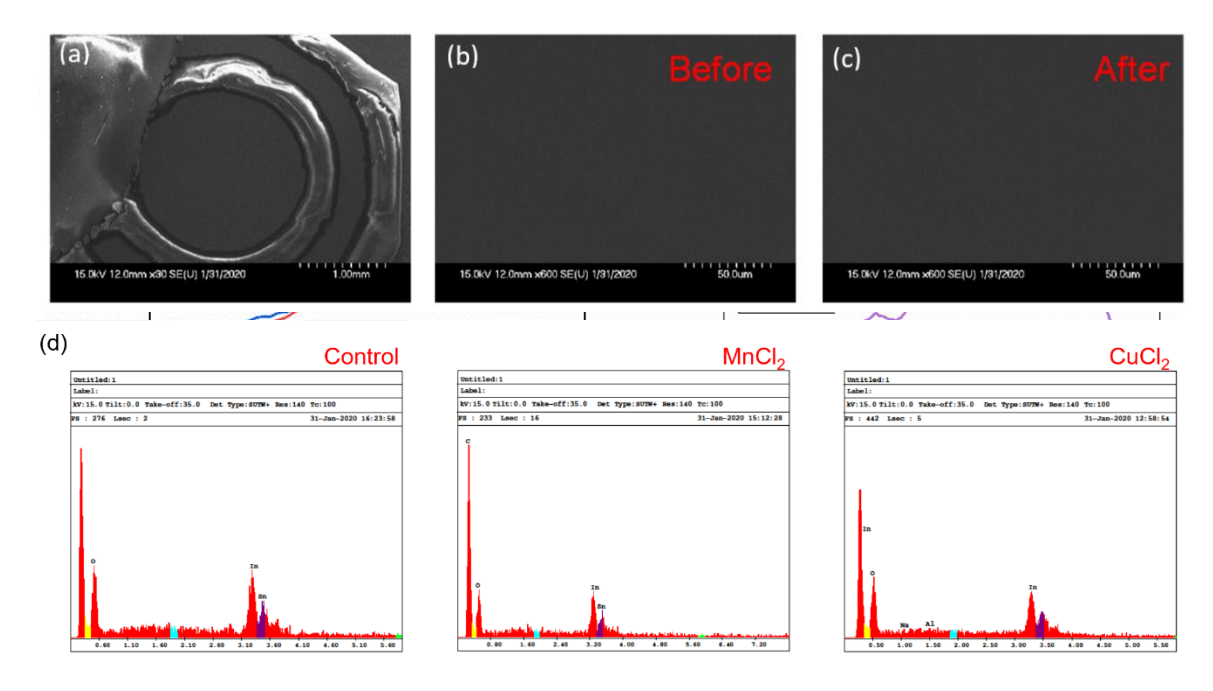


Figure 50. (a) SEM image of ITO sensor. (b) The zoom-in ITO WE surface before the 10-time consecutively DPSV. (c) The zoom-in ITO WE surface after the 10-time consecutively DPSV. A cleaning procedure was processed after each DPSV and before the next time DPSV. (d) EDS of ITO WE surface before 10-time consecutively DPSV and after 10-time consecutively DPSV in MnCl<sub>2</sub> and CuCl<sub>2</sub> solution, respectively.

## 6.2.3.3 SEM and EDS

We also inspected the electrode morphology using scanning electron microscopy (SEM) and did not observe any degradation or physical damage of the electrode after 10 scans (Figure 50). We also did the EDS before and after 10 repeated and continuous experiments, no detectable  $Cu^{2+}$  and  $Mn^{2+}$  were shown in the EDS results.

### 6.2.3.4 BDD Electrodes

We also tested the sensitivity of the BDD electrode to  $Cu^{2+}$ , since the ITO sensors could not detect  $Cu^{2+}$  effectively. For these experiments, the DPSV scan was done using the following protocol: deposition duration of 90 secs at -1V, 5 secs equilibrium at -1V to 0.5V. Compared to

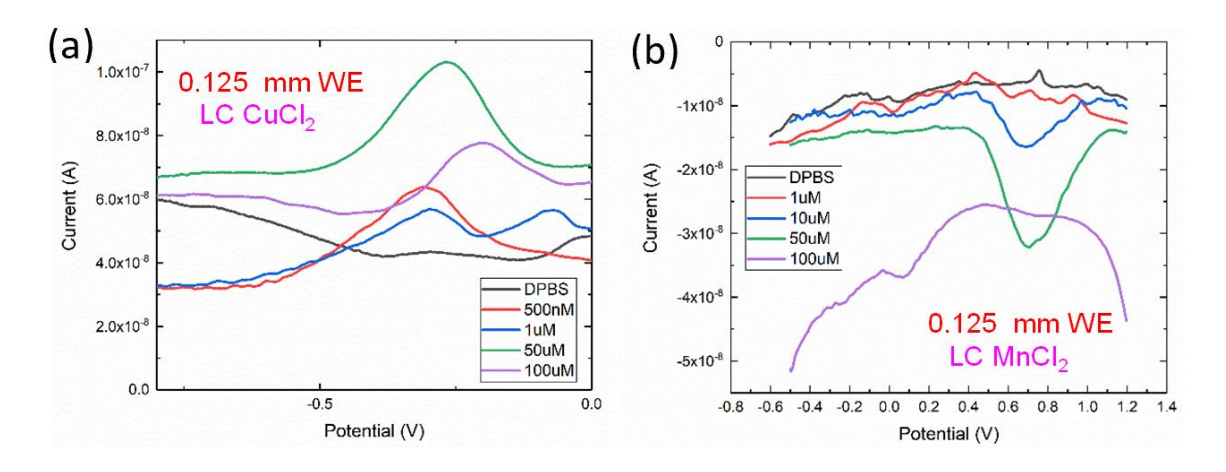


Figure 51. (a) 0.125mm diameter WE diamond sensors to measure DPBS, 500 nM, 1  $\mu$ M, 50  $\mu$ M, and 100  $\mu$ M CuCl<sub>2</sub>. (b) 0.125mm diameter WE diamond sensors to measure DPBS, 1  $\mu$ M, 10  $\mu$ M, 50  $\mu$ M, and 100  $\mu$ M MnCl<sub>2</sub>.

the ITO electrodes, the BDD electrodes show worse sensitivity to Mn<sup>2+</sup> but better sensitivity to Cu<sup>2+</sup> in the low concentration range, as shown in Figure 51 where distinct peaks can be detected for different Cu<sup>2+</sup> concentrations. Further investigations of other materials and device designs to maximize the sensitivity of the sensors are being investigated.

#### 6.2.4 Conclusion and Future Study

For this project, a miniaturized ITO-based electrochemical sensor was developed and characterized for continuous and quantitative monitoring of the concentrations of Cu and Mn ions in bodies and the soil environment with high sensitivity and accuracy. The DPSV method was selected and the testing and cleaning recipes were adjusted for achieving the repeatable and stable usage of the sensors for LC and HC of Cu and Mn ions. We found that transparent ITO material has high sensitivity to Mn<sup>2+</sup>, while BDD materials has better sensitivity to Cu<sup>2+</sup>. When the WE is smaller and the concentration of MnCl<sub>2</sub> is lower, the sensors have higher repeatability and stability

compared to the larger WE and higher solution concentration. No degradation or physical damage of the electrodes was observed after 10 scans in terms of SEM/EDS.

According to the experiment results, conventionally-deposited transparent ITO material has high sensitivity to  $Mn^{2+}$  but relatively low sensitivity to  $Cu^{2+}$ . Although BDD also has been tested and showed high sensitivity to  $Cu^{2+}$ , the sensitivity to  $Mn^{2+}$  is lower compared to ITO. Therefore, in future work, higher density ITO materials, such as ITO with Ion-beam assisted deposition (IBAD), are expected to achieve with the higher both  $Cu^{2+}$  and  $Mn^{2+}$  sensitivity, repeatability, and viability by utilizing DPSV scan method.

IBAD is a technique that combines the physical vapor deposition (PVD) with ion implantation. The ion bombardment dramatically controls the morphology, density, internal stresses, and crystallinity of the thin films. The conventional method of PVD to grow high quality ITO (high density, low resistivity, high transparency) is to increase the temperature during the deposition process. However, the required high temperature is not compatible with the flexible polymer substrate, such as Parylene C and PET. Consequently, IBAD is a good method that solves the high temperature requirement issue and improves the thin film quality at the same time. Because of the material properties changes due to the IBAD, the expected deposited ITO/PET film could have higher sensitivity to the Cu<sup>2+</sup>, which makes it a possible way to solve our previous ion sensors problem shown in above results.

APPENDIX

**Table 5. Admittance loci simulation** 

VL.		Incide	ence - A	ir	Film 1 - PEDOT:PSS												Film 2 - IT	Ю				
	Index	Angle	Fresnel	Admit.	Ir	ndex	Complex	Thick	Op. Thk.	A	ngle	Admit.	Phase	Inde	ex	Complex	Thick	Op. Thk.	Ai	ngle	Admit.	Phase
λ	n0	80	nOsin(80	η0	n1	k1	N1	d1	N1d1		cos(81)	η1	õ1	n2	k2	N2	d2	N2d2		cos(62	η2	52
550	1	0	0	1	1.488		878-0.04	0	0	0		378-0.04		1.8897	0.042	1.8897-0.0417i	0	0	0	1	1.8897-0.0417i	0
550	1	0	0	1	1.488		878-0.04	ŏ	ŏ	ŏ		378-0.04		1.8897	0.042	1.8897-0.0417i	ŏ	Ö	ō	i	1.8897-0.0417i	0
550	i	ō	Ü	1	1.488	0.04241		ŏ	Ŏ	ŏ		378-0.04	ŏ	1.8897	0.042	1.8897-0.0417i	ō	Ö	ō	i i	1.8897-0.0417i	0
550	+	0	0	-	1.488	0.04241		Ü	0	0	<u> </u>	378-0.04	_	1.8897	0.042	1.8897-0.0417i	0	0	0	+	1.8897-0.0417i	0
	+	_	_	+				0		0	_						0		_	+	-	
550	+	0	0	-	1.488		878-0.04	_	0	_	_	378-0.04		1.8897	0.042	1.8897-0.0417i	_	0	0	+	1.8897-0.0417i	0
550	1	0	0	1	1.488	0.04241		0	0	0		378-0.04	0	1.8897	0.042	1.8897-0.0417i	0	0	0	1	1.8897-0.0417i	0
550	1	0	0	1	1.488		878-0.04	0	0	0		378-0.04		1.8897	0.042	1.8897-0.0417i	0	0	0	1	1.8897-0.0417i	0
550	1	0	0	1	1.488		878-0.04	0	0	0		378-0.04		1.8897	0.042	1.8897-0.0417i	0	0	0	1	1.8897-0.0417i	0
550	1	0	0	- 1	1.488	0.04241		0	0	0	_	378-0.04	0	1.8897	0.042	1.8897-0.0417i	0	0	0	1	1.8897-0.0417i	0
550	1	0	0	- 1	1.488		878-0.04	0	0	0	1	378-0.04	0	1.8897	0.042	1.8897-0.0417i	0	0	0	1	1.8897-0.0417i	0
550	- 1	0	0	1	1.488	0.04241	878-0.04	0	0	0	1	378-0.04	0	1.8897	0.042	1.8897-0.0417i	0	0	0	- 1	1.8897-0.0417i	0
550	- 1	0	0	- 1	1.488	0.04241	878-0.04	0	0	0	1	378-0.04	0	1.8897	0.042	1.8897-0.0417i	0	0	0	- 1	1.8897-0.0417i	0
550	- 1	0	0	- 1	1.488	0.04241	878-0.04	0	0	0	1	378-0.04	0	1.8897	0.042	1.8897-0.0417i	0	0	0	- 1	1.8897-0.0417i	0
VL.	L Incidence - Air			ir			Fi	lm 1	- PEDO1	r:PSS								Film 2 - IT	О			
	Index Angle Fresnel Admit.		Ir	ndex	Complex	Thick	Op. Thk.	A	ngle	Admit. Phase		Ind	ex	Complex	Thick	Op. Thk.	Ai	ngle	Admit.	Phase		
λ	n0	80	nOsin(80	η0	n1	k1	N1	d1	N1d1	_	cos(81)	η1	ă1	n2	k2	N2	d2	N2d2		cos(62)	η2	52
550	1	0	0	1	1.488		878-0.04	Ö	0	0	_	378-0.04	_	1.8897	0.042	1.8897-0.0417i	0	0	0	1	1.8897-0.0417i	0
550	1	0	0	1	1.488		878-0.04	ŏ	Ů	ő		378-0.04		1.8897	0.042	1.8897-0.0417i	Ů	0	0	1	1.8897-0.0417i	0
550	1	0	0	1	1.488	0.04241		0	0	0		378-0.04		1.8897	0.042	1.8897-0.04171	0	0	0	1	1.8897-0.04171	0
550	1	0	0	1	1,488	0.04241		-	0	0	_	378-0.04 378-0.04		1.8897	0.042	1.8897-0.04171	0	0	0	1	1.8897-0.04171	0
_	-	_	_	-				_		_	_						_		_	1	-	
550		0	0		1.488		878-0.04	0	0	0		378-0.04		1.8897	0.042	1.8897-0.0417i	0	0	0	1	1.8897-0.0417i	0
550	1	0	0	1	1.488		878-0.04	0	0	0		378-0.04		1.8897	0.042	1.8897-0.0417i	0	0	0	1	1.8897-0.0417i	0
550	1	0	0	1	1.488	0.04241		0	0	0		378-0.04		1.8897	0.042	1.8897-0.0417i	0	0	0	1	1.8897-0.0417i	0
550	1	0	0	- 1	1.488		878-0.04	0	0	0		378-0.04		1.8897	0.042	1.8897-0.0417i	0	0	0	1	1.8897-0.0417i	0
550	- 1	0	0	- 1	1.488	0.04241	878-0.04	0	0	0	1	378-0.04	0	1.8897	0.042	1.8897-0.0417i	0	0	0	- 1	1.8897-0.0417i	0
550	1	0	0	1	1.488	0.04241	878-0.04	0	0	0	1	378-0.04	0	1.8897	0.042	1.8897-0.0417i	0	0	0	- 1	1.8897-0.0417i	0
550	- 1	0	0	- 1	1.488	0.04241	878-0.04	0	0	0	1	378-0.04	0	1.8897	0.042	1.8897-0.0417i	0	0	0	1	1.8897-0.0417i	0
				-	4.400	0.04041	878-0.04	0	0	0	1	270 0 04		1.8897	0.042	1.8897-0.0417i	0	0	0	-	1.8897-0.0417i	0
550	1	0	0	1	1.488	0.04241	010-0.04					878-0.04	0 1	1.0001	0.072							
550 550	1	0	0	1	1.488			Ť	0	0	_	878-0.04 878-0.04		1.8897	0.042		ō	0	ō	1	1.8897-0.0417i	0
	1			1			878-0.04			_	_					1.8897-0.0417i			_	1		
550	1	0	0	1 1			878-0.04	0	0	0	_							0	0	1		
	1 1 Index	0 Incide	0 nce - A		1.488		878-0.04 Fi	0 lm 1	0 - <b>PEDO</b> 1	0 :PSS	1	378-0.04	0		0.042	1.8897-0.0417i	0	0 Film 2 - IT	0			0
550		0 <b>Incide</b> Angle	0 ence - A Fresnel	Admit.	1.488 In	0.04241 ndex	878-0.04 Fi Complex	0 Im 1 Thick	0 - <b>PEDO</b> 1 : Op. Thk.	0 :PSS	1 ngle	378-0.04 Admit.	0 Phase	1.8897 Ind	0.042 ex		0 Thick	0 Film 2 - IT Op. Thk.	0 <b>0</b>	ngle	1.8897-0.0417i Admit.	0 Phase
550 <b>∀L</b>	1 1 Index n0	0 Incide Angle 80	0 ence - A Fresnel nosin(80)		1.488 In n1	0.04241 ndex k1	878-0.04 Fi Complex N1	0 Im 1 Thick d1	0 - <b>PEDO</b> 1 I, Op. Thk. N1d1	0 :PSS A sin(01)	ngle	378-0.04 Admit. η1	Phase	1.8897 Ind- n2	0.042 ex k2	1.8897-0.0417i Complex N2	0 Thick d2	0 Film 2 - IT Op. Thk. N2d2	0 O Ar sin(62)		1.8897-0.0417i  Admit.  η2	0 Phase 82
550 <b>VL</b> 1 550		0 Incide Angle 80	0 Presnel nosin(80)	Admit.	1.488 Ir n1 1.488	0.04241 odex k1 0.042	878-0.04 Fi Comples N1 878-0.04	0 Im 1 Thick d1 0	0 - <b>PEDO</b> 1 : Op. Thk. N1d1 0	0 :PSS A sin(01)	1 ngle cos(θ1)	Admit. 978-0.04	0 Phase 51 0	1.8897 Ind- n2 1.8897	0.042 ex k2 0.042	1.8897-0.0417i Complex N2 1.8897-0.0417i	0 Thick d2 0	0 Film 2 - IT Op. Thk. N2d2 0	0 Ar sin(82)	ngle	1.8897-0.0417i  Admit.  η2 1.8897-0.0417i	0 Phase 52 0
550 <b>¥L</b> 550  550		0 Incide Angle 60 0	0 Fresnel nosin(60) 0	Admit. η0	1.488 In n1 1.488 1.488	0.04241 dex k1 0.042 0.04241	Fi Complex N1 878-0.04	0 Im 1 Thick d1 0	0 - <b>PEDO1</b> Op. Thk. NId1 0	0 :PSS A sin(01 0	1 ngle cos(81)	Admit. 11 13 17 18 17 18 17 18 18 18 19 19 19 19 19 19 19 19 19 19	Phase 51 0	1.8897 Ind- n2 1.8897	0.042 ex k2 0.042 0.042	1.8897-0.0417i  Complex N2 1.8897-0.0417i 1.8897-0.0417i	0 Thick d2 0	0 Film 2 - IT Op. Thk. N2d2 0 22.9167-0.5057i	0 Ar sin(82) 0	ngle	Admit. #2 1.8897-0.0417i 1.8897-0.0417i 1.8897-0.0417i	0 Phase 52 0 0.2617-0.0
550 λ 550 550 550		O Incide Angle e0 0 0	Presnel Presnel nosin(80) 0 0	Admit. η0	1.488 Ir n1 1.488 1.488	0.04241 odex k1 0.042 0.04241 0.04241	Fil Comples N1 878-0.04 878-0.04	0 Im 1 Thick d1 0 0	0 - <b>PEDO</b> 1 : Op. Thk. N1d1 0 0	0 F:PSS A sin(01) 0 0	1 ngle cos(81) 1	Admit. ¶1 378-0.04 378-0.04 378-0.04	Phase 51 0 0 0	1.8897 Ind- n2 1.8897 1.8897	0.042 ex k2 0.042 0.042	1,8897-0,0417i  Complex N2 1,8897-0,0417i 1,8897-0,0417i 1,8897-0,0417i	0 Thick d2 0 12.1 24.3	0 Film 2 - IT Op. Thk. N2d2 0 22.9167-0.5057i 45.8333-1.0114i	0 Ar sin(62) 0 0	ngle	Admit. #2 1.8897-0.0417i 1.8897-0.0417i 1.8897-0.0417i 1.8897-0.0417i	Phase 52 0 0.2617-0.0 0.5233-0.0
VL λ 550 550 550 550		O Incide Angle 60 0 0	Fresnel nosin(60) 0 0	Admit. η0 1 1 1 1	1.488 In n1 1.488 1.488 1.488	0.04241 odex k1 0.042 0.04241 0.04241 0.04241	Fi Comples N1 878-0.04 878-0.04 878-0.04 878-0.04	0 Im 1 Thick d1 0 0 0 0	0 - <b>PEDO</b> 1 . Op. Thk. N1d1 0 0	0 F:PSS A sin(01 0 0	1 ngle cos(θ1) 1 1	Admit. ¶1 378-0.04 378-0.04 378-0.04 378-0.04	Phase 51 0 0 0 0 0	1.8897 n2 1.8897 1.8897 1.8897	0.042 ex k2 0.042 0.042 0.042	1.8897-0.0417i  Complex N2 1.8897-0.0417i 1.8897-0.0417i 1.8897-0.0417i 1.8897-0.0417i	0 Thick d2 0 12.1 24.3 36.4	0 Film 2 - IT Op. Thk. N2d2 0 22.9167-0.5057i 45.8333-1.0114i 68.75-1.5171i	0 Ar sin(02) 0 0	ngle	Admit. 122 1.8897-0.0417i 1.8897-0.0417i 1.8897-0.0417i 1.8897-0.0417i 1.8897-0.0417i 1.8897-0.0417i 1.8897-0.0417i	Phase 52 0 0.2617-0.0 0.5233-0.0
VL λ 550 550 550 550		0 Angle 60 0 0 0	0  Proce - A  Fresnel  nosin(80)  0  0  0  0	Admit. η0	1.488 In n1 1.488 1.488 1.488 1.488 1.488	0.04241 dex k1 0.042 0.04241 0.04241 0.04241 0.04241	Fi Complex N1 878-0.04 878-0.04 878-0.04 878-0.04	0 Im 1 Thick d1 0 0 0	0 - PEDO1 . Op. Thk. N1d1 0 0 0	0 F:PSS A sin(01 0 0 0	ngle cos(θ1) 1 1 1 1 1 1 1	Admit. 11 13 13 13 13 13 13 13 14 15 16 16 16 16 16 16 16 16 16 16	Phase 51 0 0 0 0 0 0 0 0	1.8897 Indi n2 1.8897 1.8897 1.8897 1.8897	0.042 ex k2 0.042 0.042 0.042 0.042	1.8897-0.0417i  Complex N2 1.8897-0.0417i 1.8897-0.0417i 1.8897-0.0417i 1.8897-0.0417i 1.8897-0.0417i	0 Thick d2 0 12.1 24.3 36.4 48.5	0 Film 2 - IT Op. Thk. N2d2 0 22.9167-0.5057i 45.8333-1.0114i 68.75-1.517ti 91.6667-2.0228i	0 Ar sin(e2) 0 0 0	ngle	Admit. 12 1.8897-0.0417i 1.8897-0.0417i 1.8897-0.0417i 1.8897-0.0417i 1.8897-0.0417i 1.8897-0.0417i	Phase 52 0 0.2617-0.0 0.5233-0.0 0.785-0.0 1.0467-0.0
λ 550 550 550 550 550 550		0 Angle 60 0 0 0 0	0 Prese - A Fresnel nosin(80) 0 0 0 0 0 0	Admit. η0 1 1 1 1	1,488 In n1 1,488 1,488 1,488 1,488 1,488	0.04241 0.042 0.042 0.04241 0.04241 0.04241 0.04241 0.04241	Fi Comples N1 878-0.04 878-0.04 878-0.04 878-0.04 878-0.04 878-0.04	0 Im 1 Thick d1 0 0 0	0 - PEDO1 Op. Thk. N1d1 0 0 0	0 :PSS A sin(01 0 0 0 0	ngle   cos(01)   1   1   1   1   1   1   1   1   1	Admit.  11 378-0.04 378-0.04 378-0.04 378-0.04 378-0.04 378-0.04	Phase 51 0 0 0 0 0 0 0 0 0 0 0 0 0 0 0 0 0 0	1.8897 Indi- n2 1.8897 1.8897 1.8897 1.8897 1.8897	0.042 ex k2 0.042 0.042 0.042 0.042 0.042	1.8897-0.0417i  Complex N2 1.8897-0.0417i 1.8897-0.0417i 1.8897-0.0417i 1.8897-0.0417i 1.8897-0.0417i	0 Thick d2 0 12.1 24.3 36.4 48.5 60.6	0 Film 2 - 17 Op. Thk. M2d2 0 22.9167-0.50571 45.8333-1.01141 68.75-1.5171 91.6667-2.02281 114.5833-2.52851	0 Ar sin(62) 0 0 0 0 0 0 0 0	ngle	Admit. 1.8897-0.0417i 1.8897-0.0417i 1.8897-0.0417i 1.8897-0.0417i 1.8897-0.0417i 1.8897-0.0417i 1.8897-0.0417i	0 Phase 52 0 0.2617-0.0 0.5233-0.0 1.0467-0.0 1.3083-0.0
λ 550 550 550 550 550 550 550		0 Angle e0 0 0 0 0 0 0 0 0 0 0 0 0 0 0 0 0 0	0 Presnel nosin(60) 0 0 0 0 0 0 0 0 0 0 0 0 0 0 0 0 0 0	Admit. η0 1 1 1 1 1 1 1	1,488 In n1 1,488 1,488 1,488 1,488 1,488 1,488 1,488	0.04241  dex  k1  0.042  0.04241  0.04241  0.04241  0.04241  0.04241  0.04241	Fi Comples N1 878-0.04 878-0.04 878-0.04 878-0.04 878-0.04 878-0.04 878-0.04	0 Im 1 Thick d1 0 0 0 0 0 0 0 0 0 0 0 0 0 0 0 0 0 0	0 - PEDO1 - Op. Thk. N1d1 - O - O - O - O - O - O - O - O - O	0 F:PSS A sin(01) 0 0 0 0 0	ngle   cos(01)   1   1   1   1   1   1   1   1   1	Admit.  11 1378-0.04 1378-0.04 1378-0.04 1378-0.04 1378-0.04 1378-0.04 1378-0.04	Phase 51 0 0 0 0 0 0 0 0 0 0 0 0 0 0 0 0 0 0	1,8897 Ind- n2 1,8897 1,8897 1,8897 1,8897 1,8897 1,8897	0.042 ex k2 0.042 0.042 0.042 0.042 0.042 0.042	1.8897-0.0417i  Complex N2 1.8897-0.0417i 1.8897-0.0417i 1.8897-0.0417i 1.8897-0.0417i 1.8897-0.0417i 1.8897-0.0417i 1.8897-0.0417i	0 Thick d2 0 12.1 24.3 36.4 48.5 60.6 72.8	0 Film 2 - 17 Op. Thk. N2d2 0 22.9167-0.5057i 45.9333-1.0114i 68.75-1.517i 18.6667-2.0228i 114.5833-2.5285i 137.5-3.0342i	0 Ar sin(02) 0 0 0 0 0 0 0 0 0 0	ngle	Admit. 92 1.8897-0.0417i 1.8897-0.0417i 1.8897-0.0417i 1.8897-0.0417i 1.8897-0.0417i 1.8897-0.0417i 1.8897-0.0417i	0 Phase 52 0 0.2617-0.0 0.5233-0.0 1.0467-0.0 1.3083-0.0 1.57-0.03
λ 550 550 550 550 550 550 550 550 550		0 Angle 60 0 0 0 0 0	0 Presnel nosin(80) 0 0 0 0 0 0 0 0 0 0	Admit. η0 1 1 1 1	1.488 In n1 1.488 1.488 1.488 1.488 1.488 1.488 1.488	0.04241  dex  k1  0.042  0.04241  0.04241  0.04241  0.04241  0.04241  0.04241  0.04241	Fi Comples N1 878-0.04 878-0.04 878-0.04 878-0.04 878-0.04 878-0.04 878-0.04 878-0.04	0 Im 1 Thick d1 0 0 0 0 0 0 0 0 0 0 0 0 0 0 0 0 0 0	0 - PEDO1 - Op. Thk. N1d1 - O - O - O - O - O - O - O - O - O - O	0 F:PSS A sin(01) 0 0 0 0 0 0	ngle   cos(01)   1   1   1   1   1   1   1   1   1	Admit.  11 1378-0.04 378-0.04 378-0.04 378-0.04 378-0.04 378-0.04 378-0.04 378-0.04	Phase 51 0 0 0 0 0 0 0 0 0 0 0 0 0 0 0 0 0 0	1,8897 Ind- n2 1,8897 1,8897 1,8897 1,8897 1,8897 1,8897 1,8897	0.042 ex k2 0.042 0.042 0.042 0.042 0.042 0.042 0.042	1.8897-0.0417i  Complex N2 1.8897-0.0417i 1.8897-0.0417i 1.8897-0.0417i 1.8897-0.0417i 1.8897-0.0417i 1.8897-0.0417i 1.8897-0.0417i 1.8897-0.0417i	0 Thick d2 0 12.1 24.3 36.4 48.5 60.6 72.8 84.9	0 Film 2 - 17 Op. Thk. N2d2 0 22.9167-0.5057/ 45.8333-1.0114/ 68.75-1.5171/ 91.6667-2.0228/ 114.5833-2.5285/ 137.5-3.0342/ 160.4167-3.5399/	0 Ai sin(02) 0 0 0 0 0 0 0 0 0 0 0 0 0 0 0 0 0 0	ngle	Admit.  12897-0.0417i  18897-0.0417i 18897-0.0417i 18897-0.0417i 18897-0.0417i 18897-0.0417i 18897-0.0417i 18897-0.0417i 18897-0.0417i	0 Phase 52 0 0.2617-0.0 0.5233-0.0 1.0467-0.0 1.3083-0.0 1.57-0.03 1.8317-0.0
λ 550 550 550 550 550 550 550 550 550		0 Incide Angle 60 0 0 0 0 0 0 0 0 0 0	0 Presnel nosin(80) 0 0 0 0 0 0 0 0 0 0 0 0	Admit. η0 1 1 1 1 1 1 1 1 1 1 1 1 1 1 1 1 1 1 1	1.488 In 1.488 1.488 1.488 1.488 1.488 1.488 1.488 1.488 1.488	0.04241  dex  k1  0.042  0.04241  0.04241  0.04241  0.04241  0.04241  0.04241  0.04241  0.04241	Fi Comples N1 878-0.04 878-0.04 878-0.04 878-0.04 878-0.04 878-0.04 878-0.04 878-0.04	0 Im 1 Thick d1 0 0 0 0 0 0 0 0 0 0 0 0 0 0 0 0 0 0	0 - PEDO1 - Op. Thk. Nid1 - 0 - 0 - 0 - 0 - 0 - 0 - 0 - 0 - 0 - 0	0 F:PSS A sin(01) 0 0 0 0 0 0 0	ngle   cos(01)   1   1   1   1   1   1   1   1   1	Admit.  1378-0.04  71  378-0.04  378-0.04  378-0.04  378-0.04  378-0.04  378-0.04  378-0.04  378-0.04	Phase 51 0 0 0 0 0 0 0 0 0 0 0 0 0 0 0 0 0 0	1,8897 Ind n2 1,8897 1,8897 1,8897 1,8897 1,8897 1,8897 1,8897	0.042 ex k2 0.042 0.042 0.042 0.042 0.042 0.042 0.042 0.042	18897-0.0417i  Complex N2 1.8897-0.0417i 1.8897-0.0417i 1.8897-0.0417i 1.8897-0.0417i 1.8897-0.0417i 1.8897-0.0417i 1.8897-0.0417i 1.8897-0.0417i 1.8897-0.0417i	Thick d2 0 12.1 24.3 36.4 48.5 60.6 72.8 84.9 97	0 Film 2 - 17 Op. Thk. N2d2 0 22.9167-0.5057i 45.8333-1.0114i 68.75-1.5171i 91.6667-2.0228i 114.5833-2.5285i 137.5-3.0342i 183.3333-4.0456i	0 Ain(62) 0 0 0 0 0 0 0 0 0 0 0 0 0 0 0 0 0 0 0	ngle	Admit.  18897-0.0417i  2 18897-0.0417i 18897-0.0417i 18897-0.0417i 18897-0.0417i 18897-0.0417i 18897-0.0417i 18897-0.0417i 18897-0.0417i 18897-0.0417i	Phase 52 0 0.2617-0.0 0.5233-0.1 0.785-0.0 1.0467-0.0 1.3083-0.0 1.57-0.03 1.8317-0.0 2.0933-0.0
×L  550  550  550  550  550  550  550  5		0 Incide Angle 60 0 0 0 0 0 0 0 0 0 0 0 0	0 Presel hosin(80) 0 0 0 0 0 0 0 0 0 0 0 0 0 0 0 0	Admit. η0 1 1 1 1 1 1 1	1.488 n1 1.488 1.488 1.488 1.488 1.488 1.488 1.488 1.488 1.488 1.488	0.04241  dex k1 0.042 0.04241 0.04241 0.04241 0.04241 0.04241 0.04241 0.04241 0.04241 0.04241 0.04241	Fi Comples N1 878-0.04 878-0.04 878-0.04 878-0.04 878-0.04 878-0.04 878-0.04 878-0.04 878-0.04	0 Im 1 Thick d1 0 0 0 0 0 0 0 0 0 0 0 0 0 0 0 0 0 0	0 - PEDO1 - Op. Thk. Nid1 - 0 - 0 - 0 - 0 - 0 - 0 - 0 - 0 - 0 - 0	0 PSS A sin(01) 0 0 0 0 0 0 0 0 0 0 0 0 0 0 0 0 0 0	1 cos(01) 1 1 1 1 1 1 1 1 1 1 1 1 1 1 1 1 1 1	Admit.  1378-0.04 378-0.04 378-0.04 378-0.04 378-0.04 378-0.04 378-0.04 378-0.04 378-0.04 378-0.04	Phase 51 0 0 0 0 0 0 0 0 0 0 0 0 0 0 0 0 0 0	1,8897 Ind n2 1,8897 1,8897 1,8897 1,8897 1,8897 1,8897 1,8897 1,8897 1,8897	0.042 ex k2 0.042 0.042 0.042 0.042 0.042 0.042 0.042 0.042 0.042	18897-0.0417i  Complex N2 1.8897-0.0417i	0 Thick d2 0 12.1 24.3 36.4 48.5 60.6 72.8 84.9 97 109	0 Film 2 - 17 Op. Thk. N2d2 0 22.9167-0.5057i 45.8333-1.014i 68.75-1.517l 91.6667-2.0228i 144.5833-2.5285i 137.5-3.0342i 160.4167-3.5393i 183.3333-4.0456i 206.25-4.5513i	0 Ar sin(02) 0 0 0 0 0 0 0 0 0 0 0 0 0 0 0 0 0 0	ngle	1.8897-0.0417i  Admit.  12 1.8897-0.0417i	Phase 52 0 0.2617-0.0 0.5233-0.1 0.785-0.0 1.3083-0.0 1.57-0.03 1.8317-0.0 2.0933-0.0
1550 Δ 1550 550 550 550 550 550 550 550 550 550		0 Incide Angle 60 0 0 0 0 0 0 0 0 0 0 0 0 0 0 0 0 0 0	0 ence - A Fresnel hosin(e0) 0 0 0 0 0 0 0 0 0 0 0 0 0 0 0	Admit. η0 1 1 1 1 1 1 1 1 1 1 1 1 1 1 1 1 1 1 1	1.488 n1 1.488 1.488 1.488 1.488 1.488 1.488 1.488 1.488 1.488 1.488 1.488	0.04241  dex k1 0.042 0.04241 0.04241 0.04241 0.04241 0.04241 0.04241 0.04241 0.04241 0.04241 0.04241 0.04241 0.04241	Fi Comples N1 878-0.04 878-0.04 878-0.04 878-0.04 878-0.04 878-0.04 878-0.04 878-0.04 878-0.04 878-0.04	0 Im 1 Thick d1 0 0 0 0 0 0 0 0 0 0 0 0 0 0 0 0 0 0	0 - PEDO1 - Op. Thk. N1d1 - 0 - 0 - 0 - 0 - 0 - 0 - 0 - 0 - 0 - 0	0 F:PSS A sin(01 0 0 0 0 0 0 0 0 0	1 cos(01) 1 1 1 1 1 1 1 1 1 1 1 1 1 1 1 1 1 1	Admit.  11  71  78-0.04  78-0.04  78-0.04  78-0.04  78-0.04  78-0.04  78-0.04  78-0.04  78-0.04  78-0.04  78-0.04  78-0.04	Phase 51 0 0 0 0 0 0 0 0 0 0 0 0 0 0 0 0 0 0	1,8897 Ind- n2 1,8897 1,8897 1,8897 1,8897 1,8897 1,8897 1,8897 1,8897 1,8897 1,8897	0.042 ex k2 0.042 0.042 0.042 0.042 0.042 0.042 0.042 0.042 0.042 0.042	18897-0.0417i  Complex N2 1.8897-0.0417i	0 Thick d2 0 12.1 24.3 36.4 48.5 60.6 72.8 84.9 97 109 121	0 Film 2 - 17 Op. Thk. N2d2 0 22.9167-0.5057i 45.8333-1.0114i 68.75-1.517i 91.6667-2.0228i 114.5833-2.5285i 137.5-3.0342i 160.4167-3.5393i 209.626-4.5513i 229.1667-5.057i	0 Ai sin(02) 0 0 0 0 0 0 0 0 0 0 0 0 0 0 0 0 0 0	ngle	Admit.  18897-0.0417i  Admit.  12  1.8897-0.0417i	0 Phase 52 0.2617-0.0 0.5233-0.1 0.785-0.0 1.0467-0.0 1.57-0.03 1.8317-0.0 2.0933-0.0 2.355-0.0 2.6167-0.0
×L  550  550  550  550  550  550  550  5		0 Incide Angle 60 0 0 0 0 0 0 0 0 0 0 0 0	0 Presel hosin(80) 0 0 0 0 0 0 0 0 0 0 0 0 0 0 0 0	Admit. η0 1 1 1 1 1 1 1 1 1 1 1 1 1 1 1 1 1 1 1	1.488 In n1 1.488	0.04241  dex k1 0.042 0.04241 0.04241 0.04241 0.04241 0.04241 0.04241 0.04241 0.04241 0.04241 0.04241	Fi Comples N1 878-0.04 878-0.04 878-0.04 878-0.04 878-0.04 878-0.04 878-0.04 878-0.04 878-0.04 878-0.04	0 Im 1 Thick d1 0 0 0 0 0 0 0 0 0 0 0 0 0 0 0 0 0 0	0 - PEDO1 - Op. Thk. Nid1 - 0 - 0 - 0 - 0 - 0 - 0 - 0 - 0 - 0 - 0	0 PSS A sin(01) 0 0 0 0 0 0 0 0 0 0 0 0 0 0 0 0 0 0	1 cos(01) 1 1 1 1 1 1 1 1 1 1 1 1 1 1 1 1 1 1	Admit.  1378-0.04 378-0.04 378-0.04 378-0.04 378-0.04 378-0.04 378-0.04 378-0.04 378-0.04 378-0.04	Phase 51 0 0 0 0 0 0 0 0 0 0 0 0 0 0 0 0 0 0	1,8897 Ind n2 1,8897 1,8897 1,8897 1,8897 1,8897 1,8897 1,8897 1,8897 1,8897	0.042 ex k2 0.042 0.042 0.042 0.042 0.042 0.042 0.042 0.042 0.042	18897-0.0417i  Complex N2 1.8897-0.0417i	0 Thick d2 0 12.1 24.3 36.4 48.5 60.6 72.8 84.9 97 109	0 Film 2 - 17 Op. Thk. N2d2 0 22.9167-0.5057i 45.8333-1.014i 68.75-1.517l 91.6667-2.0228i 144.5833-2.5285i 137.5-3.0342i 160.4167-3.5393i 183.3333-4.0456i 206.25-4.5513i	0 Ar sin(02) 0 0 0 0 0 0 0 0 0 0 0 0 0 0 0 0 0 0	ngle	Admit.  12 1.8897-0.0417i  18897-0.0417i 1.8897-0.0417i	0 Phase 52 0.2617-0.0 0.5233-0.1 0.785-0.0 1.0467-0.0 1.57-0.03 1.8317-0.0 2.0933-0.0 2.355-0.0 2.6167-0.0
1550 Δ 1550 550 550 550 550 550 550 550 550 550		0 Incide Angle 60 0 0 0 0 0 0 0 0 0 0 0 0 0 0 0 0 0 0	0 ence - A Fresnel hosin(e0) 0 0 0 0 0 0 0 0 0 0 0 0 0 0 0	Admit. η0 1 1 1 1 1 1 1 1 1 1 1 1 1 1 1 1 1 1 1	1.488 n1 1.488 1.488 1.488 1.488 1.488 1.488 1.488 1.488 1.488 1.488 1.488	0.04241  dex k1 0.042 0.04241 0.04241 0.04241 0.04241 0.04241 0.04241 0.04241 0.04241 0.04241 0.04241 0.04241 0.04241	Final Complete N1 878-0.04 878-0.04 878-0.04 878-0.04 878-0.04 878-0.04 878-0.04 878-0.04 878-0.04 878-0.04 878-0.04 878-0.04 878-0.04 878-0.04 878-0.04	0 Im 1 Thick d1 0 0 0 0 0 0 0 0 0 0 0 0 0 0 0 0 0 0	0 - PEDO1 - Op. Thk. N1d1 - 0 - 0 - 0 - 0 - 0 - 0 - 0 - 0 - 0 - 0	0 F:PSS A sin(01 0 0 0 0 0 0 0 0 0	1 cos(@1) 1 1 1 1 1 1 1 1 1 1 1 1 1 1 1 1 1 1	Admit.  11  71  78-0.04  78-0.04  78-0.04  78-0.04  78-0.04  78-0.04  78-0.04  78-0.04  78-0.04  78-0.04  78-0.04  78-0.04	Phase 51 0 0 0 0 0 0 0 0 0 0 0 0 0 0 0 0 0 0	1,8897 Ind- n2 1,8897 1,8897 1,8897 1,8897 1,8897 1,8897 1,8897 1,8897 1,8897 1,8897	0.042 ex k2 0.042 0.042 0.042 0.042 0.042 0.042 0.042 0.042 0.042 0.042	18897-0.0417i  Complex N2 1.8897-0.0417i	0 Thick d2 0 12.1 24.3 36.4 48.5 60.6 72.8 84.9 97 109 121	0 Film 2 - 17 Op. Thk. N2d2 0 22.9167-0.5057i 45.8333-1.0114i 68.75-1.517i 91.6667-2.0228i 114.5833-2.5285i 137.5-3.0342i 160.4167-3.5393i 209.626-4.5513i 229.1667-5.057i	0 Ai sin(02) 0 0 0 0 0 0 0 0 0 0 0 0 0 0 0 0 0 0	ngle	Admit.  18897-0.0417i  Admit.  12  1.8897-0.0417i	Phase 52 0 0.2617-0.0 0.785-0.0 1.0467-0.0 1.3083-0.0 1.57-0.03 1.8317-0.0 2.0933-0.0 2.355-0.0 2.8783-0.0
λ 550 550 550 550 550 550 550 55		0 Incide 60 0 0 0 0 0 0 0 0 0 0 0 0 0 0 0 0 0 0	0 Proce - A Fresnel nosin(60) 0 0 0 0 0 0 0 0 0 0 0 0 0 0 0 0 0 0	Admit.  η0 1 1 1 1 1 1 1 1 1 1 1 1 1 1 1 1 1 1	1.488 In n1 1.488	0.04241 0.042 0.04241 0.04241 0.04241 0.04241 0.04241 0.04241 0.04241 0.04241 0.04241 0.04241 0.04241 0.04241	Final Complete N1 878-0.04 878-0.04 878-0.04 878-0.04 878-0.04 878-0.04 878-0.04 878-0.04 878-0.04 878-0.04 878-0.04 878-0.04 878-0.04 878-0.04 878-0.04	0 Im 1 Thick d1 0 0 0 0 0 0 0 0 0 0 0 0 0 0 0 0 0 0	0 - PEDO1 - Op. Thk. N1d1 - 0 - 0 - 0 - 0 - 0 - 0 - 0 - 0 - 0 - 0	0 F:PSS A sin(01) 0 0 0 0 0 0 0 0	1 cos(@1) 1 1 1 1 1 1 1 1 1 1 1 1 1 1 1 1 1 1	Admit.  11  71  78-0.04  78-0.04  78-0.04  78-0.04  78-0.04  78-0.04  78-0.04  78-0.04  78-0.04  78-0.04  78-0.04  78-0.04  78-0.04	Phase 51 0 0 0 0 0 0 0 0 0 0 0 0 0 0 0 0 0 0	1,8897 1,8897 1,8897 1,8897 1,8897 1,8897 1,8897 1,8897 1,8897 1,8897 1,8897 1,8897 1,8897	ex k2 0.042 0.042 0.042 0.042 0.042 0.042 0.042 0.042 0.042 0.042 0.042	18897-0.0417i  Complex N2 1.8897-0.0417i	0 Thick d2 0 12.1 24.3 36.4 48.5 60.6 72.8 84.9 97 109 121 133	0 Film 2 - IT Op. Thk. N2d2 0 22.9167-0.5057i 45.9333-1.0114i 68.75-1.517i 191.6667-2.0228i 114.5833-2.028i 137.5-3.0342i 180.4167-3.5399i 183.3333-4.0456i 223.1667-5.057i 252.0833-5.5627i	0 Au sin(02) 0 0 0 0 0 0 0 0 0 0 0 0 0 0 0 0 0 0	ngle	Admit.  12 1.8897-0.0417i  18897-0.0417i 1.8897-0.0417i	Phase 52 0 0.2617-0.01 0.5233-0.0 0.785-0.01 1.0467-0.0 1.3083-0.01 157-0.03 18317-0.04 2.0933-0.0 2.6167-0.02 2.8783-0.0
λ 550 550 550 550 550 550 550 55		0 Incide 60 0 0 0 0 0 0 0 0 0 0 0 0 0 0 0 0 0 0	0 Proce - A Fresnel nosin(60) 0 0 0 0 0 0 0 0 0 0 0 0 0 0 0 0 0 0	Admit. η0 1 1 1 1 1 1 1 1 1 1 1 1 1 1 1 1 1 1	1.488 In n1 1.488	0.04241 0.042 0.04241 0.04241 0.04241 0.04241 0.04241 0.04241 0.04241 0.04241 0.04241 0.04241 0.04241 0.04241	File Comples N1 878-0.04 878-0.04 878-0.04 878-0.04 878-0.04 878-0.04 878-0.04 878-0.04 878-0.04 878-0.04 878-0.04 878-0.04	0 Im 1 Thick d1 0 0 0 0 0 0 0 0 0 0 0 0 0 0 0 0 0 0	0 - PEDO1 - Op. Thk. N1d1 - 0 - 0 - 0 - 0 - 0 - 0 - 0 - 0 - 0 - 0	0 F:PSS A sin(e)1 0 0 0 0 0 0 0 0 0 0 0 0 0 0 0 0 0 0 0	1 cos(@1) 1 1 1 1 1 1 1 1 1 1 1 1 1 1 1 1 1 1	Admit.  11  71  78-0.04  78-0.04  78-0.04  78-0.04  78-0.04  78-0.04  78-0.04  78-0.04  78-0.04  78-0.04  78-0.04  78-0.04  78-0.04	Phase 51 0 0 0 0 0 0 0 0 0 0 0 0 0 0 0 0 0 0	1,8897 1,8897 1,8897 1,8897 1,8897 1,8897 1,8897 1,8897 1,8897 1,8897 1,8897 1,8897 1,8897	ex k2 0.042 0.042 0.042 0.042 0.042 0.042 0.042 0.042 0.042 0.042 0.042	18897-0.0417i  Complex N2 1.8897-0.0417i	0 Thick d2 0 12.1 24.3 36.4 48.5 60.6 72.8 84.9 97 109 121 133	0 Film 2 - IT Op. Thk. N2d2 0 22.9167-0.5057i 45.9333-1.0114i 68.75-1.517i 191.6667-2.0228i 114.5833-2.028i 137.5-3.0342i 180.4167-3.5399i 183.3333-4.0456i 223.1667-5.057i 252.0833-5.5627i	0 Ai sin(82) 0 0 0 0 0 0 0 0 0 0 0 0 0 0 0 0 0 0 0	ngle	Admit.  12 1.8897-0.0417i  18897-0.0417i 1.8897-0.0417i	0 Phase
VL  λ 550 550 550 550 550 550 550 550 550	n0 1 1 1 1 1 1 1 1 1 1 1 1 1 1 1 1 1 1 1	0 Incide Angle 60 0 0 0 0 0 0 0 0 0 0 0 0 0 0 0 0 0 0	0 Prese - A Fresnel hosin(80) 0 0 0 0 0 0 0 0 0 0 0 0 0 0 0 0 0 0	Admit. η0 1 1 1 1 1 1 1 1 1 1 1 1 1 1 1 1 1 1	1.488 ir n1 1.488 1.488 1.488 1.488 1.488 1.488 1.488 1.488 1.488 1.488 1.488 1.488 1.488 1.488	0.04241 0.042 0.04241 0.04241 0.04241 0.04241 0.04241 0.04241 0.04241 0.04241 0.04241 0.04241 0.04241	Fi Comples N1 878-0.04 878-0.04 878-0.04 878-0.04 878-0.04 878-0.04 878-0.04 878-0.04 878-0.04 878-0.04 878-0.04	0   Im 1   Thick   d1   0   0   0   0   0   0   0   0   0	0 - PEDO1 - Op. Thk. N1d1 - O - O - O - O - O - O - O - O - O - O	0 F:PSS A sin(e) 0 0 0 0 0 0 0 0 0 0 0	1 ngle cos(01) 1 1 1 1 1 1 1 1 1 1 1 1 1 1 1 1 1 1	Admit.  11  1378-0.04  Admit.  11  178-0.04  178-0.04  178-0.04  178-0.04  178-0.04  178-0.04  178-0.04  178-0.04	Phase 51 0 0 0 0 0 0 0 0 0 0 0 0 0 0 0 0 0 0	1,8897 Ind- n2 1,8897 1,8897 1,8897 1,8897 1,8897 1,8897 1,8897 1,8897 1,8897 1,8897	0.042 k2 0.042 0.042 0.042 0.042 0.042 0.042 0.042 0.042 0.042 0.042 0.042	18897-0.0417i  Complex N2 1.8897-0.0417i	Thick d2 0 12.1 24.3 36.4 48.5 60.6 72.8 84.9 97 109 121 133 146	0  Film 2 - 17 Op. Thk. N2d2 0 22.9187-0.5057i 45.8333-1.0114; 91.8687-2.0228i 145.833-2.5285i 137.5-3.0342i 160.4167-3.5399i 183.3333-4.0456i 206.25-4.5513i 229.1667-5.057i 252.0833-5.5627i 275-6.0684i	0 All sin(e2) 0 0 0 0 0 0 0 0 0 0 0 0 0 0 0 0 0 0 0	ngle cos(62 1 1 1 1 1 1 1 1 1 1 1 1 1 1 1 1 1 1 1	1,8897-0,0417i  Admit.  1,2 1,8897-0,0417i	0 Phase 52 0 0.2617-0.0 0.5233-0.0 0.785-0.0 1.0467-0.0 1.57-0.0 2.0933-0.0 2.355-0.0 2.8783-0.0 3.14-0.06
VL  1  550  550  550  550  550  550  550	n0 1 1 1 1 1 1 1 1 1 1 1 1 1 1 1 1 1 1 1	0 Incide Angle 60 0 0 0 0 0 0 0 0 0 0 0 Incide Angle	0 ence - A Fresnel nosin(80) 0 0 0 0 0 0 0 0 0 0 0 0 0 0 ence - A	Admit. 10 1 1 1 1 1 1 1 1 1 1 1 1 1 1 1 1 1 1	1.488 In n1 1.488	0.04241  o.042 0.04241 0.042241 0.042241 0.042241 0.042241 0.042241 0.042241 0.042241 0.042241 0.042241 0.042241 0.042241 0.042241 0.042241 0.042241 0.042241 0.042241 0.042241 0.042241	File Comples N1 S78-0.04 File Comples	0   m 1   Thick d1   0   0   0   0   0   0   0   0   0	0 - PEDO1 - Op. Thk. N1d1 - O - O - O - O - O - O - O - O - O - O	0 F:PSS A sin(01) 0 0 0 0 0 0 0 0 0 0 0 0 0 0 0 0 0 0	1 cos(e1) 1 1 1 1 1 1 1 1 1 1 1 1 1 1 1 1 1 1	Admit.  11  1378-0.04  Admit.  11  178-0.04  178-0.04  178-0.04  178-0.04  178-0.04  178-0.04  178-0.04  178-0.04  178-0.04  Admit.	Phase 51 0 0 0 0 0 0 0 0 0 0 0 0 0 0 0 0 0 0	18997  Ind n2 18997 18997 18997 18997 18997 18997 18997 18997 18997	0.042 k2 0.042 0.042 0.042 0.042 0.042 0.042 0.042 0.042 0.042 0.042 0.042	18897-0.0417i  Complex N2 18897-0.0417i	Thick d2 0 12.1 24.3 36.4 48.5 60.6 72.8 84.9 97 109 121 133 146	0  Film 2 - 17 Op. Thk. N2d2 0 22.9167-0.5057i 45.8333-1.0114i 68.75-1.517i 91.6667-2.0228i 114.5833-2.5285i 137.5-3.0342i 160.4167-3.5399i 206.25-4.5513i 229.1667-5.057i 252.0833-5.5627i 275-6.0684i  Film 2 - 17 Op. Thk.	0 AI sin(02) 0 0 0 0 0 0 0 0 0 0 0 0 0 0 0 0 0 0	ngle cos(62 1 1 1 1 1 1 1 1 1 1 1 1 1 1 1 1 1 1 1	1.8897-0.0417i  Admit.  12 1.8897-0.0417i	0 Phase 0 0 0.2617-0.0 0.5233-0. 0.785-0.0 1.3083-0.0 1.3083-0.0 1.57-0.0 2.0933-0.0 2.355-0.0 2.8783-0.0 3.14-0.06
550  ↓ ↓ ↓ 550 550 550 550 550 550 550 5	n0 1 1 1 1 1 1 1 1 1 1 1 1 1 1 1 1 1 1 1	0 Incide Angle 60 0 0 0 0 0 0 0 0 0 0 0 Incide Angle Angle	0	Admit. η0 1 1 1 1 1 1 1 1 1 1 1 1 1 1 1 1 1 1	1488 Ir n1 1488 1488 1488 1488 1488 1488 1488 1488 1488 1488 1488 1488	0.04241  dex  k1 0.042 0.04241 0.04241 0.04241 0.04241 0.04241 0.04241 0.04241 0.04241 0.04241 0.04241 0.04241 0.04241 0.04241	878-0.04 Fi Comples N1 878-0.04 878-0.04 878-0.04 878-0.04 878-0.04 878-0.04 878-0.04 878-0.04 878-0.04 878-0.04 878-0.04 Fi Comples	0   m 1   Thick d1   0   0   0   0   0   0   0   0   0	0 - PEDO1 - Op. Thk. N1d1 - 0 - 0 - 0 - 0 - 0 - 0 - 0 - 0 - 0 - 0	0 F:PSS A sin(01) 0 0 0 0 0 0 0 0 0 0 0 0 0 F:PSS A sin(01)	1   ngle   cos(01)   1   1   1   1   1   1   1   1   1	Admit.  11 378-0.04  7878-0.04  7878-0.04  7878-0.04  7878-0.04  7878-0.04  7878-0.04  7878-0.04  7878-0.04  7878-0.04  Admit.  11	Phase 51 0 0 0 0 0 0 0 0 0 0 0 0 0 0 0 0 0 0	Ind Ind Ind Ind Ind Ind Ind Ind	0.042 k2 0.042 0.042 0.042 0.042 0.042 0.042 0.042 0.042 0.042 0.042 0.042 0.042 0.042 0.042	18897-0.0417i  Complex N2 18897-0.0417i	Thick d2 0 12.1 24.3 36.4 48.5 60.6 72.8 84.9 97 109 121 133 146	0  Film 2 - 17 Op. Thk. N2d2 0 22.9167-0.5057i 45.8333-1.0114i 68.75-1.517i 91.6667-2.0228i 114.5833-2.5285i 137.5-3.0342i 180.4167-3.5399i 183.3333-4.0456i 206.25-4.5513i 229.1667-5.057i 252.0833-5.5627i 275-6.0684i  Film 2 - 17 Op. Thk. N2d2	0 AI sin(62) 0 0 0 0 0 0 0 0 0 0 0 0 0 0 0 0 0 0 0	ngle cos(62 1 1 1 1 1 1 1 1 1 1 1 1 1 1 1 1 1 1 1	1.8897-0.0417i  Admit.  1.8897-0.0417i	0 Phase 52 0 0.2617-0.0 0.5233-0.0 0.785-0.0 1.3083-0.0 1.57-0.03 1.8317-0.0 2.0933-0.0 2.355-0.0 2.8783-0.0 3.14-0.06 Phase 52
λ 550 550 550 550 550 550 550 550 550 55	n0 1 1 1 1 1 1 1 1 1 1 1 1 1 1 1 1 1 1 1	0 Incide Angle 60 0 0 0 0 0 0 0 0 0 0 0 Incide Angle 60 0 Incide 60 0	0 ence - A Fresnel nosin(80) 0 0 0 0 0 0 0 0 0 0 0 0 0 0 ence - A	Admit. 10 1 1 1 1 1 1 1 1 1 1 1 1 1 1 1 1 1 1	1488 Ir Ir II 1488 1488 1488 1488 1488 1488 1488 1488 1488 1488 1488 1488 1488 1488	0.04241  dex  k1 0.042 0.042241 0.042241 0.042241 0.042241 0.042241 0.042241 0.042241 0.042241 0.042241 0.042241 0.042241 0.042241 0.042241 0.042241 0.042241 0.042241 0.042241	878-0.04 Fit Complex NI 878-0.04	0 Im 1 Thick d1 0 0 0 0 0 0 0 0 0 0 0 0 0 0 0 0 0 0	0 - PEDO1 0 0 0 0 0 0 0 0 0 0 0 0 0 0 0 0 0 0 0	0 F:PSS A sin(01) 0 0 0 0 0 0 0 0 0 0 0 0 0 sin(01) F:PSS A sin(01) 0 0 sin(01)	ngle	Admit.	Phase 51 0	18897  18897  18897  18897  18897  18897  18897  18897  18897  18897  18897  18897  18897	0.042  88  k2 0.042 0.042 0.042 0.042 0.042 0.042 0.042 0.042 0.042 0.042 0.042 0.042 0.042 0.042 0.042 0.042	18897-0.0417i  Complex N2 1.8897-0.0417i	Thick d2 0 12.1 24.3 36.4 48.5 60.6 72.8 84.9 97 109 121 133 146 Thick d2 24	0 Film 2 - IT Op. Thk. N2d2 0 22.9167-0.5057i 45.8333-1.0114i 68.75-1.517l 91.6667-2.0228i 114.5833-2.5285i 137.5-3.0342i 129.16667-5.057i 229.1667-5.057i 229.1667-5.057i 252.0833-5.5627i 275-6.0684i Film 2 - IT Op. Thk. N2d2 45.3528-1.0008i	0 Ai Sin(82) 0 0 0 0 0 0 0 0 0 0 0 0 0 0 0 0 0 0 0	ngle cos(62 1 1 1 1 1 1 1 1 1 1 1 1 1 1 1 1 1 1 1	1.8897-0.0417i  Admit.  12 1.8897-0.0417i	0 Phase 52 0 0.2617-0.0 0.785-0.0 1.0467-0.0 1.3083-0.0 1.577-0.03 1.8317-0.0 2.0933-0.0 2.355-0.0 2.36167-0.0 3.14-0.06 Phase 52 0.5178-0.0
\$50  \$\frac{1}{\lambda}\$ \$	n0 1 1 1 1 1 1 1 1 1 1 1 1 1 1 1 1 1 1 1	0 Incide Angle e0 0 0 0 0 0 0 0 0 0 0 Incide Angle e0 0 0 0 0 0 0 0 0 0 0 0 0 0 0 0 0 0	0  ence - A  Fresnel  0  0  0  0  0  0  0  0  0  0  0  0  0	Admit. 10 1 1 1 1 1 1 1 1 1 1 1 1 1 1 1 1 1 1	1488 Ir 11 1488	0.04241  o.04241 0.04241 0.042241 0.042241 0.042241 0.042241 0.042241 0.042241 0.042241 0.042241 0.042241 0.042241 0.042241 0.042241 0.042241 0.042241 0.042241 0.042241 0.042241 0.042241 0.042241	878-0.04 File Complete Miles 878-0.04 878-0.04 878-0.04 878-0.04 878-0.04 878-0.04 878-0.04 File Complete Miles 878-0.04 878-0.04 File Complete Miles 878-0.04 878-0.04 878-0.04	0 Im 1 Thick d1 0 0 0 0 0 0 0 0 0 0 0 0 0 0 0 0 0 0	O PEDO1 Op. This. Nidi O O O O O O O O O O O O O O O O O O O	0 F:PSS A sin(01) 0 0 0 0 0 0 0 0 0 0 0 0 F:PSS A sin(01) 0 0 0 0 0 0 0 0 0 0 0 0 0 0 0 0 0 0	ngle   cos(±1)   1   1   1   1   1   1   1   1   1	Admit.  11  Admit.  11  1378-0.04  Admit.  1378-0.04  Admit.  1378-0.04  Admit.	Phase 51 0 0 0 0 0 0 0 0 0 0 0 0 0 0 0 0 0 0	18897 Ind	0.042  88  k2 0.042	18897-0.0417i  Complex N2 18897-0.0417i	Thick d2 0 12.1 24.3 36.4 48.5 60.6 72.8 84.9 97 109 121 133 146 Thick d2 24 24	0 Film 2 - 17 Op. Thk. N2d2 0 22.9187-0.50571 45.8333-1.0141 68.75-1.5171 91.6667-2.02281 114.5833-2.52851 137.5-3.03421 160.4167-3.53991 183.3333-4.04561 206.25-4.55131 229.1667-5.0571 275-6.06841 Film 2 - 17 Op. Thk. N2d2 45.3528-1.00081	0 Ai sin(e2) 0 0 0 0 0 0 0 0 0 0 0 0 0 0 0 0 0 0 0	ngle cos(62 1 1 1 1 1 1 1 1 1 1 1 1 1	1.8897-0.0417i  Admit.  12 1.8897-0.0417i	Phass 52 2 0 0 0.2617-0.0 1.0467-0.0 1.570-0.0
VL  λ 550 550 550 550 550 550 550 550 550	n0 1 1 1 1 1 1 1 1 1 1 1 1 1 1 1 1 1 1 1	0 Incide Angle e0 0 0 0 0 0 0 0 0 0 0 Incide Angle Ang	0 ence - A Fresnel 0 0 0 0 0 0 0 0 0 0 0 0 0 Fresnel 0 0 0 0 0 0 0 0 0 0 0 0 0 0 0 0 0 0 0	$\begin{array}{c} \text{Admit.} \\ \eta 0 \\ 1 \\ 1 \\ 1 \\ 1 \\ 1 \\ 1 \\ 1 \\ 1 \\ 1 \\$	1488 Ir Ir II 1488	0.04241  o.04241 0.04241 0.04241 0.04241 0.04241 0.04241 0.042241	Fit Complet NI 878-0.04 Fit S78-0.04 F78-0.04	0 Im 1 Thick of 0 0 0 0 0 0 0 0 0 0 0 0 0 0 0 0 0 0	O PEDO1 Op. Thk. Nid1 O O O O O O O O O O O O O O O O O O O	0 F:PSS A sin(e1) 0 0 0 0 0 0 0 0 0 0 0 F:PSS A sin(e1) 0 0 0 0 0 0 0 0 0 0 0 0 0 0 0 0 0 0 0	ngle	Admit.  Admit.  1378-0.04  378-0.04  378-0.04  378-0.04  378-0.04  378-0.04  378-0.04  378-0.04  378-0.04  378-0.04  Admit.  11  378-0.04  Admit.  378-0.04	Phase 51 0 0 0 0 0 0 0 0 0 0 0 0 0 0 0 0 0 0	1,8937 1,8937	ex k2 0.042	18897-0.0417i  Complex N2 1.8897-0.0417i	Thick d2 0 12.1 24.3 36.4 48.5 60.6 72.8 84.9 97 121 133 146 Thick d2 24 24 24	0  Film 2 - 17 Op. Thk. N2d2 0 22.9167-0.5057i 45.8333-1.0114i 91.6867-2.0228i 114.5833-2.5285i 137.5-3.0342i 180.4167-3.5393i 229.1667-5.057i 252.0833-5.5627i 275-6.0684i  Film 2 - 17 Op. Thk. N2d2 45.3528-1.0008i 45.3528-1.0008i	0 Aisin(e2) 0 0 0 0 0 0 0 0 0 0 0 0 0 0 0 0 0 0 0	rigle   cos(62   1   1   1   1   1   1   1   1   1	1.8897-0.0417i  Admit.  12 1.8897-0.0417i	Phass 52 0 0.2617-0.0 .5233-0 1.0467-0.1 13083-0.0 157-0.0 13317-0.0 2.365-0.0 2.365-0.0 2.4667-0.0 578-0.0 578-0.0 0.5178-0.0
550  ↓ ↓ ↓ ↓ ↓ 550 550 550 550 550 550 5	n0 1 1 1 1 1 1 1 1 1 1 1 1 1 1 1 1 1 1 1	0 Incide Angle 60 0 0 0 0 0 0 0 0 0 0 0 0 0 0 0 0 0 0	0	$\begin{array}{c} \text{Admit.} \\ \eta 0 \\ 1 \\ 1 \\ 1 \\ 1 \\ 1 \\ 1 \\ 1 \\ 1 \\ 1 \\$	1488	0.04241  dex  k1 0.042 0.04241 0.04241 0.04241 0.04241 0.04241 0.04241 0.04241 0.04241 0.04241 0.04241 0.04241 0.04241 0.04241 0.04241 0.04241 0.04241 0.04241	Fit Completed N1   78-0.04	0 Im 1 Thick d1 0 0 0 0 0 0 0 0 0 0 0 0 0 0 0 0 0 0	0  -PEDO1 - Op. Thik. NId1 - Op. Thik. NId1 - Op.	0 F:PSS A sin(01) 0 0 0 0 0 0 0 0 0 0 0 0 0 F:PSS A sin(01) 0 0 0 0 0 0 0 0 0 0 0 0 0 0 0 0 0 0	ngle	Admit. 11 Admit. 11 Admit. 12 Admit. 12 Admit. 12 Admit. 12 Admit. 13 Admit. 14 Admit. 15 Admit. 15 Admit. 15 Admit. 16 Admit. 17 Admit.	Phase 51 0 0 0 0 0 0 0 0 0 0 0 0 0 0 0 0 0 0	18897 18897 18897 18897 18897 18897 18897 18897 18897 18897 18897 18897 18897 18897 18897 18897 18897	ex k2 0.042	Complex N2 1.8897-0.0417i	Thick d2 0 12.1 24.3 36.4 48.5 60.6 72.8 34.9 97 109 121 133 146 Thick d2 24 24 24 24	0  Film 2 - 17 Op. Thk. N2d2 0 22.9167-0.50571 45.8333-1.01141 68.75-1.5171 91.6667-2.02281 114.5833-2.52851 137.5-3.03421 180.4167-3.53991 183.3333-4.04561 206.25-4.55131 229.1667-50.571 252.0833-5.56271 252.0833-5.56271 Op. Thk. N2d2 45.3528-1.00081 45.3528-1.00081 45.3528-1.00081	0 Al sin(e2) 0 0 0 0 0 0 0 0 0 0 0 0 0 0 0 0 0 0 0	ngle cos(62 1 1 1 1 1 1 1 1 1 1 1 1 1	1.8897-0.0417i  Admit.  1.2 1.8897-0.0417i	Phass 52 2 0 0.6517-0.0 0.5233-0 0.785-0.0 1.0467-0.0 2.3857-0.0 2.3857-0.0 2.3857-0.0 2.3857-0.0 2.3857-0.0 5.787-0
\$\frac{\lambda}{\frac{\lambda}{550}}\$  \$\frac{\lambda}{\frac{\lambda}{550}}\$  \$\frac{\lambda}{550}\$	n0 1 1 1 1 1 1 1 1 1 1 1 1 1 1 1 1 1 1 1	0 Incide Angle 60 0 0 0 0 0 0 0 0 0 0 0 0 0 0 0 0 0 0	0 Prince - A Fresnel Hosin(80) 0 0 0 0 0 0 0 0 0 0 0 0 0 0 0 0 0 0	$\begin{array}{c} \text{Admit.} \\ \eta 0 \\ 1 \\ 1 \\ 1 \\ 1 \\ 1 \\ 1 \\ 1 \\ 1 \\ 1 \\$	1488 1488	0.04241  dex  k1 0.042 0.042241	578-0.04 File Complete M1 878-0.04 578-0.04 578-0.04 578-0.04 578-0.04 578-0.04 578-0.04 578-0.04 578-0.04 578-0.04 578-0.04 578-0.04 578-0.04 578-0.04 678-0.04 678-0.04	0 Im 1 Thick d1 0 0 0 0 0 0 0 0 0 0 0 0 0 0 0 0 0 0	O PEDO1 Op. Thk. Mid1 O O O O O O O O O O O O O O O O O O O	0 F:PSS A sin(61) 0 0 0 0 0 0 0 0 0 0 0 0 0 F:PSS A sin(61) 0 0 0 0 0 0 0 0 0 0 0 0 0 0 0 0 0 0 0	ngle   cos(61)   1   1   1   1   1   1   1   1   1	Admit.  11 378-0.04 378-0.04 378-0.04 378-0.04 378-0.04 378-0.04 378-0.04 378-0.04 378-0.04 378-0.04 378-0.04 378-0.04 378-0.04 378-0.04 378-0.04 378-0.04 378-0.04 378-0.04	Phase 51 0 0 0 0 0 0 0 0 0 0 0 0 0 0 0 0 0 0	1,8937 1,	0.042  k2 0.042	18897-0.0417i  Complex N2 1.8897-0.0417i	Thick d2 0 12.1 24.3 36.4 48.5 672.8 84.9 97 109 121 133 146 Thick d2 24 24 24 24 24	0 Film 2 - 17 Op. Thk. N2d2 0 22.9167-0.5057/ 45.8333-1.0114/ 68.75-1.5171/ 91.6667-2.0228/ 114.5833-2.5285/ 137.5-3.0342/ 136.457-3.5399/ 183.3333-4.0456/ 209.126-5.0634/ 229.1687-5.057/ 275-6.0684/ Film 2 - 17 Op. Thk. N2d2 45.3528-1.0008/ 45.3528-1.0008/ 45.3528-1.0008/ 45.3528-1.0008/	0 Aisin(62) 0 0 0 0 0 0 0 0 0 0 0 0 0 0 0 0 0 0 0	rigle   cos(62   1   1   1   1   1   1   1   1   1	1.8897-0.0417i  Admit.  12 1.8897-0.0417i	Phass 52 0 0.0617-0.0 0.0523-0.0 0.785-0.0 1.57-0.0 1.57-0.0 1.57-0.0 1.57-0.0 1.57-0.0 1.57-0.0 1.57-0.0 1.57-0.0 1.57-0.0 0.5178-0
550  ↓ ↓ ↓ ↓ 550 550 550 550 550 550 550	n0 1 1 1 1 1 1 1 1 1 1 1 1 1 1 1 1 1 1 1	0   Incide   Angle   60   0   0   0   0   0   0   0   0	0  Pence - A  0  0  0  0  0  0  0  0  0  0  0  0  0	$\begin{array}{c} \text{Admit.} \\ \eta 0 \\ 1 \\ 1 \\ 1 \\ 1 \\ 1 \\ 1 \\ 1 \\ 1 \\ 1 \\$	1488 1488	0.04241  odex  k1 0.042 0.042241	\$78-0.04 File Complet	0 Im 1 Thick d1 0 0 0 0 0 0 0 0 0 0 0 0 0 0 0 0 0 0	O PEDO1 Op. Thk. Nidi O O O O O O O O O O O O O O O O O O O	0 F:PSS A Sin(01) 0 0 0 0 0 0 0 0 0 0 0 F:PSS A Sin(01) 0 0 0 0 0 0 0 0 0 0 0 0 0 0 0 0 0 0	ngle   cos(±1)   1   1   1   1   1   1   1   1   1	Admit.  n1  378-0.04  7878-0.04  7878-0.04  7878-0.04  7878-0.04  7878-0.04  7878-0.04  7878-0.04  7878-0.04  7878-0.04  7878-0.04  7878-0.04  7878-0.04  7878-0.04	Phase 51 0 0 0 0 0 0 0 0 0 0 0 0 0 0 0 0 0 0	1,8937 1,	0.042  k2 0.042	Complex N2 1.8897-0.04171 1.8897-0.04171 1.8897-0.04171 1.8897-0.04171 1.8897-0.04171 1.8897-0.04171 1.8897-0.04171 1.8897-0.04171 1.8897-0.04171 1.8897-0.04171 1.8897-0.04171 1.8897-0.04171 1.8897-0.04171 1.8897-0.04171 1.8897-0.04171 1.8897-0.04171 1.8897-0.04171 1.8897-0.04171 1.8897-0.04171	Thick d2 0 12.1 24.3 36.4 48.5 60.6 72.8 84.9 97 109 121 133 146 24 24 24 24 24 24 24	0 Film 2 - 1T Op. Thk. N2d2 0 22.9167-0.5057i 45.8333-1.014i 68.75-1.517i 91.6667-2.0228i 114.5833-2.5285i 137.5-3.0342i 160.4167-3.5399i 183.3333-4.0456i 206.25-4.5513i 229.1667-5.057i 275-6.0884i Film 2 - 1T Op. Thk. N2d2 45.3528-1.0008i 45.3528-1.0008i 45.3528-1.0008i 45.3528-1.0008i 45.3528-1.0008i	0 All sin(e2) 0 0 0 0 0 0 0 0 0 0 0 0 0 0 0 0 0 0 0	1 1 1 1 1 1 1 1 1 1 1 1 1 1 1 1 1 1 1	1.8897-0.0417i  Admit.  12 1.8897-0.0417i	Phass 52 0 0.2617-0.0 0.785-0.0 0.785-0.0 157-0.0 157-0.0 157-0.0 157-0.0 2.3753-0.0 2.3753-0.0 5778-0.0 0.5778-0.0 0.5778-0.0 0.5778-0.0 0.5778-0.0
550  ↓ ↓ ↓ 550  550  550  550  550  550	n0 1 1 1 1 1 1 1 1 1 1 1 1 1 1 1 1 1 1 1	Incide	0 ence - A fresnel 0 0 0 0 0 0 0 0 0 0 0 0 0 0 0 0 0 0 0	$\begin{array}{c} \text{Admit.} \\ \eta 0 \\ 1 \\ 1 \\ 1 \\ 1 \\ 1 \\ 1 \\ 1 \\ 1 \\ 1 \\$	1488 1488	0.04241  0.042 0.04241 0.042241	Fire Complete Miles (1988) (19	0 Im 1 Thick d1 0 0 0 0 0 0 0 0 0 0 0 0 0 0 0 0 0 0	O PEDO1 Op. Thk. Mid1 O O O O O O O O O O O O O O O O O O O	0 F:PSS A Sin(01) 0 0 0 0 0 0 0 0 0 0 0 0 0 F:PSS A Sin(01) 0 0 0 0 0 0 0 0 0 0 0 0 0 0 0 0 0 0	ngle	Admit. 11 Admit. 12 Admit. 12 Admit. 13 Admit. 13 Admit. 14 Admit. 17 Admit.	Phase 51 0 0 0 0 0 0 0 0 0 0 0 0 0 0 0 0 0 0	1,8937 1,8937	0.042  k2 0.042	18897-0.0417i  Complex N2 18897-0.0417i	Thick d2 0 12.1 24.3 36.4 48.5 60.6 72.8 84.9 17.1 133 146 146 146 146 146 146 146 146 146 146	0 Film 2 - 17 Op. Thk. N2d2 0 22.9187-0.5057i 45.8333-1.0114; 91.8687-2.0228i 114.5833-2.5285i 137.5-3.0342i 160.4167-3.5399i 183.3333-4.0456i 206.25-4.5513i 229.1667-5.057i 275-6.0684i Film 2 - 17 Op. Thk. N2d2 45.3528-1.0008i 45.3528-1.0008i 45.3528-1.0008i 45.3528-1.0008i 45.3528-1.0008i 45.3528-1.0008i 45.3528-1.0008i 45.3528-1.0008i	0 Sin(82) 0 0 0 0 0 0 0 0 0 0 0 0 0 0 0 0 0 0 0	rigle   cos(62   1   1   1   1   1   1   1   1   1	1.8897-0.0417i  Admit.  12 1.8897-0.0417i	Phass 52 2 0 0 0.2617-0.0 0.5233-0 0.5233-0 0.5233-0 0.5233-0 0.5233-0 0.5235-0 0.5235-0 0.578
550  ↓ ↓ ↓ ↓ 550 550 550 550 550 550 550	n0 1 1 1 1 1 1 1 1 1 1 1 1 1 1 1 1 1 1 1	0 Incide Angle 60 0 0 0 0 0 0 0 0 0 0 0 0 0 0 0 0 0 0	0	$\begin{array}{c} \text{Admit.} \\ \eta 0 \\ 1 \\ 1 \\ 1 \\ 1 \\ 1 \\ 1 \\ 1 \\ 1 \\ 1 \\$	1488 1488 1488 1488 1488 1488 1488 1488	dex k1 0.04241	Fit Complex N1 (Complex N1 (Fit N2 (Fi	0 Im 1 Thick d1 0 0 0 0 0 0 0 0 0 0 0 0 0 0 0 0 0 0	O PEDO1 Op.Thk. Nid1 O O O O O O O O O O O O O O O O O O O	0 F:PSS A sin(01) 0 0 0 0 0 0 0 0 0 0 0 0 F:PSS A sin(01) 0 0 0 0 0 0 0 0 0 0 0 0 0 0 0 0 0 0	ngle	Admit.  11  778-0.04  Admit.  11  778-0.04	Phase 51 0 0 0 0 0 0 0 0 0 0 0 0 0 0 0 0 0 0	1,8937 1,8937	0.042  k2 0.042	18897-0.0417i  Complex N2 18897-0.0417i	Thick d2 0 12.1 24.3 36.4 48.5 60.6 72.8 84.9 97 109 121 133 146 Thick d2 24 24 24 24 24 24 24 24 24 24 24 24 24	0  Film 2 - 17 Op. Thk. N2d2 0 22.9167-0.50571 45.8333-1.01141 68.75-1.5171 91.6667-2.02281 114.5833-2.52851 137.5-3.03421 180.4167-3.53991 183.3333-4.04561 206.25-4.55131 229.1667-5.0571 252.0833-5.56271 275-6.06841  Film 2 - 17 Op. Thk. N2d2 45.3528-1.00081 45.3528-1.00081 45.3528-1.00081 45.3528-1.00081 45.3528-1.00081 45.3528-1.00081 45.3528-1.00081 45.3528-1.00081	0 All sin(e2) 0 0 0 0 0 0 0 0 0 0 0 0 0 0 0 0 0 0 0	1 1 1 1 1 1 1 1 1 1 1 1 1 1 1 1 1 1 1	18897-0.0417i  Admit.  12 18897-0.0417i	Phass 52 2 0 0.523-0.0578-0.05
550  ↓ ↓ ↓ 550  550  550  550  550  550	n0 1 1 1 1 1 1 1 1 1 1 1 1 1 1 1 1 1 1 1	Incide	0 ence - A fresnel 0 0 0 0 0 0 0 0 0 0 0 0 0 0 0 0 0 0 0	$\begin{array}{c} \text{Admit.} \\ \eta 0 \\ 1 \\ 1 \\ 1 \\ 1 \\ 1 \\ 1 \\ 1 \\ 1 \\ 1 \\$	1488 1488	dex k1 0.04241	Fire Complex N1 (Complex N1 (Fire N2 (F	0 Im 1 Thick d1 0 0 0 0 0 0 0 0 0 0 0 0 0 0 0 0 0 0	O PEDO1 Op. Thk. Mid1 O O O O O O O O O O O O O O O O O O O	0 F:PSS A sin(01) 0 0 0 0 0 0 0 0 0 0 0 0 F:PSS A sin(01) 0 0 0 0 0 0 0 0 0 0 0 0 0 0 0 0 0 0	ngle	Admit.  11  778-0.04  Admit.  11  778-0.04	Phase 51 0 0 0 0 0 0 0 0 0 0 0 0 0 0 0 0 0 0	1,8937 1,8937	0.042  k2 0.042	18897-0.0417i  Complex N2 18897-0.0417i	Thick d2 0 12.1 24.3 36.4 48.5 60.6 72.8 84.9 17.1 133 146 146 146 146 146 146 146 146 146 146	0 Film 2 - 17 Op. Thk. N2d2 0 22.9187-0.5057i 45.8333-1.0114; 91.8687-2.0228i 114.5833-2.5285i 137.5-3.0342i 160.4167-3.5399i 183.3333-4.0456i 206.25-4.5513i 229.1667-5.057i 275-6.0684i Film 2 - 17 Op. Thk. N2d2 45.3528-1.0008i 45.3528-1.0008i 45.3528-1.0008i 45.3528-1.0008i 45.3528-1.0008i 45.3528-1.0008i 45.3528-1.0008i 45.3528-1.0008i	0 Sin(82) 0 0 0 0 0 0 0 0 0 0 0 0 0 0 0 0 0 0 0	1 1 1 1 1 1 1 1 1 1 1 1 1 1 1 1 1 1 1	1.8897-0.0417i  Admit.  12 1.8897-0.0417i	Phass 52 2 0 0.523-0.0578-0.05
550  ↓ ↓ ↓ ↓ ↓ 550  550  550  550  550	n0 1 1 1 1 1 1 1 1 1 1 1 1 1 1 1 1 1 1 1	0 Incide Angle 60 0 0 0 0 0 0 0 0 0 0 0 0 0 0 0 0 0 0	0	$\begin{array}{c} \text{Admit.} \\ \eta 0 \\ 1 \\ 1 \\ 1 \\ 1 \\ 1 \\ 1 \\ 1 \\ 1 \\ 1 \\$	1488 1488 1488 1488 1488 1488 1488 1488	0.04241  dex  k1 0.042 0.042241	878-0.04 File Complete M1 878-0.04 878-0.04 878-0.04 878-0.04 878-0.04 878-0.04 878-0.04 878-0.04 878-0.04 878-0.04 878-0.04 878-0.04 878-0.04 878-0.04 878-0.04 878-0.04 878-0.04 878-0.04	0 Im 1 Thick d1 0 0 0 0 0 0 0 0 0 0 0 0 0 0 0 0 0 0	O PEDO1 Op.Thk. Nid1 O O O O O O O O O O O O O O O O O O O	0 F:PSS A sin(01) 0 0 0 0 0 0 0 0 0 0 0 0 F:PSS A sin(01) 0 0 0 0 0 0 0 0 0 0 0 0 0 0 0 0 0 0	ngle   cos(61)   1   1   1   1   1   1   1   1   1	Admit.  11 378-0.04 378-0.04 378-0.04 378-0.04 378-0.04 378-0.04 378-0.04 378-0.04 378-0.04 378-0.04 378-0.04 378-0.04 378-0.04 378-0.04 378-0.04 378-0.04	Phase 51 0 0 0 0 0 0 0 0 0 0 0 0 0 0 0 0 0 0	1,8937 1,	0.042  k2 0.042	18897-0.0417i  Complex N2 18897-0.0417i	Thick d2 0 12.1 24.3 36.4 48.5 60.6 72.8 84.9 97 109 121 133 146 Thick d2 24 24 24 24 24 24 24 24 24 24 24 24 24	0  Film 2 - 17 Op. Thk. N2d2 0 22.9167-0.50571 45.8333-1.01141 68.75-1.5171 91.6667-2.02281 114.5833-2.52851 137.5-3.03421 180.4167-3.53991 183.3333-4.04561 206.25-4.55131 229.1667-5.0571 252.0833-5.56271 275-6.06841  Film 2 - 17 Op. Thk. N2d2 45.3528-1.00081 45.3528-1.00081 45.3528-1.00081 45.3528-1.00081 45.3528-1.00081 45.3528-1.00081 45.3528-1.00081 45.3528-1.00081	O AI Sin(82) 0 0 0 0 0 0 0 0 0 0 0 0 0 0 0 0 0 0 0	1 1 1 1 1 1 1 1 1 1 1 1 1 1 1 1 1 1 1	18897-0.0417i  Admit.  12 18897-0.0417i	0 Phase 52 0 0.2617-0.0 0.783-0.0 1.3083-0.0 1.57-0.03 1.57-0.03 2.365-0.0 2.365-0.0 2.3783-0.0 3.14-0.06 Phase 52 0.5178-0.0 0.5178-0.0 0.5178-0.0 0.5178-0.0 0.5178-0.0 0.5178-0.0 0.5178-0.0 0.5178-0.0 0.5178-0.0
VL  1 550 550 550 550 550 550 550 550 550	n0 1 1 1 1 1 1 1 1 1 1 1 1 1 1 1 1 1 1 1	Incide	0 Pence - A O O O O O O O O O O O O O O O O O O O	Admit.	1488 1488 1488 1488 1488 1488 1488 1488	0.04241  odex  k1 0.042 0.042241	578-0.04 File Complete MI 878-0.04 578-0.04	0 Im 1 Thick d1 0 0 0 0 0 0 0 0 0 0 0 0 0 0 0 0 0 0	PEDD1  Op. Thk. Mid1  O  O  O  O  O  O  O  O  O  O  O  O  O	0 F:PSS A sin(e) 0 0 0 0 0 0 0 0 0 0 0 0 0 0 0 0 0 0 0	ngle   cos(61)   1   1   1   1   1   1   1   1   1	Admit.  11 378-0.04	Phase 51 0 0 0 0 0 0 0 0 0 0 0 0 432-0.00 884-0.00 1559-0.00 227-0.00 228-0.00 886-0.00	1,8937 1,	88 k2 0.042	18897-0.0417i  Complex N2 18897-0.0417i	Thick d2 0 12.1 24.3 36.4 48.5 60.6 72.8 84.9 97 109 121 133 146 Thick d2 24 24 24 24 24 24 24 24 24 24 24 24 24	0 Film 2 - IT Op. Thk. N2d2 0 22.9167-0.5057i 45.8333-1.0114i 68.75-1.517l' 91.6667-2.0228i 114.5833-2.5285i 137.5-3.0342i 160.4167-3.5399i 183.333-4.9456i 206.25-4.5513i 223.1667-5.057i 225.0833-5.5627i 275-6.0684i Film 2 - IT Op. Thk. N2d2 45.3528-1.0008i	O All sin(82) 0 0 0 0 0 0 0 0 0 0 0 0 0 0 0 0 0 0 0	trgle	18897-0.0417i  Admit.  12 18897-0.0417i 18997-0.0417i 18997-0.0417i 18997-0.0417i 18997-0.0417i 18997-0.0417i 18997-0.0417i 18997-0.0417i	0 Phase 52 0 0.2617-0.00 0.5233-0.0 1.0467-0.0 1.3083-0.0 1.573-0.0 2.355-0.0 2.355-0.0 2.355-0.0 2.314-0.06: Phase 52 0.5178-0.0 0.5178-0.0 0.5178-0.0 0.5178-0.0 0.5178-0.0 0.5178-0.0 0.5178-0.0 0.5178-0.0 0.5178-0.0
VL  1 550 550 550 550 550 550 550 550 550	n0 1 1 1 1 1 1 1 1 1 1 1 1 1 1 1 1 1 1 1	0 Incide Angle 60 0 0 0 0 0 0 0 0 0 0 0 0 0 0 0 0 0 0	0 ence - A Fresnel 0 0 0 0 0 0 0 0 0 0 0 0 0 0 0 0 0 0 0	Admit.	1488 1488	0.04241  0.042 0.04241	578-0.04 Fire Complete M1 878-0.04 578-0.04	0 Im 1 Thick d1 0 0 0 0 0 0 0 0 0 0 0 0 0 0 0 0 0 0	PEDO1  Op. Thk. Mid1  O	0 F:PSS A sin(01) 0 0 0 0 0 0 0 0 0 0 0 0 0 0 0 0 0 0	ngle   cos(±1)   1   1   1   1   1   1   1   1   1	Admit.  11 378-0.04	Phase 0 0 0 0 0 0 0 0 0 0 0 0 0 0 432-0.00 864-0.00 955-0.00 591-0.00 591-0.00 318-0.01	1,8937 1,	ex k2 0.042	18897-0.0417i  Complex N2 18897-0.0417i	Thick d2 44 24 24 24 24 24 24 24 24 24 24 24 24	0 Film 2 - 17 Op. Thk. N2d2 0 22.9187-0.5057i 45.8333-1.0114; 91.8687-2.0228i 114.5833-2.5285i 137.5-3.0342i 160.4167-3.5399i 183.3333-4.0456i 206.25-4.5513i 229.1667-5.057i 275-6.0884i Film 2 - 17 Op. Thk. 0p. Thk. 45.3528-1.0008i	O AI SIN(82) 0 0 0 0 0 0 0 0 0 0 0 0 0 0 0 0 0 0 0	trgle	1.8897-0.0417i  Admit.  12 1.8897-0.0417i	0 Phase 52 0 0.2617-0.00 0.5233-0.0 0.785-0.01 13083-0.01 157-0.03 18317-0.04 2.355-0.0 2.355-0.0 2.3753-0.0 6.5178-0.0 0.5178-0.0 0.5178-0.0 0.5178-0.0 0.5178-0.0 0.5178-0.0 0.5178-0.0 0.5178-0.0 0.5178-0.0 0.5178-0.0 0.5178-0.0 0.5178-0.0 0.5178-0.0 0.5178-0.0 0.5178-0.0 0.5178-0.0
\$500  \$\frac{1}{\lambda}\$	n0 1 1 1 1 1 1 1 1 1 1 1 1 1 1 1 1 1 1 1	Incide	0 Pence - A O O O O O O O O O O O O O O O O O O O	Admit.	1488 1488 1488 1488 1488 1488 1488 1488	0.04241  0.042 0.04241	Fire Complex N1 (178-0.04 Fire Complex N1 (178-0.04 F78-0.04 F78-0	0 Im 1 Thick d1 0 0 0 0 0 0 0 0 0 0 0 0 0 0 0 0 0 0	PEDD1 Op. Thk. Mid1 O O O O O O O O O O O O O O O O O O O	OF:PSS A Sin(e1) O O O O O O O O O O O O O O O O O O O	ngle	Admit.  11  778-0.04  7878-0.04	Phase 51 0 0 0 0 0 0 0 0 0 0 0 432-0.00 884-0.00 1559-0.00 22-7.00 22-7.00 886-0.00	1,8937 1,8937	ex k2 0.042	18897-0.0417i  Complex N2 18897-0.0417i	Thick d2	0 Film 2 - IT Op. Thk. N2d2 0 22.9167-0.5057i 45.8333-1.0114i 68.75-1.517l' 91.6667-2.0228i 114.5833-2.5285i 137.5-3.0342i 160.4167-3.5399i 183.333-4.9456i 206.25-4.5513i 223.1667-5.057i 225.0833-5.5627i 275-6.0684i Film 2 - IT Op. Thk. N2d2 45.3528-1.0008i	O All sin(82) 0 0 0 0 0 0 0 0 0 0 0 0 0 0 0 0 0 0 0	trgle	18897-0.0417i  Admit.  12 18897-0.0417i 18997-0.0417i 18997-0.0417i 18997-0.0417i 18997-0.0417i 18997-0.0417i 18997-0.0417i 18997-0.0417i	Phase 52 0 0.2617-0.00 0.7835-0.01 1.0467-0.0 1.3083-0.01 1.57-0.03 2.0933-0.0 2.355-0.0 2.6167-0.09 2.8783-0.0 0.5178-0.0 0.5178-0.0 0.5178-0.0 0.5178-0.0 0.5178-0.0 0.5178-0.0 0.5178-0.0 0.5178-0.0 0.5178-0.0 0.5178-0.0

Table 5 (cont'd)

Film 3 - Ag		Film 4 - ITO Substrate - Parglene C																
	ngle	Admit.	Phase	Inc	lex	Complex	Thick.	Op. Thk.	_	ngle	Admit.	Phase		Index		An	_	Admit.
	) cos(83	η3	83	n4	k4	N4	d4	N4d4	sin(84)	cos(64)	η4	ō <b>4</b>	n4	k4	N4	sin(64)	cos(64)	η4
0.137   3.073   375-3.072   0   0   0	1	375-3.07	0	1.8897	0.042	1.8897-0.0417i	0	0	0	- 1	1.8897-0.0417i	0	1,5936	0	1.5936	0	- 1	1,5936
0.137   3.073   375-3.072   0   0   0	1	375-3.07	0	1.8897	0.042	1.8897-0.0417i	12.13	22,9167-0,5057i	0	1	1.8897-0.0417i	0.2617-0.0058i	1.5936	0	1.5936	0	1	1,5936
0.137 3.073 375-3.072 0 0 0	1 1	375-3.07	0	1.8897	0.042		24.25	45.8333-1.0114i	0	1	1.8897-0.04171	0.5233-0.0115i	1.5936	0	1.5936	0	1	1.5936
0.137 3.073 375-3.074 0 0 0	++	375-3.07	0	1.8897	0.042	1.8897-0.0417	36.38	68.75-1.5171i	0	1	1.8897-0.04171	0.785-0.01731	1,5936	0	1,5936	0	1	1,5936
0.137   3.073   375-3.073   0   0   0   0   0   0   0   0   0	++	375-3.07 375-3.07	0	1.8897 1.8897	0.042	1.8897-0.0417i 1.8897-0.0417i	48.51 60.64	91.6667-2.0228i 114.5833-2.5285i	0	1	1.8897-0.0417i 1.8897-0.0417i	1.0467-0.0231i 1.3083-0.0289i	1.5936 1.5936	0	1.5936 1.5936	0	1	1.5936 1.5936
0.137 3.073 375-3.074 0 0 0	+ †	375-3.07	0	1.8897	0.042	1.8897-0.0417i	72.76	137.5-3.0342i	0	1	1.8897-0.04171	1.57-0.0346i	1.5936	0	1.5936	0	1	1.5936
0.137 3.073 375-3.072 0 0 0	<del>l i</del>	375-3.07	0	1.8897	0.042	1.8897-0.0417i	84.89	160,4167-3,5399i	Ů	i	1.8897-0.0417i	1.8317-0.0404i	1.5936	0	1.5936	0	1	1.5936
0.137 3.073 375-3.072 0 0 0	T i	375-3.07	0	1.8897	0.042	1.8897-0.0417i	97.02	183.3333-4.0456i	ō	i	1.8897-0.0417i	2.0933-0.0462i	1.5936	Ō	1.5936	Ō	1	1.5936
0.137 3.073 375-3.073 0 0 0	1	375-3.07	0	1.8897	0.042	1.8897-0.0417i	109.1	206.25-4.5513i	0	1	1.8897-0.0417i	2.355-0.052i	1.5936	0	1.5936	0	1	1.5936
0.137 3.073 375-3.072 0 0 0	1	375-3.07	0	1.8897	0.042	1.8897-0.0417i	121.3	229.1667-5.057i	0	1	1.8897-0.0417i	2.6167-0.0577i	1.5936	0	1.5936	0	- 1	1.5936
0.137   3.073   375-3.074   0   0   0	1	375-3.07	0	1.8897	0.042	1.8897-0.0417i	133.4	252.0833-5.5627	0	- 1	1.8897-0.0417i	2.8783-0.0635i	1.5936	0	1.5936	0	- 1	1.5936
0.137   3.073   375-3.072   0   0   0	1	375-3.07	0	1.8897	0.042	1.8897-0.0417i	145.5	275-6.0684i	0	- 1	1.8897-0.0417i	3.14-0.0693i	1.5936	0	1.5936	0	- 1	1,5936
(C++1)																		
Ctrl) Film 3 - Ag		1 1						Film 4 - I						-	bstrate	- Pary		
	ngle	Admit.		Inc		Complex	Thick.	Op. Thk.		igle	Admit.	Phase	-4	Index	874	An	_	Admit.
>=====================================	) cos(83		53 0	n4 1.8897	k4 0.042	N4 1.8897-0.0417i	d4 20	N4d4 37.794-0.834i	sin(84)	cos(64)	η4 1.8897-0.0417i	54 0.4315-0.0095i	n4 1.5936	k4 0	N4 15920	sin(84)	cos(64)	η4 15000
0.137   3.073   375-3.073   0   0   0   0   0   0   0   0   0	1	375-3.07 375-3.07		1.8897	0.042		20	37.794-0.834i 37.794-0.834i	0	1	1.8897-0.04171	0.4315-0.0095i	1,5936	0	1.5936 1.5936	0	1	1.5936 1.5936
0.137 3.073 375-3.072 7.46 0256-22.916 0	1	375-3.07 375-3.07		1.8897	0.042	1.8897-0.04171	20	37.794-0.834i 37.794-0.834i	0	1	1.8897-0.04171	0.4315-0.00951	1.5936	0	1.5936	0	1	1.5936
0.137 3.073 375-3.073 49.3 031140.833 0	1	375-3.07		1.8897	0.042	1.8897-0.04171	20	37.794-0.834i	0	1	1.8897-0.04171	0.4315-0.0035i	1.5936	0	1.5936	0	1	1,5936
0.137 3.073 375-3.074 29.8 1023-91.666 0	1	375-3.07			0.042		20	37.794-0.834i	0	i	1.8897-0.0417i	0.4315-0.0095i	1.5936	0	1.5936	0	1	1.5936
0.137 3.073 375-3.073 37.3 278-114.58 0	1	375-3.07		1.8897	0.042	1.8897-0.0417i	20	37.794-0.834i	Ö	1	1.8897-0.0417i	0.4315-0.0095i	1.5936	0	1.5936	0	1	1.5936
0.137 3.073 375-3.073 44.8 3.1534-137.5 0	1	375-3.07		1.8897	0.042		20	37.794-0.834i	0	- 1	1.8897-0.0417i	0.4315-0.0095i	1.5936	0	1.5936	0	- 1	1.5936
0.137 3.073 375-3.072 52.2 789-160.41 0	1	375-3.07	082-1.83	1.8897	0.042	1.8897-0.0417i	20	37.794-0.834i	0	1	1.8897-0.0417i	0.4315-0.0095i	1.5936	0	1.5936	0	- 1	1,5936
0.137   3.073   375-3.072   59.7   045-183.33   0	1	375-3.07		1.8897	0.042	1.8897-0.0417i	20	37.794-0.834i	0	1	1.8897-0.0417i	0.4315-0.0095i	1.5936	0	1.5936	0	- 1	1,5936
0.137 3.073 375-3.073 67.1 2301-206.2 0	1	375-3.07		1.8897	0.042	1.8897-0.0417i	20	37.794-0.834i	0	1	1.8897-0.0417i	0.4315-0.0095i	1.5936	0	1.5936	0	- 1	1,5936
0.137 3.073 375-3.073 74.6 2556-229.16 0	1 !	375-3.07		1.8897	0.042	1.8897-0.0417i	20	37.794-0.834i	0	1	1.8897-0.0417i	0.4315-0.0095i	1.5936	0	1.5936	0	1	1,5936
0.137 3.073 3375-3.074 82 812-252.08 0	+ !-	375-3.07		1.8897	0.042	1.8897-0.04171	20	37.794-0.834i	0	1	1.8897-0.04171	0.4315-0.0095i	1.5936	0	1.5936	0	1	1.5936
0.137   3.073   375-3.072   89.5   2.3068-275   0	1	375-3.07	1405-3.	1.8897	0.042	1.8897-0.0417i	20	37.794-0.834i	0	1	1.8897-0.0417i	0.4315-0.0095i	1.5936	0	1,5936	0	- 1	1.5936
Film 3 - Ag								Film 4 - I	TO					Ç.	hetrate	- Pare	lana C	
	nale	Admit	Phase	Inc	lex	Complex	Thick	Film 4 - I	_	nale	Admit	Phase				- Pary		Admit
Index Complex Thick, Op. Thk. A	ngle	Admit.		Inc n4		Complex N4	Thick.	Op. Thk.	Ar	ngle	Admit.	Phase 84	n4	Index		An	gle	Admit.
		Admit. 193 375-3.07	83	Inc n4 1.8897	k4	Complex N4 1.8897-0.0417i	Thick.		_	gle cos(84)	Admit. η4 1.8897-0.0417i	Phase 54 0.4315-0.0095i	n4 1.5936			_		Admit. η4 1.5936
Index		η3	53 148-0.3	n4	k4	N4	d4	Op. Thk. N4d4	Ar sin(64)	_	η4	54		Index k4	N4	An sin(64)	gle	η4
Index		η3 375-3.07	53 148-0.3 148-0.3	n4 1.8897	k4 0.042	N4 1.8897-0.0417i	d4 20	Op. Thk. N4d4 37.794-0.834i	Ar sin(84) 0	_	η4 1.8897-0.0417i	84 0.4315-0.0095i	1.5936	Index k4 0	N4 1.5936	An sin(64) 0	gle	η4 1.5936
Index         Complex Thick, Op. This.         AB           n3         k3         M3         d3         M3d3         sine3           0.137         3.073         375-3072         945         294-2903         0           0.137         3.073         375-3073         9.45         2994-2903         0           0.137         3.073         375-3073         9.45         2994-2903         0           0.137         3.073         375-3074         9.45         2994-2903         0	) cos(83 1	η3 375-3.07 375-3.07 375-3.07 375-3.07	53 148-0.3 148-0.3 148-0.3 148-0.3	n4 1.8897 1.8897 1.8897 1.8897	0.042 0.042 0.042 0.042 0.042	N4 1.8897-0.0417i 1.8897-0.0417i 1.8897-0.0417i 1.8897-0.0417i	d4 20 20 20 20 20	Op. Thk. N4d4 37.794-0.834i 37.794-0.834i 37.794-0.834i 37.794-0.834i	Ar sin(84) 0 0 0 0 0	cos(θ4) 1 1	η4 1.8897-0.0417i 1.8897-0.0417i	54 0.4315-0.0095i 0.4315-0.0095i 0.4315-0.0095i 0.4315-0.0095i	1.5936 1.5936 1.5936 1.5936	k4 0	N4 1.5936 1.5936 1.5936 1.5936	An sin(84) 0 0 0	gle	η4 1.5936 1.5936 1.5936 1.5936
Index         Complex Thick, Op.	) cos(83 1	η3 375-3.07 375-3.07 375-3.07 375-3.07	53 148-0.3 148-0.3 148-0.3 148-0.3	n4 1.8897 1.8897 1.8897 1.8897	k4 0.042 0.042 0.042 0.042 0.042	N4 1.8897-0.0417i 1.8897-0.0417i 1.8897-0.0417i 1.8897-0.0417i	d4 20 20 20 20 20 20	Op. Thk. N4d4 37.794-0.834i 37.794-0.834i 37.794-0.834i 37.794-0.834i 37.794-0.834i	Ar sin(84) 0 0 0 0	cos(θ4) 1 1	η4 1.8897-0.0417i 1.8897-0.0417i 1.8897-0.0417i 1.8897-0.0417i	54 0.4315-0.0095i 0.4315-0.0095i 0.4315-0.0095i 0.4315-0.0095i	1.5936 1.5936 1.5936 1.5936 1.5936	k4 0 0 0 0 0	N4 1.5936 1.5936 1.5936 1.5936 1.5936	An sin(64) 0 0 0 0	gle	η4 1.5936 1.5936 1.5936 1.5936 1.5936
Index         Complex Thick, Dp. Thick, Op.	) cos(83 1	η3 375-3.07 375-3.07 375-3.07 375-3.07 375-3.07	53 148-0.3 148-0.3 148-0.3 148-0.3 148-0.3	n4 1.8897 1.8897 1.8897 1.8897 1.8897	k4 0.042 0.042 0.042 0.042 0.042	N4 1.8897-0.0417i 1.8897-0.0417i 1.8897-0.0417i 1.8897-0.0417i 1.8897-0.0417i	20 20 20 20 20 20 20 20	Op. Thk. N4d4 37.794-0.834i 37.794-0.834i 37.794-0.834i 37.794-0.834i 37.794-0.834i 37.794-0.834i	Ar sin(04) 0 0 0 0 0 0 0 0	cos(θ4) 1 1	n4 1.8897-0.0417i 1.8897-0.0417i 1.8897-0.0417i 1.8897-0.0417i 1.8897-0.0417i 1.8897-0.0417i	54 0.4315-0.0095i 0.4315-0.0095i 0.4315-0.0095i 0.4315-0.0095i 0.4315-0.0095i	1.5936 1.5936 1.5936 1.5936 1.5936 1.5936	k4 0 0 0 0 0	N4 1.5936 1.5936 1.5936 1.5936 1.5936	An sin(04) 0 0 0 0 0	gle	η4 1.5936 1.5936 1.5936 1.5936 1.5936 1.5936
Index         Complex Thick         Op. Thick         A           n3         k3         M3         d3         M3d3         sine3           0.137         3.073         375-3074         9.45         2994-2903         0           0.137         3.073         375-3074         9.45         2994-2903         0           0.137         3.073         375-3074         9.45         2994-2903         0           0.137         3.073         375-3074         9.45         2994-2903         0           0.137         3.073         375-3077         9.45         2994-2903         0           0.137         3.073         375-3074         9.45         2994-2903         0           0.137         3.073         375-3074         9.45         2994-2903         0	) cos(83 1	η3 375-3.07 375-3.07 375-3.07 375-3.07 375-3.07 375-3.07 375-3.07	53 148-0.3 148-0.3 148-0.3 148-0.3 148-0.3	n4 1.8897 1.8897 1.8897 1.8897 1.8897 1.8897	k4 0.042 0.042 0.042 0.042 0.042 0.042	N4 1.8897-0.0417i 1.8897-0.0417i 1.8897-0.0417i 1.8897-0.0417i 1.8897-0.0417i 1.8897-0.0417i	20 20 20 20 20 20 20 20 20	Op. Thk. N4d4 37.794-0.834i 37.794-0.834i 37.794-0.834i 37.794-0.834i 37.794-0.834i 37.794-0.834i 37.794-0.834i	Ar sin(64) 0 0 0 0 0 0 0 0 0 0	cos(θ4) 1 1	n4 1.8897-0.0417i 1.8897-0.0417i 1.8897-0.0417i 1.8897-0.0417i 1.8897-0.0417i 1.8897-0.0417i	54 0.4315-0.0095i 0.4315-0.0095i 0.4315-0.0095i 0.4315-0.0095i 0.4315-0.0095i 0.4315-0.0095i	1.5936 1.5936 1.5936 1.5936 1.5936 1.5936	0 0 0 0 0 0 0	N4 1.5936 1.5936 1.5936 1.5936 1.5936 1.5936	An sin(84) 0 0 0 0 0 0 0 0 0 0 0 0 0 0 0 0 0 0 0	gle	η4 1.5936 1.5936 1.5936 1.5936 1.5936 1.5936 1.5936
Index         Complex Thick, Dp. Thick, and 3         Qp. Thick, a	) cos(03 1 1 1 1 1 1 1 1 1	η3 375-3.07 375-3.07 375-3.07 375-3.07 375-3.07 375-3.07 375-3.07	53 148-0.3 148-0.3 148-0.3 148-0.3 148-0.3 148-0.3	n4 1.8897 1.8897 1.8897 1.8897 1.8897 1.8897 1.8897	k4 0.042 0.042 0.042 0.042 0.042 0.042 0.042	N4 1.8897-0.0417i 1.8897-0.0417i 1.8897-0.0417i 1.8897-0.0417i 1.8897-0.0417i 1.8897-0.0417i 1.8897-0.0417i	20 20 20 20 20 20 20 20 20 20	Op. Thk. N4d4 37.794-0.834i 37.794-0.834i 37.794-0.834i 37.794-0.834i 37.794-0.834i 37.794-0.834i 37.794-0.834i 37.794-0.834i	Ar sin(64) 0 0 0 0 0 0 0 0 0 0 0 0	cos(θ4) 1 1	n4 1.8897-0.0417i 1.8897-0.0417i 1.8897-0.0417i 1.8897-0.0417i 1.8897-0.0417i 1.8897-0.0417i 1.8897-0.0417i 1.8897-0.0417i	54 0.4315-0.0095i 0.4315-0.0095i 0.4315-0.0095i 0.4315-0.0095i 0.4315-0.0095i 0.4315-0.0095i 0.4315-0.0095i	15936 15936 15936 15936 15936 15936 15936	0 0 0 0 0 0 0 0	N4 15936 15936 15936 15936 15936 15936 15936	An sin(84) 0 0 0 0 0 0 0 0 0 0 0	gle	η4 1.5936 1.5936 1.5936 1.5936 1.5936 1.5936 1.5936 1.5936
Index         Complex Thick, Dp. Thick, and 3         Op. Thick, and 3         M33         M33         M33         M33         M33         M33         M343         sine3           0.137         3.073         375-3.072         345         394-29.03         0           0.137         3.073         375-3.073         345         394-29.03         0           0.137         3.073         375-3.074         945         394-29.03         0           0.137         3.073         375-3.074         945         394-29.03         0           0.137         3.073         375-3.077         345         394-29.03         0           0.137         3.073         375-3.074         345         394-29.03         0           0.137         3.073         375-3.074         345         394-29.03         0           0.137         3.073         375-3.074         345         394-29.03         0           0.137         3.073         375-3.074         345         394-29.03         0           0.137         3.073         375-3.074         345         394-29.03         0           0.137         3.073         375-3.074         345         394-29.03         0 <td>) cos(83 1</td> <td>η3 375-3.07 375-3.07 375-3.07 375-3.07 375-3.07 375-3.07 375-3.07 375-3.07</td> <td>53 148-0.3 148-0.3 148-0.3 148-0.3 148-0.3 148-0.3 148-0.3</td> <td>n4 1.8897 1.8897 1.8897 1.8897 1.8897 1.8897 1.8897 1.8897</td> <td>k4 0.042 0.042 0.042 0.042 0.042 0.042 0.042 0.042</td> <td>N4 1.8897-0.0417i 1.8897-0.0417i 1.8897-0.0417i 1.8897-0.0417i 1.8897-0.0417i 1.8897-0.0417i 1.8897-0.0417i 1.8897-0.0417i</td> <td>d4 20 20 20 20 20 20 20 20 20 20 20 20</td> <td>Op. Thk. N4d4 37.794-0.834i 37.794-0.834i 37.794-0.834i 37.794-0.834i 37.794-0.834i 37.794-0.834i 37.794-0.834i 37.794-0.834i</td> <td>Ar sin(84) 0 0 0 0 0 0 0 0 0 0 0 0 0 0</td> <td>cos(θ4) 1 1</td> <td>n4 1.8897-0.0417i 1.8897-0.0417i 1.8897-0.0417i 1.8897-0.0417i 1.8897-0.0417i 1.8897-0.0417i 1.8897-0.0417i 1.8897-0.0417i</td> <td>54 0.4315-0.0095i 0.4315-0.0095i 0.4315-0.0095i 0.4315-0.0095i 0.4315-0.0095i 0.4315-0.0095i 0.4315-0.0095i 0.4315-0.0095i</td> <td>15936 15936 15936 15936 15936 15936 15936 15936</td> <td>  Index   k4   0   0   0   0   0   0   0   0</td> <td>N4 1.5936 1.5936 1.5936 1.5936 1.5936 1.5936 1.5936 1.5936</td> <td>An sin(84) 0 0 0 0 0 0 0 0 0 0 0 0 0 0</td> <td>gle</td> <td>η4 1.5936 1.5936 1.5936 1.5936 1.5936 1.5936 1.5936 1.5936 1.5936</td>	) cos(83 1	η3 375-3.07 375-3.07 375-3.07 375-3.07 375-3.07 375-3.07 375-3.07 375-3.07	53 148-0.3 148-0.3 148-0.3 148-0.3 148-0.3 148-0.3 148-0.3	n4 1.8897 1.8897 1.8897 1.8897 1.8897 1.8897 1.8897 1.8897	k4 0.042 0.042 0.042 0.042 0.042 0.042 0.042 0.042	N4 1.8897-0.0417i 1.8897-0.0417i 1.8897-0.0417i 1.8897-0.0417i 1.8897-0.0417i 1.8897-0.0417i 1.8897-0.0417i 1.8897-0.0417i	d4 20 20 20 20 20 20 20 20 20 20 20 20	Op. Thk. N4d4 37.794-0.834i 37.794-0.834i 37.794-0.834i 37.794-0.834i 37.794-0.834i 37.794-0.834i 37.794-0.834i 37.794-0.834i	Ar sin(84) 0 0 0 0 0 0 0 0 0 0 0 0 0 0	cos(θ4) 1 1	n4 1.8897-0.0417i 1.8897-0.0417i 1.8897-0.0417i 1.8897-0.0417i 1.8897-0.0417i 1.8897-0.0417i 1.8897-0.0417i 1.8897-0.0417i	54 0.4315-0.0095i 0.4315-0.0095i 0.4315-0.0095i 0.4315-0.0095i 0.4315-0.0095i 0.4315-0.0095i 0.4315-0.0095i 0.4315-0.0095i	15936 15936 15936 15936 15936 15936 15936 15936	Index   k4   0   0   0   0   0   0   0   0	N4 1.5936 1.5936 1.5936 1.5936 1.5936 1.5936 1.5936 1.5936	An sin(84) 0 0 0 0 0 0 0 0 0 0 0 0 0 0	gle	η4 1.5936 1.5936 1.5936 1.5936 1.5936 1.5936 1.5936 1.5936 1.5936
Index	) cos(03 1 1 1 1 1 1 1 1 1	η3 375-3.07 375-3.07 375-3.07 375-3.07 375-3.07 375-3.07 375-3.07 375-3.07 375-3.07 375-3.07	53 148-0.3 148-0.3 148-0.3 148-0.3 148-0.3 148-0.3 148-0.3	n4 1.8897 1.8897 1.8897 1.8897 1.8897 1.8897 1.8897 1.8897 1.8897	k4 0.042 0.042 0.042 0.042 0.042 0.042 0.042 0.042 0.042	N4 1.8897-0.0417i 1.8897-0.0417i 1.8897-0.0417i 1.8897-0.0417i 1.8897-0.0417i 1.8897-0.0417i 1.8897-0.0417i 1.8897-0.0417i	d4 20 20 20 20 20 20 20 20 20 20 20 20 20	Op. Thk. N4d4 37.794-0.834i	Ar sin(64)  0  0  0  0  0  0  0  0  0  0  0  0  0	cos(θ4) 1 1	η4 1.8897-0.0417i 1.8897-0.0417i 1.8897-0.0417i 1.8897-0.0417i 1.8897-0.0417i 1.8897-0.0417i 1.8897-0.0417i 1.8897-0.0417i 1.8897-0.0417i	54 0.4315-0.0095i 0.4315-0.0095i 0.4315-0.0095i 0.4315-0.0095i 0.4315-0.0095i 0.4315-0.0095i 0.4315-0.0095i 0.4315-0.0095i	1,5936 1,5936 1,5936 1,5936 1,5936 1,5936 1,5936 1,5936 1,5936	0 0 0 0 0 0 0 0	N4 1.5936 1.5936 1.5936 1.5936 1.5936 1.5936 1.5936 1.5936 1.5936	An sin(64) 0 0 0 0 0 0 0 0 0 0 0 0 0 0 0	gle	η4 1.5936 1.5936 1.5936 1.5936 1.5936 1.5936 1.5936 1.5936 1.5936 1.5936
Index         Complex Thick, Dp. Thick, and 3 k3         N3         d3         M3d3 sines         sines           0.137         3.073         375-3074         9.45         2994-2903         0           0.137         3.073         375-3074         9.45         2994-2903         0           0.137         3.073         375-3074         9.45         2994-2903         0           0.137         3.073         375-3074         9.45         2994-2903         0           0.137         3.073         375-3074         9.45         2994-2903         0           0.137         3.073         375-3074         9.45         2994-2903         0           0.137         3.073         375-3074         9.45         2994-2903         0           0.137         3.073         375-3074         9.45         2994-2903         0           0.137         3.073         375-3074         9.45         2994-2903         0           0.137         3.073         375-3074         9.45         2994-2903         0           0.137         3.073         375-3074         9.45         2994-2903         0           0.137         3.073         375-3077         9.45	) cos(03 1 1 1 1 1 1 1 1 1	η3 375-3.07 375-3.07 375-3.07 375-3.07 375-3.07 375-3.07 375-3.07 375-3.07 375-3.07 375-3.07 375-3.07	53 148-0.3 148-0.3 148-0.3 148-0.3 148-0.3 148-0.3 148-0.3 148-0.3	n4 1.8897 1.8897 1.8897 1.8897 1.8897 1.8897 1.8897 1.8897 1.8897 1.8897	k4 0.042 0.042 0.042 0.042 0.042 0.042 0.042 0.042 0.042 0.042	N4 1.8897-0.0417i 1.8897-0.0417i 1.8897-0.0417i 1.8897-0.0417i 1.8897-0.0417i 1.8897-0.0417i 1.8897-0.0417i 1.8897-0.0417i 1.8897-0.0417i	d4 20 20 20 20 20 20 20 20 20 20 20 20 20	Op. Thk. N4d4 37.794-0.834i	Ar sin(84) 0 0 0 0 0 0 0 0 0 0 0 0 0 0	cos(θ4) 1 1	η4 1.8897-0.0417i 1.8897-0.0417i 1.8897-0.0417i 1.8897-0.0417i 1.8897-0.0417i 1.8897-0.0417i 1.8897-0.0417i 1.8897-0.0417i 1.8897-0.0417i	54 0.4315-0.0095i 0.4315-0.0095i 0.4315-0.0095i 0.4315-0.0095i 0.4315-0.0095i 0.4315-0.0095i 0.4315-0.0095i 0.4315-0.0095i 0.4315-0.0095i	1,5936 1,5936 1,5936 1,5936 1,5936 1,5936 1,5936 1,5936 1,5936 1,5936	0 0 0 0 0 0 0 0 0	N4 15936 15936 15936 15936 15936 15936 15936 15936 15936 15936	An sin(64)  0  0  0  0  0  0  0  0  0  0  0  0  0	gle	η4 1.5936 1.5936 1.5936 1.5936 1.5936 1.5936 1.5936 1.5936 1.5936 1.5936 1.5936
Index         Complex Thick, 10p. Thick, 20p.	) cos(03 1 1 1 1 1 1 1 1 1	n3 375-3.07 375-3.07 375-3.07 375-3.07 375-3.07 375-3.07 375-3.07 375-3.07 375-3.07 375-3.07 375-3.07 375-3.07	53 148-0.3 148-0.3 148-0.3 148-0.3 148-0.3 148-0.3 148-0.3 148-0.3 148-0.3	n4 1.8897 1.8897 1.8897 1.8897 1.8897 1.8897 1.8897 1.8897 1.8897	k4 0.042 0.042 0.042 0.042 0.042 0.042 0.042 0.042 0.042 0.042	N4 1.8897-0.0417i 1.8897-0.0417i 1.8897-0.0417i 1.8897-0.0417i 1.8897-0.0417i 1.8897-0.0417i 1.8897-0.0417i 1.8897-0.0417i 1.8897-0.0417i	d4 20 20 20 20 20 20 20 20 20 20 20 20 20	Op. Thk. N4d4 37.794-0.834i	Ar sin(64)  0  0  0  0  0  0  0  0  0  0  0  0  0	cos(θ4) 1 1	η4 1.8897-0.0417i 1.8897-0.0417i 1.8897-0.0417i 1.8897-0.0417i 1.8897-0.0417i 1.8897-0.0417i 1.8897-0.0417i 1.8897-0.0417i 1.8897-0.0417i	0.4315-0.0095i 0.4315-0.0095i 0.4315-0.0095i 0.4315-0.0095i 0.4315-0.0095i 0.4315-0.0095i 0.4315-0.0095i 0.4315-0.0095i 0.4315-0.0095i 0.4315-0.0095i	1,5936 1,5936 1,5936 1,5936 1,5936 1,5936 1,5936 1,5936 1,5936	0 0 0 0 0 0 0 0	N4 1.5936 1.5936 1.5936 1.5936 1.5936 1.5936 1.5936 1.5936 1.5936	An sin(64) 0 0 0 0 0 0 0 0 0 0 0 0 0 0 0	gle	η4 1.5936 1.5936 1.5936 1.5936 1.5936 1.5936 1.5936 1.5936 1.5936 1.5936 1.5936 1.5936
Index         Complex Thick, 10p. Thick, 2nd         Op. Thick, 2nd         Add           n3         k3         M3         d3         M3d3         sine3           0.137         3.073         375-307         9.45         2994-2903         0           0.137         3.073         375-307         9.45         2994-2903         0           0.137         3.073         375-307         9.45         2994-2903         0           0.137         3.073         375-307         9.45         2994-2903         0           0.137         3.073         375-307         9.45         2994-2903         0           0.137         3.073         375-307         9.45         2994-2903         0           0.137         3.073         375-307         9.45         2994-2903         0           0.137         3.073         375-307         9.45         2994-2903         0           0.137         3.073         375-307         9.45         2994-2903         0           0.137         3.073         375-307         9.45         2994-2903         0           0.137         3.073         375-307         9.45         2994-2903         0           <	) cos(03 1 1 1 1 1 1 1 1 1	η3 375-3.07 375-3.07 375-3.07 375-3.07 375-3.07 375-3.07 375-3.07 375-3.07 375-3.07 375-3.07 375-3.07	53 148-0.3 148-0.3 148-0.3 148-0.3 148-0.3 148-0.3 148-0.3 148-0.3 148-0.3	n4 1.8897 1.8897 1.8897 1.8897 1.8897 1.8897 1.8897 1.8897 1.8897 1.8897 1.8897	k4 0.042 0.042 0.042 0.042 0.042 0.042 0.042 0.042 0.042 0.042	N4 1.8897-0.0417i 1.8897-0.0417i 1.8897-0.0417i 1.8897-0.0417i 1.8897-0.0417i 1.8897-0.0417i 1.8897-0.0417i 1.8897-0.0417i 1.8897-0.0417i 1.8897-0.0417i	20 20 20 20 20 20 20 20 20 20 20 20 20 2	Op. Thk. N444 37.794-0.834i	Ar sin(84) 0 0 0 0 0 0 0 0 0 0 0 0 0 0 0 0 0 0 0	cos(θ4) 1 1	18897-0.04171 1.8897-0.04171 1.8897-0.04171 1.8897-0.04171 1.8897-0.04171 1.8897-0.04171 1.8897-0.04171 1.8897-0.04171 1.8897-0.04171 1.8897-0.04171 1.8897-0.04171	54 0.4315-0.0095i 0.4315-0.0095i 0.4315-0.0095i 0.4315-0.0095i 0.4315-0.0095i 0.4315-0.0095i 0.4315-0.0095i 0.4315-0.0095i 0.4315-0.0095i	1,5936 1,5936 1,5936 1,5936 1,5936 1,5936 1,5936 1,5936 1,5936 1,5936 1,5936	Index   k4   0   0   0   0   0   0   0   0   0   0	N4 15936 15936 15936 15936 15936 15936 15936 15936 15936 15936 15936	An sin(84) 0 0 0 0 0 0 0 0 0 0 0 0 0 0 0 0 0 0 0	gle	η4 1.5936 1.5936 1.5936 1.5936 1.5936 1.5936 1.5936 1.5936 1.5936 1.5936 1.5936
Index         Complex Thick, Dp. Thick, and 3         Op. Thick, sines; and 3         AS         M3         d3         M3d3         sines; and 3           0.137         3.073         375-3.073         9.45         2994-29.03         0         0         0.137         3.073         375-3.073         9.45         2994-29.03         0         0         0.137         3.073         375-3.074         9.45         2994-29.03         0         0         0.137         3.073         375-3.074         9.45         2994-29.03         0         0         0.137         3.073         375-3.074         9.45         2994-29.03         0         0         0.137         3.073         375-3.074         9.45         2994-29.03         0         0         0.137         3.073         375-3.074         9.45         2994-29.03         0         0         0.137         3.073         375-3.074         9.45         2994-29.03         0         0         0.137         3.073         375-3.074         9.45         2994-29.03         0         0         0         0.137         3.073         375-3.074         9.45         2994-29.03         0         0         0         0.137         3.073         375-3.074         9.45         2994-29.03         0	) cos(03 1 1 1 1 1 1 1 1 1	η3 375-3.07 375-3.07 375-3.07 375-3.07 375-3.07 375-3.07 375-3.07 375-3.07 375-3.07 375-3.07 375-3.07	53 148-0.3 148-0.3 148-0.3 148-0.3 148-0.3 148-0.3 148-0.3 148-0.3 148-0.3 148-0.3	n4 1.8897 1.8897 1.8897 1.8897 1.8897 1.8897 1.8897 1.8897 1.8897 1.8897 1.8897	k4 0.042 0.042 0.042 0.042 0.042 0.042 0.042 0.042 0.042 0.042	N4 1.8897-0.0417i 1.8897-0.0417i 1.8897-0.0417i 1.8897-0.0417i 1.8897-0.0417i 1.8897-0.0417i 1.8897-0.0417i 1.8897-0.0417i 1.8897-0.0417i 1.8897-0.0417i	20 20 20 20 20 20 20 20 20 20 20 20 20 2	Op. Thk. N444 37.794-0.834i	Ar sin(84) 0 0 0 0 0 0 0 0 0 0 0 0 0 0 0 0 0 0 0	cos(θ4) 1 1	18897-0.04171 1.8897-0.04171 1.8897-0.04171 1.8897-0.04171 1.8897-0.04171 1.8897-0.04171 1.8897-0.04171 1.8897-0.04171 1.8897-0.04171 1.8897-0.04171 1.8897-0.04171	0.4315-0.0095i 0.4315-0.0095i 0.4315-0.0095i 0.4315-0.0095i 0.4315-0.0095i 0.4315-0.0095i 0.4315-0.0095i 0.4315-0.0095i 0.4315-0.0095i 0.4315-0.0095i	1,5936 1,5936 1,5936 1,5936 1,5936 1,5936 1,5936 1,5936 1,5936 1,5936 1,5936	0 0 0 0 0 0 0 0 0 0 0 0	N4 1.5936 1.5936 1.5936 1.5936 1.5936 1.5936 1.5936 1.5936 1.5936 1.5936 1.5936 1.5936	An sin(84) 0 0 0 0 0 0 0 0 0 0 0 0 0 0 0 0 0 0 0	gle cos(64) 1 1 1 1 1 1 1 1 1 1 1 1 1	η4 1.5936 1.5936 1.5936 1.5936 1.5936 1.5936 1.5936 1.5936 1.5936 1.5936 1.5936 1.5936 1.5936
Index	) cos(e3	n3 375-3.07 375-3.07 375-3.07 375-3.07 375-3.07 375-3.07 375-3.07 375-3.07 375-3.07 375-3.07 375-3.07 375-3.07	53 148-0.3 148-0.3 148-0.3 148-0.3 148-0.3 148-0.3 148-0.3 148-0.3 148-0.3	n4 1.8897 1.8897 1.8897 1.8897 1.8897 1.8897 1.8897 1.8897 1.8897 1.8897 1.8897	k4 0.042 0.042 0.042 0.042 0.042 0.042 0.042 0.042 0.042 0.042 0.042	N4 1.8897-0.0417i	d4 20 20 20 20 20 20 20 20 20 20 20 20 20	Op. Thk. N444 37.794-0.834i	Ar sin(84) 0 0 0 0 0 0 0 0 0 0 0 0 0 0 0 0 0 0 0	cos(θ4) 1 1	18897-0.04171 1.8897-0.04171 1.8897-0.04171 1.8897-0.04171 1.8897-0.04171 1.8897-0.04171 1.8897-0.04171 1.8897-0.04171 1.8897-0.04171 1.8897-0.04171 1.8897-0.04171	0.4315-0.0095i 0.4315-0.0095i 0.4315-0.0095i 0.4315-0.0095i 0.4315-0.0095i 0.4315-0.0095i 0.4315-0.0095i 0.4315-0.0095i 0.4315-0.0095i 0.4315-0.0095i	1,5936 1,5936 1,5936 1,5936 1,5936 1,5936 1,5936 1,5936 1,5936 1,5936 1,5936	Index	N4 15936 15936 15936 15936 15936 15936 15936 15936 15936 15936 15936 15936 15936	An sin(84) 0 0 0 0 0 0 0 0 0 0 0 0 0 0 0 0 0 0 0	gle	η4 1.5936 1.5936 1.5936 1.5936 1.5936 1.5936 1.5936 1.5936 1.5936 1.5936 1.5936 1.5936 1.5936
Index	) cos(83 1 1 1 1 1 1 1 1 1 1 1 1 1 1 1 1 1 1 1	η3 375-3.07 375-3.07 375-3.07 375-3.07 375-3.07 375-3.07 375-3.07 375-3.07 375-3.07 375-3.07 375-3.07 375-3.07	53 148-0.3 148-0.3 148-0.3 148-0.3 148-0.3 148-0.3 148-0.3 148-0.3 148-0.3 148-0.3	n4 1.8897 1.8897 1.8897 1.8897 1.8897 1.8897 1.8897 1.8897 1.8897 1.8897 1.8897	k4 0.042 0.042 0.042 0.042 0.042 0.042 0.042 0.042 0.042 0.042 0.042	N4 1.8897-0.0417i	d4 20 20 20 20 20 20 20 20 20 20 20 20 20	Op. Thk. N4d4 37.794-0.834i	Ar sin(64)  0  0  0  0  0  0  0  0  0  0  0  0  0	00(84) 1 1 1 1 1 1 1 1 1 1 1 1 1 1 1 1 1 1 1	η4 1.8897-0.0417i	0.4315-0.0095i	1,5936 1,5936 1,5936 1,5936 1,5936 1,5936 1,5936 1,5936 1,5936 1,5936 1,5936 1,5936 1,5936	Index	N4 1.5936 1.5936 1.5936 1.5936 1.5936 1.5936 1.5936 1.5936 1.5936 1.5936 1.5936 1.5936 1.5936	Ansin(64)  O O O O O O O O O O O O O O O O O O	gle	η4 15936 15936 15936 15936 15936 15936 15936 15936 15936 15936 15936 15936 15936 15936 15936
Index	) cos(e3	η3 375-3.07 375-3.07 375-3.07 375-3.07 375-3.07 375-3.07 375-3.07 375-3.07 375-3.07 375-3.07 375-3.07 375-3.07 375-3.07	53 148-0.3 148-0.3 148-0.3 148-0.3 148-0.3 148-0.3 148-0.3 148-0.3 148-0.3 148-0.3 148-0.3 148-0.3	n4 1.8897 1.8897 1.8897 1.8897 1.8897 1.8897 1.8897 1.8897 1.8897 1.8897 1.8897	k4   0.042   0.042	N4 1.8897-0.0417i	04 20 20 20 20 20 20 20 20 20 20 20 20 20	Op. Thk. N4d4 37.794-0.834i	Ar sin(64)  0  0  0  0  0  0  0  0  0  0  0  0  0	008(84) 1 1 1 1 1 1 1 1 1 1 1 1 1 1 1 1 1 1 1	η4 1,8897-0,0417i	0.4315-0.0095i	15936 15936 15936 15936 15936 15936 15936 15936 15936 15936 15936 15936 15936 15936	Index   k4   0   0   0   0   0   0   0   0   0   0	N4 1.5936 1.5936 1.5936 1.5936 1.5936 1.5936 1.5936 1.5936 1.5936 1.5936 1.5936 1.5936 1.5936 1.5936	An sin(64) 0 0 0 0 0 0 0 0 0 0 0 0 0	gle	π <sup>4</sup> 1.5936 1.5936 1.5936 1.5936 1.5936 1.5936 1.5936 1.5936 1.5936 1.5936 1.5936 1.5936 1.5936 1.5936 1.5936 1.5936
Index	) cos(83 1 1 1 1 1 1 1 1 1 1 1 1 1 1 1 1 1 1 1	η3 375-3.07 375-3.07 375-3.07 375-3.07 375-3.07 375-3.07 375-3.07 375-3.07 375-3.07 375-3.07 375-3.07 375-3.07 375-3.07 375-3.07 375-3.07 375-3.07	53 148-0.3 148-0.3 148-0.3 148-0.3 148-0.3 148-0.3 148-0.3 148-0.3 148-0.3 148-0.3 148-0.3 148-0.3	n4 1.8897 1.8897 1.8897 1.8897 1.8897 1.8897 1.8897 1.8897 1.8897 1.8897 1.8897 1.8897 1.8897 1.8897 1.8897 1.8897	k4 0.042 0.042 0.042 0.042 0.042 0.042 0.042 0.042 0.042 0.042 0.042	N4 1.8897-0.0417i	04 20 20 20 20 20 20 20 20 20 20 20 20 20	Op. Thk. N4d4 37.794-0.834i	Ar sin(84)  0  0  0  0  0  0  0  0  0  0  0  0  0	008(84) 1 1 1 1 1 1 1 1 1 1 1 1 1 1 1 1 1 1 1	η4 1,8897-0,0417i	0.4315-0.0095i	1.5936 1.5936 1.5936 1.5936 1.5936 1.5936 1.5936 1.5936 1.5936 1.5936 1.5936 1.5936 1.5936 1.5936 1.5936	Index   k4   0   0   0   0   0   0   0   0   0   0	N4 1.5936 1.5936 1.5936 1.5936 1.5936 1.5936 1.5936 1.5936 1.5936 1.5936 1.5936 1.5936 1.5936 1.5936 1.5936	Ansin(64)  O O O O O O O O O O O O O O O O O O	gle	π <sup>4</sup> 1.5936 1.5936 1.5936 1.5936 1.5936 1.5936 1.5936 1.5936 1.5936 1.5936 1.5936 1.5936 1.5936 1.5936 1.5936 1.5936 1.5936 1.5936
Index	) cos(83 1 1 1 1 1 1 1 1 1 1 1 1 1 1 1 1 1 1 1	η3 375-3.07 375-3.07 375-3.07 375-3.07 375-3.07 375-3.07 375-3.07 375-3.07 375-3.07 375-3.07 375-3.07 375-3.07 375-3.07 375-3.07 375-3.07	53 148-0.3 148-0.3 148-0.3 148-0.3 148-0.3 148-0.3 148-0.3 148-0.3 148-0.3 148-0.3 148-0.3	n4 18897 18897 18897 18897 18897 18897 18897 18897 18897 18997 18997 18997 18997	k4   0.042   0.042 	N4 1.8897-0.0417i	04 20 20 20 20 20 20 20 20 20 20 20 20 20	Op. Thk. N444 37.794-0.834i	Ar sin(64) 0 0 0 0 0 0 0 0 0 0 0 0 0 0 0 0 TO Ar sin(64) 0 0 0 0 0 0 0 0 0 0 0 0 0 0 0 0 0 0 0	008(84) 1 1 1 1 1 1 1 1 1 1 1 1 1 1 1 1 1 1 1	η4 1.8897-0.0417i	0.4315-0.0095i	1.5936 1.5936 1.5936 1.5936 1.5936 1.5936 1.5936 1.5936 1.5936 1.5936 1.5936 1.5936 1.5936 1.5936 1.5936	Index	N4 1.5936 1.5936 1.5936 1.5936 1.5936 1.5936 1.5936 1.5936 1.5936 1.5936 1.5936 1.5936 1.5936 1.5936 1.5936 1.5936	Annotation (Annotation (Annota	gle	π <sup>4</sup> 1.5936 1.5936 1.5936 1.5936 1.5936 1.5936 1.5936 1.5936 1.5936 1.5936 1.5936 1.5936 1.5936 1.5936 1.5936 1.5936 1.5936 1.5936
Index		η3 375-3.07 375-3.07 375-3.07 375-3.07 375-3.07 375-3.07 375-3.07 375-3.07 375-3.07 375-3.07 375-3.07 375-3.07 375-3.07 375-3.07 375-3.07 375-3.07	53 148-0.3 148-0.3 148-0.3 148-0.3 148-0.3 148-0.3 148-0.3 148-0.3 148-0.3 148-0.3 148-0.3 148-0.3 148-0.3	n4 18897 18897 18897 18897 18897 18897 18897 18897 18897 18897 18897 18897 18897 18897	k4 0.042 0.042 0.042 0.042 0.042 0.042 0.042 0.042 0.042 0.042 0.042 0.042 0.042 0.042	N4 1.8897-0.0417i	04 20 20 20 20 20 20 20 20 20 20 20 20 20	Op. Thk. N4d4 37.794-0.834i	Arr sin(84) 0 0 0 0 0 0 0 0 0 0 0 0 0 0 0 0 0 0 0	008(84) 1 1 1 1 1 1 1 1 1 1 1 1 1 1 1 1 1 1 1	η4 1.8897-0.0417i	0.4315-0.0095i	15936 15936 15936 15936 15936 15936 15936 15936 15936 15936 15936 15936 15936 15936 15936 15936 15936 15936	Index	N4 15936 15936 15936 15936 15936 15936 15936 15936 15936 15936 15936 15936 15936 15936 15936	Anna (Anna (	gle	π <sup>4</sup> 1,5336 1,5
Index	) cos(83	η3 375.3.07	53 148-0.3 148-0.3 148-0.3 148-0.3 148-0.3 148-0.3 148-0.3 148-0.3 148-0.3 148-0.3 148-0.3 148-0.3 148-0.3 148-0.3 148-0.3 148-0.3 148-0.3 148-0.3 148-0.3	n4 18897 18897 18897 18897 18897 18897 18897 18897 18897 18897 18897 18897 18897 18897 18897	k4 0.042 0.042 0.042 0.042 0.042 0.042 0.042 0.042 0.042 0.042 0.042 0.042 0.042 0.042 0.042	N4 1.8897-0.0417i	04 20 20 20 20 20 20 20 20 20 20 20 20 20	Op. Thk. N4d4 37.794-0.834i	Ar sin(e4) 0 0 0 0 0 0 0 0 0 0 0 0 0 0 0 0 0 0 0	008(84) 1 1 1 1 1 1 1 1 1 1 1 1 1 1 1 1 1 1 1	74 1.8897-0.0417i	0.4315-0.0095i	15936 15936 15936 15936 15936 15936 15936 15936 15936 15936 15936 15936 15936 15936 15936 15936 15936 15936 15936	New	N4 15936 15936 15936 15936 15936 15936 15936 15936 15936 15936 15936 15936 15936 15936 15936 15936 15936	Ann (84) 0 0 0 0 0 0 0 0 0 0 0 0 0 0 0 0 0 0 0	gle	η4 1,5936 1,593
Index		n3 375.307 375.307 375.307 375.307 375.307 375.307 375.307 375.307 375.307 375.307 375.307 375.307 375.307 375.307 375.307	53 148-0.3 148-0.3 148-0.3 148-0.3 148-0.3 148-0.3 148-0.3 148-0.3 148-0.3 148-0.3 148-0.3 148-0.3 148-0.3 148-0.3 148-0.3	n4 18897 18897 18897 18897 18897 18897 18897 18897 18897 18897 18897 18897 18897 18897 18897 18897 18897 18897	k4 0.042	N4 18897-0.0417i	044 20 20 20 20 20 20 20 20 20 20 20 20 20	Op. Thk.	Ar Sin(04) 0 0 0 0 0 0 0 0 0 0 0 0 0 0 0 0 0 0	008(84) 1 1 1 1 1 1 1 1 1 1 1 1 1 1 1 1 1 1 1	η4 1,8897-0,0417i	0.4315-0.0095i	15936 15936 15936 15936 15936 15936 15936 15936 15936 15936 15936 15936 15936 15936 15936 15936 15936 15936 15936	New	N4 15936 15936 15936 15936 15936 15936 15936 15936 15936 15936 15936 15936 15936 15936 15936 15936 15936 15936	Anno Anno Anno Anno Anno Anno Anno Anno	gle	η4 1,5936 1,593
Index		7375-307 375-307 375-307 375-307 375-307 375-307 375-307 375-307 375-307 375-307 375-307 375-307 375-307 375-307 375-307 375-307 375-307 375-307 375-307	148-0.3 148-0.3 148-0.3 148-0.3 148-0.3 148-0.3 148-0.3 148-0.3 148-0.3 148-0.3 148-0.3 148-0.3 148-0.3 148-0.3 148-0.3 148-0.3	n4 18897 18897 18897 18897 18897 18897 18897 18897 18897 18897 18897 18897 18897 18897 18897 18897	k4 0.042	N4 1.8897-0.0417i	044 20 20 20 20 20 20 20 20 20 20 20 20 20	Op. Thk.	Ar Sin(04) 0 0 0 0 0 0 0 0 0 0 0 0 0 0 0 0 0 0	Cos(64)	η4 1.8897-0.0417i	0.4315-0.0095i	15936 15936 15936 15936 15936 15936 15936 15936 15936 15936 15936 15936 15936 15936 15936 15936 15936 15936 15936 15936	Index	N4 15936	Anno Anno Anno Anno Anno Anno Anno Anno	gle	η <sup>4</sup> 1,5936 1,5
Index	) cos(83	η3 375-307	148-0.3 148-0.3 148-0.3 148-0.3 148-0.3 148-0.3 148-0.3 148-0.3 148-0.3 148-0.3 148-0.3 148-0.3 148-0.3 148-0.3 148-0.3 148-0.3 148-0.3 148-0.3 148-0.3	n4 18897 18897 18897 18897 18897 18897 18897 18897 18897 18897 18897 18897 18897 18897 18897 18897 18897 18897	k4   0.042   0.042 	N4 18897-0.0417i	044 20 20 20 20 20 20 20 20 20 20 20 20 20	Op. Thk. N444 37.794-0.834i	Ar Sin(04) 0 0 0 0 0 0 0 0 0 0 0 0 0 0 0 0 0 0	008(84) 1 1 1 1 1 1 1 1 1 1 1 1 1 1 1 1 1 1 1	η4 1.8897-0.0417i	0.4315-0.0095i	15936 15936	Index	N4 15936	Anno Anno Anno Anno Anno Anno Anno Anno	gle	η4 1,5936 1,593
Index	cos(83	7375-307 375-307 375-307 375-307 375-307 375-307 375-307 375-307 375-307 375-307 375-307 375-307 375-307 375-307 375-307 375-307 375-307 375-307 375-307	53 148-0.3 148-0.3 148-0.3 148-0.3 148-0.3 148-0.3 148-0.3 148-0.3 148-0.3 148-0.3 148-0.3 148-0.3 148-0.3 148-0.3 148-0.3 148-0.3 148-0.3 148-0.3 148-0.3	n4 18897 18897 18897 18897 18897 18897 18897 18897 18897 18897 18897 18897 18897 18897 18897 18897 18897	K4   0.042   0.042 	N4 1.8897-0.0417i	04 20 20 20 20 20 20 20 20 20 20 20 20 20	Op. Thk.	Ar Sin(84) 0 0 0 0 0 0 0 0 0 0 0 0 0 0 0 0 0 0 0	Cos(64)	74 1.8897-0.0417i	0.4315-0.0095i	1.5936 1.5936	Index	N4 15936	Annotation (A)	gle	η4 1,5936 1,593
Index	) cos(83 1 1 1 1 1 1 1 1 1 1 1 1 1 1 1 1 1 1 1	13 375-3.07	53 148-0.3	n4 18897 18897 18897 18897 18897 18897 18897 18897 18897 18897 18897 18897 18897 18897 18897 18897 18897 18897	K4   0.042	N4 1.8897-0.0417i	044 20 20 20 20 20 20 20 20 20 20 20 20 20	Op. Thk. N4d4 37.794-0.834i	Ar Sin(θ4) 0 0 0 0 0 0 0 0 0 0 0 0 0 0 0 0 0 0 0	Cos(64)	1887-0.0417i 18897-0.0417i 18997-0.0417i	0.4315-0.0095i	15936 15936	Index	N4 1.5936	Annotation	gle	η4 1,5336 1,533
Index	) cos(83	n3 375.307	148-0.3 148-0.3	n4 18897	K4 0.042	N4 1.8897-0.0417i	04 20 20 20 20 20 20 20 20 20 20 20 20 20	Op. Thk.	Ar sin(84) 0 0 0 0 0 0 0 0 0 0 0 0 0 0 0 0 0 0 0	Cos(64)	η4 1.8897-0.0417i	0.4315-0.0095i	1.5936 1.	Index	N4 1.5936	Anno Anno Anno Anno Anno Anno Anno Anno	gle	15936 15936
Index	cos(83	73375307 375-307	63 148-0.3	n4 1,8897	K4   0.042   0.042 	N4 1.8887-0.0417i	20 20 20 20 20 20 20 20 20 20 20 20 20 2	Op. Thk.	Ar Sin(84) 0 0 0 0 0 0 0 0 0 0 0 0 0 0 0 0 0 0 0	Cos(64)	η4 1.8897-0.0417i	0.4315-0.0095i	1.5936 1.	Index	N4 1.5936	Annotation (Annotation (Annota	gle	15936 15936

This Excel was used with specific reflective index (n) values of PEDOT:PSS, ITO, Ag, and Parylene C materials. This Excel can also be used for other multilayered thin film design with

various materials for calculating each layer thickness for achieving the highest transmission and lowest reflection. Detailed equations were demonstrated in Chapter 4.

**BIBLIOGRAPHY** 

## **BIBLIOGRAPHY**

- [1] S. Siuly and Y. Zhang, "Medical big data: neurological diseases diagnosis through medical data analysis," *Data Sci. Eng.*, vol. 1, no. 2, pp. 54–64, 2016.
- [2] F. Seifar *et al.*, "α-Lipoic acid, functional fatty acid, as a novel therapeutic alternative for central nervous system diseases: A review," *Nutr. Neurosci.*, vol. 22, no. 5, pp. 306–316, 2019.
- [3] M. M. Kurtis, T. Rajah, L. F. Delgado, and H. S. Dafsari, "The effect of deep brain stimulation on the non-motor symptoms of Parkinson's disease: a critical review of the current evidence," *npj Park. Dis.*, vol. 3, no. 1, pp. 1–12, 2017.
- [4] H. Cagnan, T. Denison, C. McIntyre, and P. Brown, "Emerging technologies for improved deep brain stimulation," *Nat. Biotechnol.*, vol. 37, no. 9, pp. 1024–1033, 2019.
- [5] J. Dierkes, J. G. Pilitsis, and S. Falowski, "Deep Brain Stimulation," in *Deer's Treatment of Pain*, Springer, 2019, pp. 507–514.
- [6] S. B. Goncalves, J. F. Ribeiro, A. F. Silva, R. M. Costa, and J. H. Correia, "Design and manufacturing challenges of optogenetic neural interfaces: a review," *J. Neural Eng.*, vol. 14, no. 4, p. 41001, 2017.
- [7] E. A. Pama, L. S. Colzato, and B. Hommel, "Optogenetics as a neuromodulation tool in cognitive neuroscience," *Front. Psychol.*, vol. 4, p. 610, 2013.
- [8] G. Nagel *et al.*, "Channelrhodopsin-2, a directly light-gated cation-selective membrane channel," *Proc. Natl. Acad. Sci.*, vol. 100, no. 24, pp. 13940–13945, 2003.
- [9] W. Yang, W. Khan, J. Wu, and W. Li, "Single-channel opto-neurostimulators: a review," *J. Micromechanics Microengineering*, vol. 29, no. 4, p. 43001, 2019.
- [10] Z. Cheng, R. Cui, T. Ge, W. Yang, and B. Li, "Optogenetics: what it has uncovered in potential pathways of depression," *Pharmacol. Res.*, p. 104596, 2019.
- [11] J. W. Reddy, I. Kimukin, E. Towe, and M. Chamanzar, "Flexible, Monolithic, High-Density μLED Neural Probes for Simultaneous Optogenetics Stimulation and Recording," in 2019 9th International IEEE/EMBS Conference on Neural Engineering (NER), 2019, pp. 831–834.

- [12] D. Ryu, S. Jeon, Y.-K. Kim, S. B. Jun, and C.-H. Ji, "Implantable Wireless Neural Interface for Multichannel Neural Recording and Optogenetic Neuromodulation," in *2019 International Conference on Optical MEMS and Nanophotonics (OMN)*, 2019, pp. 8–9.
- [13] K. Y. Kwon, H.-M. Lee, M. Ghovanloo, A. Weber, and W. Li, "Design, fabrication, and packaging of an integrated, wirelessly-powered optrode array for optogenetics application," *Front. Syst. Neurosci.*, vol. 9, p. 69, 2015.
- [14] K. Y. Kwon, B. Sirowatka, W. Li, and A. Weber, "Opto-μECoG array: transparent μECoG electrode array and integrated LEDs for optogenetics," in *2012 IEEE Biomedical Circuits and Systems Conference (BioCAS)*, 2012, pp. 164–167.
- [15] S. M. Ojovan *et al.*, "A feasibility study of multi-site, intracellular recordings from mammalian neurons by extracellular gold mushroom-shaped microelectrodes," *Sci. Rep.*, vol. 5, no. 1, pp. 1–14, 2015.
- [16] D. Khodagholy *et al.*, "In vivo recordings of brain activity using organic transistors," *Nat. Commun.*, vol. 4, no. 1, pp. 1–7, 2013.
- [17] D.-W. Park *et al.*, "Graphene-based carbon-layered electrode array technology for neural imaging and optogenetic applications," *Nat. Commun.*, vol. 5, p. 5258, 2014.
- [18] O. Tuna, Y. Selamet, G. Aygun, and L. Ozyuzer, "High quality ITO thin films grown by dc and RF sputtering without oxygen," *J. Phys. D. Appl. Phys.*, vol. 43, no. 5, p. 55402, 2010.
- [19] A. Ahani, L. Saadati-Fard, A. M. Sodagar, and F. A. Boroumad, "Flexible PET/ITO electrode array for implantable biomedical applications," in *2011 Annual International Conference of the IEEE Engineering in Medicine and Biology Society*, 2011, pp. 2878–2881.
- [20] M. Boehme and C. Charton, "Properties of ITO on PET film in dependence on the coating conditions and thermal processing," *Surf. Coatings Technol.*, vol. 200, no. 1–4, pp. 932–935, 2005.
- [21] M. O. Heuschkel, Fabrication of multi-electrode array devices for electrophysiological monitoring of in-vitro cell/tissue cultures. Hartung-Gorre, 2001.
- [22] W. Franks, I. Schenker, P. Schmutz, and A. Hierlemann, "Impedance characterization and modeling of electrodes for biomedical applications," *IEEE Trans. Biomed. Eng.*, vol. 52, no. 7, pp. 1295–1302, 2005.
- [23] D. I. Yakubovsky, A. V Arsenin, Y. V Stebunov, D. Y. Fedyanin, and V. S. Volkov, "Optical

- constants and structural properties of thin gold films," *Opt. Express*, vol. 25, no. 21, pp. 25574–25587, 2017.
- [24] W. Lee *et al.*, "Transparent, conformable, active multielectrode array using organic electrochemical transistors," *Proc. Natl. Acad. Sci.*, vol. 114, no. 40, pp. 10554–10559, 2017.
- [25] D. Kuzum *et al.*, "Transparent and flexible low noise graphene electrodes for simultaneous electrophysiology and neuroimaging," *Nat. Commun.*, vol. 5, no. 1, pp. 1–10, 2014.
- [26] F. Greco *et al.*, "Ultra-thin conductive free-standing PEDOT/PSS nanofilms," *Soft Matter*, vol. 7, no. 22, pp. 10642–10650, 2011.
- [27] C.-K. Cho, W.-J. Hwang, K. Eun, S.-H. Choa, S.-I. Na, and H.-K. Kim, "Mechanical flexibility of transparent PEDOT: PSS electrodes prepared by gravure printing for flexible organic solar cells," *Sol. Energy Mater. Sol. Cells*, vol. 95, no. 12, pp. 3269–3275, 2011.
- [28] P. Ledochowitsch, E. Olivero, T. Blanche, and M. M. Maharbiz, "A transparent μECoG array for simultaneous recording and optogenetic stimulation," in *2011 Annual International Conference of the IEEE Engineering in Medicine and Biology Society*, 2011, pp. 2937–2940.
- [29] D.-W. Park *et al.*, "Fabrication and utility of a transparent graphene neural electrode array for electrophysiology, in vivo imaging, and optogenetics," *Nat. Protoc.*, vol. 11, no. 11, p. 2201, 2016.
- [30] Z. Zhao, R. Gong, L. Zheng, and J. Wang, "In vivo neural recording and electrochemical performance of microelectrode arrays modified by rough-surfaced AuPt alloy nanoparticles with nanoporosity," *Sensors*, vol. 16, no. 11, p. 1851, 2016.
- [31] Y. H. Kim, A. Y. Kim, G. H. Kim, Y. H. Han, M.-A. Chung, and S.-D. Jung, "Electrochemical and in vitro neuronal recording characteristics of multi-electrode arrays surface-modified with electro-co-deposited gold-platinum nanoparticles," *Biomed. Microdevices*, vol. 18, no. 1, p. 14, 2016.
- [32] J. Pas *et al.*, "Neurospheres on patterned PEDOT: PSS microelectrode arrays enhance electrophysiology recordings," *Adv. Biosyst.*, vol. 2, no. 1, p. 1700164, 2018.
- [33] S. Rathi *et al.*, "PEDOT: PSS as a transparent electrically conducting polymer for brain stimulation electrodes," in *2019 IEEE 16th India Council International Conference (INDICON)*, 2019, pp. 1–4.

- [34] A. Blau *et al.*, "Flexible, all-polymer microelectrode arrays for the capture of cardiac and neuronal signals," *Biomaterials*, vol. 32, no. 7, pp. 1778–1786, 2011.
- [35] K. J. Seo *et al.*, "Transparent, Flexible, Penetrating Microelectrode Arrays with Capabilities of Single-Unit Electrophysiology," *Adv. Biosyst.*, vol. 3, no. 3, p. 1800276, 2019.
- [36] V. Castagnola *et al.*, "Parylene-based flexible neural probes with PEDOT coated surface for brain stimulation and recording," *Biosens. Bioelectron.*, vol. 67, pp. 450–457, 2015.
- [37] V. L. Feigin *et al.*, "Global, regional, and national burden of neurological disorders, 1990–2016: a systematic analysis for the Global Burden of Disease Study 2016," *Lancet Neurol.*, vol. 18, no. 5, pp. 459–480, 2019.
- [38] T. Wijeratne, W. Grisold, C. Trenkwalder, and A. M. W. Carroll, "World Brain Day 2020: Move together to end Parkinson's disease," *J. Neurol. Sci.*, 2020.
- [39] F. Hashemi Noshahr, M. Nabavi, and M. Sawan, "Multi-Channel Neural Recording Implants: A Review," *Sensors*, vol. 20, no. 3, p. 904, 2020.
- [40] U. R. Acharya *et al.*, "Characterization of focal EEG signals: a review," *Futur. Gener. Comput. Syst.*, vol. 91, pp. 290–299, 2019.
- [41] A. Thukral, F. Ershad, N. Enan, Z. Rao, and C. Yu, "Soft ultrathin silicon electronics for soft neural interfaces: a review of recent advances of soft neural interfaces based on ultrathin silicon," *IEEE Nanotechnol. Mag.*, vol. 12, no. 1, pp. 21–34, 2018.
- [42] S. T. Kanth and S. Ray, "Electrocorticogram (ECoG) is highly informative in primate visual cortex," *J. Neurosci.*, vol. 40, no. 12, pp. 2430–2444, 2020.
- [43] O. Herreras, "Local field potentials: myths and misunderstandings," *Front. Neural Circuits*, vol. 10, p. 101, 2016.
- [44] R. Chen, A. Canales, and P. Anikeeva, "Neural recording and modulation technologies," *Nat. Rev. Mater.*, vol. 2, no. 2, pp. 1–16, 2017.
- [45] X. Jiang, G.-B. Bian, and Z. Tian, "Removal of artifacts from EEG signals: a review," *Sensors*, vol. 19, no. 5, p. 987, 2019.
- [46] D. Khodagholy *et al.*, "NeuroGrid: recording action potentials from the surface of the brain," *Nat. Neurosci.*, vol. 18, no. 2, pp. 310–315, 2015.

- [47] G. Hong and C. M. Lieber, "Novel electrode technologies for neural recordings," *Nat. Rev. Neurosci.*, vol. 20, no. 6, pp. 330–345, 2019.
- [48] P. Fattahi, G. Yang, G. Kim, and M. R. Abidian, "A review of organic and inorganic biomaterials for neural interfaces," *Adv. Mater.*, vol. 26, no. 12, pp. 1846–1885, 2014.
- [49] C. Russell, A. D. Roche, and S. Chakrabarty, "Peripheral nerve bionic interface: a review of electrodes," *Int. J. Intell. Robot. Appl.*, vol. 3, no. 1, pp. 11–18, 2019.
- [50] Y. Gong, W. Liu, R. Wang, M. H. Brauer, K. Zheng, and W. Li, "Stability performance analysis of various packaging materials and coating strategies for chronic neural implants under accelerated, reactive aging tests," *Micromachines*, vol. 11, no. 9, p. 810, 2020.
- [51] K. Kostarelos, M. Vincent, C. Hebert, and J. A. Garrido, "Graphene in the design and engineering of next-generation neural interfaces," *Adv. Mater.*, vol. 29, no. 42, p. 1700909, 2017.
- [52] E. B. Aydın and M. K. Sezgintürk, "Indium tin oxide (ITO): A promising material in biosensing technology," *TrAC Trends Anal. Chem.*, vol. 97, pp. 309–315, 2017.
- [53] Y. Guo *et al.*, "Polymer composite with carbon nanofibers aligned during thermal drawing as a microelectrode for chronic neural interfaces," *ACS Nano*, vol. 11, no. 7, pp. 6574–6585, 2017.
- [54] V. Saunier, E. Flahaut, C. Blatché, C. Bergaud, and A. Maziz, "Carbon nanofiber-PEDOT composite films as novel microelectrode for neural interfaces and biosensing," *Biosens. Bioelectron.*, p. 112413, 2020.
- [55] R. K. Shepherd, J. Villalobos, O. Burns, and D. A. X. Nayagam, "The development of neural stimulators: a review of preclinical safety and efficacy studies," *J. Neural Eng.*, vol. 15, no. 4, p. 41004, 2018.
- [56] C. Zhang *et al.*, "Implantable electrode array with platinum black coating for brain stimulation in fish," *Microsyst. Technol.*, vol. 21, no. 1, pp. 139–145, 2015.
- [57] C. Chen, S. Ruan, X. Bai, C. Lin, C. Xie, and I.-S. Lee, "Patterned iridium oxide film as neural electrode interface: biocompatibility and improved neurite outgrowth with electrical stimulation," *Mater. Sci. Eng. C*, vol. 103, p. 109865, 2019.
- [58] E. M. Hudak, D. W. Kumsa, H. B. Martin, and J. T. Mortimer, "Electron transfer processes occurring on platinum neural stimulating electrodes: calculated charge-storage capacities

- are inaccessible during applied stimulation," J. Neural Eng., vol. 14, no. 4, p. 46012, 2017.
- [59] A. Vanhoestenberghe and N. Donaldson, "Corrosion of silicon integrated circuits and lifetime predictions in implantable electronic devices," *J. Neural Eng.*, vol. 10, no. 3, p. 31002, 2013.
- [60] N. Donaldson and G. S. Brindley, "The historical foundations of bionics," *Neurobionics Biomed. Eng. neural prostheses. Hoboken, NJ, USA John Wiley Sons, Inc*, pp. 1–37, 2016.
- [61] N. Amanat, N. L. James, and D. R. McKenzie, "Welding methods for joining thermoplastic polymers for the hermetic enclosure of medical devices," *Med. Eng. Phys.*, vol. 32, no. 7, pp. 690–699, 2010.
- [62] J. M. Anderson, "Biological responses to materials," *Annu. Rev. Mater. Res.*, vol. 31, no. 1, pp. 81–110, 2001.
- [63] J. M. Anderson, "Inflammatory response to implants," *ASAIO J.*, vol. 34, no. 2, pp. 101–107, 1988.
- [64] K. Shen and M. M. Maharbiz, "Ceramic Packaging in Neural Implants," bioRxiv, 2020.
- [65] E. Patrick, M. E. Orazem, J. C. Sanchez, and T. Nishida, "Corrosion of tungsten microelectrodes used in neural recording applications," *J. Neurosci. Methods*, vol. 198, no. 2, pp. 158–171, 2011.
- [66] P. Takmakov, K. Ruda, K. S. Phillips, I. S. Isayeva, V. Krauthamer, and C. G. Welle, "Rapid evaluation of the durability of cortical neural implants using accelerated aging with reactive oxygen species," *J. Neural Eng.*, vol. 12, no. 2, p. 26003, 2015.
- [67] S. M. Wahl, H. Wong, and N. McCartney-Francis, "Role of growth factors in inflammation and repair," *J. Cell. Biochem.*, vol. 40, no. 2, pp. 193–199, 1989.
- [68] Y. Fong, L. L. Moldawer, G. T. Shires, and S. F. Lowry, "The biologic characteristics of cytokines and their implication in surgical injury.," *Surg. Gynecol. Obstet.*, vol. 170, no. 4, p. 363, 1990.
- [69] G. F. Pierce, T. A. Mustoe, B. W. Altrock, T. F. Deuel, and A. Thomason, "Role of platelet-derived growth factor in wound healing," *J. Cell. Biochem.*, vol. 45, no. 4, pp. 319–326, 1991.
- [70] J. M. Anderson, A. Rodriguez, and D. T. Chang, "Foreign body reaction to biomaterials," in

- Seminars in immunology, 2008, vol. 20, no. 2, pp. 86–100.
- [71] B. D. Ratner and S. J. Bryant, "Biomaterials: where we have been and where we are going," *Annu. Rev. Biomed. Eng.*, vol. 6, pp. 41–75, 2004.
- [72] J. M. H. Morales and C. Clément, "Technical Challenges of Active Implantable Medical Devices for Neurotechnology," in *2018 IEEE CPMT Symposium Japan (ICSJ)*, 2018, pp. 77–80.
- [73] T. Stieglitz, "Manufacturing, assembling and packaging of miniaturized neural implants," *Microsyst. Technol.*, vol. 16, no. 5, pp. 723–734, 2010.
- [74] A. Booth, Sterilization of medical devices. CRC Press, 1998.
- [75] J. L. Elechiguerra, L. Larios-Lopez, C. Liu, D. Garcia-Gutierrez, A. Camacho-Bragado, and M. J. Yacaman, "Corrosion at the nanoscale: the case of silver nanowires and nanoparticles," *Chem. Mater.*, vol. 17, no. 24, pp. 6042–6052, 2005.
- [76] X. Chu, K. Wang, J. Tao, S. Li, S. Ji, and C. Ye, "Tackling the stability issues of silver nanowire transparent conductive films through FeCl3 dilute solution treatment," *Nanomaterials*, vol. 9, no. 4, p. 533, 2019.
- [77] A. Lecomte, E. Descamps, and C. Bergaud, "A review on mechanical considerations for chronically-implanted neural probes," *J. Neural Eng.*, vol. 15, no. 3, p. 31001, 2018.
- [78] C. Wiegand *et al.*, "Effect of the sterilization method on the performance of collagen type I on chronic wound parameters in vitro," *J. Biomed. Mater. Res. Part B Appl. Biomater. An Off. J. Soc. Biomater. Japanese Soc. Biomater. Aust. Soc. Biomater. Korean Soc. Biomater.*, vol. 90, no. 2, pp. 710–719, 2009.
- [79] T. Yucel, M. L. Lovett, and D. L. Kaplan, "Silk-based biomaterials for sustained drug delivery," *J. Control. Release*, vol. 190, pp. 381–397, 2014.
- [80] K. A. Athanasiou, G. G. Niederauer, and C. M. Agrawal, "Sterilization, toxicity, biocompatibility and clinical applications of polylactic acid/polyglycolic acid copolymers," *Biomaterials*, vol. 17, no. 2, pp. 93–102, 1996.
- [81] A. Schander *et al.*, "Design and fabrication of novel multi-channel floating neural probes for intracortical chronic recording," *Sensors Actuators A Phys.*, vol. 247, pp. 125–135, 2016.
- [82] G. C. C. Mendes, T. R. S. Brandao, and C. L. M. Silva, "Ethylene oxide sterilization of

- medical devices: a review," Am. J. Infect. Control, vol. 35, no. 9, pp. 574–581, 2007.
- [83] L. Golberg, Hazard assessment of ethylene oxide. CRC Press, 2018.
- [84] B. McEvoy and N. J. Rowan, "Terminal sterilization of medical devices using vaporized hydrogen peroxide: a review of current methods and emerging opportunities," *J. Appl. Microbiol.*, vol. 127, no. 5, pp. 1403–1420, 2019.
- [85] J. R. Eles, A. L. Vazquez, T. D. Y. Kozai, and X. T. Cui, "In vivo imaging of neuronal calcium during electrode implantation: spatial and temporal mapping of damage and recovery," *Biomaterials*, vol. 174, pp. 79–94, 2018.
- [86] M. D. Ferro and N. A. Melosh, "Electronic and ionic materials for neurointerfaces," *Adv. Funct. Mater.*, vol. 28, no. 12, p. 1704335, 2018.
- [87] K. M. Szostak, L. Grand, and T. G. Constandinou, "Neural interfaces for intracortical recording: Requirements, fabrication methods, and characteristics," *Front. Neurosci.*, vol. 11, p. 665, 2017.
- [88] J. P. Neto *et al.*, "Does impedance matter when recording spikes with polytrodes?," *Front. Neurosci.*, vol. 12, p. 715, 2018.
- [89] S. Arcot Desai, J. D. Rolston, L. Guo, and S. M. Potter, "Improving impedance of implantable microwire multi-electrode arrays by ultrasonic electroplating of durable platinum black," *Front. Neuroeng.*, vol. 3, p. 5, 2010.
- [90] T. Chung, J. Q. Wang, J. Wang, B. Cao, Y. Li, and S. W. Pang, "Electrode modifications to lower electrode impedance and improve neural signal recording sensitivity," *J. Neural Eng.*, vol. 12, no. 5, p. 56018, 2015.
- [91] T. D. Y. Kozai *et al.*, "Comprehensive chronic laminar single-unit, multi-unit, and local field potential recording performance with planar single shank electrode arrays," *J. Neurosci. Methods*, vol. 242, pp. 15–40, 2015.
- [92] Y. Fang, X. Li, and Y. Fang, "Organic bioelectronics for neural interfaces," *J. Mater. Chem. C*, vol. 3, no. 25, pp. 6424–6430, 2015.
- [93] M. Wang, G. Mi, D. Shi, N. Bassous, D. Hickey, and T. J. Webster, "Nanotechnology and nanomaterials for improving neural interfaces," *Adv. Funct. Mater.*, vol. 28, no. 12, p. 1700905, 2018.

- [94] D. A. Stenger and T. M. McKenna, *Enabling technologies for cultured neural networks*. Academic Press, 1994.
- [95] G. Baranauskas *et al.*, "Carbon nanotube composite coating of neural microelectrodes preferentially improves the multiunit signal-to-noise ratio," *J. Neural Eng.*, vol. 8, no. 6, p. 66013, 2011.
- [96] C. Xie, Z. Lin, L. Hanson, Y. Cui, and B. Cui, "Intracellular recording of action potentials by nanopillar electroporation," *Nat. Nanotechnol.*, vol. 7, no. 3, pp. 185–190, 2012.
- [97] J. Bobacka, A. Lewenstam, and A. Ivaska, "Electrochemical impedance spectroscopy of oxidized poly (3, 4-ethylenedioxythiophene) film electrodes in aqueous solutions," *J. Electroanal. Chem.*, vol. 489, no. 1–2, pp. 17–27, 2000.
- [98] X. Cui et al., "Surface modification of neural recording electrodes with conducting polymer/biomolecule blends," J. Biomed. Mater. Res. An Off. J. Soc. Biomater. Japanese Soc. Biomater. Aust. Soc. Biomater. Korean Soc. Biomater., vol. 56, no. 2, pp. 261–272, 2001.
- [99] S. M. Wellman *et al.*, "A materials roadmap to functional neural interface design," *Adv. Funct. Mater.*, vol. 28, no. 12, p. 1701269, 2018.
- [100] D. F. Williams, "European society for biomaterials," in *Definitions in biomaterials:* proceedings of a consensus conference of the European Society for Biomaterials, Chester, England, March 3-5, 1986.
- [101] X. Navarro, T. B. Krueger, N. Lago, S. Micera, T. Stieglitz, and P. Dario, "A critical review of interfaces with the peripheral nervous system for the control of neuroprostheses and hybrid bionic systems," *J. Peripher. Nerv. Syst.*, vol. 10, no. 3, pp. 229–258, 2005.
- [102] G. Márton *et al.*, "The neural tissue around SU-8 implants: A quantitative in vivo biocompatibility study," *Mater. Sci. Eng. C*, p. 110870, 2020.
- [103] K. Feron, R. Lim, C. Sherwood, A. Keynes, A. Brichta, and P. C. Dastoor, "Organic bioelectronics: materials and biocompatibility," *Int. J. Mol. Sci.*, vol. 19, no. 8, p. 2382, 2018.
- [104] S. Frederick, "Biocompatibility of materials in medical devices," *Wiley Encycl. Chem. Biol.*, pp. 1–8, 2007.
- [105] S. HANSON et al., "Testing biomaterials," in Biomaterials Science, Elsevier, 1996, pp.

- 215-242.
- [106] J. Tang *et al.*, "Influence of silver nanoparticles on neurons and blood-brain barrier via subcutaneous injection in rats," *Appl. Surf. Sci.*, vol. 255, no. 2, pp. 502–504, 2008.
- [107] N. Lago and A. Cester, "Flexible and organic neural interfaces: A review," *Appl. Sci.*, vol. 7, no. 12, p. 1292, 2017.
- [108] R. Li, L. Wang, D. Kong, and L. Yin, "Recent progress on biodegradable materials and transient electronics," *Bioact. Mater.*, vol. 3, no. 3, pp. 322–333, 2018.
- [109] C.-H. Chiang *et al.*, "Development of a neural interface for high-definition, long-term recording in rodents and nonhuman primates," *Sci. Transl. Med.*, vol. 12, no. 538, 2020.
- [110] R. Porrazzo, S. Bellani, A. Luzio, E. Lanzarini, M. Caironi, and M. R. Antognazza, "Improving mobility and electrochemical stability of a water-gated polymer field-effect transistor," *Org. Electron.*, vol. 15, no. 9, pp. 2126–2134, 2014.
- [111] L. Chen, S. J. Ilham, T. Guo, S. Emadi, and B. Feng, "In vitro multichannel single-unit recordings of action potentials from the mouse sciatic nerve," *Biomed. Phys. Eng. express*, vol. 3, no. 4, p. 45020, 2017.
- [112] J. T. McFadden, "Metallurgical principles in neurosurgery," *J. Neurosurg.*, vol. 31, no. 4, pp. 373–385, 1969.
- [113] S. F. Cogan, P. R. Troyk, J. Ehrlich, and T. D. Plante, "In vitro comparison of the charge-injection limits of activated iridium oxide (AIROF) and platinum-iridium microelectrodes," *IEEE Trans. Biomed. Eng.*, vol. 52, no. 9, pp. 1612–1614, 2005.
- [114] D. C. Rodger *et al.*, "Flexible parylene-based multielectrode array technology for high-density neural stimulation and recording," *Sensors Actuators B Chem.*, vol. 132, no. 2, pp. 449–460, 2008.
- [115] A. S. Pranti, A. Schander, A. Bödecker, and W. Lang, "Highly stable PEDOT: PSS coating on gold microelectrodes with improved charge injection capacity for chronic neural stimulation," in *Multidisciplinary Digital Publishing Institute Proceedings*, 2017, vol. 1, no. 4, p. 492.
- [116] G. Dijk, A. L. Rutz, and G. G. Malliaras, "Stability of PEDOT: PSS-Coated Gold Electrodes in Cell Culture Conditions," *Adv. Mater. Technol.*, vol. 5, no. 3, p. 1900662, 2020.

- [117] B. Halliwell, "Reactive oxygen species and the central nervous system," *J. Neurochem.*, vol. 59, no. 5, pp. 1609–1623, 1992.
- [118] M. De Vittorio, L. Martiradonna, and J. Assad, *Nanotechnology and neuroscience: nanoelectronic, photonic and mechanical neuronal interfacing*, vol. 8. Springer, 2014.
- [119] W. Yang, J. Wu, Q. H. Fan, and W. Li, "Transparent and ultra-flexible PEDOT: PSS/ITO/Ag/ITO on Parylene thin films with tunable properties," in *Oxide-based Materials and Devices X*, 2019, vol. 10919, p. 109191W.
- [120] T. D. Y. Kozai, N. A. Alba, H. Zhang, N. A. Kotov, R. A. Gaunt, and X. T. Cui, "Nanostructured coatings for improved charge delivery to neurons," in *Nanotechnology and neuroscience: nano-electronic, photonic and mechanical neuronal interfacing*, Springer, 2014, pp. 71–134.
- [121] J. P. Seymour and D. R. Kipke, "Neural probe design for reduced tissue encapsulation in CNS," *Biomaterials*, vol. 28, no. 25, pp. 3594–3607, 2007.
- [122] Z. J. Du, X. Luo, C. L. Weaver, and X. T. Cui, "Poly (3, 4-ethylenedioxythiophene)-ionic liquid coating improves neural recording and stimulation functionality of MEAs," *J. Mater. Chem. C*, vol. 3, no. 25, pp. 6515–6524, 2015.
- [123] G. Justin and A. Guiseppi-Elie, "Electroconductive blends of poly (HEMA-co-PEGMA-co-HMMAco-SPMA) and poly (Py-co-PyBA): in vitro biocompatibility," *J. Bioact. Compat. Polym.*, vol. 25, no. 2, pp. 121–140, 2010.
- [124] D. N. Heo, D. H. Yang, J. B. Lee, M. S. Bae, H. N. Park, and I. K. Kwon, "Cell fouling resistance of PEG-grafted polyimide film for neural implant applications," in *Third International Conference on Smart Materials and Nanotechnology in Engineering*, 2012, vol. 8409, p. 84091F.
- [125] J. Cheng *et al.*, "Photopatterning of self-assembled poly (ethylene) glycol monolayer for neuronal network fabrication," *J. Neurosci. Methods*, vol. 213, no. 2, pp. 196–203, 2013.
- [126] S. Meijs *et al.*, "Biofouling resistance of boron-doped diamond neural stimulation electrodes is superior to titanium nitride electrodes in vivo," *J. Neural Eng.*, vol. 13, no. 5, p. 56011, 2016.
- [127] B. Fan *et al.*, "Flexible, diamond-based microelectrodes fabricated using the diamond growth side for neural sensing," *Microsystems Nanoeng.*, vol. 6, no. 1, pp. 1–12, 2020.

- [128] C. A. R. Chapman, L. Wang, H. Chen, J. Garrison, P. J. Lein, and E. Seker, "Nanoporous gold biointerfaces: modifying nanostructure to control neural cell coverage and enhance electrophysiological recording performance," *Adv. Funct. Mater.*, vol. 27, no. 3, p. 1604631, 2017.
- [129] C. Boehler, D. M. Vieira, U. Egert, and M. Asplund, "NanoPt—A Nanostructured Electrode Coating for Neural Recording and Microstimulation," *ACS Appl. Mater. Interfaces*, vol. 12, no. 13, pp. 14855–14865, 2020.
- [130] S. M. Won, E. Song, J. Zhao, J. Li, J. Rivnay, and J. A. Rogers, "Recent advances in materials, devices, and systems for neural interfaces," *Adv. Mater.*, vol. 30, no. 30, p. 1800534, 2018.
- [131] S.-K. Kang *et al.*, "Bioresorbable silicon electronic sensors for the brain," *Nature*, vol. 530, no. 7588, pp. 71–76, 2016.
- [132] L. Lu *et al.*, "Biodegradable monocrystalline silicon photovoltaic microcells as power supplies for transient biomedical implants," *Adv. Energy Mater.*, vol. 8, no. 16, p. 1703035, 2018.
- [133] F. Wu, L. W. Tien, F. Chen, J. D. Berke, D. L. Kaplan, and E. Yoon, "Silk-backed structural optimization of high-density flexible intracortical neural probes," *J. microelectromechanical Syst.*, vol. 24, no. 1, pp. 62–69, 2014.
- [134] N. Xue *et al.*, "A biodegradable porous silicon and polymeric hybrid probe for electrical neural signal recording," *Sensors Actuators B Chem.*, vol. 272, pp. 314–323, 2018.
- [135] K. Xu *et al.*, "Bioresorbable Electrode Array for Electrophysiological and Pressure Signal Recording in the Brain," *Adv. Healthc. Mater.*, vol. 8, no. 15, p. 1801649, 2019.
- [136] D. Lewitus, K. L. Smith, W. Shain, and J. Kohn, "Ultrafast resorbing polymers for use as carriers for cortical neural probes," *Acta Biomater.*, vol. 7, no. 6, pp. 2483–2491, 2011.
- [137] D. Lewitus *et al.*, "Designing tyrosine-derived polycarbonate polymers for biodegradable regenerative type neural interface capable of neural recording," *IEEE Trans. Neural Syst. Rehabil. Eng.*, vol. 19, no. 2, pp. 204–212, 2010.
- [138] A. Lecomte, A. Degache, E. Descamps, L. Dahan, and C. Bergaud, "In vitro and in vivo biostability assessment of chronically-implanted Parylene C neural sensors," *Sensors Actuators B Chem.*, vol. 251, pp. 1001–1008, 2017.

- [139] Y. K. Lee *et al.*, "Dissolution of monocrystalline silicon nanomembranes and their use as encapsulation layers and electrical interfaces in water-soluble electronics," *ACS Nano*, vol. 11, no. 12, pp. 12562–12572, 2017.
- [140] A. C. Patil and N. V Thakor, "Implantable neurotechnologies: a review of micro-and nanoelectrodes for neural recording," *Med. Biol. Eng. Comput.*, vol. 54, no. 1, pp. 23–44, 2016.
- [141] A. Gilletti and J. Muthuswamy, "Brain micromotion around implants in the rodent somatosensory cortex," *J. Neural Eng.*, vol. 3, no. 3, p. 189, 2006.
- [142] S. P. Lacour, G. Courtine, and J. Guck, "Materials and technologies for soft implantable neuroprostheses," *Nat. Rev. Mater.*, vol. 1, no. 10, pp. 1–14, 2016.
- [143] S. F. Cogan, A. A. Guzelian, W. F. Agnew, T. G. H. Yuen, and D. B. McCreery, "Overpulsing degrades activated iridium oxide films used for intracortical neural stimulation," *J. Neurosci. Methods*, vol. 137, no. 2, pp. 141–150, 2004.
- [144] C. Marin and E. Fernández, "Biocompatibility of intracortical microelectrodes: current status and future prospects," *Front. Neuroeng.*, vol. 3, p. 8, 2010.
- [145] S. Wang et al., "Mechanics of epidermal electronics," J. Appl. Mech., vol. 79, no. 3, 2012.
- [146] I. R. Minev *et al.*, "Electronic dura mater for long-term multimodal neural interfaces," *Science (80-.).*, vol. 347, no. 6218, pp. 159–163, 2015.
- [147] Y. Sun, B. Akhremitchev, and G. C. Walker, "Using the adhesive interaction between atomic force microscopy tips and polymer surfaces to measure the elastic modulus of compliant samples," *Langmuir*, vol. 20, no. 14, pp. 5837–5845, 2004.
- [148] J. H. Lee, H. Kim, J. H. Kim, and S.-H. Lee, "Soft implantable microelectrodes for future medicine: prosthetics, neural signal recording and neuromodulation," *Lab Chip*, vol. 16, no. 6, pp. 959–976, 2016.
- [149] M. S. Beattie, A. A. Farooqui, and J. C. BRESNAHAN, "Review of current evidence for apoptosis after spinal cord injury," *J. Neurotrauma*, vol. 17, no. 10, pp. 915–925, 2000.
- [150] M. B. Christensen, S. M. Pearce, N. M. Ledbetter, D. J. Warren, G. A. Clark, and P. A. Tresco, "The foreign body response to the Utah Slant Electrode Array in the cat sciatic nerve," *Acta Biomater.*, vol. 10, no. 11, pp. 4650–4660, 2014.

- [151] S. K. Moore, "Shape-shifting electrodes for the brain: Materials that have memory could make medical implants easier to place-[News]," *IEEE Spectr.*, vol. 56, no. 2, pp. 10–11, 2019.
- [152] R. Zhao *et al.*, "3D Expandable Microwire Electrode Arrays Made of Programmable Shape Memory Materials," in *2018 IEEE International Electron Devices Meeting (IEDM)*, 2018, pp. 22–29.
- [153] A. Lendlein and S. Kelch, "Shape-memory polymers," *Angew. Chemie Int. Ed.*, vol. 41, no. 12, pp. 2034–2057, 2002.
- [154] M. Ecker *et al.*, "Sterilization of thiol-ene/acrylate based shape memory polymers for biomedical applications," *Macromol. Mater. Eng.*, vol. 302, no. 2, p. 1600331, 2017.
- [155] B. J. Black *et al.*, "In vitro compatibility testing of thiol-ene/acrylate-based shape memory polymers for use in implantable neural interfaces," *J. Biomed. Mater. Res. Part A*, vol. 106, no. 11, pp. 2891–2898, 2018.
- [156] Z. Fekete and A. Pongrácz, "Multifunctional soft implants to monitor and control neural activity in the central and peripheral nervous system: A review," *Sensors Actuators B Chem.*, vol. 243, pp. 1214–1223, 2017.
- [157] D.-W. Park *et al.*, "Electrical neural stimulation and simultaneous in vivo monitoring with transparent graphene electrode arrays implanted in GCaMP6f mice," *ACS Nano*, vol. 12, no. 1, pp. 148–157, 2018.
- [158] E. Castagnola *et al.*, "Recording high frequency neural signals using conformable and low-impedance ECoG electrodes arrays coated with PEDOT-PSS-PEG," in *Advances in Science and Technology*, 2017, vol. 102, pp. 77–85.
- [159] W. Yang, A. Broski, J. Wu, Q. H. Fan, and W. Li, "Characteristics of transparent, PEDOT: PSS-coated indium-tin-oxide (ITO) microelectrodes," *IEEE Trans. Nanotechnol.*, vol. 17, no. 4, pp. 701–704, 2017.
- [160] K. J. Seo *et al.*, "Transparent electrophysiology microelectrodes and interconnects from metal nanomesh," *ACS Nano*, vol. 11, no. 4, pp. 4365–4372, 2017.
- [161] Y. Qiang *et al.*, "Transparent arrays of bilayer-nanomesh microelectrodes for simultaneous electrophysiology and two-photon imaging in the brain," *Sci. Adv.*, vol. 4, no. 9, p. eaat0626, 2018.

- [162] J.-M. Kim, C. Im, and W. R. Lee, "Plateau-shaped flexible polymer microelectrode array for neural recording," *Polymers (Basel)*., vol. 9, no. 12, p. 690, 2017.
- [163] L. Ren *et al.*, "Fabrication of flexible microneedle array electrodes for wearable bio-signal recording," *Sensors*, vol. 18, no. 4, p. 1191, 2018.
- [164] A. N. Zorzos, E. S. Boyden, and C. G. Fonstad, "Multiwaveguide implantable probe for light delivery to sets of distributed brain targets," *Opt. Lett.*, vol. 35, no. 24, pp. 4133–4135, 2010.
- [165] A. Soltan *et al.*, "High Density, High Radiance \$\mu \$ LED Matrix for Optogenetic Retinal Prostheses and Planar Neural Stimulation," *IEEE Trans. Biomed. Circuits Syst.*, vol. 11, no. 2, pp. 347–359, 2017.
- [166] K. Y. Kwon, B. Sirowatka, A. Weber, and W. Li, "Opto-μECoG array: A hybrid neural interface with transparent μECoG electrode array and integrated LEDs for optogenetics," *IEEE Trans. Biomed. Circuits Syst.*, vol. 7, no. 5, pp. 593–600, 2013.
- [167] S. K. Mohanty and N. V Thakor, *Optogenetics: optical methods for cellular control*, vol. 8586. 2013.
- [168] S. Royer, B. V Zemelman, M. Barbic, A. Losonczy, G. Buzsáki, and J. C. Magee, "Multi-array silicon probes with integrated optical fibers: light-assisted perturbation and recording of local neural circuits in the behaving animal," *Eur. J. Neurosci.*, vol. 31, no. 12, pp. 2279–2291, 2010.
- [169] J. C. Williams and T. Denison, "From optogenetic technologies to neuromodulation therapies," *Sci. Transl. Med.*, vol. 5, no. 177, pp. 177ps6-177ps6, 2013.
- [170] G. H. Kim *et al.*, "Recent progress on microelectrodes in neural interfaces," *Materials* (*Basel*)., vol. 11, no. 10, p. 1995, 2018.
- [171] J. C. Barrese, J. Aceros, and J. P. Donoghue, "Scanning electron microscopy of chronically implanted intracortical microelectrode arrays in non-human primates," *J. Neural Eng.*, vol. 13, no. 2, p. 26003, 2016.
- [172] A. Burton *et al.*, "Wireless, battery-free subdermally implantable photometry systems for chronic recording of neural dynamics," *Proc. Natl. Acad. Sci.*, vol. 117, no. 6, pp. 2835–2845, 2020.
- [173] P. A. House, J. D. MacDonald, P. A. Tresco, and R. A. Normann, "Acute microelectrode

- array implantation into human neocortex: preliminary technique and histological considerations," *Neurosurg. Focus*, vol. 20, no. 5, pp. 1–4, 2006.
- [174] D.-H. Kim *et al.*, "Dissolvable films of silk fibroin for ultrathin conformal bio-integrated electronics," *Nat. Mater.*, vol. 9, no. 6, pp. 511–517, 2010.
- [175] J. A. Fairfield, "Nanostructured materials for neural electrical interfaces," *Adv. Funct. Mater.*, vol. 28, no. 12, p. 1701145, 2018.
- [176] H.-B. Zhou *et al.*, "Integration of Au nanorods with flexible thin-film microelectrode arrays for improved neural interfaces," *J. microelectromechanical Syst.*, vol. 18, no. 1, pp. 88–96, 2009.
- [177] J.-H. Kim, G. Kang, Y. Nam, and Y.-K. Choi, "Surface-modified microelectrode array with flake nanostructure for neural recording and stimulation," *Nanotechnology*, vol. 21, no. 8, p. 85303, 2010.
- [178] C. Nick, S. Quednau, R. Sarwar, H. F. Schlaak, and C. Thielemann, "High aspect ratio gold nanopillars on microelectrodes for neural interfaces," *Microsyst. Technol.*, vol. 20, no. 10–11, pp. 1849–1857, 2014.
- [179] Q. Zeng, K. Xia, B. Sun, Y. Yin, T. Wu, and M. S. Humayun, "Electrodeposited iridium oxide on platinum nanocones for improving neural stimulation microelectrodes," *Electrochim. Acta*, vol. 237, pp. 152–159, 2017.
- [180] B. J. Black *et al.*, "Chronic recording and electrochemical performance of Utah microelectrode arrays implanted in rat motor cortex," *J. Neurophysiol.*, vol. 120, no. 4, pp. 2083–2090, 2018.
- [181] W.-H. Chen *et al.*, "Simple fabrication of a highly conductive and passivated PEDOT: PSS film via cryo-controlled quasi-congealing spin-coating for flexible perovskite solar cells," *J. Mater. Chem. C*, vol. 7, no. 33, pp. 10247–10256, 2019.
- [182] A. Ghazavi, J. Maeng, M. Black, S. Salvi, and S. F. Cogan, "Electrochemical characteristics of ultramicro-dimensioned SIROF electrodes for neural stimulation and recording," *J. Neural Eng.*, vol. 17, no. 1, p. 16022, 2020.
- [183] G. E. Loeb, R. A. Peck, and J. Martyniuk, "Toward the ultimate metal microelectrode," *J. Neurosci. Methods*, vol. 63, no. 1–2, pp. 175–183, 1995.
- [184] I. R. Cassar et al., "Electrodeposited platinum-iridium coating improves in vivo recording

- performance of chronically implanted microelectrode arrays," *Biomaterials*, vol. 205, pp. 120–132, 2019.
- [185] L. Maiolo, D. Polese, and A. Convertino, "The rise of flexible electronics in neuroscience, from materials selection to in vitro and in vivo applications," *Adv. Phys. X*, vol. 4, no. 1, p. 1664319, 2019.
- [186] M. Zhang, Z. Tang, X. Liu, and J. Van der Spiegel, "Electronic neural interfaces," *Nat. Electron.*, pp. 1–10, 2020.
- [187] Y. Jiang and B. Tian, "Inorganic semiconductor biointerfaces," *Nat. Rev. Mater.*, vol. 3, no. 12, pp. 473–490, 2018.
- [188] J. J. Jun *et al.*, "Fully integrated silicon probes for high-density recording of neural activity," *Nature*, vol. 551, no. 7679, pp. 232–236, 2017.
- [189] J. T. Robinson, M. Jorgolli, A. K. Shalek, M.-H. Yoon, R. S. Gertner, and H. Park, "Vertical nanowire electrode arrays as a scalable platform for intracellular interfacing to neuronal circuits," *Nat. Nanotechnol.*, vol. 7, no. 3, pp. 180–184, 2012.
- [190] R. Liu *et al.*, "High density individually addressable nanowire arrays record intracellular activity from primary rodent and human stem cell derived neurons," *Nano Lett.*, vol. 17, no. 5, pp. 2757–2764, 2017.
- [191] E. Saracino *et al.*, "A Glial-Silicon Nanowire Electrode Junction Enabling Differentiation and Noninvasive Recording of Slow Oscillations from Primary Astrocytes," *Adv. Biosyst.*, vol. 4, no. 4, p. 1900264, 2020.
- [192] X. Dai, W. Zhou, T. Gao, J. Liu, and C. M. Lieber, "Three-dimensional mapping and regulation of action potential propagation in nanoelectronics-innervated tissues," *Nat. Nanotechnol.*, vol. 11, no. 9, pp. 776–782, 2016.
- [193] M. Hutzler, A. Lambacher, B. Eversmann, M. Jenkner, R. Thewes, and P. Fromherz, "High-resolution multitransistor array recording of electrical field potentials in cultured brain slices," *J. Neurophysiol.*, vol. 96, no. 3, pp. 1638–1645, 2006.
- [194] F. Patolsky, "Detection, Stimulation, and Inhibition of Neuronal," *Am. Phys. Soc.*, vol. 14, 2006.
- [195] F. Veliev, Z. Han, D. Kalita, A. Briançon-Marjollet, V. Bouchiat, and C. Delacour, "Recording spikes activity in cultured hippocampal neurons using flexible or transparent

- graphene transistors," Front. Neurosci., vol. 11, p. 466, 2017.
- [196] K. J. Yu *et al.*, "Bioresorbable silicon electronics for transient spatiotemporal mapping of electrical activity from the cerebral cortex," *Nat. Mater.*, vol. 15, no. 7, pp. 782–791, 2016.
- [197] A. Falco, B. Matarese, P. Feyen, F. Benfenati, P. Lugli, and J. C. de Mello, "Investigation of the stability and biocompatibility of commonly used electrode materials in organic neurooptoelectronics," *IEEE Trans. Nanotechnol.*, vol. 15, no. 5, pp. 746–753, 2016.
- [198] R. Gao *et al.*, "Outside looking in: nanotube transistor intracellular sensors," *Nano Lett.*, vol. 12, no. 6, pp. 3329–3333, 2012.
- [199] C. Dagdeviren *et al.*, "Transient, biocompatible electronics and energy harvesters based on ZnO," *small*, vol. 9, no. 20, pp. 3398–3404, 2013.
- [200] J. Lee, I. Ozden, Y.-K. Song, and A. V Nurmikko, "Transparent intracortical microprobe array for simultaneous spatiotemporal optical stimulation and multichannel electrical recording," *Nat. Methods*, vol. 12, no. 12, pp. 1157–1162, 2015.
- [201] G. Gutierrez-Heredia, O. Rodriguez-Lopez, A. Garcia-Sandoval, and W. E. Voit, "Highly Stable Indium-Gallium-Zinc-Oxide Thin-Film Transistors on Deformable Softening Polymer Substrates," *Adv. Electron. Mater.*, vol. 3, no. 10, p. 1700221, 2017.
- [202] D. Mao, J. Morley, Z. Zhang, M. Donnelly, and G. Xu, "High-yield passive Si photodiode array towards optical neural recording," *IEEE Electron Device Lett.*, vol. 39, no. 4, pp. 524–527, 2018.
- [203] F. L. Huerta *et al.*, "Biocompatibility and surface properties of hydrogenated amorphous silicon-germanium thin films prepared by LF-PECVD," in *IOP Conference Series: Materials Science and Engineering*, 2019, vol. 628, no. 1, p. 12003.
- [204] R. Green and M. R. Abidian, "Conducting polymers for neural prosthetic and neural interface applications," *Adv. Mater.*, vol. 27, no. 46, pp. 7620–7637, 2015.
- [205] J. Rivnay *et al.*, "Structural control of mixed ionic and electronic transport in conducting polymers," *Nat. Commun.*, vol. 7, no. 1, pp. 1–9, 2016.
- [206] J. Rivnay, H. Wang, L. Fenno, K. Deisseroth, and G. G. Malliaras, "Next-generation probes, particles, and proteins for neural interfacing," *Sci. Adv.*, vol. 3, no. 6, p. e1601649, 2017.
- [207] T.-H. Le, Y. Kim, and H. Yoon, "Electrical and electrochemical properties of conducting

- polymers," *Polymers (Basel).*, vol. 9, no. 4, p. 150, 2017.
- [208] M. Ganji, A. T. Elthakeb, A. Tanaka, V. Gilja, E. Halgren, and S. A. Dayeh, "Scaling Effects on the Electrochemical Performance of poly (3, 4-ethylenedioxythiophene (PEDOT), Au, and Pt for Electrocorticography Recording," *Adv. Funct. Mater.*, vol. 27, no. 42, p. 1703018, 2017.
- [209] D. Khodagholy *et al.*, "Organic electronics for high-resolution electrocorticography of the human brain," *Sci. Adv.*, vol. 2, no. 11, p. e1601027, 2016.
- [210] W. Yang, J. Wu, Q. H. Fan, and W. Li, "Highly Conductive, Transparent, and Antireflective PEDOT: PSS/ITO/Ag/ITO on Parylene-C with Tunable Peak Transmittance," in *2019 IEEE 32nd International Conference on Micro Electro Mechanical Systems (MEMS)*, 2019, pp. 525–528.
- [211] A. S. Pranti, A. Schander, A. Bödecker, and W. Lang, "PEDOT: PSS coating on gold microelectrodes with excellent stability and high charge injection capacity for chronic neural interfaces," *Sensors Actuators B Chem.*, vol. 275, pp. 382–393, 2018.
- [212] J. Yang, D. H. Kim, J. L. Hendricks, M. Leach, R. Northey, and D. C. Martin, "Ordered surfactant-templated poly (3, 4-ethylenedioxythiophene)(PEDOT) conducting polymer on microfabricated neural probes," *Acta Biomater.*, vol. 1, no. 1, pp. 125–136, 2005.
- [213] M. R. Abidian, J. M. Corey, D. R. Kipke, and D. C. Martin, "Conducting-polymer nanotubes improve electrical properties, mechanical adhesion, neural attachment, and neurite outgrowth of neural electrodes," *small*, vol. 6, no. 3, pp. 421–429, 2010.
- [214] C. Boehler, F. Oberueber, S. Schlabach, T. Stieglitz, and M. Asplund, "Long-term stable adhesion for conducting polymers in biomedical applications: IrOx and nanostructured platinum solve the chronic challenge," *ACS Appl. Mater. Interfaces*, vol. 9, no. 1, pp. 189–197, 2017.
- [215] L. J. Juarez-Hernandez *et al.*, "Bio-hybrid interfaces to study neuromorphic functionalities: New multidisciplinary evidences of cell viability on poly (anyline)(PANI), a semiconductor polymer with memristive properties," *Biophys. Chem.*, vol. 208, pp. 40–47, 2016.
- [216] Z. D. Kojabad, S. A. Shojaosadati, S. M. Firoozabadi, and S. Hamedi, "Polypyrrole nanotube modified by gold nanoparticles for improving the neural microelectrodes," *J. Solid State Electrochem.*, vol. 23, no. 5, pp. 1533–1539, 2019.
- [217] S. Nagane et al., "Functionalized Polythiophene Copolymers for Electronic Biomedical

- Devices," MRS Adv., vol. 5, no. 18–19, pp. 943–956, 2020.
- [218] N. K. Guimard, N. Gomez, and C. E. Schmidt, "Conducting polymers in biomedical engineering," *Prog. Polym. Sci.*, vol. 32, no. 8–9, pp. 876–921, 2007.
- [219] A. F. Diaz and B. Hall, "Mechanical properties of electrochemically prepared polypyrrole films," *IBM J. Res. Dev.*, vol. 27, no. 4, pp. 342–347, 1983.
- [220] B. Sevil and K. Zuhal, "Synthesis and characterization of polypyrrole nanoparticles and their nanocomposites with poly (propylene)," in *Macromolecular symposia*, 2010, vol. 295, no. 1, pp. 59–64.
- [221] D. Passeri, A. Alippi, A. Bettucci, M. Rossi, E. Tamburri, and M. L. Terranova, "Indentation modulus and hardness of polyaniline thin films by atomic force microscopy," *Synth. Met.*, vol. 161, no. 1–2, pp. 7–12, 2011.
- [222] X.-S. Wang and X.-Q. Feng, "Effects of thickness on mechanical properties of conducting polythiophene films," *J. Mater. Sci. Lett.*, vol. 21, no. 9, pp. 715–717, 2002.
- [223] K. I. Bolotin *et al.*, "Ultrahigh electron mobility in suspended graphene," *Solid State Commun.*, vol. 146, no. 9–10, pp. 351–355, 2008.
- [224] A. A. Balandin *et al.*, "Superior thermal conductivity of single-layer graphene," *Nano Lett.*, vol. 8, no. 3, pp. 902–907, 2008.
- [225] J. Wang, F. Ma, and M. Sun, "Graphene, hexagonal boron nitride, and their heterostructures: properties and applications," *RSC Adv.*, vol. 7, no. 27, pp. 16801–16822, 2017.
- [226] A. Armano and S. Agnello, "Two-dimensional carbon: a review of synthesis methods, and electronic, optical, and vibrational properties of single-layer graphene," *C—Journal Carbon Res.*, vol. 5, no. 4, p. 67, 2019.
- [227] X. Liu *et al.*, "Transparent artifact-free graphene electrodes for compact closed-loop optogenetics systems," in 2017 IEEE International Electron Devices Meeting (IEDM), 2017, pp. 21–26.
- [228] D. Shin *et al.*, "Synthesis and applications of graphene electrodes," *Carbon Lett.* (*Carbon Lett.*), vol. 13, no. 1, pp. 1–16, 2012.
- [229] C.-H. Chen *et al.*, "A flexible hydrophilic-modified graphene microprobe for neural and cardiac recording," *Nanomedicine Nanotechnology, Biol. Med.*, vol. 9, no. 5, pp. 600–604,

2013.

- [230] D. Kireev *et al.*, "Graphene field-effect transistors for in vitro and ex vivo recordings," *IEEE Trans. Nanotechnol.*, vol. 16, no. 1, pp. 140–147, 2016.
- [231] T. D. Y. Kozai *et al.*, "Ultrasmall implantable composite microelectrodes with bioactive surfaces for chronic neural interfaces," *Nat. Mater.*, vol. 11, no. 12, pp. 1065–1073, 2012.
- [232] V. Patel *et al.*, "Addressing the burden of mental, neurological, and substance use disorders: key messages from Disease Control Priorities," *Lancet*, vol. 387, no. 10028, pp. 1672–1685, 2016.
- [233] P. R. Patel *et al.*, "Carbon Fiber Electrode Array for the Detection of Electrophysiological and Dopaminergic Activity," in *232nd ECS Meeting (October 1-5, 2017)*, 2017.
- [234] M. A. Hejazi *et al.*, "High Fidelity Bidirectional Neural Interfacing with Carbon Fiber Microelectrodes Coated with Boron-Doped Carbon Nanowalls: An Acute Study," *Adv. Funct. Mater.*, p. 2006101, 2020.
- [235] G. Guitchounts, J. E. Markowitz, W. A. Liberti, and T. J. Gardner, "A carbon-fiber electrode array for long-term neural recording," *J. Neural Eng.*, vol. 10, no. 4, p. 46016, 2013.
- [236] P. R. Patel *et al.*, "Insertion of linear 8.4 µm diameter 16 channel carbon fiber electrode arrays for single unit recordings," *J. Neural Eng.*, vol. 12, no. 4, p. 46009, 2015.
- [237] F. Deku, A. Joshi-Imre, A. Mertiri, T. J. Gardner, and S. F. Cogan, "Electrodeposited iridium oxide on carbon fiber ultramicroelectrodes for neural recording and stimulation," *J. Electrochem. Soc.*, vol. 165, no. 9, p. D375, 2018.
- [238] W. F. Gillis *et al.*, "Carbon fiber on polyimide ultra-microelectrodes," *J. Neural Eng.*, vol. 15, no. 1, p. 16010, 2018.
- [239] T. L. Massey, S. R. Santacruz, J. F. Hou, K. S. J. Pister, J. M. Carmena, and M. M. Maharbiz, "A high-density carbon fiber neural recording array technology," *J. Neural Eng.*, vol. 16, no. 1, p. 16024, 2019.
- [240] Z. Yu, T. E. McKnight, M. N. Ericson, A. V Melechko, M. L. Simpson, and B. Morrison III, "Vertically aligned carbon nanofiber as nano-neuron interface for monitoring neural function," *Nanomedicine Nanotechnology, Biol. Med.*, vol. 8, no. 4, pp. 419–423, 2012.
- [241] L. Lu et al., "Soft and MRI compatible neural electrodes from carbon nanotube fibers,"

- Nano Lett., vol. 19, no. 3, pp. 1577–1586, 2019.
- [242] Q. Zhang, J. Huang, M. Zhao, W. Qian, and F. Wei, "Carbon nanotube mass production: principles and processes," *ChemSusChem*, vol. 4, no. 7, pp. 864–889, 2011.
- [243] A. Eatemadi *et al.*, "Carbon nanotubes: properties, synthesis, purification, and medical applications," *Nanoscale Res. Lett.*, vol. 9, no. 1, p. 393, 2014.
- [244] N. Saifuddin, A. Z. Raziah, and A. R. Junizah, "Carbon nanotubes: a review on structure and their interaction with proteins," *J. Chem.*, vol. 2013, 2013.
- [245] E. W. Keefer, B. R. Botterman, M. I. Romero, A. F. Rossi, and G. W. Gross, "Carbon nanotube coating improves neuronal recordings," *Nat. Nanotechnol.*, vol. 3, no. 7, pp. 434–439, 2008.
- [246] I. Yoon, K. Hamaguchi, I. V Borzenets, G. Finkelstein, R. Mooney, and B. R. Donald, "Intracellular neural recording with pure carbon nanotube probes," *PLoS One*, vol. 8, no. 6, p. e65715, 2013.
- [247] A. Ansaldo, E. Castagnola, E. Maggiolini, L. Fadiga, and D. Ricci, "Superior electrochemical performance of carbon nanotubes directly grown on sharp microelectrodes," *ACS Nano*, vol. 5, no. 3, pp. 2206–2214, 2011.
- [248] C.-M. Lin, Y.-T. Lee, S.-R. Yeh, and W. Fang, "Flexible carbon nanotubes electrode for neural recording," *Biosens. Bioelectron.*, vol. 24, no. 9, pp. 2791–2797, 2009.
- [249] C.-H. Chen *et al.*, "Hydrophilic modification of neural microelectrode arrays based on multi-walled carbon nanotubes," *Nanotechnology*, vol. 21, no. 48, p. 485501, 2010.
- [250] H.-C. Su *et al.*, "A cone-shaped 3D carbon nanotube probe for neural recording," *Biosens. Bioelectron.*, vol. 26, no. 1, pp. 220–227, 2010.
- [251] A. I. Pan *et al.*, "Direct-growth carbon nanotubes on 3D structural microelectrodes for electrophysiological recording," *Analyst*, vol. 141, no. 1, pp. 279–284, 2016.
- [252] S.-J. Yen *et al.*, "The enhancement of neural growth by amino-functionalization on carbon nanotubes as a neural electrode," *Biosens. Bioelectron.*, vol. 26, no. 10, pp. 4124–4132, 2011.
- [253] D. Furtado, M. Björnmalm, S. Ayton, A. I. Bush, K. Kempe, and F. Caruso, "Overcoming the blood–brain barrier: the role of nanomaterials in treating neurological diseases," *Adv.*

- Mater., vol. 30, no. 46, p. 1801362, 2018.
- [254] M. Vomero *et al.*, "A novel pattern transfer technique for mounting glassy carbon microelectrodes on polymeric flexible substrates," *J. Micromechanics Microengineering*, vol. 26, no. 2, p. 25018, 2016.
- [255] E. Castagnola *et al.*, "In vivo dopamine detection and single unit recordings using intracortical glassy carbon microelectrode arrays," *MRS Adv.*, vol. 3, no. 29, p. 1629, 2018.
- [256] B. Chen *et al.*, "Penetrating glassy carbon neural electrode arrays for brain-machine interfaces.," *Biomed. Microdevices*, vol. 22, no. 3, p. 43, 2020.
- [257] M. Alcaide, A. Taylor, M. Fjorback, V. Zachar, and C. P. Pennisi, "Boron-doped nanocrystalline diamond electrodes for neural interfaces: in vivo biocompatibility evaluation," *Front. Neurosci.*, vol. 10, p. 87, 2016.
- [258] C. Hébert *et al.*, "Monitoring the evolution of boron doped porous diamond electrode on flexible retinal implant by OCT and in vivo impedance spectroscopy," *Mater. Sci. Eng. C*, vol. 69, pp. 77–84, 2016.
- [259] M. McDonald, A. Monaco, F. Vahidpour, K. Haenen, M. Giugliano, and M. Nesladek, "Diamond microelectrode arrays for in vitro neuronal recordings," *Mrs Commun.*, vol. 7, no. 3, pp. 683–690, 2017.
- [260] K.-H. Yang and R. J. Narayan, "Biocompatibility and functionalization of diamond for neural applications," *Curr. Opin. Biomed. Eng.*, vol. 10, pp. 60–68, 2019.
- [261] C. Wild and E. Wörner, "The CVD diamond booklet," *Website. www. diamond-materials. com/download*, 2004.
- [262] D. J. Garrett, W. Tong, D. A. Simpson, and H. Meffin, "Diamond for neural interfacing: a review," *Carbon N. Y.*, vol. 102, pp. 437–454, 2016.
- [263] B. Fan, Y. Zhu, R. Rechenberg, C. A. Rusinek, M. F. Becker, and W. Li, "Large-scale, all polycrystalline diamond structures transferred onto flexible Parylene-C films for neurotransmitter sensing," *Lab Chip*, vol. 17, no. 18, pp. 3159–3167, 2017.
- [264] N. Driscoll *et al.*, "Two-dimensional Ti3C2 MXene for high-resolution neural interfaces," *ACS Nano*, vol. 12, no. 10, pp. 10419–10429, 2018.
- [265] N. Driscoll et al., "Fabrication of Ti3C2 MXene Microelectrode Arrays for In Vivo Neural

- Recording," JoVE (Journal Vis. Exp., no. 156, p. e60741, 2020.
- [266] R. K. Pal, A. A. Farghaly, C. Wang, M. M. Collinson, S. C. Kundu, and V. K. Yadavalli, "Conducting polymer-silk biocomposites for flexible and biodegradable electrochemical sensors," *Biosens. Bioelectron.*, vol. 81, pp. 294–302, 2016.
- [267] U. Lee, C.-J. Yoo, Y.-J. Kim, and Y.-M. Yoo, "Cytotoxicity of gold nanoparticles in human neural precursor cells and rat cerebral cortex," *J. Biosci. Bioeng.*, vol. 121, no. 3, pp. 341–344, 2016.
- [268] A. Zátonyi, F. Fedor, Z. Borhegyi, and Z. Fekete, "In vitro and in vivo stability of black-platinum coatings on flexible, polymer microECoG arrays," *J. Neural Eng.*, vol. 15, no. 5, p. 54003, 2018.
- [269] Y. J. Lee, H. Kim, J. Y. Kang, S. H. Do, and S. H. Lee, "Biofunctionalization of nerve interface via biocompatible polymer-roughened Pt black on cuff electrode for chronic recording," *Adv. Healthc. Mater.*, vol. 6, no. 6, p. 1601022, 2017.
- [270] Y.-S. Sohn *et al.*, "Mechanical properties of silicon nanowires," *Nanoscale Res. Lett.*, vol. 5, no. 1, p. 211, 2010.
- [271] L. Marcon and R. Boukherroub, "Biocompatibility of semiconducting silicon nanowires," in *Semiconducting Silicon Nanowires for Biomedical Applications*, Elsevier, 2014, pp. 62–85.
- [272] W. Bai *et al.*, "Bioresorbable photonic devices for the spectroscopic characterization of physiological status and neural activity," *Nat. Biomed. Eng*, vol. 3, no. 8, pp. 644–654, 2019.
- [273] T.-C. Li and R.-C. Chang, "Improving the performance of ITO thin films by coating PEDOT: PSS," *Int. J. Precis. Eng. Manuf. Technol.*, vol. 1, no. 4, pp. 329–334, 2014.
- [274] S. K. Lee, H. Kim, and B. S. Shim, "Graphene: an emerging material for biological tissue engineering," *Carbon Lett*, vol. 14, no. 2, pp. 63–75, 2013.
- [275] S. Farzamfar *et al.*, "A novel polycaprolactone/carbon nanofiber composite as a conductive neural guidance channel: An in vitro and in vivo study," *Prog. Biomater.*, vol. 8, no. 4, pp. 239–248, 2019.
- [276] J. G. Lawrence, L. M. Berhan, and A. Nadarajah, "Elastic properties and morphology of individual carbon nanofibers," *ACS Nano*, vol. 2, no. 6, pp. 1230–1236, 2008.

- [277] L. Deng, S. J. Eichhorn, C.-C. Kao, and R. J. Young, "The effective Young's modulus of carbon nanotubes in composites," *ACS Appl. Mater. Interfaces*, vol. 3, no. 2, pp. 433–440, 2011.
- [278] M. Vomero *et al.*, "Highly stable glassy carbon interfaces for long-term neural stimulation and low-noise recording of brain activity," *Sci. Rep.*, vol. 7, no. 1, pp. 1–14, 2017.
- [279] B. Fan and W. Li, "Miniaturized optogenetic neural implants: a review," *Lab Chip*, vol. 15, no. 19, pp. 3838–3855, 2015.
- [280] X. Guo, X. Liu, F. Lin, H. Li, Y. Fan, and N. Zhang, "Highly conductive transparent organic electrodes with multilayer structures for rigid and flexible optoelectronics," *Sci. Rep.*, vol. 5, p. 10569, 2015.
- [281] M.-C. Tsai and P.-Y. Chen, "Voltammetric study and electrochemical detection of hexavalent chromium at gold nanoparticle-electrodeposited indium tinoxide (ITO) electrodes in acidic media," *Talanta*, vol. 76, no. 3, pp. 533–539, 2008.
- [282] A. Al-Chalabi, R. S. Delamont, and M. R. Turner, *The brain: A beginner's guide*. Oneworld Publications, 2008.
- [283] A. A. Guex, N. Vachicouras, A. E. Hight, M. C. Brown, D. J. Lee, and S. P. Lacour, "Conducting polymer electrodes for auditory brainstem implants," *J. Mater. Chem. B*, vol. 3, no. 25, pp. 5021–5027, 2015.
- [284] M. P. De Jong, L. J. Van Ijzendoorn, and M. J. A. De Voigt, "Stability of the interface between indium-tin-oxide and poly (3, 4-ethylenedioxythiophene)/poly (styrenesulfonate) in polymer light-emitting diodes," *Appl. Phys. Lett.*, vol. 77, no. 14, pp. 2255–2257, 2000.
- [285] B. Gosselin *et al.*, "A mixed-signal multichip neural recording interface with bandwidth reduction," *IEEE Trans. Biomed. Circuits Syst.*, vol. 3, no. 3, pp. 129–141, 2009.
- [286] D. Zhao *et al.*, "Highly flexible and conductive cellulose-mediated PEDOT: PSS/MWCNT composite films for supercapacitor electrodes," *ACS Appl. Mater. Interfaces*, vol. 9, no. 15, pp. 13213–13222, 2017.
- [287] H. A. Macleod, *Thin-film optical filters*. CRC press, 2017.
- [288] J. Gasiorowski, R. Menon, K. Hingerl, M. Dachev, and N. S. Sariciftci, "Surface morphology, optical properties and conductivity changes of poly (3, 4-ethylenedioxythiophene): poly (styrenesulfonate) by using additives," *Thin Solid Films*, vol.

- 536, pp. 211–215, 2013.
- [289] D. Zhou and E. Greenbaum, "Implantable neural prostheses 2, Techniques and Engineering Approaches. New York: Springer," 2010.
- [290] H. Hillebrandt and M. Tanaka, "Electrochemical characterization of self-assembled alkylsiloxane monolayers on indium—tin oxide (ITO) semiconductor electrodes," *J. Phys. Chem. B*, vol. 105, no. 19, pp. 4270–4276, 2001.
- [291] T. Yokota *et al.*, "Ultraflexible organic photonic skin," *Sci. Adv.*, vol. 2, no. 4, p. e1501856, 2016.
- [292] N. M. Ahmed, F. A. Sabah, H. I. Abdulgafour, A. Alsadig, A. Sulieman, and M. Alkhoaryef, "The effect of post annealing temperature on grain size of indium-tin-oxide for optical and electrical properties improvement," *Results Phys.*, vol. 13, p. 102159, 2019.
- [293] J.-B. Lyau, H.-C. Wu, and H. Chen, "Biological studies with tin oxide materials," in *Tin Oxide Materials*, Elsevier, 2020, pp. 599–613.
- [294] S. Ziaei, Q. Wu, J. Fitch, M. Elbadry, and M. A. Zikry, "Channel Cracking and Interfacial Delamination of Indium Tin Oxide (ITO) Nano-Sized Films on Polyethylene Terephthalate (PET) Substrates: Experiments and Modeling," *Exp. Mech.*, vol. 59, no. 5, pp. 703–712, 2019.
- [295] A. Zátonyi *et al.*, "Transparent, low-autofluorescence microECoG device for simultaneous Ca2+ imaging and cortical electrophysiology in vivo," *J. Neural Eng.*, vol. 17, no. 1, p. 16062, 2020.
- [296] Y. Bi *et al.*, "Ultrathin Metal Films as the Transparent Electrode in ITO-Free Organic Optoelectronic Devices," *Adv. Opt. Mater.*, vol. 7, no. 6, p. 1800778, 2019.
- [297] Z. Chen *et al.*, "Flexible and Transparent Metal Oxide/Metal Grid Hybrid Interfaces for Electrophysiology and Optogenetics," *Adv. Mater. Technol.*, p. 2000322.
- [298] Y. Qiang *et al.*, "Bilayer nanomesh structures for transparent recording and stimulating microelectrodes," *Adv. Funct. Mater.*, vol. 27, no. 48, p. 1704117, 2017.
- [299] L. V Kayser and D. J. Lipomi, "Stretchable conductive polymers and composites based on PEDOT and PEDOT: PSS," *Adv. Mater.*, vol. 31, no. 10, p. 1806133, 2019.
- [300] J. Hossain, B. K. Mondal, S. K. Mostaque, S. R. Al Ahmed, and H. Shirai, "Optimization

- of multilayer anti-reflection coatings for efficient light management of PEDOT: PSS/c-Si heterojunction solar cells," *Mater. Res. Express*, vol. 7, no. 1, p. 15502, 2019.
- [301] E. Klein, K. Huber, O. Paul, and P. Ruther, "Low-temperature plasma annealing of sputtered indium tin oxide for transparent and conductive thin-films on glass and polymer substrates," *Thin Solid Films*, vol. 693, p. 137715, 2020.
- [302] H. Ohsaki, M. Suzuki, Y. Shibayama, A. Kinbara, and T. Watanabe, "Room temperature crystallization of indium tin oxide films on glass and polyethylene terephthalate substrates using rf plasma," *J. Vac. Sci. Technol. A Vacuum, Surfaces, Film.*, vol. 25, no. 4, pp. 1052–1055, 2007.
- [303] W. Chung, M. O. Thompson, P. Wickboldt, D. Toet, and P. G. Carey, "Room temperature indium tin oxide by XeCl excimer laser annealing for flexible display," *Thin Solid Films*, vol. 460, no. 1–2, pp. 291–294, 2004.
- [304] S. Ishibashi, Y. Higuchi, Y. Ota, and K. Nakamura, "Low resistivity indium—tin oxide transparent conductive films. II. Effect of sputtering voltage on electrical property of films," *J. Vac. Sci. Technol. A Vacuum, Surfaces, Film.*, vol. 8, no. 3, pp. 1403–1406, 1990.
- [305] C.-W. Lin *et al.*, "Admittance loci design method for multilayer surface plasmon resonance devices," *Sensors Actuators B Chem.*, vol. 117, no. 1, pp. 219–229, 2006.
- [306] Y.-J. Jen, W.-C. Liu, T.-K. Chen, S. Lin, and Y.-C. Jhang, "Design and deposition of a metal-like and admittance-matching metamaterial as an ultra-thin perfect absorber," *Sci. Rep.*, vol. 7, no. 1, pp. 1–10, 2017.
- [307] C. A. Schuh, "Nanoindentation studies of materials," *Mater. today*, vol. 9, no. 5, pp. 32–40, 2006.
- [308] Y. Sun, R. P. Padbury, H. I. Akyildiz, M. P. Goertz, J. A. Palmer, and J. S. Jur, "Influence of subsurface hybrid material growth on the mechanical properties of atomic layer deposited thin films on polymers," *Chem. Vap. Depos.*, vol. 19, no. 4-6, pp. 134–141, 2013.
- [309] D. K. Y. Tam, S. Ruan, P. Gao, and T. Yu, "High-performance ballistic protection using polymer nanocomposites," in *Advances in Military Textiles and Personal Equipment*, Elsevier, 2012, pp. 213–237.
- [310] F. Ejserholm *et al.*, "Biocompatibility of a polymer based on Off-Stoichiometry Thiol-Enes+ Epoxy (OSTE+) for neural implants," *Biomater. Res.*, vol. 19, no. 1, p. 19, 2015.

- [311] T. Wittkowski, J. Jorzick, H. Seitz, B. Schröder, K. Jung, and B. Hillebrands, "Elastic properties of indium tin oxide films," *Thin Solid Films*, vol. 398, pp. 465–470, 2001.
- [312] X. Xu, T. Mee, and X. Jia, "New era of optogenetics: from the central to peripheral nervous system," *Crit. Rev. Biochem. Mol. Biol.*, vol. 55, no. 1, pp. 1–16, 2020.
- [313] E. Montagni, F. Resta, A. L. A. Mascaro, and F. S. Pavone, "Optogenetics in Brain Research: From a Strategy to Investigate Physiological Function to a Therapeutic Tool," in *Photonics*, 2019, vol. 6, no. 3, p. 92.
- [314] B. Ji *et al.*, "Flexible and stretchable opto-electric neural interface for low-noise electrocorticogram recordings and neuromodulation in vivo," *Biosens. Bioelectron.*, p. 112009, 2020.
- [315] L. D. Garma, L. M. Ferrari, P. Scognamiglio, F. Greco, and F. Santoro, "Inkjet-printed PEDOT: PSS multi-electrode arrays for low-cost in vitro electrophysiology," *Lab Chip*, vol. 19, no. 22, pp. 3776–3786, 2019.
- [316] J. Park, F. Sun, Y. Xie, Z. Xiong, and G. Xu, "Low-Impedance Low-Artifact PEDOT: PSS-Coated Graphene Electrodes Towards High Density Optogenetic Electrophysiology," *IEEE Electron Device Lett.*, vol. 41, no. 8, pp. 1261–1264, 2020.
- [317] P. Kshirsagar *et al.*, "Transparent Graphene/PEDOT: PSS Microelectrodes for Electro-and Optophysiology," *Adv. Mater. Technol.*, vol. 4, no. 1, p. 1800318, 2019.
- [318] M. Le Van Quyen *et al.*, "Comparison of Hilbert transform and wavelet methods for the analysis of neuronal synchrony," *J. Neurosci. Methods*, vol. 111, no. 2, pp. 83–98, 2001.
- [319] C. Zhang, Y. Zhu, P. Yi, L. Peng, and X. Lai, "Fabrication of flexible silver nanowire conductive films and transmittance improvement based on moth-eye nanostructure array," *J. Micromechanics Microengineering*, vol. 27, no. 7, p. 75010, 2017.
- [320] K. Minoura *et al.*, "Antibacterial effects of the artificial surface of nanoimprinted moth-eye film," *PLoS One*, vol. 12, no. 9, 2017.
- [321] M. S. Farhan, E. Zalnezhad, A. R. Bushroa, and A. A. D. Sarhan, "Electrical and optical properties of indium-tin oxide (ITO) films by ion-assisted deposition (IAD) at room temperature," *Int. J. Precis. Eng. Manuf.*, vol. 14, no. 8, pp. 1465–1469, 2013.
- [322] S. Nasralla, D. D. Rhoads, and B. S. Appleby, "Prion Diseases," in *Neurological Complications of Infectious Diseases*, Springer, 2021, pp. 365–380.

- [323] M. Meattini, G. Giaccone, L. D'Incerti, and A. R. Giovagnoli, "Early and long-term cognitive features in sporadic Creutzfeldt-Jakob disease," *Neurol. Sci.*, pp. 1–3, 2021.
- [324] D. J. Stevens *et al.*, "Early onset prion disease from octarepeat expansion correlates with copper binding properties," *PLoS Pathog*, vol. 5, no. 4, p. e1000390, 2009.
- [325] C.-F. Yen, D. S. Harischandra, A. Kanthasamy, and S. Sivasankar, "Copper-induced structural conversion templates prion protein oligomerization and neurotoxicity," *Sci. Adv.*, vol. 2, no. 7, p. e1600014, 2016.
- [326] E. Koutsouraki *et al.*, "A probable role of copper in the comorbidity in Wilson's and Creutzfeldt-Jakob's Diseases: a case report," *Virol. J.*, vol. 17, no. 1, pp. 1–5, 2020.
- [327] B.-S. Wong *et al.*, "Copper refolding of prion protein," *Biochem. Biophys. Res. Commun.*, vol. 276, no. 3, pp. 1217–1224, 2000.
- [328] E. Leclerc, H. Serban, S. B. Prusiner, D. R. Burton, and R. A. Williamson, "Copper induces conformational changes in the N-terminal part of cell-surface PrP C," *Arch. Virol.*, vol. 151, no. 11, pp. 2103–2109, 2006.
- [329] D. S. Harischandra *et al.*, "Manganese-induced neurotoxicity: new insights into the triad of protein misfolding, mitochondrial impairment, and neuroinflammation," *Front. Neurosci.*, vol. 13, p. 654, 2019.
- [330] S. Manne *et al.*, "MANGANESE ACCELERATES TEMPLATE-DRIVEN PRION PROTEIN SEEDING ACTIVITY IN CELLS AND SLICE CULTURE MODELS OF PRION DISEASE," *Dev. diagnostic biomarkers proteinopathies Relev. early diagnosis Prions Park. Disord.*, vol. 1001, p. 68, 2019.
- [331] A. C. Martins Jr *et al.*, "Manganese-induced neurodegenerative diseases and possible therapeutic approaches," *Expert Rev. Neurother.*, vol. 20, no. 11, pp. 1109–1121, 2020.
- [332] D. S. Harischandra *et al.*, "Manganese promotes the aggregation and prion-like cell-to-cell exosomal transmission of α-synuclein," *Sci. Signal.*, vol. 12, no. 572, 2019.
- [333] P. Borah *et al.*, "Assessment of mobility and environmental risks associated with copper, manganese and zinc in soils of a dumping site around a Ramsar site," *Chemosphere*, vol. 254, p. 126852, 2020.
- [334] M. Kawahara, M. Kato-Negishi, and K. Tanaka, "Neurometals in the Pathogenesis of Prion Diseases," *Int. J. Mol. Sci.*, vol. 22, no. 3, p. 1267, 2021.